

5-1-2014

Physics of Gamma-ray Bursts and Multi-messenger Signals from Double Neutron Star Mergers

He Gao

University of Nevada, Las Vegas, gaoh2@unlv.nevada.edu

Follow this and additional works at: <https://digitalscholarship.unlv.edu/thesesdissertations>



Part of the [Cosmology, Relativity, and Gravity Commons](#), and the [Physics Commons](#)

Repository Citation

Gao, He, "Physics of Gamma-ray Bursts and Multi-messenger Signals from Double Neutron Star Mergers" (2014). *UNLV Theses, Dissertations, Professional Papers, and Capstones*. 2083.
<https://digitalscholarship.unlv.edu/thesesdissertations/2083>

This Dissertation is protected by copyright and/or related rights. It has been brought to you by Digital Scholarship@UNLV with permission from the rights-holder(s). You are free to use this Dissertation in any way that is permitted by the copyright and related rights legislation that applies to your use. For other uses you need to obtain permission from the rights-holder(s) directly, unless additional rights are indicated by a Creative Commons license in the record and/or on the work itself.

This Dissertation has been accepted for inclusion in UNLV Theses, Dissertations, Professional Papers, and Capstones by an authorized administrator of Digital Scholarship@UNLV. For more information, please contact digitalscholarship@unlv.edu.

PHYSICS OF GAMMA-RAY BURSTS AND MULTI-MESSENGER SIGNALS
FROM DOUBLE NEUTRON STAR MERGERS

by

He Gao

Bachelor of Science
Beijing Normal University
2007

Master of Science
Beijing Normal University
2010

A dissertation submitted in partial fulfillment
of the requirements for the

Doctor of Philosophy - Astronomy

**Department of Physics and Astronomy
College of Science
The Graduate College**

**University of Nevada, Las Vegas
May 2014**

Copyright by He Gao 2014
All Rights Reserved



THE GRADUATE COLLEGE

We recommend the dissertation prepared under our supervision by

He Gao

entitled

Physics of Gamma-Ray Bursts and Multi-messenger Signals from Double Neutrons Star Mergers

is approved in partial fulfillment of the requirements for the degree of

Doctor of Philosophy - Astronomy

Department of Physics and Astronomy

Bing Zhang, Ph.D., Committee Chair

Daniel Proga, Ph.D., Committee Member

Kentaro Nagamine, Ph.D., Committee Member

Amei Amei, Ph.D., Graduate College Representative

Kathryn Hausbeck Korgan, Ph.D., Interim Dean of the Graduate College

May 2014

ABSTRACT

Physics of Gamma-ray Bursts and Multi-messenger Signals from Double Neutron Star Mergers

by

He Gao

Dr. Bing Zhang, Examination Committee Chair
Professor of Physics
University of Nevada, Las Vegas

My dissertation includes two parts:

Physics of Gamma-Ray Bursts (GRBs): Gamma-ray bursts are multi-wavelength transients, with both prompt γ -ray emission and late time afterglow emission observed by telescopes in different wavelengths. I have carried out three investigations to understand GRB prompt emission and afterglow. Chapter 2 develops a new method, namely, “Stepwise Filter Correlation” method, to decompose the variability components in a light curve. After proving its reliability through simulations, we apply this method to 266 bright GRBs and find that the majority of the bursts have clear evidence of superposition of fast and slow variability components. Chapter 3 gives a complete presentation of the analytical approximations for synchrotron self-compton emission for all possible orders of the characteristic synchrotron spectral breaks (ν_a , ν_m , and ν_c). We identify a “strong absorption” regime when $\nu_a > \nu_c$, and derive the critical condition for this regime. The external shock theory is an elegant theory to model GRB afterglows. It invokes a limit number of model parameters, and has well predicted spectral and temporal properties. Chapter 4 gives a complete reference of all the analytical synchrotron external shock afterglow models by deriving the temporal and spectral indices of all the models in all spectral regimes. This complete reference will serve as a useful tool for afterglow observers to quickly identify relevant models to interpret their data and identify new physics when the models fail.

Multi-messenger signals from double neutron star merger: As the multi-messenger era of astronomy ushers in, the second part of the dissertation studies the possible electromagnetic (EM) and neutrino emission counterparts of double neutron star mergers. Chapter 6 suggests that if double neutron star mergers leave behind a massive magnetar rather than a black hole, the magnetar wind could push the ejecta launched during the merger process, and under certain conditions, accelerates it to a relativistic speed. Such a magnetar-powered ejecta, when interacting with the ambient medium, would develop a bright broad-band afterglow due to external shock synchrotron radiation. We study this physical scenario in detail, and present the predicted X-ray, optical and radio light curves for a range of magnetar and ejecta parameters. Chapter 7 applies the model to interpret one optical transient discovered recently. In chapter 8, we show that protons accelerated in the external shock would interact with photons generated in the dissipating magnetar wind and emit high energy neutrinos and photons. We find that \sim PeV neutrinos could be emitted from the shock front as long as the ejecta could be accelerated to a relativistic speed. These events would contribute to the diffuse Pev neutrino background and sub-TeV gamma-ray background.

ACKNOWLEDGMENTS

I would like to give my sincere thanks to many people who made this dissertation possible.

The first one is my supervisor, Prof. Bing Zhang. During the four-year Ph.D. program, Bing taught me what astrophysics is and how to do astrophysical research; he taught me what confidence is and how to become a mature researcher; he changed my attitude to science and inspired my passion; he showed me how easy “hard working” is by his own practice. To him, I am more thankful than I can express. The only sentence I want to say is “Thank you for changing my life!”

My sincerely thanks also go to Dr. Xue-Feng Wu and Dr. Wei-Hua Lei. Both of them are my close collaborators and good friends. I got lots of benefits from them both in research and in daily life. My special thanks go to Dr. En-Wei Liang for his excellent advices and suggestions both on my research and life. I would like to thank other members in our group, Dr. Qiang Yuan, Dr. Bin-Bin Zhang, Dr. Francisco Virgili, Dr. Amanda Maxham, Dr. Z. Lucas Uhm, Dr. Massimiliano De Pasquale, Dr. Resmi Lekshmi, Dr. Xiang-Gao Wang, Dr. Bo Zhang, Wei Deng, Hou-Jun Lv, Ye Li, Shuang-Xi Yi, Robert Gex, Tesla Birnbaum for great discussion, comments, suggestions and collaborations. Besides our group members, there are many people who also helped me a lot on my research projects. I’d like to thank my industrial collaborators, in particular, Dr. Zi-Gao Dai, Dr. Jian-Yan Wei, Dr. Ye Lu, Dr. Zhuo Li, Dr Yuan-Chuan Zou, Dr. Yun-Wei Yu, Dr, Tong Liu, Dr. Lin-Qing Wen, Qi Chu, Shu-Jin Hou and Xuan Ding.

I would like to thank many professors in Department of Physics & Astronomy of UNLV. I would like to thank Dr. Daniel Proga, Dr. Kentaro Nagamine, Dr. Stephen Lepp, Dr. George Rhee, Dr. Bernard Zygelman and Dr. Lon Spight for their excellent classes from which I learned a lot. In particular, I'd like to thank Dr. Daniel Proga, Dr. Kentaro Nagamine for serving in my committee and their great suggestions and discussion which improved this dissertation significantly. Also thank my committee member and graduate faculty representative, Dr. Amei Amei for her patience and suggestions.

I would like to thank some graduate students in the department, Timothy Water, Robert Thompson, John Howard, Jared Rice, Keita Todoroki, Gabriel Gobeli and Sandamali Weerasooriya for their help and discussion.

Last, but definitely not the least, I would like to thank my wife, Nan Xing, for her love and support during the past ten years! I'd like to quote the movie lines in "A Beautiful Mind": I'm only here tonight because of you. You are the reason I am. You are all my reasons.

This work is dedicated to :

My parents who have always been there for me, even though they have no idea what astrophysics is at all!

TABLE OF CONTENTS

ABSTRACT	iii
ACKNOWLEDGMENTS.....	v
LIST OF TABLES	xi
LIST OF FIGURES	xv
I PHYSICS OF GAMMA-RAY BURSTS	1
CHAPTER 1 INTRODUCTION OF PART I	2
Where does the Huge Amount of Energy Come From?	3
Hyper-accreting black holes	3
Millisecond magnetar	7
What is the Relativistic Effect?	8
Compactness problem	8
Doppler effects	10
Equal arrival time surface and curvature effect	13
How could the Ejecta Get Acceleration to Ultra-relativistic Regime?	14
Thermal energy dominated jet	16
Magnetic energy dominated jet	17
A jet with comparable thermal energy and magnetic energy	18
How could These Energy Be Converted into the Observed Radiation?	19
Internal shock dissipation	20
External shock dissipation	21
CHAPTER 2 STEPWISE FILTER CORRELATION METHOD AND EVIDENCE OF SUPERPOSED VARIABILITY COMPONENTS IN GRB PROMPT EMISSION LIGHTCURVES	22
Stepwise Filter Correlation Method	25
The method	25
Simulation tests	26
Application to GRB Data	28
Conclusions and Discussion	33
Theoretical Derivation and Monte Carlo Simulation Test for SFC Method	45
Butterworth low-pass filter	45
Simulation tests of the SFC algorithm	46
Case studies of GRBs not belonging to the good sample	48
CHAPTER 3 COMPTON SCATTERING OF SELF-ABSORBED SYNCHROTRON EMISSION	53
Weak Synchrotron Self-Absorption Cases	55
Case I: $\nu_a < \nu_m < \nu_c$	57
Case II: $\nu_m < \nu_a < \nu_c$	59

Case III: $\nu_a < \nu_c < \nu_m$	60
Strong Synchrotron Self-Absorption Cases	63
Case IV: $\nu_c < \nu_a < \nu_m$	64
Case V and VI: $\nu_a > \max(\nu_m, \nu_c)$	66
Conclusion and Discussion	69
Condition of electron pile-up and strong absorption	71
CHAPTER 4 A COMPLETE REFERENCE OF THE ANALYTICAL SYN- CHROTRON EXTERNAL SHOCK MODELS OF GAMMA-RAY BURSTS	75
General Description of the Synchrotron External Shock Models of GRBs ..	78
Analytical Synchrotron External Shock Models	85
Phase 1: reverse shock crossing phase	86
Phase 2: relativistic, pre-jet-break, self-similar deceleration phase ...	104
Phase 3: post jet break phase	113
Phase 4: newtonian phase	114
Applications of the Models	119
Limitations of the Analytical Models	122
<p>-dependent Coefficients in Analytical Solutions</p>	173
CHAPTER 5 INTRODUCTION OF PART II	179
General Introduction for Neutron-Star Binary System	179
Gravitational Wave Signal	183
Electromagnetic Signal	184
Short gamma-ray bursts	185
Li-Paczyński Nova/macro-nova/kilo-nova	187
Long lasting radio afterglow	188
Dissipated early x-ray afterglow	189
Merger-nova	190
Double neutron star merger afterglow	190
Possible High-Energy Neutrino and Photon Signals	191
CHAPTER 6 BRIGHT BROD-BAND AFTERGLOWS OF GRAVITATIONAL WAVE BRSTS OF BINARY NEUTRON STARS	192
The Double Neutron Star Merger Afterglow Model	192
Detectability and Implications	198
CHAPTER 7 A DOUBLE NEUTRON STAR MERGER ORIGIN FOR THE COSMOLOGICAL RELATIVISTIC FADING SOURCE PTF11AGG?	206
Introduction	206
Observations of PTF11agg	207
Applying DNS Merger Afterglow Model to PTF11agg	208
Discussion	213

CHAPTER 8 POSSIBLE HIGH-ENERGY NEUTRINO AND PHOTON SIGNALS FROM GRAVITATIONAL WAVE BURSTS DUE TO DOUBLE NEUTRON STAR MERGERS	216
General Picture	216
Neutrino Energy and Fluence	220
Detection Prospect	224
High Energy Photon Emission	225
REFERENCES	227
VITA	242

LIST OF TABLES

Table 1	Characteristic timescales identified in BATSE bright Gamma-Ray Bursts, part I	37
Table 2	Characteristic timescales identified in BATSE bright Gamma-Ray Bursts, part II	38
Table 3	Characteristic timescales identified in BATSE bright Gamma-Ray Bursts, part III	39
Table 4	Characteristic timescales identified in BATSE bright Gamma-Ray Bursts, part IV	39
Table 5	The temporal decay index α and spectral index β in thin shell forward shock model with $\nu_a < \min(\nu_m, \nu_c)$	90
Table 6	The temporal decay index α and spectral index β in thin shell forward shock model in the $\nu_m < \nu_a < \nu_c$ regime.	90
Table 7	Temporal decay index α and spectral index β in the thin shell reverse shock model during the reverse shock crossing phase in the $\nu_a < \min(\nu_m, \nu_c)$ spectral regime.	95
Table 8	Temporal decay index α and spectral index β in the thin shell reverse shock model during the reverse shock crossing phase in the $\nu_m < \nu_a < \nu_c$ spectral regime.	96
Table 9	Temporal decay index α and spectral index β in thin shell reverse shock model after reverse shock crossing in the $\nu_a < \min(\nu_m, \nu_{\text{cut}})$ spectral regime.	96
Table 10	Temporal decay index α and spectral index β in thin shell reverse shock model after reverse shock crossing in the $\nu_m < \nu_a < \nu_{\text{cut}}$ spectral regime.	96
Table 11	The temporal decay index α and spectral index β of the thick shell forward shock model in the $\nu_a < \min(\nu_m, \nu_c)$ spectral regime.	99
Table 12	The temporal decay index α and spectral index β of the thick shell forward shock model in the $\nu_m < \nu_a < \nu_c$ spectral regime.	99
Table 13	The temporal decay index α and spectral index β of the thick shell reverse shock model during the shock crossing phase in the $\nu_a < \min(\nu_m, \nu_c)$ spectral regime.	104
Table 14	The temporal decay index α and spectral index β for the thick shell reverse shock model during the reverse shock crossing phase in the $\nu_m < \nu_a < \nu_c$ spectral regime.	105
Table 15	The temporal decay index α and spectral index β of the thick shell reverse shock model in the post-shock crossing phase in the $\nu_a < \min(\nu_m, \nu_{\text{cut}})$ spectral regime.	105
Table 16	The temporal decay index α and spectral index β of the thick shell reverse shock model in the post-shock crossing phase in the $\nu_m < \nu_a < \nu_{\text{cut}}$ spectral regime.	105
Table 17	The temporal decay index α and spectral index β in relativistic, isotropic, self-similar deceleration phase for $\nu_a < \min(\nu_m, \nu_c)$ and $p > 2$	111
Table 18	The temporal decay index α and spectral index β in relativistic, isotropic, self-similar deceleration phase for $\nu_m < \nu_a < \nu_c$ and $p > 2$	112

Table 19	The temporal decay index α and spectral index β in relativistic, isotropic, self-similar deceleration phase for $\nu_a < \min(\nu_m, \nu_c)$ and $1 < p < 2$.	112
Table 20	The temporal decay index α and spectral index β in relativistic, isotropic, self-similar deceleration phase for $\nu_m < \nu_a < \nu_c$ and $1 < p < 2$.	113
Table 21	Collection of jet break time and temporal indices changes $\Delta\alpha = \alpha_2 - \alpha_1$ for different regimes.	114
Table 22	The temporal decay index α and spectral index β after jet break for $\nu_a < \min(\nu_m, \nu_c)$, considering edge effect only.	115
Table 23	The temporal decay index α and spectral index β after jet break for $\nu_m < \nu_a < \nu_c$, considering edge effect only.	115
Table 24	The temporal decay index α and spectral index β in the Newtonian phase for $\nu_a < \min(\nu_m, \nu_c)$.	118
Table 25	The temporal decay index α and spectral index β in the Newtonian phase for $\nu_m < \nu_a < \nu_c$.	118
Table 26	Collection of figure numbers corresponding to different dynamical models and initial spectra regimes.	127
Table 27	List of observed double neutron star binaries.	180
Table 28	Expression of the Lorentz factor and radius as a function of model parameters in different temporal regimes for all dynamical cases.	201
Table 29	Temporal scaling indices of various parameters in different temporal regimes for all dynamical cases.	202
Table 30	Adopt parameters for fitting the optical and radio data of PTF11agg for different redshift.	212

LIST OF FIGURES

Figure 1 The geometric configuration among the GRB central engine, relativistic emitting shells and the observer, taken from Zhang and Mészáros (2004a)	12
Figure 2 Examples that prove the validity of the SFC method	40
Figure 3 Examples for the one-dip only bursts	41
Figure 4 Examples for the multi-dip bursts	42
Figure 5 Statistical results of the identified characteristic frequencies I	43
Figure 6 Statistical results of the identified characteristic frequencies II	44
Figure 7 Mock catalog of lightcurves with different pulse profile and their relevant correlation curves I.	49
Figure 8 Mock catalog of lightcurves with different pulse properties and their relevant correlation curves II.	50
Figure 9 Original and synthetic lightcurve for GRB930120	52
Figure 10 Total synchrotron + SSC spectra for weak synchrotron reabsorption cases ($\nu_a < \nu_c$)	62
Figure 11 Same as Figure 10, but for strong synchrotron reabsorption cases . . .	68
Figure 12 All possible forward shock lightcurves during Phase 1 (reverse shock crossing phase), for thin shell ISM model and the initial characteristic frequency order $\nu_a < \nu_m < \nu_c$	128
Figure 13 Figure 12 continued	129
Figure 14 Same as Fig. 12, but with the initial characteristic frequency order $\nu_a < \nu_c < \nu_m$	130
Figure 15 Same as Fig. 12, but with the initial characteristic frequency order $\nu_m < \nu_a < \nu_c$	131
Figure 16 All possible reverse shock lightcurves during Phase 1 (reverse shock crossing phase), for thin shell ISM model and the initial characteristic frequency order $\nu_a < \nu_m < \nu_c$	132
Figure 17 Same as Fig. 16, but with the initial characteristic frequency order $\nu_a < \nu_c < \nu_m$	133
Figure 18 Same as Fig. 16, but with the initial characteristic frequency order $\nu_m < \nu_a < \nu_c$	134
Figure 19 All possible reverse shock lightcurves after reverse shock crossing the shell, for thin shell ISM model and the initial characteristic frequency order $\nu_a < \nu_m < \nu_c$	135
Figure 20 Same as Fig. 19, but with the initial characteristic frequency order $\nu_m < \nu_a < \nu_c$	136
Figure 21 All possible forward shock lightcurves during Phase 1 (reverse shock crossing phase), for thick shell ISM model and the initial characteristic frequency order $\nu_a < \nu_m < \nu_c$	137
Figure 22 Same as Fig. 21, but with the initial characteristic frequency order $\nu_a < \nu_c < \nu_m$	138
Figure 23 Same as Fig. 21, but with the initial characteristic frequency order $\nu_m < \nu_a < \nu_c$	139

Figure 24 All possible reverse shock lightcurves during Phase 1 (reverse shock crossing phase), for thick shell ISM model and the initial characteristic frequency order $\nu_a < \nu_m < \nu_c$.	140
Figure 25 Same as Fig. 24, but with the initial characteristic frequency order $\nu_a < \nu_c < \nu_m$.	141
Figure 26 Same as Fig. 24, but with the initial characteristic frequency order $\nu_m < \nu_a < \nu_c$.	142
Figure 27 All possible reverse shock lightcurves after reverse shock crosses the shell, for thick shell ISM model and the initial characteristic frequency order $\nu_a < \nu_m < \nu_c$.	143
Figure 28 Same as Fig. 27, but with the initial characteristic frequency order $\nu_m < \nu_a < \nu_c$.	144
Figure 29 All possible forward shock lightcurves during Phase 2 (relativistic, isotropic, self-similar deceleration phase), with an ISM medium and initial characteristic frequency order $\nu_a < \nu_m < \nu_c$.	145
Figure 30 Same as Fig. 29, but with the initial characteristic frequency order $\nu_a < \nu_c < \nu_m$.	146
Figure 31 Figure 30 continued.	147
Figure 32 Same as Fig. 29, but with the initial characteristic frequency order $\nu_m < \nu_a < \nu_c$.	148
Figure 33 All possible forward shock lightcurves during Phase 4 (Newtonian phase), with an ISM medium and initial characteristic frequency order $\nu_a < \nu_m < \nu_c$.	149
Figure 34 Same as Fig. 33, but with the initial characteristic frequency order $\nu_m < \nu_a < \nu_c$.	150
Figure 35 All possible forward shock lightcurves during Phase 1 (reverse shock crossing phase), for thin shell wind model and the initial characteristic frequency order $\nu_a < \nu_m < \nu_c$.	151
Figure 36 Same as Fig. 35, but with the initial characteristic frequency order $\nu_a < \nu_c < \nu_m$.	152
Figure 37 Same as Fig. 35, but with the initial characteristic frequency order $\nu_m < \nu_a < \nu_c$.	153
Figure 38 All possible reverse shock lightcurves during Phase 1 (reverse shock crossing phase), for thin shell wind model and the initial characteristic frequency order $\nu_a < \nu_m < \nu_c$.	154
Figure 39 Same as Fig. 38, but with the initial characteristic frequency order $\nu_a < \nu_c < \nu_m$.	155
Figure 40 Same as Fig. 38, but with the initial characteristic frequency order $\nu_m < \nu_a < \nu_c$.	156
Figure 41 All possible reverse shock lightcurves after reverse shock crossing, for thin shell wind model and the initial characteristic frequency order $\nu_a < \nu_m < \nu_c$.	157
Figure 42 Same as Fig. 41, but with the initial characteristic frequency order $\nu_m < \nu_a < \nu_c$.	158

Figure 43 All possible forward shock lightcurves during Phase 1 (reverse shock crossing phase), for thick shell wind model and the initial characteristic frequency order $\nu_a < \nu_m < \nu_c$	159
Figure 44 All possible forward shock lightcurves during Phase 1 (reverse shock crossing phase), for thick shell wind model and the initial characteristic frequency order $\nu_a < \nu_c < \nu_m$	160
Figure 45 Same as Fig. 43, but with the initial characteristic frequency order $\nu_m < \nu_a < \nu_c$	161
Figure 46 All possible reverse shock lightcurves during Phase 1 (reverse shock crossing phase), for thick shell wind model and the initial characteristic frequency order $\nu_a < \nu_m < \nu_c$	162
Figure 47 Same as Fig. 46, but with the initial characteristic frequency order $\nu_a < \nu_c < \nu_m$	163
Figure 48 Same as Fig. 46, but with the initial characteristic frequency order $\nu_m < \nu_a < \nu_c$	164
Figure 49 All possible reverse shock lightcurves after reverse shock crossing, for thick shell wind model and the initial characteristic frequency order $\nu_a < \nu_m < \nu_c$	165
Figure 50 Same as Fig. 49, but with the initial characteristic frequency order $\nu_m < \nu_a < \nu_c$	166
Figure 51 All possible forward shock lightcurves during Phase 2 (relativistic, isotropic, self-similar deceleration phase), for a wind medium and the initial characteristic frequency order $\nu_a < \nu_m < \nu_c$	167
Figure 52 Same as Fig. 51, but with the initial characteristic frequency order $\nu_a < \nu_c < \nu_m$	168
Figure 53 Same as Fig. 51, but with the initial characteristic frequency order $\nu_m < \nu_a < \nu_c$	169
Figure 54 All possible forward shock lightcurves during Phase 4 (Newtonian phase), for a wind medium and the initial characteristic frequency order $\nu_a < \nu_m < \nu_c$	170
Figure 55 Same as Fig. 54, but with the initial characteristic frequency order $\nu_m < \nu_a < \nu_c$	171
Figure 56 Example light curves in the radio, optical and X-ray bands for a set of typical parameter values (see text)	172
Figure 57 Cartoon showing standard formation channels for close NS–NS binaries through binary stellar evolution, taken from Lorimer (2008)	181
Figure 58 A physical picture for several EM emission components appearing after the merger, black hole as the remnant	185
Figure 59 A physical picture for several EM emission components appearing after the merger, magnetar as the remnant	186
Figure 60 Calculation results for Case I: $L_0 \sim 10^{47}$ erg s ⁻¹ and $M_{\text{ej}} \sim 10^{-4}M_\odot$ (for all the examples, we adopt $\xi = 0.5$, $p = 2.3$)	203
Figure 61 Calculation results for Case II: $L_0 \sim 10^{49}$ erg s ⁻¹ and $M_{\text{ej}} \sim 10^{-4}M_\odot$	204
Figure 62 Calculation results for Case III: $L_0 \sim 10^{49}$ erg s ⁻¹ and $M_{\text{ej}} \sim 10^{-3}M_\odot$	205

Figure 63 Optical and radio (8 GHz) light curves for PTF11agg, with best fittings by assuming different redshift for the source.	213
Figure 64 Examples of the evolution of neutrino energy ϵ_ν and fluence f_ν for different dynamics	223

PART I

**PHYSICS OF GAMMA-RAY
BURSTS**

CHAPTER 1

INTRODUCTION OF PART I

Gamma-Ray Bursts (GRBs) are the most extreme explosive events in the universe. The fascinating GRB story started in the late 1960s, when they were first detected by the Vela satellites (Klebesadel et al., 1973). The name “Gamma-Ray Bursts” was first proposed in Klebesadel et al. (1973), since they were found to be short, intense, and non-repeating flashes of \sim MeV γ -rays at that time. Later on, people found that the initial burst is usually followed by a longer-lived broad band emission (X-ray, ultraviolet, optical, infrared, microwave and radio), inferring that GRBs are actually multi-wavelength transients instead of simple bursts in γ -rays. The initial γ -ray emission is then often called “prompt emission” and the longer wavelength emission is often called “afterglow emission”. Thanks to the detection of afterglow emission, the cosmological origin of GRBs was confirmed. The isotropic-equivalent energy released in one individual GRB could be $10^{49} \sim 10^{55}$ ergs, and the luminosity of prompt phase could be $10^{47} \sim 10^{53}$ erg s $^{-1}$ (Zhang and Mészáros, 2004a), a million times larger than the peak electromagnetic luminosity of a supernova, people thus title GRBs as the most luminous explosions in the universe. Hereafter the convention $Q_s = Q/10^s$ is adopted in cgs units throughout the dissertation.

Thanks to the smooth handover of several space-borne high energy telescope missions: Compton Gamma Ray Observation (CGRO); BeppoSAX mission; NASA missions Swift and Fermi, the field of GRBs has rapidly advanced. Every time when a new mission unveiled a new temporal or spectral window, a rich trove of new phenomenology could be uncovered. While solving some old problems, new questions and challenges are raised, keeping the GRBs field remain active and relatively young. The statistical analysis of certain samples of observational data, or the study of some specific bursts have triggered a lot of hot topics in the GRB field, such as classification, progenitor, central engine, ejecta composition, energy dissipation and particle

acceleration mechanism, radiation mechanism, long term engine activity, external shock afterglow physics, origin of high energy emission, cosmological setting and so on (Zhang, 2011b).

In the literature, there are several expert reviews about GRBs (Mészáros, 2002; Zhang and Mészáros, 2004a; Piran, 2004; Zhang, 2007b; Gehrels & Razzaque, 2013; Zhang, 2014), one can refer to those papers for the details of GRBs. Here I would give a general picture of “physics of GRBs” by answering a couple of simple physical questions: (1) Where does the huge amount of energy come from? Such energy released in short variability timescale (down to milliseconds) would lead to the “compactness problem” (Ruderman, 1975), requiring relativistic motion for the GRBs ejecta to solve the problem. (2) What is the relativistic effect then? (3) How could the ejecta get acceleration to ultra-relativistic regime? (4) How could this energy be converted into the observed radiation?

I want to acknowledge that the general framework and some derivations of the following discussion is based on the lecture notes of “Gamma-Ray Bursts”, taught by Prof. Bing Zhang in UNLV. For equations that taken from the notes, I will cite as “GRBs notes”.

Where does the Huge Amount of Energy Come From?

Two scenarios are usually invoked as the central engine to power the GRBs: hyper-accreting black holes (BH) (Paczynski, 1998; Mészáros and Rees, 1997a) or rapidly spinning magnetars (Usov, 1992).

Hyper-accreting black holes

If GRBs are powered by accretion onto the BH, to achieve the required luminosity for GRBs, the accretion rate should be (GRBs note)

$$\dot{M}_{\text{acc}} = \frac{L_{\gamma}}{\eta c^2} = 0.56 M_{\odot} s^{-1} \eta_{-2} L_{\gamma,52}. \quad (1.1)$$

Due to high accretion rate, the accretion flow is extremely hot, the disk becomes dense and hot enough in the inner region, with neutrino-dominated cooling. On the other hand, the accreting BH could carry large angular momentum, since the BH is likely formed in a rapidly rotating core and it could also be spin-up by the accretion disk. For such a fast spinning BH with hyper-accretion disk, energy can be extracted to power GRBs by (1) neutrino annihilation process from the hot disk or by (2) large-scale magnetic field from the rotating BH.

(1) Neutrino annihilation Model

Under the hyper-accretion situation, the gas photo opacities are so high that radiation would be trapped (Katz, 1977; Begelman, 1978; Abramowicz et al., 1988). But neutrinos could still escape and tap the thermal energy of the disk produced by viscous dissipation. Nevertheless, neutrino annihilation along the spin axis can drive a hot jet in regions of low baryon density, and the jet power is defined by the neutrino annihilation power $\dot{E}_{\nu\bar{\nu}}$.

One popular method for numerically calculating $\dot{E}_{\nu\bar{\nu}}$ is proposed by Popham et al. (1999): the disk is modeled as a grid of cells in the equatorial plane. A cell k has its neutrino mean energy $\epsilon_{\nu_i}^k$ and luminosity $l_{\nu_i}^k$, and the height above (or below) the disk is d_k . Neutrinos from cell k would encounter antineutrinos from another cell k' at angle $\theta_{kk'}$. Then the summation over all pairs of cells could give the neutrino annihilation power at that point,

$$\dot{E}_{\nu\bar{\nu}} = A_1 \sum_k \frac{l_{\nu_i}^k}{d_k^2} \sum_{k'} \frac{l_{\nu_i}^{k'}}{d_{k'}^2} (\epsilon_{\nu_i}^k + \epsilon_{\bar{\nu}_i}^{k'}) (1 - \cos\theta_{kk'})^2 +$$

$$A_2 \sum_k \frac{l_{\nu_i}^k}{d_k^2} \sum_{k'} \frac{l_{\nu_i}^k}{d_{k'}^2} \frac{\epsilon_{\nu_i}^k + \epsilon_{\bar{\nu}_i}^{k'}}{\epsilon_{\nu_i}^k \epsilon_{\bar{\nu}_i}^{k'}} (1 - \cos\theta_{kk'}), \quad (1.2)$$

where $A_1 \approx 1.7 \times 10^{-44} \text{ cm} \cdot \text{erg}^{-2} \cdot \text{s}^{-1}$ and $A_2 \approx 1.6 \times 10^{-56} \text{ cm} \cdot \text{erg}^{-2} \cdot \text{s}^{-1}$. The total neutrino annihilation power is obtained by integrating over the whole space outside the BH and the disk.

Recently, Zalamea & Beloborodov (2011) obtained a power-law fit for numerical results of $\dot{E}_{\nu\bar{\nu}}$ as

$$\dot{E}_{\nu\bar{\nu}} \simeq 1.1 \times 10^{52} \left(\frac{r}{r_{\text{ms}}}\right)^{-4.8} \left(\frac{M_\bullet}{3M_\odot}\right)^{-3/2} \times \begin{cases} 0 & \dot{m} < \dot{m}_{\text{ign}} \\ \dot{m}^{9/4} & \dot{m}_{\text{ign}} < \dot{m} < \dot{m}_{\text{trap}} \\ \dot{m}_{\text{trap}}^{9/4} & \dot{m} > \dot{m}_{\text{trap}} \end{cases} \text{ erg s}^{-1}, \quad (1.3)$$

where \dot{m}_{ign} and \dot{m}_{trap} are two critical accretion rates. If $\dot{m} < \dot{m}_{\text{ign}}$, the disk temperature is not high enough to ignite the neutrino emitting reactions. If $\dot{m} > \dot{m}_{\text{trap}}$, the emitted neutrinos become trapped in the disk and advected into the black hole Zalamea & Beloborodov (2011).

(2) Magnetic Model

Blandford & Znajek (1977) proposed that the BH horizon and the remote astrophysical load are connected by the open magnetic field lines, so that energy and angular momentum could be transported from the spinning BH to the remote load. Such energy extracting mechanism is usually referred as BZ process, which could power GRBs when the magnetic field of BH is strong enough (Paczynski, 1998; Mészáros and Rees, 1997a; Lee et al., 2000). Here I present the main results of this model.

The rotational energy of a BH with angular momentum J is a fraction of the BH

rest energy $M_{\bullet}c^2$,

$$E_{\text{rot}} = 1.8 \times 10^{54} f_{\text{rot}}(a_{\bullet}) \frac{M_{\bullet}}{M_{\odot}} \text{erg}, \quad (1.4)$$

$$f_{\text{rot}}(a_{\bullet}) = 1 - \sqrt{(1+q)/2}, \quad (1.5)$$

where $q = \sqrt{1 - a_{\bullet}^2}$, and $a_{\bullet} = J_{\bullet}c/GM_{\bullet}^2$ is the BH spin parameter. For a maximally rotating BH ($a_{\bullet} = 1$), $f(1) = 0.29$.

The BZ jet power is (Lee et al., 2000)

$$\dot{E}_{\text{B}} = 1.7 \times 10^{50} a_{\bullet}^2 (M_{\bullet}/M_{\odot})^2 (B_{\bullet}/10^{15} \text{G})^2 F(a_{\bullet}) \text{ erg s}^{-1}, \quad (1.6)$$

where

$$F(a_{\bullet}) = [(1+q^2)/q^2][(q+1/q) \arctan q - 1], \quad (1.7)$$

$q = a_{\bullet}/(1 + \sqrt{1 - a_{\bullet}^2})$, and $2/3 \leq F(a_{\bullet}) \leq \pi - 2$ for $0 \leq a_{\bullet} \leq 1$. It apparently depends on M_{\bullet} , B_{\bullet} , and a_{\bullet} and strong magnetic field of $\sim 10^{15} \text{G}$ is required to produce the high luminosity of GRBs (Lee et al., 2000).

Since the magnetic field on the BH is supported by the surrounding disk, one can estimate its value by assuming the balance between the pressure of the magnetic field on the horizon and the ram pressure of the innermost parts of an accretion flow (e.g. Moderski et al. (1997)),

$$\frac{B_{\bullet}^2}{8\pi} = P_{\text{ram}} \sim \rho c^2 \sim \frac{\dot{M}_{\text{acc}} c}{4\pi r_{\bullet}^2}. \quad (1.8)$$

We can then rewrite the magnetic power as a function of mass accretion rate as

$$\dot{E}_B = 9.3 \times 10^{53} a_\bullet^2 \frac{\dot{M}}{M_\odot s^{-1}} X(a_\bullet) \text{ erg s}^{-1}, \quad (1.9)$$

where

$$X(a_\bullet) = F(a_\bullet)/(1 + \sqrt{1 - a_\bullet^2})^2. \quad (1.10)$$

It is found that $X(0) = 1/6$, and $X(1) = \pi - 2$. In general, a faster BH spin is more favorable for GRB production, as revealed also by recent GRMHD numerical simulations (Nagataki, 2009, 2011).

Millisecond magnetar

Besides hyper-accreting black holes, rapidly rotating neutron stars with surface magnetic fields of order $\sim 10^{15}$ G (and higher), often called “millisecond magnetars”, also be able to satisfy the essential conditions for a GRB central engine, e.g., energy, duration, variability, baryon loading, birth rate, etc(Usov, 1992; Zhang and Mészáros, 2004a). Here we only discuss the total energy and luminosity. The total spin energy for a millisecond magnetar is (GRBs note)

$$E_{\text{rot}} = (1/2)I\Omega_0^2 \simeq 2 \times 10^{52} \text{ erg } I_{45} P_{0,-3}^{-2}, \quad (1.11)$$

where P_0 ms is the initial spin period of the proto-magnetar. Notice that this is the maximum energy of the magnetar model, namely if the total energy of a GRB turns to be larger than this, the magnetar model can not be applied.

The simplest dipolar spindown formula gives the evolution of the spindown luminosity as (Zhang and Mészáros, 2001a)

$$L(t) = L_{\text{sd},0}/(1 + t/T_{\text{sd}})^2 = \begin{cases} L_{\text{sd},0}, & t \ll T_{\text{sd}}; \\ L_{\text{sd},0}(t/T_{\text{sd}})^{-2}, & t \gg T_{\text{sd}}, \end{cases} \quad (1.12)$$

where

$$T_{\text{sd}} = \frac{3c^3 I}{B_p^2 R^6 \Omega_0^2} = 2.05 \times 10^3 \text{ s } (I_{45} B_{p,15}^{-2} P_{0,-3}^2 R_6^{-6}) \quad (1.13)$$

is the characteristic spindown time scale, and

$$L_{\text{sd},0} = \frac{I \Omega_0^2}{2T_{\text{sd}}} = 1.0 \times 10^{49} \text{ erg s}^{-1} (I_{45} B_{p,15}^2 P_{0,-3}^{-4} R_6^{-6}) \quad (1.14)$$

is the characteristic spindown luminosity. Here B_p is the polar-cap dipole magnetic field strength and R is the neutron star radius. We can see that for a slightly stronger B_p and a slightly shorter P_0 , $L_{\text{sd},0}$ can be boosted to the typical GRB luminosity, and T_{sd} can be reduced to typical GRB duration.

What is the Relativistic Effect?

Compactness problem

The variability time scale of GRBs, δt , could be as small as millisecond (Bhat et al., 1992), indicating that GRBs are related to stellar scale scenario, with emission region size as

$$R \sim 10^7 \text{ cm } (\delta t/0.33\text{ms}). \quad (1.15)$$

The total isotropic energy of GRBs in γ -ray band could be $E_{\gamma,\text{iso}} \sim 10^{51} - 10^{55}$ ergs (Zhang and Mészáros, 2004a). Such huge amount of γ -ray photons releasing in a relatively small region, the pair production ($\gamma\gamma \rightarrow e^\pm$) optical depth $\tau_{\gamma\gamma}$ must be very

large. Here we make a simple estimation for $\tau_{\gamma\gamma}$: for a fireball with pure photons, its total energy could be derived with blackbody formula

$$E_{\gamma,\text{iso}} = \frac{4\pi}{3} R^3 a T_0^4, \quad (1.16)$$

where $a = 7.56 \times 10^{-15} \text{erg cm}^{-3} \text{K}^{-4}$ is radiation density constant. The typical photon energy is

$$kT_0 = 11.5 E_{\gamma,\text{iso},52}^{1/4} R_7^{-3/4} \text{Mev} \gg 0.511 \text{Mev}. \quad (1.17)$$

In this case, the pair production optical depth could be roughly estimated as

$$\tau_{\gamma\gamma} \simeq \frac{aT_0^4}{kT_0} \sigma_T R = 3.9 \times 10^{17} E_{\gamma,\text{iso},52}^{2/3} R_7^{-5/4}. \quad (1.18)$$

Here we use Thomson cross section σ_T to replace the pair production cross section, which should be fine for estimation to order of magnitude, since the pair production cross section is close to the Thomson cross section near threshold. Nevertheless, we also assume all the photons are with typical photon energy and thus all satisfy the pair production condition. In reality, only a fraction f of photons are above the threshold. Obviously, even taking such f factor into account, the pair production optical depth should be still much larger than unity, which raises the so-called ‘‘Compactness problem’’ (Ruderman, 1975) : the high energy photons of GRBs should be in principle converted to electron-positron pairs, and cannot escape due to the large pair production optical depths, but the fact is we do observe these photons.

The only way to solve this problem is invoking relativistic motion for the GRBs ejecta (fireball). The reason includes two folds: (1) due to the Doppler de-boosting effect, photon energy in comoving frame is significantly reduced (see later part of this

section for detail), which essentially makes f factor much lower; (2) in the comoving frame, the emission region size is larger by a factor of Γ (where Γ is the bulk Lorentz factor for ejecta moving). From Eq. 1.18, this effect would make a correction of Γ^{-2} for the pair production optical depth. For typical observational properties of GRBs, the optical depth drops to below unity when Γ is above several hundreds.

Although most theoretical contents about GRBs, including the so called “standard fireball model”, are still debated, the fact that GRBs must move relatively towards earth is one robust inference from GRB data. All GRB physics theory should be under the framework of special relativity. Here I will give some basic relativistic effects and their applications for GRB physics.

Doppler effects

A typical GRB problem involves three major physical elements (Fig. 1): a central engine, a relativistically moving shell (ejected by the central engine) which produces the GRB emission, and an observer (Zhang and Mészáros, 2004a). Each element should have their own rest frame: (Ref I) rest frame of the central engine; (Ref II) rest frame of the relativistic ejecta; (Ref III) rest frame of the observer. Ref I and III share the same inertial frame, the difference between these two rest frame is from the cosmological redshift effect (which is small compared to special relativistic effects). Ref II, also called comoving frame of the relativistic shell, corresponds to another inertial frame. The physical quantities as viewed in the two inertial frames are different, and are related through special relativistic Lorentz transformations. For example, there are two sets of clocks attached in both inertia frames, so that $dt' = d\hat{t}/\Gamma$, where $d\hat{t}$ and dt' are the time intervals elapsed for *the same pair of events* in the central engine/observer frame and the comoving frame, respectively.

The transformations between Ref II quantities and the Ref III quantities would suffer the Doppler effect, which is the combination of both relativistic effect and

propagation effect. We will also take the time transformation as an example. In general, we can consider a point emitter moving with a dimensionless speed $\beta = v/c$, at an angle θ with respect to the line of sight of the observer (Fig. 1). In rest frame of the central engine/observer, the shell emits a first photon towards the observer at the time \hat{t}_1 at the location A (the radius r , corresponding to t'_1 in Ref II), and emits a second photon towards the observer at time \hat{t}_2 at the location B (the radius $r + dr$, corresponding to t'_2 in Ref II), as recorded by clocks precisely adjusted in this inertia frame. The first photon arrives at the observer at $t_1 = \hat{t}_1 + L/c$, while the second photon arrives at the observer at $t_2 = \hat{t}_2 + (L/c - \beta\mu d\hat{t})$ where $\mu = \cos\theta$, L is the distance between the observer and the location A. The time interval for the observer to receive the two adjacent photon signals is simply

$$t_2 - t_1 = (1 - \beta\mu)(\hat{t}_2 - \hat{t}_1). \quad (1.19)$$

We thus have

$$dt = \mathcal{D}^{-1} dt', \quad (1.20)$$

where $\mathcal{D} = \frac{1}{\Gamma(1-\beta\cos\theta)}$ is known as the Doppler factor.

Similarly, one could get other useful transformations (Begelman et al., 1984), such as

$$d\nu = \mathcal{D} d\nu';$$

$$dr = \mathcal{D} dr';$$

$$dV = \mathcal{D} dV';$$

$$d\Omega = \mathcal{D}^{-2} d\Omega';$$

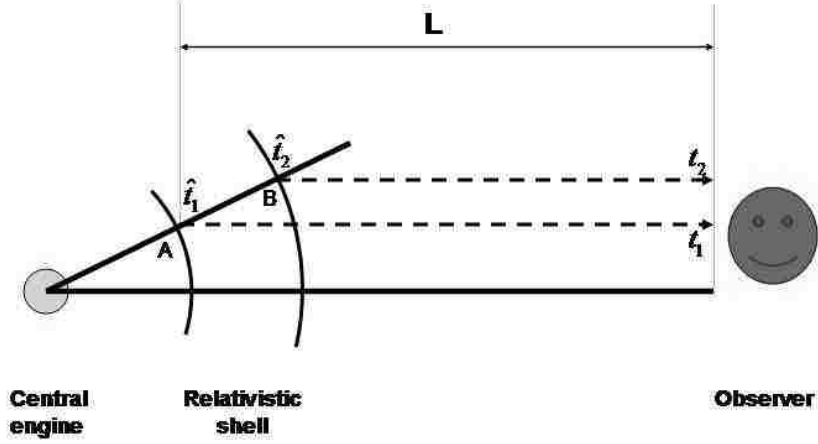


Figure 1 The geometric configuration among the GRB central engine, relativistic emitting shells and the observer, taken from Zhang and Mészáros (2004a)

$$\begin{aligned}
 I_\nu(\nu) &= \mathcal{D}I'_{\nu'}(\nu'); \\
 j_\nu(\nu) &= \mathcal{D}j'_{\nu'}(\nu'); \\
 \alpha_\nu(\nu) &= \mathcal{D}\alpha'_{\nu'}(\nu'),
 \end{aligned}
 \tag{1.21}$$

where I_ν is radiation intensity, j_ν is emission emissivity and α_ν is absorption coefficient.

Specifically, the observed flux from an optically thin source could be given by

$$\begin{aligned}
 F_\nu &= \int j_\nu dV / D_L^2 \\
 &= \int \mathcal{D}^3 j'_{\nu'} dV' / D_L^2,
 \end{aligned}
 \tag{1.22}$$

where D_L is the luminosity distance.

Particularly, for a point source moving to a direction θ , the Doppler factor is fixed, so that one would have (Granot et al., 2002)

$$F_\nu = \mathcal{D}^3 \int j'_{\nu'} dV' / D_L^2.
 \tag{1.23}$$

Equal arrival time surface and curvature effect

Other than solving the compactness problem, there are another two important implications for the relativistic effects: equal arrival time surface and curvature effect.

(1) *Equal arrival time surface*

Due to the propagation effect, for given observational time t_{obs} , detected photons are not emitted simultaneously in the lab frame, but comes from different radius R for different θ (Waxman, 1997c; Sari, 1998b; Panaitescu and Meszaros, 1998b), such surface that confines the volume constituting the locus of points from which photons reach the detector simultaneously is usually called the equal-arrival-time surface (EATS).

For specific dynamics of the ejecta, numerical calculation is required to solve the EATS. For the most simple case, i.e., a shell moving with a constant velocity βc , one can easily derived

$$R(\theta) = \frac{\beta c t_{\text{obs}}}{1 - \beta \mu}, \quad (1.24)$$

which describes an ellipsoid.

(2) *Curvature effect*

Supposing when the emitting region of GRBs expand to certain radius R_s , somehow the emission stops everywhere abruptly in the lab frame. In this case, the observed flux would not stop accordingly, since the high-latitude emission comes later with a delayed time and lower Doppler boost. This is called “curvature effect” (Fenimore et al., 1996; Kumar and Panaitescu, 2000a; Dermer, 2004; Dyks et al., 2005; Qin, 2008). Same as the EATS, numerical calculating is required for precise flux value. However, under some simple assumptions, a rough estimation could be also achievable: (1) considering one thin shell with half opening angle θ_j (2) the shell is moving with constant velocity βc ; (2) the radiation is isotropic in comoving frame

and the emission power per particle is just a function of ν' as $p'_{\nu'} = P'_{\nu'}/n' \propto (\nu')^{-\alpha}$; Under these assumptions, the Eq. 1.23 reads

$$F_{\nu}(t) = \int \mathcal{D}^{3+\alpha} dV n p'_{\nu'} / (4\pi D_L^2), \quad (1.25)$$

where the integration volume should be under the EATS corresponding to t but with $R \leq R_s$, namely

$$F_{\nu}(t) \propto \int_{\mu_1}^{\mu_2} (1 - \beta\mu)^{-(3+\alpha)} d\mu, \quad (1.26)$$

where $\mu_1 = \cos\theta_j$ and $\mu_2 = [1 - (t/t_0)(1 - \beta)]/\beta$. We thus have

$$F_{\nu}(t) \simeq F_{\nu}(t_0)(t/t_0)^{-(\beta+2)}, \quad (1.27)$$

where t_0 is the time when the emission from $R = R_s, \theta = 0$ reaches the observer.

How could the Ejecta Get Acceleration to Ultra-relativistic Regime?

To give GRBs, the ejecta must be ultra-relativistic. In the following, we will present how to convert the initial energy into kinetic energy of baryons. In general, a GRB jet launched from the central engine may have two components, one “hot” component due to neutrino heating from the accretion disk or the proto neutron star, and a “cold” component related to a magnetic Poynting flux launched from the black hole or the neutron star. The dynamics of the flow could be governed by the ideal MHD equations for the conservation of energy, momentum and mass. For the relativistic treatment the equations are formally best written in tensorial form (e.g.

Weinberg, 1973):

$$T^{\mu\nu}{}_{;\nu} = 0, \quad (1.28)$$

$$(\rho u^\mu)_{;\mu} = 0, \quad (1.29)$$

where

$$T^{\mu\nu} = \underbrace{wu^\mu u^\nu + pg^{\mu\nu}}_{\text{matter part}} + \frac{1}{4\pi} \underbrace{\left[\left(u^\mu u^\nu + \frac{1}{2}g^{\mu\nu} \right) b_\alpha b^\alpha - b^\mu b^\nu \right]}_{\text{electromagnetic part}} \quad (1.30)$$

is the energy-momentum tensor for ideal MHD (Drenkhahn & Spruit, 2002a). Here, ρ , w and p are the mass density, the enthalpy density and the pressure in the proper frame of the fluid, which is moving with a 4-velocity $u^\mu = (\Gamma, \vec{u})$. $b^\mu = {}^*F^{\mu\nu}u_\nu$ is the 4-vector of the magnetic field where ${}^*F^{\mu\nu}$ is the dual electromagnetic field strength tensor.

The dynamic solution sensitively depends on the composition of the initial ejecta, namely whether the “hot” component is dominated or the “cold” component is dominated. Initial composition is usually characterized by a parameter σ_0 (Zhang, 2014), which could be the ratio between Poynting flux and matter flux, or ratio between comoving magnetic energy density and rest mass energy density. Here we adopt

$$\sigma_0 \equiv \frac{L_c}{L_h} = \frac{L_P}{\eta \dot{M} c^2}. \quad (1.31)$$

The dynamic solution for system with comparable thermal energy and magnetic energy at the central engine is very complicated, and has not been studied carefully

in the literature. People usually discuss the dynamics for two extreme regimes: a thermally driven fireball ($\sigma_0 \ll 1$) or a magnetically-driven jet ($\sigma_0 \gg 1$). Note that the prompt emission lightcurve may contain some information to diagnose the ejecta composition, we will discuss this in detail in Chapter 2.

Thermal energy dominated jet

For $\sigma_0 \ll 1$ case, the electromagnetic part in Eq. 1.30 could be neglected. Piran et al. (1993) rewrote the Eq. 1.28 - 1.30 as

$$\frac{\partial}{\partial t}(n\Gamma) + \frac{1}{r^2} \frac{\partial}{\partial r}(r^2 n u) = 0, \quad (1.32)$$

$$\frac{\partial}{\partial t}(e^{3/4}\Gamma) + \frac{1}{r^2} \frac{\partial}{\partial r}(r^2 e^{3/4} u) = 0, \quad (1.33)$$

$$\frac{\partial}{\partial t} \left[\left(n + \frac{4}{3}e \right) \Gamma u \right] + \frac{1}{r^2} \frac{\partial}{\partial r} \left[r^2 \left(n + \frac{4}{3}e \right) u^2 \right] = -\frac{1}{3} \frac{\partial e}{\partial r}. \quad (1.34)$$

Change variables from r, t to $r, s = t - r$. Equations 1.32-1.34 then become

$$\frac{1}{r^2} \frac{\partial}{\partial r}(r^2 n u) = -\frac{\partial}{\partial s} \left(\frac{n}{\Gamma + u} \right), \quad (1.35)$$

$$\frac{1}{r^2} \frac{\partial}{\partial r}(r^2 e^{3/4} u) = -\frac{\partial}{\partial s} \left(\frac{e^{3/4}}{\Gamma + u} \right), \quad (1.36)$$

$$\frac{1}{r^2} \frac{\partial}{\partial r} \left[r^2 \left(n + \frac{4}{3}e \right) u^2 \right] = -\frac{\partial}{\partial s} \left[\left(n + \frac{4}{3}e \right) \frac{u}{\Gamma + u} \right] + \frac{1}{3} \left[\frac{\partial e}{\partial s} - \frac{\partial e}{\partial r} \right]. \quad (1.37)$$

For a relativistic fireball, one has $\gamma \gg 1$ and $\gamma \sim u$, so the right hand side of all

three equations would be ~ 0 . This gives simplified conservation laws as

$$r^2 n \Gamma = \text{constant}, \quad r^2 e^{3/4} \Gamma = \text{constant}, \quad r^2 \left(n + \frac{4}{3} e \right) \Gamma^2 = \text{constant}. \quad (1.38)$$

Two regimes of behavior are then immediately apparent. In the radiation-dominated phase ($e \gg n$), we have

$$\Gamma \propto r, \quad n \propto r^{-3}, \quad e \propto r^{-4}, \quad T_{obs} \sim \text{constant}. \quad (1.39)$$

In the alternate matter-dominated regime ($e \ll n$), we obtain

$$\Gamma \rightarrow \text{constant}, \quad n \propto r^{-2}, \quad e \propto r^{-8/3}, \quad T_{obs} \propto r^{-2/3}. \quad (1.40)$$

Therefore, the Γ evolution for a thermally driven fireball is like this: initially the Lorentz factor Γ increases linearly with r until reaching the maximum Lorentz factor $\eta \simeq \frac{L_b}{Mc^2}$ at coasting radius $R_c \sim R_0 \eta$, where R_0 is the radius where the fireball is launched. The Lorentz factor then ‘‘coasts’’ with the maximum value, reduces through later dissipation, such as the internal shocks (due to loss of radiation energy), and finally decreases smoothly as a power law beyond the deceleration radius (we will discuss these dissipation in detail later).

Magnetic energy dominated jet

For $\sigma_0 \gg 1$ case, Drenkhahn (2002b) expanded Eq. 1.28 and 1.29 in coordinate form under stationarity. He assumed that the flow is spherically symmetric and the field dominated by its toroidal component. In this case $\vec{u} \perp \vec{B}$ and the components of the magnetic four vector are simply $b^\mu = (0, -\vec{B}/\Gamma)$ and $b_\mu b^\mu = B_{co}^2 = B^2/\Gamma^2$. The

conservation laws for energy, momentum and mass are then

$$0 = \partial_r r^2 \left(w\Gamma u + \frac{\beta B^2}{4\pi} \right), \quad (1.41)$$

$$0 = \partial_r r^2 \left(wu^2 + (1 + \beta^2) \frac{B^2}{8\pi} \right) + r^2 \partial_r p, \quad (1.42)$$

$$0 = \partial_r r^2 \rho u, \quad (1.43)$$

where $\beta = u/\Gamma$.

In this case, the Γ evolution history for the magnetically-driven jet is like this: the jet would first undergo a rapid acceleration until reaching $R = R_A$, where $\Gamma(R_A) = \sigma_0^{1/3}$ and $\sigma(R_A) = \sigma_0^{2/3}$, and then go through a very slow acceleration process as $\Gamma \propto R^{1/3}$. Ideally, the jet could reach maximum Lorentz factor $\Gamma = \sigma_0$ at the saturation radius $R_{\text{sat}} = R_A \sigma_0^2$. After that, similar with the fireball jet scenario, Γ reduces through later dissipation. We note that the jet may start to decelerate before reaching the saturation radius if σ_0 is large enough so that $R_{\text{sat}} > R_{\text{dec}}$. Also magnetic dissipation can reduce the final coasting Γ , since energy is released as prompt emission (Zhang, 2014).

A jet with comparable thermal energy and magnetic energy

For a jet with comparable thermal energy and magnetic energy, since thermal acceleration proceeds more rapidly, it would be reasonable to assume that the thermal energy gets converted to kinetic energy first, after which additional acceleration proceeds magnetically if σ_0 is large enough. Based on this assumption, the Γ resolution for this hybrid system could be roughly approximated as

$$\Gamma(R) = \begin{cases} \frac{R}{R_0}, & R_0 < R < \eta R_0; \\ \eta^{2/3} \left(\frac{R}{R_0}\right)^{1/3}, & \eta R_0 < R < \eta R_0 \sigma_0^3; \\ \eta(1 + \sigma_0), & R > \eta R_0 \sigma_0^3. \end{cases}$$

Note that above approximation is only applicable when $\eta > \sigma_0^3 \gg 1$, namely the maximum Lorentz factor from thermal acceleration is larger than Alfvén speed of the initial Poynting flux. Otherwise, the dynamic should approach the magnetic dominated regime.

How could These Energy Be Converted into the Observed Radiation?

After the acceleration, the initial energy has been converted into three parts (or two parts beyond the photosphere radius): the energy of trapped photons within the ejecta, the kinetic energy of baryons and the magnetic energy. The photon energy will be naturally released when the ejecta reaches the photosphere radius. For the other two parts, certain dissipation process would be invoked, we call them kinetic dissipation and magnetic dissipation respectively. The kinetic dissipation could happen via shocks, either by internal shocks or external shocks (see details in the later part of this section). The magnetic dissipation could happen directly beyond certain radius, if the outflow is magnetically dominated at small radii and the field configuration is *striped-wind-like* (McKinney & Uzdensky, 2012). But if the field configuration is *helical*, enough repetitive collisions would be required to induce rapid magnetic dissipation (Zhang & Yan, 2011a).

Note that both kinetic dissipation and magnetic dissipation could happen under or beyond the photosphere radius, leading to different prompt emission models (see Zhang (2014) and reference therein). For example, if dissipation is not significant (e.g. no substantial amount of non-thermal particles), a quasi-thermal photon spectrum

is emitted from the photosphere, and later dissipation process will give the observed non-thermal emission. Otherwise, if dissipation is significant under the photosphere radius, non-thermal electrons accelerated from the dissipative photosphere would up-scatter the seed thermal photons to make it non-thermal, many authors intend to explain the observed GRB Band spectrum with this model (see Zhang (2014) and reference therein).

Here, I give a brief introduction to two important concepts under the “standard theoretical framework of GRBs”: internal shock and external shock.

Internal shock dissipation

The mass (or energy) flow generate from GRBs central engine is very like unsteady with a distribution of Lorentz factors [$\Gamma \in (\Gamma_{\min}, \Gamma_{\max})$]. Approximating the outflow as a series of “mini-shells”, one would expect a series of collisions due to the interactions between the late, fast shells and the early, slow shells. These collisions are supersonic, resulting in internal shocks from which particles are accelerated, this is usually called internal shock dissipation. For two shells with parameters (Γ_s, Δ_s) and (Γ_f, Δ_f) separated by $d = c\delta t$ (with the fast shell lagging behind the slow shell), the internal shock radius is (noticing $\beta = (1 - \Gamma^{-2})^{1/2}$)

$$R_{\text{IS}} = \frac{d}{\beta_f - \beta_s} \simeq 2\Gamma_s^2 c\delta t = 6 \times 10^{14} \text{ cm } \Gamma_{s,2.5}^2 \delta t_{-1} , \quad (1.44)$$

where $\Gamma_{s,2.5} = \Gamma_s/10^{2.5}$. And suppose the collision is full inelastic, with energy conservation, $\Gamma_1 m_1 + \Gamma_2 m_2 = \Gamma_m(m_1 + m_2 + U'/c^2)$, and momentum conservation, $\Gamma_1 \beta_1 m_1 + \Gamma_2 \beta_2 m_2 = \Gamma_m \beta_m(m_1 + m_2 + U'/c^2)$, one can derive the Lorentz factor of the merged shell

$$\Gamma_m = \left(\frac{\Gamma_1 m_1 + \Gamma_2 m_2}{m_1/\Gamma_1 + m_2/\Gamma_2} \right)^{1/2} . \quad (1.45)$$

where U' is internal energy generated through the collision. The energy dissipation efficiency (which is the upper limit of the radiation efficiency when the “fast cooling” condition is satisfied) of the collision is

$$\begin{aligned}\eta_{\text{is}} &= \frac{\Gamma_m U'}{\Gamma_1 m_1 c^2 + \Gamma_2 m_2 c^2} \\ &= 1 - \frac{m_1 + m_2}{\sqrt{m_1^2 + m_2^2 + m_1 m_2 \left(\frac{\Gamma_2}{\Gamma_1} + \frac{\Gamma_1}{\Gamma_2} \right)}} .\end{aligned}\tag{1.46}$$

Kinetic energy could be converted into radiation with such efficiency, and the leading radiation mechanisms for internal shock dissipation include synchrotron (or jitter) radiation and synchrotron self-Compton (SSC). This is because they are the most natural non-thermal emission mechanism, especially considering that the GRB central engine is likely magnetized and internal shocks can also generate magnetic fields through plasma instabilities (for detailed discussion of synchrotron and SSC, see Chapter 3).

External shock dissipation

The ejecta would always be decelerated through interaction with the ambient medium, which is known as external shock dissipation. During the initial interaction, a pair of shocks (forward and reverse) propagate into the ambient medium and the ejecta, respectively. After the reverse shock crosses the shell, the blastwave enters a self-similar phase described by the Blandford-McKee self-similar solution (Blandford and McKee, 1976). Finally, the blastwave would enter the Newtonian phase when the velocity is much smaller than speed of light. The dynamics is then described by the well-known Sedov solution widely used to study supernova remnants. The electrons accelerated in these shocks radiate synchrotron emission to power the broad-band afterglow of GRBs. In chapter 4, we give a detailed review for a complete reference of all the analytical synchrotron external shock afterglow models.

CHAPTER 2

STEPWISE FILTER CORRELATION METHOD AND EVIDENCE OF SUPERPOSED VARIABILITY COMPONENTS IN GRB PROMPT EMISSION LIGHTCURVES

This chapter is part of the following published paper :

Gao H., Zhang B.-B., Zhang B., 2012, Astrophysics Journal 748,134

The temporal structure of Gamma-Ray Bursts (GRBs) exhibits diverse morphologies (Fishman & Meegan, 1995). They can vary from a single smooth pulse to extremely complex lightcurves with many erratic pulses with different durations, amplitudes, and fine structures. Based on temporal information, it has been difficult to categorize GRBs.

Physically, several mechanisms have been invoked to interpret GRB temporal variability. The leading scenario is to attribute the lightcurve variability to the irregularity of the central engine¹. For the commonly discussed internal shock scenario (Rees and Mészáros, 1994; Sari, 1997; Daigne & Mochkovitch, 2003; Maxham and Zhang, 2009), the observed time sequence tracks that of the central engine very well (Kobayashi et al., 1997; Maxham and Zhang, 2009). Alternatively, if the emission is from the central engine photosphere, then the observed lightcurve time history tracks that of the central engine directly (e.g. Lazzati et al., 2009). Within such a scenario, the observed lightcurves can be directly connected to the behavior of the central engine (e.g. Lei et al., 2007; Lu et al., 2008). A second scenario takes the opposite view: The observed variability originates in the emission region, which is not directly related to the history of central engine activity. Since the GRB outflow is relativistic, this requires that the emission region is not uniform. Rather, it contains locally Lorentz boosted emission regions, such as mini-jets (Lyutikov & Blandford, 2003) or relativistic turbulence (Narayan & Kumar, 2009; Kumar & Narayan, 2009a).

¹The central engine in general sense refers to the central compact object (e.g. an accreting black hole or a spinning down neutron star) as well as the stellar envelope (if any) that regulates the time history of the outflow.

A third scenario discussed in the literature invoked a clumpy circumburst medium to interpret variability within the external shock model of GRB prompt emission (e.g. Dermer & Mitman, 1999). Swift observations of early X-ray afterglows of GRBs revealed a steep decay phase connected to the prompt emission lightcurve (Tagliaferri et al., 2005; Barthelmy et al., 2005a). This suggests that the GRB prompt emission region is detached from the afterglow region, and therefore prompt emission should be of an “internal” origin (Zhang et al., 2006). This disfavors this third model of GRB variability.

Recently, Zhang & Yan (2011a) proposed a new model of GRB prompt emission in the Poynting-flux-dominated regime, namely, the Internal-Collisioninduced MAgnetic Reconnection and Turbulence (ICMART) model. This model invokes a central engine powered, magnetically dominated outflow, which self-interacts and triggers fast magnetic turbulent reconnection to power the observed GRBs. An important prediction of the ICMART model is that it has two variability components: a broad (slow) component related to the central engine activity, and a narrow (fast) component associated with relativistic magnetic turbulence. Zhang & Yan (2011a) conjectured that the visually apparent broad pulses in GRB lightcurves are related to the time history of the central engine (with each broad pulse corresponding to an ICMART event), while the much faster variabilities superposed on the broad pulses are related to relativistic, magnetic turbulence.

Alternatively, Morsony et al. (2010) simulated jet propagation from a massive star, and suggest that the broad pulses of several seconds duration are due to interaction of the jet with the progenitor, while the shorter scale variability in the millisecond range is related to that of the base of the inner engine (e.g. the black hole or the millisecond pulsar).

It would be essential to use rigorous mathematical methods to study GRB lightcurves to investigate whether the time sequence demands superposition of multiple variabil-

ity components. Power density spectrum (PDS) is the most commonly used tool to study the temporal behavior of astronomical objects. Beloborodov et al. (1998, 2000) found that although the PDS of individual GRBs are diverse, the average PDS of a stack of GRBs is in accord with a power law with index $-5/3$ over 2 orders of magnitude in frequency. By locating the PDS peaks, Shen & Song (2003) revealed the typical variability time scales of some GRBs. In general, this method is not powerful to address whether a GRB lightcurve has superposed variability components. This is because it is insensitive to the lower frequency component (if it exists) since the GRB durations are typically not much longer than the broad pulses themselves. In the time domain, several methods have been developed to study temporal properties of GRBs. For example, lightcurves were decomposed into individual pulses using some parameterized empirical pulse functions (Norris et al., 1996) or a peak-finding algorithm (Li & Fenimore, 1996; McBreen et al., 2001; Nakar & Piran, 2002), and the temporal properties of the resulting pulses were analyzed. When performing the empirical pulse modeling, Norris et al. (1996) noted that some bursts are too complex to fit, possibly indicating pulse superposition. However, their matrix inversion algorithm failed to handle the problem. The peak finding selection method can decompose a lightcurve into many individual peaks. However, the method is not developed to reveal the superposed variability components.

Nonetheless, the possibility of superposition was suggested from other observational evidence. From a frequency-dependent analysis of prompt X-ray lightcurves of a sample of BeppoSAX GRBs, Vetere et al. (2006) discovered that the lightcurve tends to become smoother in softer energy bands. They then speculated that there might be a slow component superposed on a fast component. It is therefore of great interest to develop a rigorous mathematical method to identify such a superposition effect, if any, in gamma-ray lightcurves alone without the assistance of multi-wavelength data. Hereafter, we define a *slow component* as an underlying broad pulse component, while

a *fast component* as the component of rapid variability that overlaps on top of the slow component.

In this chapter, we develop a mathematical method to process GRB lightcurves as an effort of identifying the superposition effect. This method, known as the *stepwise filter correlation* (SFC) method, is presented in detail first. Then we delineate its mathematical basis, and justify its robustness in identifying the superposed slow component through simulations. We apply this method to a sample of bright BATSE GRBs, and indeed identify the superposition effect in the majority of them. The properties of the identified slow components are studied statistically. The data analysis results and their physical implications are presented in later section.

Stepwise Filter Correlation Method

The method

In signal processing, a filter is a device or process that removes some unwanted component or feature from a time sequence signal. Our method is based on a low-pass filter named Butterworth filter. For a certain cutoff frequency, this filter passes low-frequency signals below this frequency but attenuates signals above (see the final section in this chapter for mathematical details). Our method is based on the following concept. Suppose that one specific time series (lightcurve) can be decomposed into the summation of N pulses, either horizontally (pulses are laid out side by side) or vertically (superposition). One may denote the time scales (durations) of these pulses as $t_j, j=1\dots N$. The corresponding frequency for each pulse is therefore $f_j = 1/t_j$. If one applies a stepwise filter in the frequency space, one would get a series of residual lightcurves (RLCs). If there is no pulse falling into the range between the cutoff frequencies $f_{c,i}$ and $f_{c,i+1}$, then the two RLCs should be identical. If there are some pulses whose frequencies fall into this range, the RLC with the lower cutoff frequency (RLC _{i}) should be smoother than the one with the higher cutoff frequency (RLC _{$i+1$}),

since these pulses are screened after performing the low-pass filter at $f_{c,i}$. The more pulses falling into this frequency range or the higher the amplitudes of these pulses, the more different the two RLCs look like. One can quantify the difference between the two RLCs using a statistical correlation method. A cluster of many pulses or a high amplitude of pulses within a frequency range would result in a correlation coefficient R_i (defined between RLC_i and RLC_{i+1}) to be more less than unity. By plotting R_i against $f_{c,i}$, a “dip” in the curve would reveal such a clustering, and hence, would lead to the identification of a variability component around a particular frequency.

We realize such a concept based on the following procedure:

(1) For a time series, define a frequency range (f_{\min}, f_{\max}) to be searched from. We then divide this frequency range into many discrete frequency bins uniformly in logarithmic scale. For all the GRBs, our frequency step is uniformly chosen as $\log(\Delta f) = 0.05$. This gives a sequence of the cutoff frequencies $f_{c,i}(i = 1, \dots, M)$, where M is the total number of frequency bins. The low-pass filter to the original time series is then performed with each cutoff frequency $f_{c,i}$ in turn. The RLC for each cutoff frequency, e.g. RLC_i corresponding to $f_{c,i}$, is recorded.

(2) Perform a correlation analysis between each pair of adjunct RLCs (e.g. RLC_i vs. RLC_{i+1}). Record the Pearson’s correlation coefficient R_i for each pair.

(3) Plot R_i against $f_{c,i}$, and identify apparent dips in the curve.

Simulation tests

To prove the validity of the method, we perform some simulations. We start with a simple two-component lightcurve as shown in Fig.2 top row left panel. We superpose two periodic signals, both with the function form $A|\sin(\pi t/T)|$, where the periods of the two components are $T_s = 100\pi$ s for the slow component and $T_f = 10\pi$ s for the fast component, and the amplitude ratio between the two components is $A_s : A_f = 2 : 1$. The middle panel of the top row shows the PDS of the lightcurve, which clearly shows

the two components. The right panel of top row is the $R_i - f_{c,i}$ figure of our SFC method. Two dips that correspond to the two frequencies ($f_s = 1/100\pi \text{ s}^{-1}$ and $f_f = 1/10\pi \text{ s}^{-1}$) are clearly identified. We also add some white noise to the mock lightcurve. We find that even when the amplitude of the white noise is comparable to the signal, the dip in the lower frequency still shows up. This suggests that this method is powerful in identifying the low frequency component in the superposition.

Next, we simulate a more realistic lightcurve (middle row of Fig.2). The lightcurve (left panel of the middle row) is now a superposition of a slow component with pulse widths randomly distributed in the range of $T_s = (10-20) \text{ s}$ and a fast component with pulse widths randomly distributed in the range of $T_f = (1-3) \text{ s}$. The amplitudes of the two components are randomly chosen in the range of $A_s = (0.5-3)$ and $A_f = (0.5-1)$, respectively. Since there is no strict periodicity and since the duration of the time series is not much longer than the slow component time scale, the PDS method (middle panel of the middle row) fails to identify the two frequency components. On the other hand, our SFC method (right panel of the middle row) clearly identifies a dip around $1/17 \text{ s}^{-1}$, which is right within the frequency range of the slow component. This simulation suggests that the SFC method is much more powerful in identifying the superposed components than the PDS method.

We note that the absolute value of the correlation coefficient R depends on the step length of the cutoff frequency. A smaller frequency bin means smaller differences between consecutive RLCs, so that R would be closer to 1. In any case, the global shape of the SFC $R_i - f_{c,i}$ curve (e.g. the location of the dips) does not depend on the size of the frequency bin, as long as it is small enough.

In order to further understand the SFC algorithm, we have performed a series of additional simulation tests (see final section for details). These tests suggest that the SFC method is sensitive to significant clustering structures of a lightcurve in the frequency domain. A significant clustering structure is a cluster of frequencies that

is separated from other frequency clusters, and that has a large enough amplitude. If a frequency cluster is too wide, or is too close to another frequency cluster, the corresponding dip is diminished. Similarly, if the amplitude of a frequency cluster component is too small, the corresponding dip would be too shallow or disappear completely. An interesting finding is that the quiescent gaps that separate pulses in GRB lightcurves (Ramirez-Ruiz et al., 2001) would complicate the analysis. Only when the gaps are removed manually, can one identify the corresponding frequencies of the slow pulse components (see final section for details). Another finding is that if the slow component has only one pulse, the long tail of pulse tends to extend the duration, so that the identified duration can be much longer than the full width at half maximum.

Application to GRB Data

We now apply the SFC method to real GRBs. In this work, our aim is to demonstrate the validity of the SFC method and to investigate whether the superposition effect exists in GRBs. So we do not pursue sample completeness. Rather, we only focus on some bright GRBs that have clear temporal structures.

We select 266 bright GRBs detected by Burst and Transient Source Experiment (BATSE) (Kaneko et al., 2006), whose lightcurve data and T_{90} values are publically available from the online database <http://heasarc.gsfc.nasa.gov/docs/cgro/batse/>. In our analysis, we use light curves with 64 ms resolution obtained by BATSE in the four Large Area Detector energy channels, 20 – 300 keV. The background is subtracted in each channel using linear fits to the 1024 ms data. The SFC method is then applied to these bursts. For all the analyses, we adopt a fixed maximum frequency of $f_{\max} = 5$, which is based on the consideration of having at least 3 time bins for a 64 ms time resolution. The minimum frequency varies from burst to burst, but is related to a duration at least (sometimes larger than) T_{90} , in order to catch the slowest variability

component. After fixing the frequency range, the frequency step is chosen evenly in the logarithmic space with $\log(\Delta f) = 0.05$.

In order to quantitatively delineate the significance and confidence level of each dip, we define two parameters. The significance parameter, s , delineates the deepness/shalowness of a dip in the SFC $R_i - f_{c,i}$ curve. A dip is typically asymmetric, we apply the shallower wing of the dip to define its shallowness. We first identify the local minimum point at the bottom of the dip, e.g. for the n -th dip the coordinate (f_n, R_n) in the SFC curve. Next, we find out the inflection points (where the second derivatives change sign), or the turning points (where the first derivatives change sign) if an inflection point does not exist, in the left and right wings of the dip, respectively. These two points, i.e. $(f_{n,left}, R_{n,left})$ and $(f_{n,right}, R_{n,right})$, could be defined as “boundaries” of the dip. One can then define

$$S_n = \text{Min}\left\{\frac{R_{n,left} - R_n}{\log(f_n) - \log(f_{n,left})}, \frac{R_{n,right} - R_n}{\log(f_{n,right}) - \log(f_n)}\right\} \quad (2.1)$$

for each dip. A larger S_n means a more significant dip. To reduce the bin-size effect, we normalize S_n to the most significant one, S_n^{\max} (which is usually the slowest one S_1), i.e. we define $s_n = S_n/S_n^{\max}$ for each dip. This s parameter (which is $s \leq 1$) is then the significance parameter.

Next, we define a confidence level parameter, c , based on Monte-Carlo simulations. For each time bin with a particular observed count rate, we can generate a mock count rate based on the observed count rate \mathcal{C} by randomly generating the data based on a normal distribution with $(\mathcal{C}, \sqrt{\mathcal{C}})$. We then generate 1000 mock lightcurves by collecting these randomly generated count rates for each time bin. We apply the SFC method to each mock lightcurve, and identify the frequencies of the dips in each realization. For each dip in the original lightcurve, we define c as the fraction that the simulations reproduce. We regard a component with high confidence level if

$c \geq 0.9$, i.e., more than 900 simulations have revealed the component. We note that even though in general high-significance dips have a high confidence level, the two parameters are not always correlated. Some high “s” dips turn out to have a low “c”. We therefore evaluate both parameters for every dip measured in the SFC $R_i - f_{c,i}$ curves.

We take GRB 930331A as an example (bottom row of Fig.2). The left panel shows the original lightcurve, and the middle and right panels show the PDS and SFC analysis results, respectively. Although the PDS does not show any interesting feature, the SFC curve indeed shows a prominent dip around $1/38 \text{ s}^{-1}$ (both significance and confidence level parameters equal unity, i.e. $s = 1, c = 1$). Checking back in the lightcurve, one indeed sees one broad pulse with a time scale of 38 s and another with the pulse width slightly shorter. Rapid spikes overlap on top of these two broad pulses. To verify whether the 38s component truly exists, we apply the SFC method to a portion of the lightcurve, from the trigger time T_0 to a certain time T , with T stepwisely increasing in the range of $0 < T - T_0 < T_{90}$. We found that once $T - T_0$ is longer than 38s, the dip at $1/38\text{s}^{-1}$ persists in all SFC curves, indicating that the 38s component is a real slow component.

Applying this method to our entire GRB sample, we find the following interesting facts.

(1) The total 266 bursts could be grouped into four categories based on both their lightcurves and SFC curves: (I) Good sample: 117/266 (44.0%) of the bursts can be included in this sample. They clearly show at least one dip in the SFC curve. Checking back the lightcurves, one can usually find one or more pulses with the identified characteristic frequencies. Superposed on the identified slow component, there are always more rapid variability features. This clearly suggests a superposition of at least two variability components in the lightcurves. (II) Gap/long tail sample: 88/266(33.1%) of the bursts have quiescent periods in the lightcurve whose durations

are comparable to the broad pulses, or have one FRED-like pulse with extended tail. For these cases, dips in the SFC curve are affected by the quiescent periods (gaps) and the tails. For the gap case, the real slow component can be revealed by manually removing the gaps in the lightcurves (see examples in final section). These bursts also clearly show the superposition effect as seen in the sample (I). However, since the identified frequencies do not well match the pulse durations, we have excluded these bursts in the statistical study presented below; (III) Irregular (noisy) sample: 24/266 (9%) of the bursts show dips in the SFC curve. However, their lightcurves are too noisy to identify the corresponding components (see examples in final section). To be cautious, we do not include these bursts in the statistical analysis. (IV) Short/low temporal resolution sample: Finally, 37/266 (13.9%) of the bursts are short bursts or long bursts whose lightcurves have a poor temporal resolution (see example in final section). These bursts have too narrow a frequency range to perform the SFC analysis. All the lightcurves and their corresponding SFC curves for the samples I-III are presented at the UNLV GRB group website <http://grb.physics.unlv.edu/sfc>. An example to each of the groups II, III and IV is presented in final section.

(2) Within Sample I (good sample), 30/117 (25.6%) bursts show just one dip in the low frequency regime. Due to space limitation, we only present some examples in Fig.3. All the other cases are disseminated at the group website. The identified slow component time scales, as well as the s and c parameters for each dip are presented in Table 2-2. Since there is no strict periodicity in the lightcurves, the time scales of all the components we have identified are rough values, and we have rounded them to the nearest 0.5.

(3) The rest 87/117 bursts (74.4%) in Sample I show more than one dips. For each dip we try to identify the corresponding component in the lightcurve. Some examples are presented in Fig.4. Others are presented in the group website. We present the time scales of all the identified components T_i and their relevant s and c parameters

also in Table 2, with increasing frequencies for ascending number i . Only dips with $c \geq 0.9$ are selected.

Inspecting the lightcurves with multiple dips in the SFC curve, we find that it is not always straightforward to relate dips with pulses in the lightcurves. In some cases (e.g. GRB 910430 and GRB 940414B), the low-frequency dip corresponds to a broad pulse with overlapping fast variability whose frequency corresponds to the high-frequency dips. In these cases, it is straightforward to identify the underlying broad pulses as the slow component, while to identify the overlapping narrow pulses as the fast component. In more complicated cases (e.g. GRB 940228A), besides identifying some slow components (e.g. 8s and 4s) that correspond to individual broad pulses, one also identifies a very slow (21s) component. This is due to clustering of multiple pulses to make a 21s “cluster”. In general, we caution that the SFC method, although sensitive to identify variability components not easy to unveil using the PDS method, may be over-sensitive to pick up variability components. We therefore caution that one should always go back to the lightcurves to clarify the physical nature of the frequency components identified in the SFC curves.

To understand the results better, we perform a statistical analysis on the time scales identified using the SFC technique. Figure 5 presents the identified variability timescales T_i vs. the duration T_{90} of the bursts, histogram of T_i , and histogram of T_{90}/T_i . First we focus on the one-dip only sample. The characteristic time scales T_1 of this sample are marked in red in Fig.5. The following trends can be observed: first, it seems that there is a very rough positive correlation between T_1 and T_{90} (Fig.5a). This suggests that one tends to find longer slow components in longer bursts. Since there is a wide distribution in T_{90} , T_1 distributes from 2 s to 108 s (Fig.5b). On the other hand, the scatter of correlation is large. The ratio T_{90}/T_1 spans in at least one decade for this one-dip only sample. In some bursts, T_1 as small as 1/10 of T_{90} can be found (Fig.5c). Next, we include all the identified components (T_i) in the multi-dip sample

(black circles in Fig.5a, and dashed histograms in Figs.5b and 5c). It is found that all the distributions are much wider. The overall histograms including all T_i in the entire sample (solid histogram in Fig.5b and Fig.5c) cover 2 orders of magnitude in both T_i and T_{90}/T_i . The spreading is mostly caused by the fast components identified in the multi-dip sample, but the long clusters (such as the 21s component identified in GRB 940228A) also contribute to the scatter. Since our frequency interval $\log \Delta f = 0.05$ is uniform for all the bursts regardless of their T_{90} , our result does not suffer from the possible selection effect caused by different T_{90} . Inspecting the one-dip only sample, one usually also see the overlapping fast component, but with a lower amplitude than the multiple-dip ones. So these bursts are intrinsically similar to the multiple dip sample. The fast-component dips only show up when the high-frequency component amplitudes are large enough.

Another way to look at the distribution is to isolate the slowest component T_1 from other higher frequency ones. Figure 6 shows such a separation: T_1 in red and T_i ($i > 1$) in black. It can be seen that the $T_i - T_{90}$ correlation is more prominent for T_1 . This may be because the longer the burst, the more probable that a long cluster (e.g. 21s cluster in GRB 940228A) would show up. The correlation between T_i ($i > 1$) is much weaker. In particular, variability time scales as short as seconds can appear in very long GRBs (e.g. $T_{90} \sim 250$ s). This suggests that the fastest variability component essentially does not depend on the duration of the burst.

Conclusions and Discussion

We have developed a new method (Stepwise Filter Correlation) to decompose variability components in a time series. Through Monte Carlo simulations, we demonstrate that this method can identify significant clustering structures of a lightcurve in the frequency domain, and is more powerful than the traditional methods (e.g. PDS) to identify superposed variability components, especially the slow variability

component with duration comparable to the duration of the time series.

We then apply this method to GRB lightcurves as an effort to investigate whether the lightcurve is a superposition of multiple variability components. Our findings can be summarized as follows:

(1) We have applied this method to 266 BATSE bright GRBs, which may be grouped into 4 categories. In general, most bursts show a clear dip in the low frequency range, suggesting a slow component. By checking back to the lightcurves, we were able to identify the corresponding pulses with the relevant dip frequency in most of bursts. We found that such a slow component usually has superposed rapid variability components. We therefore conclude that GRB lightcurves are typically the superposition of multiple variability components.

(2) We selected 117 bursts as the good sample, and carried out a statistical statistical analysis sample. Among them, 30 show only one dip in the correlation curve. The other 87 GRBs have more than one dips. For the one-dip only sample in which the dip corresponds to a slow component, the distribution of this time scale T_1 spreads from several seconds to ~ 100 s, with no typical time scales, and T_{90}/T_1 spreads in one order of magnitude (from ~ 1 to ~ 10). There is a rough trend of correlation between T_1 and T_{90} . Including all the variability components, the distributions of T_i and T_{90}/T_i spread in two orders of magnitude, without a characteristic value. The fastest time scale of order ~ 1 s can be found in bursts with a wide range of durations.

The identification of the variability superposition effect (i.e. the existence of a slow component with overlapping faster variabilities) suggests that the causes of GRB lightcurve variabilities may be diverse. There might be more than one physical mechanisms that define the observed variability. This is in align with the prediction of the ICMART model (Zhang & Yan, 2011a) and the jet propagation model (Morsony et al., 2010). The common aspect of these two suggestions is that the slow component (duration of seconds to 10s of seconds) is attributed to the engine that defines the

jet variability. The difference between the two scenarios is the origin of the fast component. While the envelope model (Morsony et al., 2010) attributes it to the intrinsic variability at the base of the inner engine, i.e. the central black hole or magnetar, the ICMART model (Zhang & Yan, 2011a) attributes it to relativistic magnetic turbulence in the emission region. These two scenarios may be further differentiated through testing more detailed predictions in both models. For example, in the jet-star interaction model, the inner engine powered variability shows up only if the input PDS is hard enough, e.g. $E(k) \propto k^0$, or essentially the same power per decade. It is not known whether this can be achieved in the inner engine, and such a hard PDS is not observed in the high frequency regime of GRBs. On the other hand, the fast variability in the ICMART model arises from locally Lorentz-boosted mini-jets due to relativistic turbulent reconnection. Simulations suggest that the it can reproduce the observed PDS (Zhang & Zhang , 2014). In any case, neither model predicts a characteristic time scale for the fast component. It is therefore still a theoretical challenge to account for the typical fast component time scales identified in some bursts.

Finally, we'd like to justify the Butterworth low-pass filter we have adopted. In principle, one can use low-pass, high-pass, or band-pass filters. First, a band-pass filter only passes signals in a certain frequency band, which is disfavored by the SFC method. This is because a good correlation between two adjacent frequency bins may simply reflect that the changes between the two frequency bins are similar. One may not get a “dip” even though the changes are significant. Second, the purpose of this work is to find out whether superposition exists in GRB lightcurves. We therefore care more about the underlying slow component. We therefore choose a low-pass filter, which is more sensitive to the slow component. A high-pass filter, on the other hand, would be more sensitive to fast components. As for specific digital low-pass filters, we have done simulation tests for several types, including the Butterworth filter, the

Chebyshev filter, and the Gaussian filter. We find that different choices of filter would not change the results significantly. Among them, the Butterworth filter is designed to have as flat a frequency response as possible in the unscreened bandpass, which is beneficial to retain information of the slow component. We therefore adopt it in this work. We have also tried the wavelet transform method. It is a useful tool to unveil multiple variability components in the lightcurves (see e.g. Vetere et al. 2006). However, we did not find an easy way to quantify the results. We therefore do not apply the wavelet transform in this work.

GRB	T_{90}	T_1^a (s/c)	T_2^b (s/c)	T_3^c (s/c)	T_4^d (s/c)
910627	15.2	5 (1/1)	0	0	0
910807	59.6	12 (1/1)	0	0	0
911031A	90.0	23 (1/1)	0	0	0
911118A	19.2	22.5 (1/1)	0	0	0
920218C	122.5	55 (1/1)	0	0	0
920511A	48.5	3 (1/1)	0	0	0
920524	66.1	7.5 (1/1)	0	0	0
920622B	36.0	7 (1/1)	0	0	0
930331A	119.1	38 (1/1)	0	0	0
930425A	29.2	30 (1/1)	0	0	0
930916B	74.3	4 (1/1)	0	0	0
931106	152.1	108 (1/1)	0	0	0
931221A	57.9	29 (1/1)	0	0	0
940306	42.6	47 (1/1)	0	0	0
940520	32.8	2.5 (1/1)	0	0	0
940529D	37.6	42.5 (1/1)	0	0	0
941020B	56	28 (1/1)	0	0	0
950111B	46.3	48 (1/1)	0	0	0
950403A	14	12 (1/1)	0	0	0
950425	59.1	42.5 (1/1)	0	0	0
951202	28.5	34 (1/1)	0	0	0
960114	36.5	32.5 (1/1)	0	0	0
960807	12.7	6 (1/1)	0	0	0
961102	71.4	85 (1/1)	0	0	0
970202	26.7	34 (1/1)	0	0	0
970223	16.3	16 (1/1)	0	0	0
970807B	37.6	7 (1/1)	0	0	0
970912B	65.6	37 (1/1)	0	0	0
971029A	89.9	23 (1/1)	0	0	0
971220A	13.6	15 (1/1)	0	0	0
980124A	45.1	32 (1/1)	0	0	0
980225	127.7	81 (1/1)	0	0	0
980329A	18.5	20 (1/1)	0	0	0
991121	112.2	71 (1/1)	0	0	0
000302A	22.7	28.5 (1/1)	0	0	0

Table 1 Characteristic timescales identified in BATSE bright Gamma-Ray Bursts, part I

GRB	T_{90}	$T_1^a(s/c)$	$T_2^b(s/c)$	$T_3^c(s/c)$	$T_4^d(s/c)$
910425	90.2	106 (1/1)	9.5 (0.65/1)	4 (0.41/1)	0
910430	62.0	35 (1/1)	6 (0.11/1)	0	0
910601	28.5	20 (1/1)	4.5 (0.36/1)	0	0
910614	146.9	83 (0.65/1)	33 (1/1)	2.5 (0.02/0.98)	0
910619	106.1	67 (1/1)	11 (0.06/1)	2 (0.05/1)	0
910814A	77.8	62 (1/1)	10 (0.3/1)	0	0
910905	81.5	58 (1/1)	18 (0.64/0.96)	9 (0.77/1)	0
911127A	18.8	18 (1/1)	2 (0.046/1)	0	0
911202A	20.1	22 (1/1)	7 (0.2/0.99)	0	0
920110A	318.6	225.5 (1/1)	56.5 (0.33/1)	11.5 (0.1/1)	3 (0.027/1)
920210B	51.8	60 (1/1)	15 (0.25/0.97)	0	0
920308A	51.1	11 (1/1)	5 (0.53/1)	1 (0.15/1)	0.5 (0.03/0.99)
920513	88.6	70 (1/1)	4 (0.74/1)	2 (0.42/1)	0
920525B	16.1	8 (1/1)	4 (0.67/1)	0	0
920617B	67.7	34 (0.03/1)	27 (1/1)	0	0
920627B	52.8	26.5 (1/1)	4 (0.11/1)	3 (0.1/1)	1 (0.17/1)
921015	272.4	108 (0.6/1)	48 (1/1)	0	0
921118	174.7	78 (1/1)	10 (0.18/1)	0	0
921206B	53.8	21 (1/1)	3 (0.46/1)	0	0
921209B	38.1	9.5 (1/1)	3 (0.76/1)	0	0
921230A	18.8	16 (1/1)	2 (0.17/0.9)	0	0
930309A	90.1	72 (0.83/1)	7 (1/1)	1 (0.8/1)	0
930506B	22.1	22 (1/1)	5.5 (0.03/1)	2 (0.15/1)	0
930720A	45.9	26 (0.7/1)	5 (0.5/1)	2.5 (1/1)	0
930910C	83.1	52 (1/1)	4 (0.03/1)	3 (0.07/1)	1 (0.11/1)
931026	134.7	142 (1/1)	6.5 (0.04/1)	0	0
940128B	45.2	18 (1/1)	7 (0.2/1)	0	0
940210	30.7	12 (1/1)	1.5 (0.16/1)	1 (0.28/1)	0
940228A	33.3	21 (0.3/1)	8 (1/0.93)	4 (0.65/1)	2 (0.4/1)
940301	42.5	42.5 (1/1)	2 (0.05/1)	0	0
940302	119.9	67 (0.82/1)	12 (0.59/1)	2 (0.21/1)	0
940319	75.9	60 (1/1)	10 (0.3/1)	2.5 (0.08/1)	1 (0.11/1)
910321	51.6	16 (1/1)	3 (0.2/1)	0.5 (0.15/1)	0
940323	60.7	6 (1/1)	2.5 (0.19/1)	0	0
940414B	42.8	13.5 (1/1)	4 (0.2/1)	1 (0.16/1)	0
940619	88.4	56 (0.34/1)	31.5 (0.67/1)	20 (1/0.98)	5 (0.35/1)
940703A	34.9	30 (1/1)	15 (0.4/1)	3.5 (0.12/1)	0.5 (0.03/1)
940806D	10.2	3.5 (0.5/1)	0.5 (1/1)	0	0
940817	32.2	34 (0.62/1)	19 (1/1)	8.5 (0.5/1)	2.5 (0.7/1)

Table 2 Characteristic timescales identified in BATSE bright Gamma-Ray Bursts, part II

GRB	T_{90}	$T_1^a(s/c)$	$T_2^b(s/c)$	$T_3^c(s/c)$	$T_4^d(s/c)$
941014A	45.4	23 (1/1)	11 (0.65/1)	6 (0.15/1)	4 (0.25/1)
941017A	77.1	85 (1/1)	7 (0.05/1)	4 (0.03/1)	1.5 (0.09/1)
941023A	34.9	22 (1/1)	11 (0.2/1)	5.5 (0.34/1)	0
941119	33.4	24 (1/1)	5 (0.06/1)	2.5 (0.09/1)	0
941126E	36.1	13 (1/1)	1 (0.03/0.99)	0	0
950208	58.6	18.5 (1/1)	7 (0.24/1)	1 (0.21/1)	0
950211B	54.3	34 (0.43/1)	14 (1/1)	3 (0.43/1)	0
950608	142.0	101 (0.77/1)	45 (1/1)	2.5 (0.15/0.97)	0
950701B	10.6	7 (0.95/1)	4 (1/1)	0	0
950706	68.9	27 (1/1)	14 (0.38/1)	0	0
950909	65.7	21 (1/1)	7 (0.2/1)	0	0
951011	31.5	28 (1/1)	4 (0.55/1)	2.5 (0.75/0.98)	0
951219	58.8	21 (1/1)	4 (0.8/1)	1.5 (0.15/1)	0
960322A	22.8	25 (1/1)	2.5 (0.14/1)	0	0
960524C	80.6	64 (0.84/1)	23 (1/1)	3.5 (0.28/0.93)	1 (0.3/1)
960607B	140.5	112 (0.11/1)	88.5 (1/1)	14 (0.69/1)	2 (0.11/0.91)
960824	229.9	82 (1/1)	6.5 (0.05/1)	2.5 (0.07/0.9)	0
961228C	60.0	34 (0.54/1)	12 (0.4/1)	4 (1/1)	0
970111	31.5	13 (0.07/1)	9 (1/1)	0	0
970306	122.5	34.5 (0.52/1)	14 (0.18/1)	6 (1/1)	0
970315B	16.8	6.5 (0.98/1)	3.5 (0.1/1)	2 (1/1)	1 (0.76/1)
970411	58.9	53.5 (1/1)	3.5 (0.06/1)	0	0
970420	10.5	8 (1/1)	2 (0.81/1)	1 (0.5/1)	0
970612B	37.6	24 (0.07/1)	13 (1/1)	2.5 (0.4/1)	0
970816	6.5	5 (1/1)	1.5 (0.36/1)	0	0
970831	114.5	126 (1/1)	28 (0.34/0.94)	10 (0.11/1)	0
971110	195.2	123 (1/1)	55 (0.21/1)	28 (0.95/1)	9 (0.53/1)
971207C	48.3	38 (0.74/1)	5.5 (1/1)	0	0
980105	36.8	10 (0.42/1)	6.5 (1/1)	1 (0.24/1)	0
980203B	23.0	6 (1/1)	2 (0.42/1)	1.5 (0.9/1)	0.5 (0.42/1)
980208B	31.2	12 (1/1)	6.5 (0.42/0.96)	1.5 (0.16/1)	0
980315B	105.0	74 (0.93/1)	23.5 (1/1)	2 (0.13/0.96)	0
980703B	108.4	77 (1/1)	17 (0.25/1)	0	0
980803	19.8	21 (0.03/1)	7.5 (1/1)	1.5 (0.1/1)	0.5 (0.29/1)
980923	33.0	15 (1/1)	5 (0.44/1)	2 (0.39/1)	1 (0.15/1)
990108	145.7	58 (0.04/0.98)	36 (1/1)	3 (0.05/0.99)	0
990111A	15.0	14 (1/1)	1.5 (0.12/1)	0	0
990123A	63.4	56 (1/1)	16 (0.74/1)	0	0
990316B	100.5	89 (1/1)	18 (0.14/1)	2 (0.05/1)	1 (0.05/1)

Table 3 Characteristic timescales identified in BATSE bright Gamma-Ray Bursts, part III

GRB	T_{90}	$T_1^a(s/c)$	$T_2^b(s/c)$	$T_3^c(s/c)$	$T_4^d(s/c)$
990323C	49.5	17.5 (1/1)	5 (0.18/1)	2 (0.46/1)	0
990728	42.8	15 (1/1)	3 (0.39/1)	0	0
990803	19.4	1 (1/1)	0.5 (0.45/0.99)	0	0
991004D	77.4	39 (0.69/1)	9.5 (1/1)	0.5 (0.22/1)	0
991009	131.6	83 (1/1)	23.5 (0.29/1)	6 (0.11/1)	0
991113	61.4	13 (1/1)	3 (0.76/1)	0	0
991127	52.7	8 (1/1)	1.5 (0.39/1)	0	0
991216	15.2	16 (1/1)	3 (0.55/1)	1 (0.11/1)	0.5 (0.1/1)
000101	51.8	33 (0.8/1)	7 (1/1)	0	0
000103	67.4	21 (0.79/1)	10 (1/1)	0	0
000201A	95.0	42 (1/1)	13.5 (0.19/1)	6 (0.08/1)	0
000221	26.2	12 (1/1)	0.5 (0.05/1)	0	0
000511A	115.0	73 (1/1)	14.5 (0.1/1)	0	0

Table 4 Characteristic timescales identified in BATSE bright Gamma-Ray Bursts, part IV

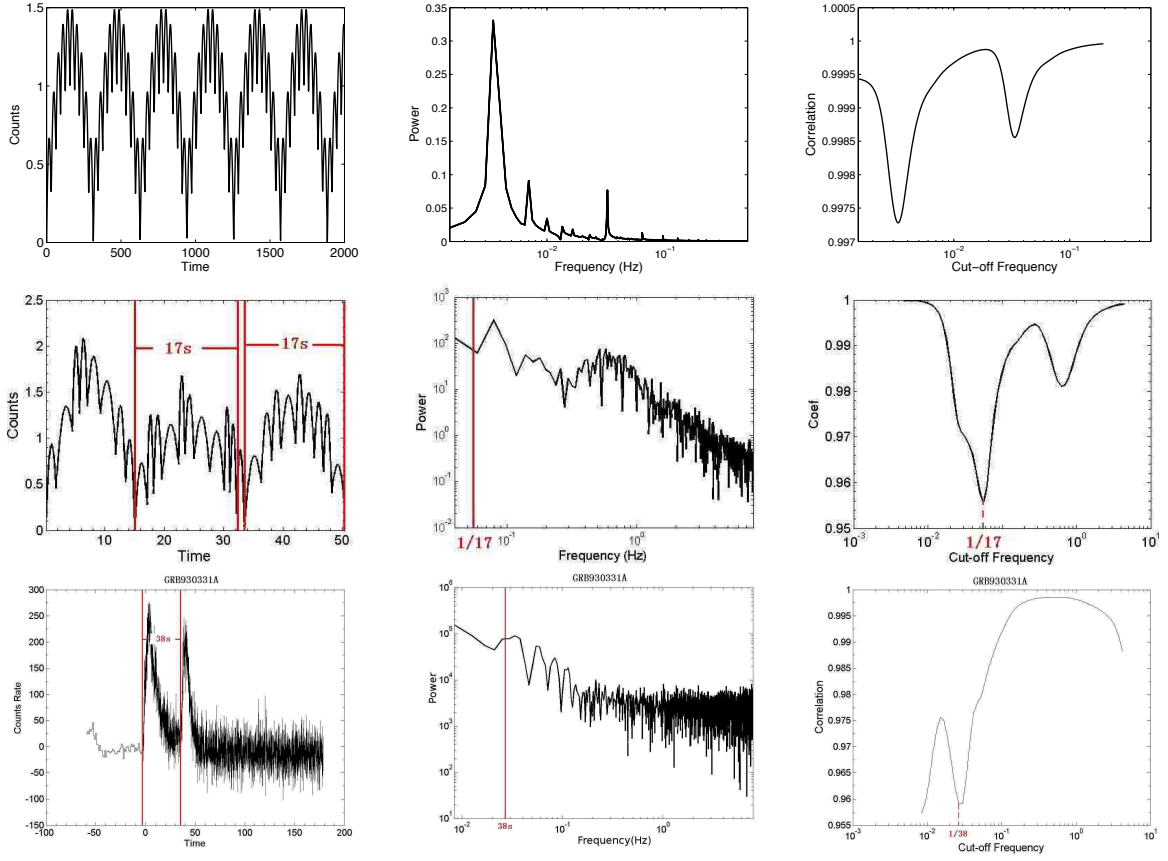


Figure 2 Examples that prove the validity of the SFC method. *Top panel:* The first simulation test; *Middle panel:* the second simulation test; *Lower panel:* a real GRB (930331A). In all three panels, the left figure is the simulated or real lightcurve, the middle figure is power density spectrum, and the right figure is the correlation curve, i.e. the correlation coefficient R_i versus the cutoff frequency $f_{c,i}$.

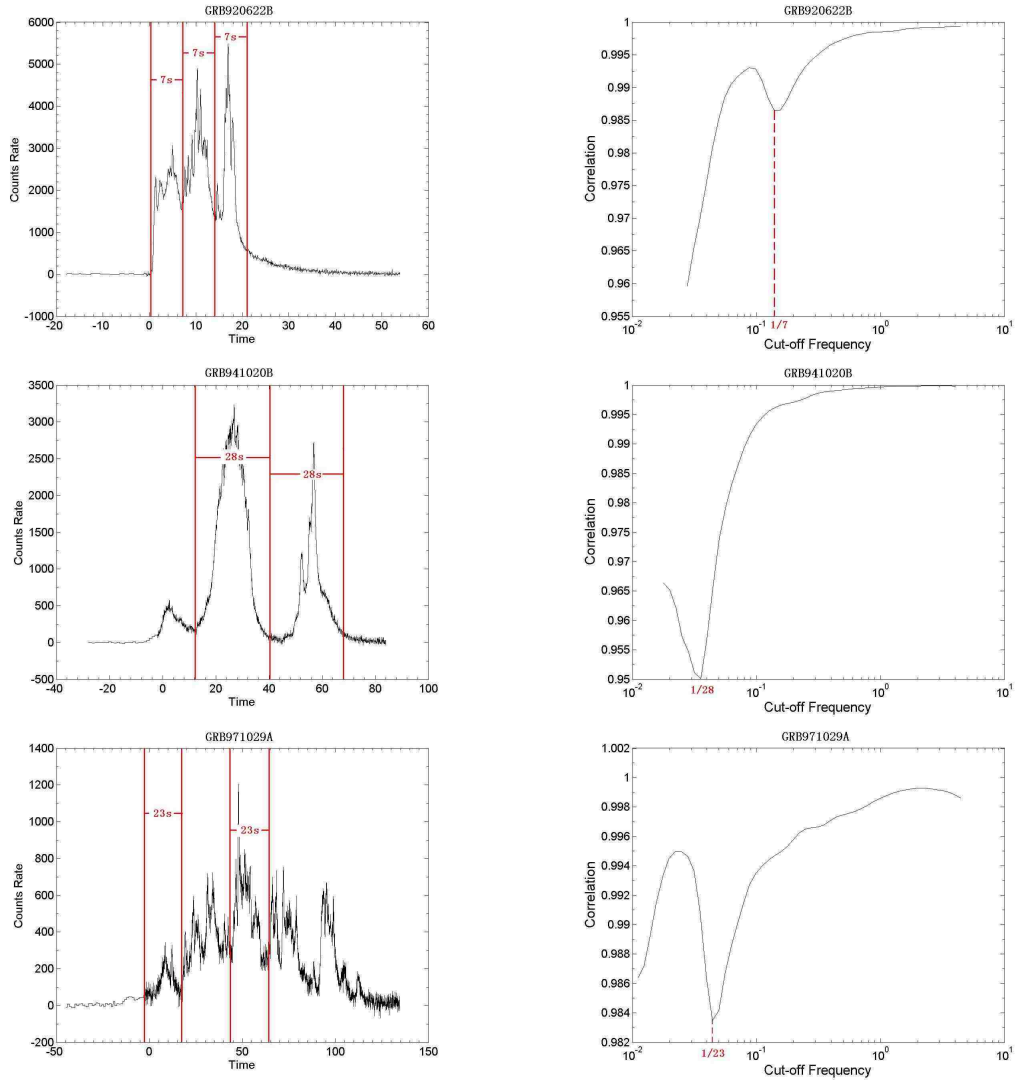


Figure 3 Examples for the one-dip only bursts. The left panel are the lightcurves, and the right panel are the correlation curves. The pulses that correspond to the identified frequencies are marked in the lightcurves. The time scales are rounded to the nearest 0.5.

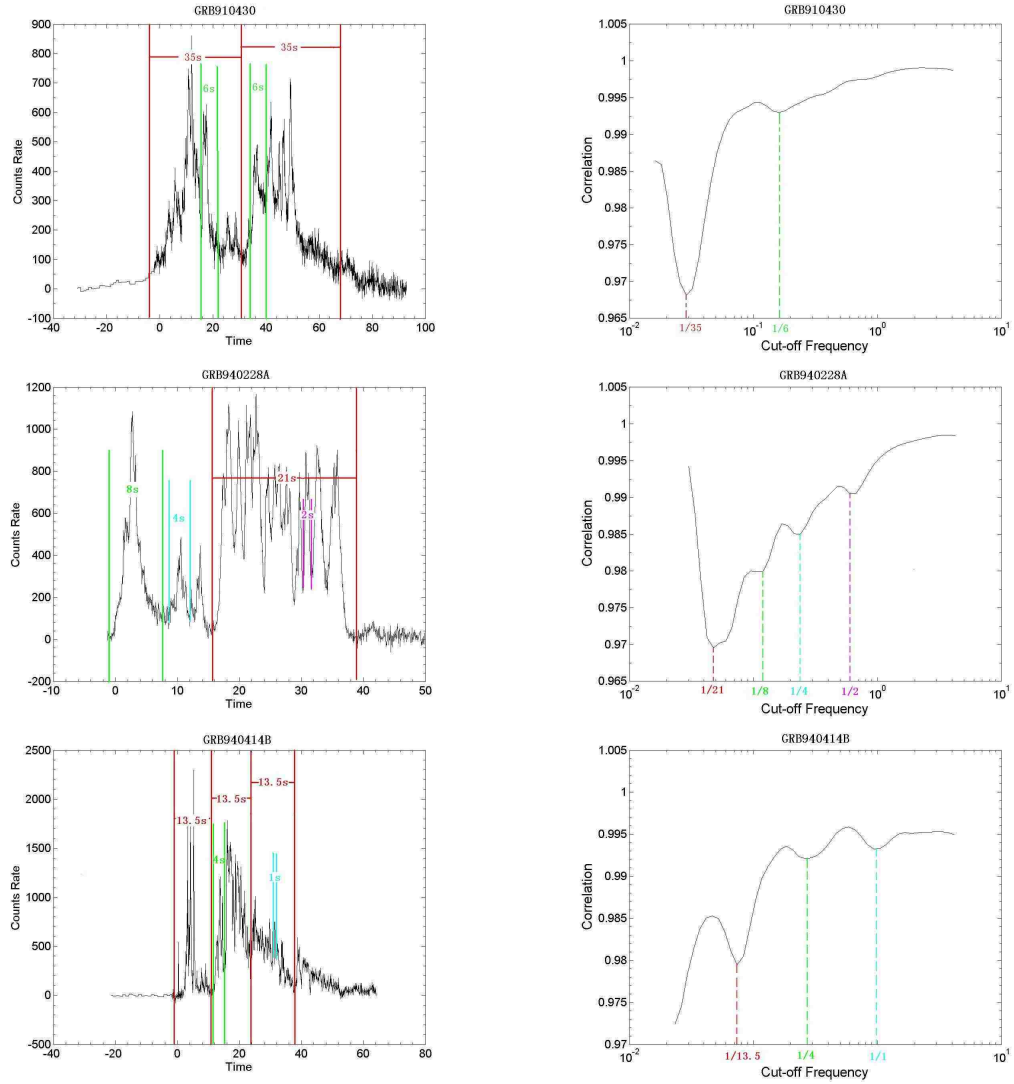


Figure 4 Examples for the multi-dip bursts. The left panel are the lightcurves, and the right panel are the correlation curves. The pulses that correspond to the identified frequencies are marked in different colors in the lightcurves. The time scales are rounded to the nearest 0.5.

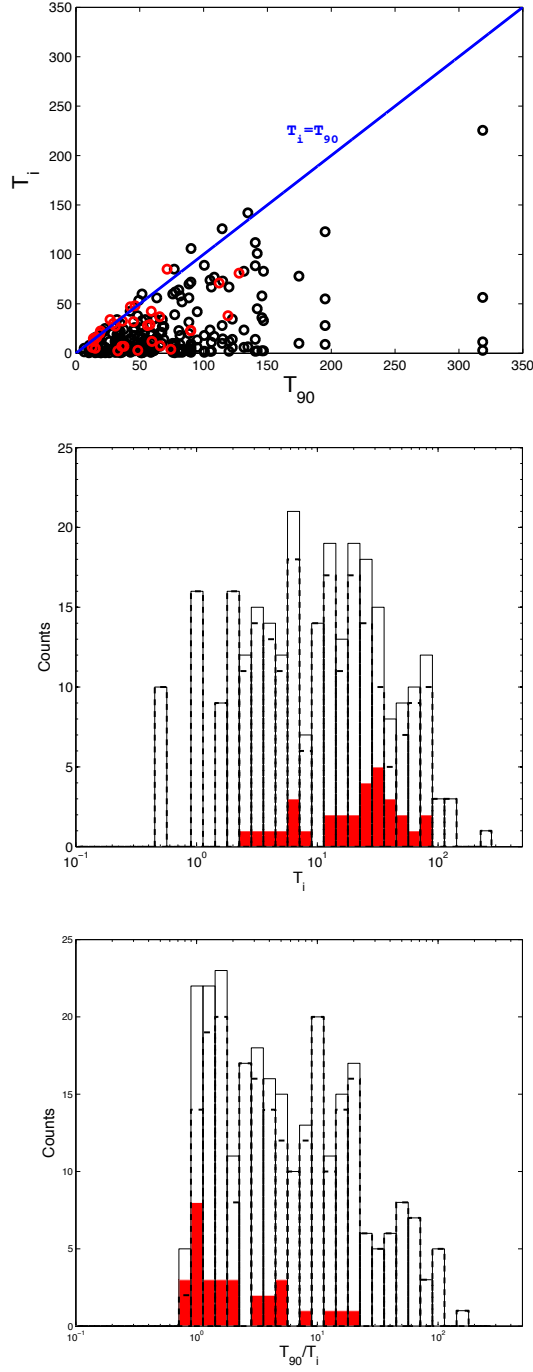


Figure 5 Statistical results of the identified characteristic frequencies I. (a) The $T_i - T_{90}$ distribution; (b) histogram of T_i ; and (c) histogram of T_{90}/T_i . The time scales identified in the one-dip sample are marked in red. In (a) the black circles denote the time scales identified in multi-dip GRBs. In (b) and (c), the dashed histograms are for the multi-dip sample, and the final solid histograms are for the entire sample.

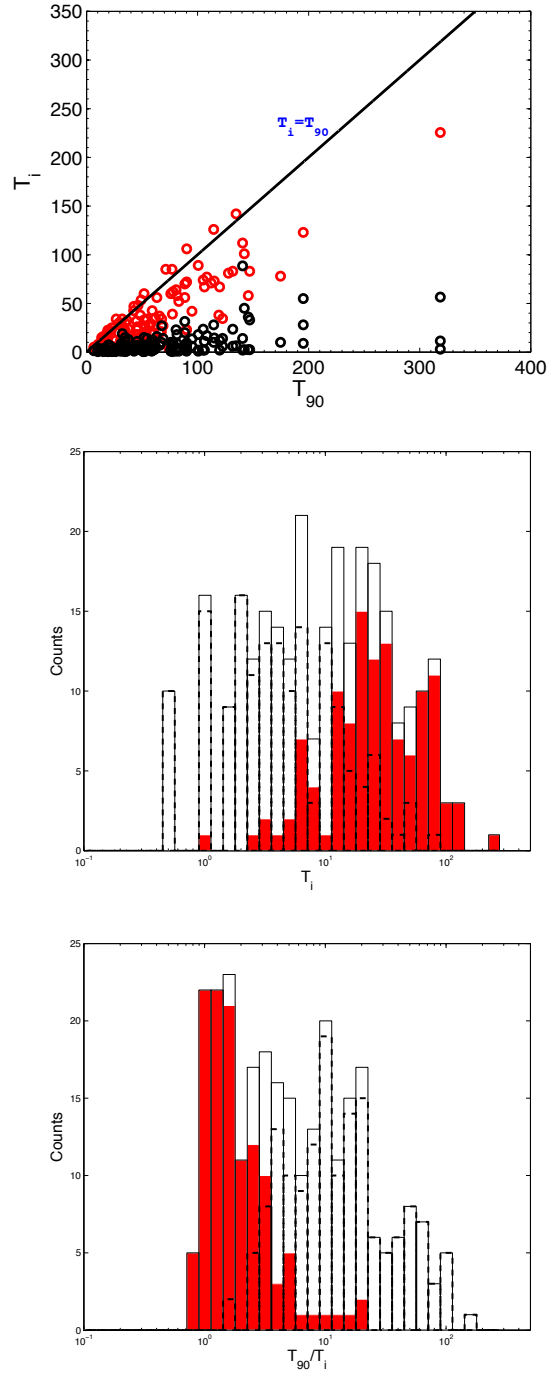


Figure 6 Statistical results of the identified characteristic frequencies II. The red color denotes the slowest time scale in all bursts, and black denotes the rest.

Theoretical Derivation and Monte Carlo Simulation Test for SFC

Method

Butterworth low-pass filter

For a time series signal $S(t)$ passing an ideal low-pass filter with cutoff angular frequency $\omega_c = 2\pi f_c$, the residual signal would read (Oppenheim et al., 1998)

$$S(\tau, \omega_c) = \frac{1}{\pi} \int_{-\infty}^{\infty} \frac{S(t) \sin[\omega_c(\tau - t)]}{\tau - t} dt. \quad (2.2)$$

For example, if $S(t) = \sin(At)$, then one has

$$S(\tau, \omega_c) = \frac{\sin(A\tau)}{2} \times [\text{Sign}(1 - \frac{A}{\omega_c}) + \text{Sign}(1 + \frac{A}{\omega_c})], \quad (2.3)$$

where “Sign” is the sign symbol of the expression. This formula can be translated to

$$S(\tau, \omega_c) = \begin{cases} 0, & \omega_c < A \\ \frac{\sin(A\tau)}{2}, & \omega_c = A \\ \sin(A\tau), & \omega_c > A \end{cases} \quad (2.4)$$

which shows that the high-frequency signal is attenuated.

For a signal as the sum of two periodic components, e.g., $S(t) = \sin(At) + \sin(Bt)$ with $A < B$, one can derive

$$S(\tau, \omega_c) = \begin{cases} 0, & \omega_c < A \\ \frac{\sin(A\tau)}{2}, & \omega_c = A \\ \sin(A\tau), & A < \omega_c < B \\ \sin(A\tau) + \frac{\sin(B\tau)}{2}, & \omega_c = B \\ \sin(A\tau) + \sin B\tau, & \omega_c > B \end{cases} \quad (2.5)$$

It is obvious to see how the two signals are screened when a progressively lower

angular cutoff frequency is applied. If one chooses two angular cutoff frequencies that satisfy $\omega_{c,i} - \omega_{c,i-1} < B - A$, one would get a correlation coefficient between two RLCs to be $R_i = 1$ if $A \& B \not\subseteq (\omega_{c,i} \sim \omega_{c,i-1})$, or $R_i \ll 1$ if $A|B \subseteq (\omega_{c,i} \sim \omega_{c,i-1})$.

Similar results can be obtained if one sets $S(t) = \cos(At)$ or $S(t) = \cos(At) + \cos(Bt)$ with $A < B$.

For a more complicated time series, one can always decompose it into the summation of many *Sine* or *Cosine* functions through Fourier transforms. For any angular cutoff frequency $\omega_{c,i}$ (and the corresponding cutoff frequency $f_{c,i} = \omega_{c,i}/2\pi$), the low-pass filter then attenuates the signal above this frequency.

Simulation tests of the SFC algorithm

In order to better understand the SFC algorithm, we perform a set of additional simulations.

1) Pulse profiles: We test four different pulse profile functions, $A|\sin(\pi t/T)|$ (sine) function, Gaussian function, and two ‘‘FRED’’ profiles proposed by Kocevski et al. (2003) and Norris et al. (1996). First, we generate multiple pulses lying side-by-side with a fast component superposed on the slow component. For all four different pulse functions, the pulse durations of the slow and fast components are fixed to 100π and 10π , respectively, with the amplitude ratio between the two components fixed as $A_s : A_f = 2 : 1$. As shown in Fig.7(a-h), we can see that SFC is not sensitive to the pulse profile function in the multi-pulse case. In the rest of the simulation tests invoking multi-pulse lightcurves, we adopt the sine function as examples, and use Fig.7(a,b) as our nominal test to be compared with others (see tests 2-6 below). Since the SFC method can catch a frequency component even if only one pulse exists (test 3 below) and since some GRBs indeed only have one broad pulse, next we test the four pulse profile functions for one pulse only. We fix the full width at half maximum (FWHM) to ~ 200 s, and vary the function shapes. To our surprise, it is found that

the identified typical durations from the SFC curve dip frequencies are very different for the four functions (Fig.7(i-p)): ~ 470 s for the sine shape, ~ 500 for the Gaussian shape, ~ 676 s for the Norris' shape, and ~ 708 s for the Kocevski's shape. A closer investigation suggests that the longer durations for the FRED shapes are mostly due to the extended tails for these profile functions (Norris et al., 1996; Kocevski et al., 2003). This explains the identified long durations for some FRED-like lightcurves in Sample II (gaps and long tails), which can be longer than T_{90} in some cases.

2) Amplitude of pulses: The amplitude of a frequency components is an important factor. For our superposition tests, the relative depths of the dips depend on the amplitude ratio of the slow and fast components. This can be seen from the comparison of Fig.7(a,b) for $A_s : A_f = 2 : 1$ and Fig.8(a,b) for $A_s : A_f = 1 : 1$ (with the nominal parameters $T_s = 100\pi$ s, and $T_f = 10\pi$ s). For this set of parameters, the fast component dip disappears when $A_s : A_f > 15 : 1$, while the slow component dip disappears when $A_s : A_f < 1 : 25$. The asymmetry is understandable since a low pass filter favors the slow component.

3) Number of pulses: Similar with 2), we change the number of pulses rather than the amplitude ratio, and also fix other parameters. Fixing the nominal parameters but increasing the number of pulses, we find that the corresponding dips in the SFC $R_i - f_{c,i}$ curve become deeper. See Fig.8(c,d) as compared with Fig.7(a,b). On the other hand, the slow component can be detected even with one single broad pulse, as long as its amplitude is large enough. See Fig.7(i-p).

4) Pulse duration spread: Similar to the mock light curve shown in the middle panel of Fig.2, we generate a set of light curves whose slow component duration range is fixed in $T_s = (50 - 100)$ s and the amplitude ratio is fixed to $A_s : A_f = 2 : 1$. We gradually spread the fast component duration range. We find that the significance of the relevant dip of the fast component in the SFC $R_i - f_{c,i}$ curve diminishes and eventually disappears as the frequency spread is wide enough (Fig.8(e-h)). and then

disappear (see Fig.7(m)~ 7(p)). We propose that the pulse duration spread is another important properties the SFC sensitive to.

5) Separation between two components: Back to the two-frequency case, we fix the amplitude ratio as $A_s : A_f = 1 : 1$ and the slow component duration as $T_s = 100$, and then gradually brings the fast component duration closer and closer to the slow one. We find that the significance of the relevant dip of fast component in the SFC $R_i - f_{c,i}$ curve diminishes, and merges with the slow frequency component when $\frac{f_f - f_s}{f_s} \leq 0.5$ is satisfied (Fig.8(i-n)). Fig.7(o)~ Fig.7(t)).

6) Gaps between pulses: Here we still test the simple two-frequency case. We fix the pulse duration of slow component as 100π , fast component as 10π , and the amplitude ratio between the two components as $A_s : A_f = 1 : 1$. We then add gaps in the lightcurve between the slow component pulses. The gap duration is fixed to 100π (Fig.8(o,p)), Fig.7(u)~ Fig.7(v)) or is randomly distributed in the range $0 - 100\pi$ (Fig.8(q,r)). We find that the SFC curve still shows two components. However, the corresponding period for slow component is larger than 100π , indicating that part of the gap duration is added to the pulse. We therefore draw the conclusion that one should be careful to perform SFC analysis when substantial gaps exist in a lightcurve. Indeed, only when the gap is manually removed, can the original pulse width restored (see final section for a case study).

Case studies of GRBs not belonging to the good sample

We take GRB 930120 as an example in Group II (gaps/long tails). As shown in Fig.9(a), the burst has two brief activities with durations ~ 10 s, followed by the main emission episode. The three episodes are separated by two gaps. The SFC curve (Fig.9(b)) shows only one dip, which corresponds to the main pulse with duration around 34.5 s.

The puzzling fact is that the ~ 10 s feature and the high-frequency spikes overlap-

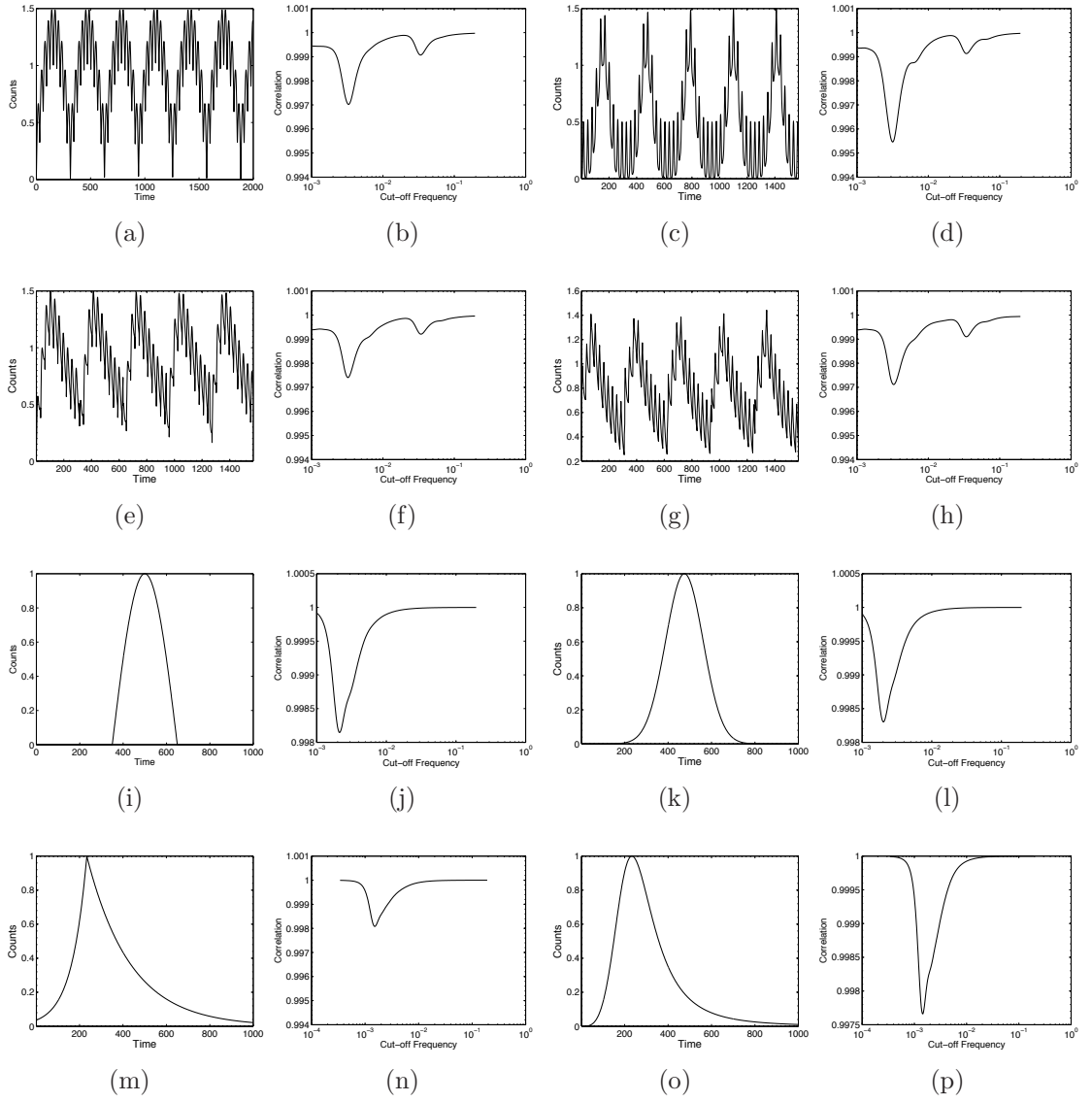


Figure 7 Mock catalog of lightcurves with different pulse profile and their relevant correlation curves I.

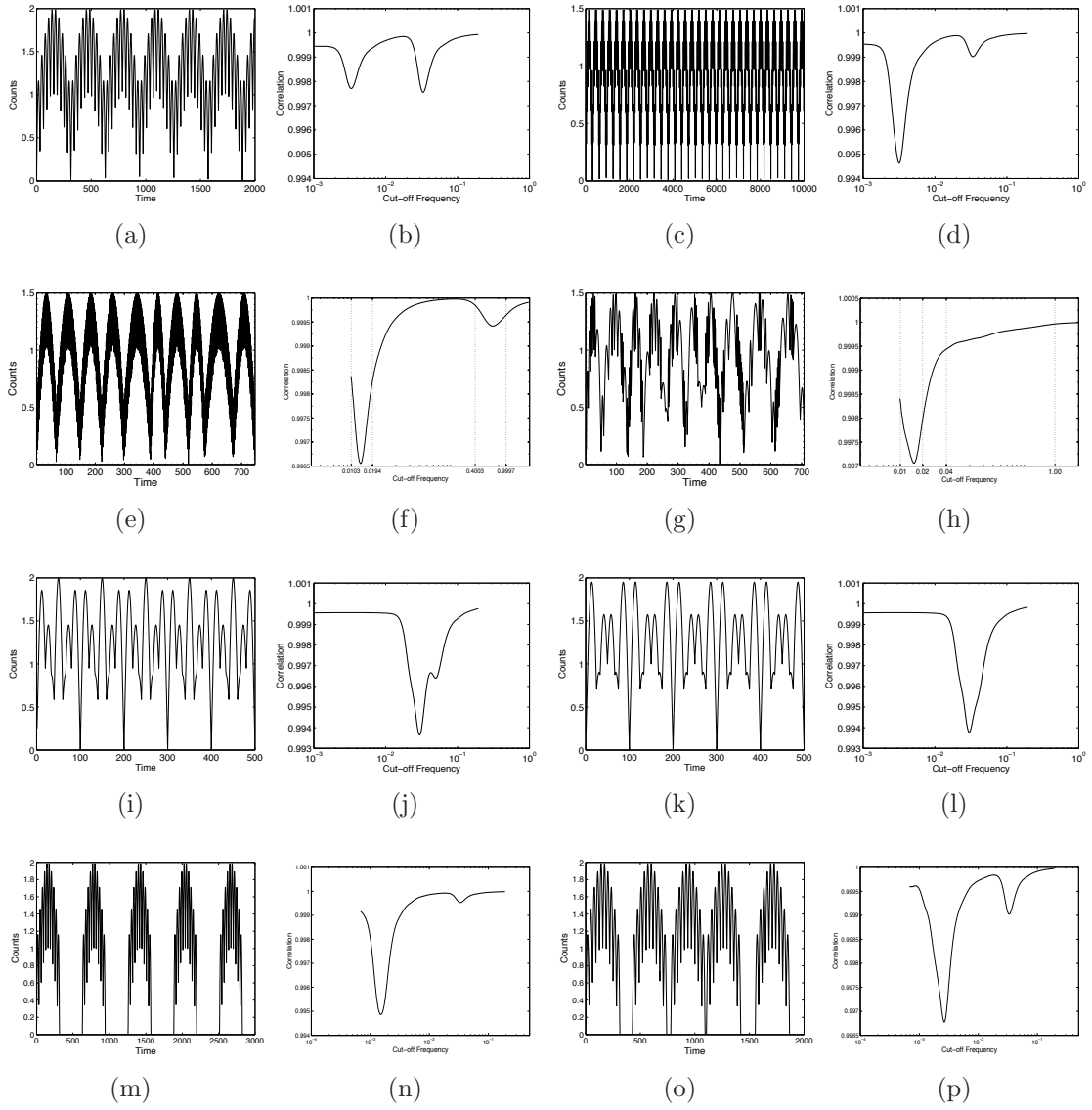


Figure 8 Mock catalog of lightcurves with different pulse properties and their relevant correlation curves II.

ping the main pulse are not captured. The missing high-frequency spiky component is due to the low amplitude of this component. The lack of the ~ 10 s component may be understood in two ways. (1) The amplitudes of those two pulses are too small compared with the main pulse; (2) The existence of the gaps modified the durations of those pulses from ~ 10 s to ~ 30 s, which is close to the duration of the main pulse so that the two dips merge to one. To test these possibilities, we perform several tests. First, we manually remove the quiescent periods (the gaps) in the lightcurve. The SFC curve still does not show the ~ 10 s component (Fig.9(c,d)). Next, we manually increase the amplitudes of the two pulses to be comparable to that of the main pulse, the ~ 10 s component then shows up in the SFC curve (Fig.9(e,f)). Finally, we increase the amplitude of the two pulses but do not remove the gaps. The ~ 10 s dip in the SFC curve disappears again (Fig.9(g,h)). This suggests that both reasons (low amplitude and influence of gaps) play a role in missing the ~ 10 s component in the original lightcurve.

In the irregular group (III) we chose GRB 910522 as an example. The lightcurve is very noisy (Fig.9(i)), and the SFC curve is irregular (Fig.9(j)).

Finally, the group IV includes bursts with short durations or poor temporal resolution. The SFC method is no longer applicable to these bursts. An example (GRB 920718B) is presented in Fig.9(k,l).

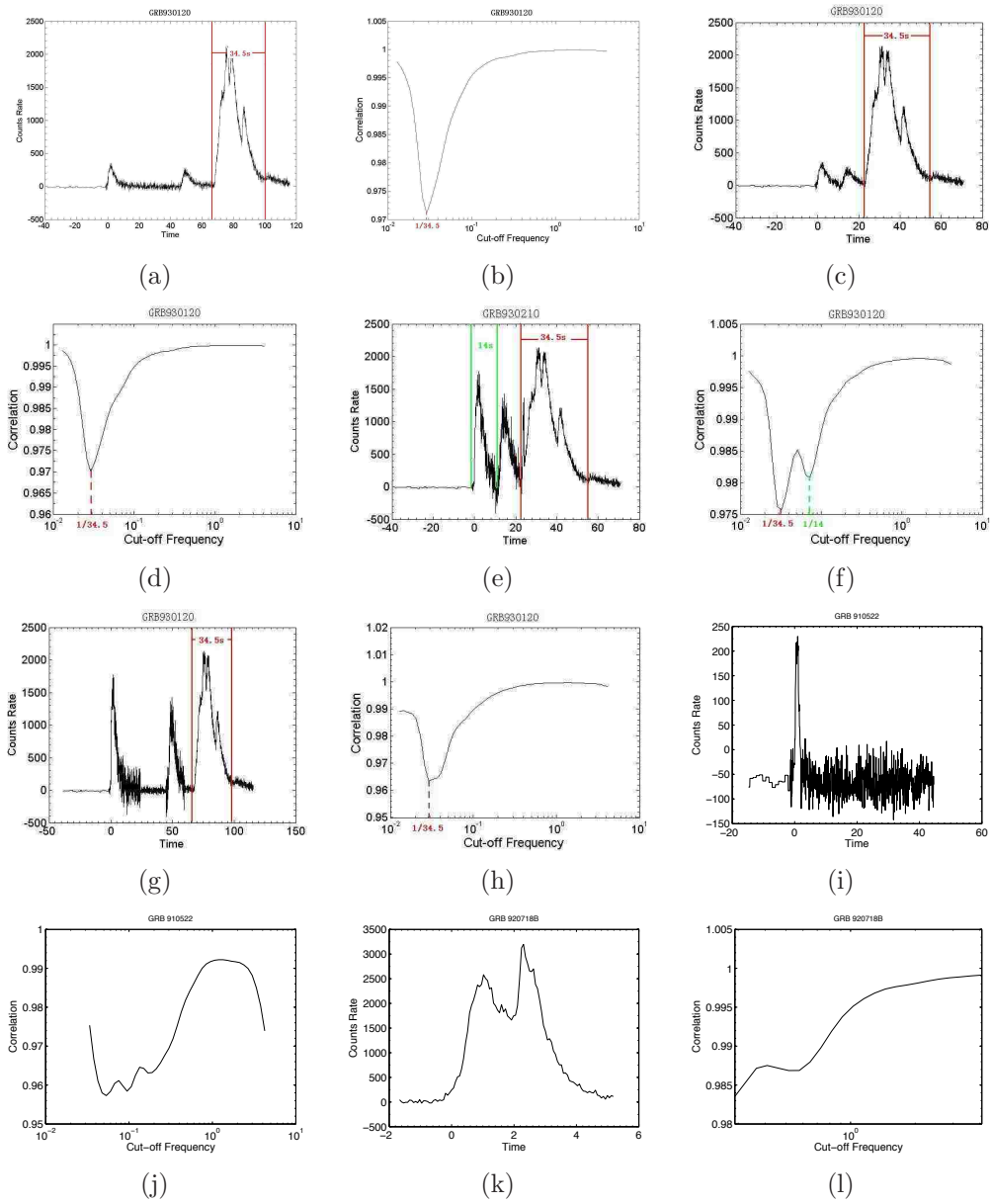


Figure 9 Original and synthetic lightcurve for GRB930120. The top and middle panel are original and synthetic lightcurve for GRB930120. The pulses that correspond to the identified frequencies are marked in different colors in the lightcurves. The time scales are rounded to the nearest 0.5. The bottom panel is lightcurve and SFC curve for GRB910522 and GRB920718B.

CHAPTER 3

COMPTON SCATTERING OF SELF-ABSORBED SYNCHROTRON EMISSION

This chapter is part of the following published paper :

Gao H., Lei W.-H., Wu, X.-F., Zhang B., 2013, Monthly Notices of the Royal Astronomical Society, 435,2520

Astrophysical sources powered by synchrotron radiation should have a synchrotron self-Compton (SSC) scattering component. The same electrons that radiate synchrotron photons would scatter these synchrotron seed photons to high energies, forming a distinct spectral component. The SSC mechanism has been invoked to account for the observed high energy emission in many astrophysical sources, such as gamma-ray bursts (GRBs) (e.g. Mészáros et al., 1994; Wei and Lu, 1998; Dermer et al., 2000a; Panaitescu & Kumar, 2000; Sari and Esin, 2001; Wang et al., 2001a; Wu et al., 2004) and active galactic nuclei (AGNs) (e.g. Ghisellini et al., 1998b; Chiang & Böttcher, 2002; Zhang et al., 2012).

SSC is a complex process. The flux at each observed frequency includes the contributions from electrons in a wide range of energies, which scatter seed photons in a wide range of frequencies. Therefore, a precise description of the SSC spectrum invokes a complex convolution of the seed photon spectrum and electron energy distribution, which requires numerical calculations. However, for a synchrotron source with shock-accelerated electrons, the injected electron spectrum is usually assumed to be a simple power-law function, the corresponding electron energy distribution and seed synchrotron spectrum thus have simple patterns. Some analytical approximations for the SSC spectrum can be then made if Compton scattering is in the Thomson regime.

Besides the injected electron spectrum, two other factors are essential to define the shape of the final electron energy distribution in a synchrotron source: radia-

tion cooling and self-absorption heating. There are three characteristic synchrotron frequencies in the spectrum: the minimum injection frequency (ν_m), the cooling frequency (ν_c), and the self-absorption frequency (ν_a). When $\nu_a < \nu_c$, the heating effect due to self-absorption is not important in modifying the electron energy spectrum. For a continuous injection of a power-law electron spectrum, the final electron energy distribution is a broken power law. The seed synchrotron spectrum for SSC is characterized by a multi-segment broken power law, separated by ν_m , ν_c , and ν_a . Different ordering of the three characteristic frequencies leads to different shapes of the seed synchrotron spectrum. In the literature, usually $\nu_a < \min(\nu_m, \nu_c)$ is assumed. Sari and Esin (2001) have derived the approximated expressions of the SSC spectrum in the $\nu_a < \nu_m < \nu_c$ and $\nu_a < \nu_c < \nu_m$ regimes, respectively¹.

When $\nu_a > \nu_c$, synchrotron self-absorption becomes an important heating source for the low-energy electrons. Consequently, the electrons are dominated by a quasi-thermal component until a “transition” Lorentz factor γ_t , above which the electrons are no longer affected by the self-absorption heating and keep the normal power law distribution (Ghisellini et al., 1988, 1991, 1998a). For these strong absorption cases, a thermal peak due to pile-up electrons would appear around ν_a in the synchrotron spectrum (Kobayashi et al., 2004), which would also result in some new features in the SSC spectrum.

In this work, we extend the analysis of Sari and Esin (2001) and present the full analytical approximated expressions of the SSC spectrum in all six possible cases of ν_a , ν_m , ν_c ordering. Firstly, three weak synchrotron self-absorption cases ($\nu_a < \nu_c$) are discussed. Then we focus on the strong synchrotron self-absorption regime ($\nu_a > \nu_c$), where synchrotron self-absorption significantly affects the electron energy distribution. By adopting a simplified prescription of the pile-up electron distribution, we derive the expressions of both synchrotron and SSC spectral components. All the

¹Assuming weak self-absorption, Gou et al. (2007) derived analytical approximations of the SSC component for several other spectral regimes.

expressions in this work are valid in the Thomson regime, so that the Klein-Nishina correction effect (e.g. Rees, 1967; Nakar et al., 2009) is not important in the first order SSC component. We also limit our treatment to the first-order SSC, and assume that the higher-order SSC components (e.g. Kobayashi et al., 2007; Piran et al., 2009) are suppressed by the Klein-Nishina effect. Such an assumption is usually valid for most problems. In order to make a simple analytical treatment, we have applied a simplified approximation for the synchrotron spectra, and adopted the simplification that the inverse Compton scattering of mono-energetic electrons off mono-energetic seed photons is also mono-energetic (Sari and Esin, 2001). This would not significantly deteriorate precision of the analysis, while making it much simpler.

Weak Synchrotron Self-Absorption Cases

In the single scattering regime, the inverse Compton volume emissivity for a power-law distribution of electrons is (Rybicki and Lightman, 1979; Sari and Esin, 2001)

$$j_{\nu}^{IC} = 3\sigma_T \int_{\gamma_m}^{\infty} d\gamma N(\gamma) \int_0^1 dx g(x) \tilde{f}_{\nu_s}(x), \quad (3.1)$$

where $x \equiv \nu/4\gamma^2\nu_s$ (an angle-dependent parameter), \tilde{f}_{ν_s} is the incident specific flux in the shock front, σ_T is Thomson scattering cross section, and $g(x) = 1+x+2x \ln x - 2x^2$ takes care of the angular dependence of the scattering cross section in the limit of $\gamma \gg 1$ (Blumenthal & Gould, 1970). One can approximate $g(x) = 1$ for $0 < x < x_0$ to simplify the integration, which would yield a correct behavior for $x \ll 1$ (Sari & Esin 2001). With such a simplification, the SSC spectrum is given by (Sari & Esin 2001),

$$f_{\nu}^{IC} = R\sigma_T \int_{\gamma_m}^{\infty} d\gamma N(\gamma) \int_0^{x_0} dx f_{\nu_s}(x), \quad (3.2)$$

where $f_{\nu_s}(x)$ is the synchrotron flux, R is the co-moving size of the emission region, and the value of the parameter x_0 is set by ensuring energy conservation, i.e. $\int_0^1 x g(x) dx = \int_0^{x_0} x dx$.

When $\nu_a < \nu_c$, in the slow cooling regime ($\gamma_m < \gamma_c$), the electron energy distribution is

$$N(\gamma) = \begin{cases} n(p-1)\gamma_m^{p-1}\gamma^{-p}, & \gamma_m \leq \gamma \leq \gamma_c, \\ n(p-1)\gamma_m^{p-1}\gamma_c\gamma^{-p-1}, & \gamma > \gamma_c. \end{cases} \quad (3.3)$$

Here γ_m is the minimum Lorentz factor of the injected electrons, and p is electron spectral index. Cooling is efficient for electrons with Lorentz factor above the critical value γ_c . Notice that Eq.3.3 is only valid for $p > 1$.

In the fast cooling regime ($\gamma_c < \gamma_m$), the electron energy distribution is²

$$N(\gamma) = \begin{cases} n\gamma_c\gamma^{-2}, & \gamma_c \leq \gamma \leq \gamma_m, \\ n\gamma_m^{p-1}\gamma_c\gamma^{-p-1}, & \gamma > \gamma_m. \end{cases} \quad (3.4)$$

In this regime, all the injected electrons are able to cool on the dynamical timescale. Therefore, there is a population of electrons with Lorentz factor below the injection minimum Lorentz factor γ_m .

The seed synchrotron spectrum f_{ν_s} has spectral beaks at ν_a , ν_m and ν_c , where ν_a is the self-absorption frequency, below which the system becomes optically thick, and ν_m and ν_c are the characteristic synchrotron frequencies for the electrons with Lorentz factors γ_m and γ_c , respectively.

As shown in Sari and Esin (2001), the critical frequencies in the SSC component are defined by different combination of γ_a , γ_m , γ_c and ν_a , ν_m , ν_c . For convenience, we

²This is valid only in the deep fast cooling regime. For a non-steady state with not too deep fast cooling, the electron spectrum can be harder than -2 (Uhm and Zhang, 2013b).

use a new notation in this work

$$\nu_{ij}^{\text{IC}} = 4\gamma_i^2 \nu_j x_0, \quad i, j = a, c, m. \quad (3.5)$$

The physical meaning is the characteristic upscattered frequency for mono-energetic electrons with Lorentz factor γ_i scattering off mono-energetic photons with frequency ν_j .

Case I: $\nu_a < \nu_m < \nu_c$

This case has been studied by Sari and Esin (2001). The synchrotron spectrum reads³

$$f_\nu = \begin{cases} f_{\text{max}} \left(\frac{\nu_a}{\nu_m} \right)^{\frac{1}{3}} \left(\frac{\nu}{\nu_a} \right)^2, & \nu \leq \nu_a; \\ f_{\text{max}} \left(\frac{\nu}{\nu_m} \right)^{\frac{1}{3}}, & \nu_a < \nu \leq \nu_m; \\ f_{\text{max}} \left(\frac{\nu}{\nu_m} \right)^{\frac{1-p}{2}}, & \nu_m < \nu \leq \nu_c; \\ f_{\text{max}} \left(\frac{\nu_c}{\nu_m} \right)^{\frac{1-p}{2}} \left(\frac{\nu}{\nu_c} \right)^{-\frac{p}{2}}, & \nu > \nu_c, \end{cases} \quad (3.6)$$

where $f_{\text{max}} = f_\nu(\nu_m)$ is the peak flux density of the synchrotron component, which is taken as a constant. Substituting this seed photon spectrum into equation (3.2), the inner integral reads (Sari and Esin, 2001)

$$I = \begin{cases} I_1 \simeq \frac{5}{2} f_{\text{max}} x_0 \left(\frac{\nu_a}{\nu_m} \right)^{\frac{1}{3}} \left(\frac{\nu}{4\gamma^2 \nu_a x_0} \right), & \nu < 4\gamma^2 \nu_a x_0 \\ I_2 \simeq \frac{3}{2} f_{\text{max}} x_0 \left(\frac{\nu}{4\gamma^2 \nu_m x_0} \right)^{\frac{1}{3}}, & 4\gamma^2 \nu_a x_0 < \nu < 4\gamma^2 \nu_m x_0 \\ I_3 \simeq \frac{2}{(p+1)} f_{\text{max}} x_0 \left(\frac{\nu}{4\gamma^2 \nu_m x_0} \right)^{\frac{1-p}{2}}, & 4\gamma^2 \nu_m x_0 < \nu < 4\gamma^2 \nu_c x_0 \\ I_4 \simeq \frac{2}{(p+2)} f_{\text{max}} x_0 \left(\frac{\nu_c}{\nu_m} \right)^{\frac{1-p}{2}} \left(\frac{\nu}{4\gamma^2 \nu_c x_0} \right)^{-\frac{p}{2}}, & \nu > 4\gamma^2 \nu_c x_0. \end{cases} \quad (3.7)$$

³Hereafter, the synchrotron spectra are denoted as $f_\nu(\nu)$ for simple presentation. Notice that when they are taken as seed spectrum, one should consider them as $f_{\nu_s}(\nu_s)$ and apply equation (3.2) to calculate the SSC spectra.

Similar to Sari and Esin (2001), only the leading order of ν and zeroth order of ν_a/ν_m and ν_m/ν_c are shown. However, we note that higher order small terms are needed to derive the following SSC spectrum (3.8) through integrating the outer integral of equation (3.2).

After integration, f_ν^{IC} is very complex. Keeping only the dominant terms, one gets the analytical approximation

$$f_\nu^{\text{IC}} \simeq R\sigma_T n f_{\text{max}} x_0 \quad (3.8)$$

$$\times \begin{cases} \frac{5}{2} \frac{(p-1)}{(p+1)} \left(\frac{\nu_a}{\nu_m}\right)^{\frac{1}{3}} \left(\frac{\nu}{\nu_{\text{ma}}^{\text{IC}}}\right), & \nu < \nu_{\text{ma}}^{\text{IC}}; \\ \frac{3}{2} \frac{(p-1)}{(p-1/3)} \left(\frac{\nu}{\nu_{\text{mm}}^{\text{IC}}}\right)^{\frac{1}{3}}, & \nu_{\text{ma}}^{\text{IC}} < \nu < \nu_{\text{mm}}^{\text{IC}}; \\ \frac{(p-1)}{(p+1)} \left(\frac{\nu}{\nu_{\text{mm}}^{\text{IC}}}\right)^{\frac{1-p}{2}} \left[\frac{4(p+1/3)}{(p+1)(p-1/3)} + \ln\left(\frac{\nu}{\nu_{\text{mm}}^{\text{IC}}}\right) \right], & \nu_{\text{mm}}^{\text{IC}} < \nu < \nu_{\text{mc}}^{\text{IC}}; \\ \frac{(p-1)}{(p+1)} \left(\frac{\nu}{\nu_{\text{mm}}^{\text{IC}}}\right)^{\frac{1-p}{2}} \left[\frac{2(2p+3)}{(p+2)} - \frac{2}{(p+1)(p+2)} + \ln\left(\frac{\nu_{\text{cc}}^{\text{IC}}}{\nu}\right) \right], & \nu_{\text{mc}}^{\text{IC}} < \nu < \nu_{\text{cc}}^{\text{IC}}; \\ \frac{(p-1)}{(p+1)} \left(\frac{\nu}{\nu_{\text{mm}}^{\text{IC}}}\right)^{-\frac{p}{2}} \left(\frac{\nu_c}{\nu_m}\right) \left[\frac{2(2p+3)}{(p+2)} - \frac{2}{(p+2)^2} + \frac{(p+1)}{(p+2)} \ln\left(\frac{\nu}{\nu_{\text{cc}}^{\text{IC}}}\right) \right], & \nu > \nu_{\text{cc}}^{\text{IC}}. \end{cases}$$

Notice that Sari and Esin (2001) presented an opposite sign for the term $\frac{2}{(p+2)^2}$ in the last segment, which might be a typo in that paper.

The normalized synchrotron + SSC spectra for this and other two weak self-absorption cases are presented in Figure 10. We note that these analytical expressions are not continuous around the breaks because of dropping the small order terms (see also Sari & Esin 2001), but the mis-match is small. When plotting the SSC curve in Figure 10, we have used the analytical approximations, but added back some smaller order terms to remove the discontinuity.

Case II: $\nu_m < \nu_a < \nu_c$

The synchrotron photons spectrum reads

$$f_\nu = \begin{cases} f_{\max} \left(\frac{\nu_m}{\nu_a} \right)^{\frac{p+4}{2}} \left(\frac{\nu}{\nu_m} \right)^2, & \nu \leq \nu_m; \\ f_{\max} \left(\frac{\nu_a}{\nu_m} \right)^{\frac{1-p}{2}} \left(\frac{\nu}{\nu_a} \right)^{\frac{5}{2}}, & \nu_m < \nu \leq \nu_a; \\ f_{\max} \left(\frac{\nu}{\nu_m} \right)^{\frac{1-p}{2}}, & \nu_a < \nu \leq \nu_c; \\ f_{\max} \left(\frac{\nu_c}{\nu_m} \right)^{\frac{1-p}{2}} \left(\frac{\nu}{\nu_c} \right)^{-\frac{p}{2}}, & \nu > \nu_c; \end{cases} \quad (3.9)$$

Evaluating the inner integral in equation (3.2), we obtain

$$I = \begin{cases} I_1 \simeq \frac{2(p+4)}{3(p+1)} f_{\max} x_0 \left(\frac{\nu_m}{\nu_a} \right)^{\frac{p+1}{2}} \frac{\nu}{4\gamma^2 \nu_m x_0}, & \nu < 4\gamma^2 \nu_a x_0 \\ I_2 \simeq \frac{2}{p+1} f_{\max} x_0 \left(\frac{\nu}{4\gamma^2 \nu_m x_0} \right)^{\frac{1-p}{2}}, & 4\gamma^2 \nu_a x_0 < \nu < 4\gamma^2 \nu_c x_0 \\ I_3 \simeq \frac{2}{(p+2)} f_{\max} x_0 \left(\frac{\nu_c}{\nu_m} \right)^{\frac{1}{2}} \left(\frac{\nu}{4\gamma^2 \nu_m x_0} \right)^{-\frac{p}{2}}, & \nu > 4\gamma^2 \nu_c x_0 \end{cases} \quad (3.10)$$

An interesting feature of this result is that I_1 is linear with ν all the way to $\nu = 4\gamma^2 \nu_a x_0$, indicating that a break corresponding to the break in the synchrotron spectrum at ν_m does not show up in the SSC spectrum for monoenergetic electron scattering. When $\nu > 4\gamma^2 \nu_a x_0$, the SSC spectrum follows the same frequency dependence as the corresponding seed synchrotron spectrum.

After second integration, we get the analytical approximation in this regime:

$$f_\nu^{\text{IC}} \simeq R\sigma_T n f_{\max} x_0 \quad (3.11)$$

$$\times \begin{cases} \frac{2(p+4)(p-1)}{3(p+1)^2} \left(\frac{\nu_m}{\nu_a} \right)^{\frac{p+1}{2}} \left(\frac{\nu}{\nu_{\text{mm}}^{\text{IC}}} \right), & \nu < \nu_{\text{ma}}^{\text{IC}}; \\ \frac{(p-1)}{(p+1)} \left(\frac{\nu}{\nu_{\text{mm}}^{\text{IC}}} \right)^{\frac{1-p}{2}} \left[\frac{2(2p+5)}{(p+1)(p+4)} + \ln \left(\frac{\nu}{\nu_{\text{ma}}^{\text{IC}}} \right) \right], & \nu_{\text{ma}}^{\text{IC}} < \nu < \nu_{\text{mc}}^{\text{IC}}; \\ \frac{(p-1)}{(p+1)} \left(\frac{\nu}{\nu_{\text{mm}}^{\text{IC}}} \right)^{\frac{1-p}{2}} \left[2 + \frac{2}{p+4} + \ln \left(\frac{\nu_c}{\nu_a} \right) \right], & \nu_{\text{mc}}^{\text{IC}} < \nu < \nu_{\text{ca}}^{\text{IC}}; \\ \frac{(p-1)}{(p+1)} \left(\frac{\nu}{\nu_{\text{mm}}^{\text{IC}}} \right)^{\frac{1-p}{2}} \left[\frac{2(2p+1)}{(p+1)} + \ln \left(\frac{\nu_{\text{cc}}^{\text{IC}}}{\nu} \right) \right], & \nu_{\text{ca}}^{\text{IC}} < \nu < \nu_{\text{cc}}^{\text{IC}}; \\ \frac{(p-1)}{(p+2)} \left(\frac{\nu_c}{\nu_m} \right) \left(\frac{\nu}{\nu_{\text{mm}}^{\text{IC}}} \right)^{-\frac{p}{2}} \left[\frac{2(2p+5)}{(p+2)} + \ln \left(\frac{\nu}{\nu_{\text{cc}}^{\text{IC}}} \right) \right], & \nu > \nu_{\text{cc}}^{\text{IC}}. \end{cases}$$

Similar to the I result, there is no spectral break around $\nu_{\text{mm}}^{\text{IC}}$. Another comment is that the logarithmic terms make the SSC spectrum harder than the simple broken power-law approximation above the νF_ν peak frequency. At high frequencies, the simple broken power-law approximation may not be adequate to represent the true SSC spectrum.

Case III: $\nu_a < \nu_c < \nu_m$

This case was also studied by Sari and Esin (2001). The seed synchrotron spectrum reads

$$f_\nu = \begin{cases} f_{\text{max}} \left(\frac{\nu_a}{\nu_c} \right)^{\frac{1}{3}} \left(\frac{\nu}{\nu_a} \right)^2, & \nu \leq \nu_a; \\ f_{\text{max}} \left(\frac{\nu}{\nu_c} \right)^{\frac{1}{3}}, & \nu_a < \nu \leq \nu_c; \\ f_{\text{max}} \left(\frac{\nu}{\nu_c} \right)^{-\frac{1}{2}}, & \nu_c < \nu \leq \nu_m; \\ f_{\text{max}} \left(\frac{\nu_c}{\nu_m} \right)^{\frac{1}{2}} \left(\frac{\nu}{\nu_m} \right)^{-\frac{p}{2}}, & \nu > \nu_m; \end{cases} \quad (3.12)$$

This gives

$$I = \begin{cases} I_1 \simeq \frac{5}{2} f_{\text{max}} x_0 \left(\frac{\nu_a}{\nu_c} \right)^{\frac{1}{3}} \left(\frac{\nu}{4\gamma^2 \nu_a x_0} \right), & \nu < 4\gamma^2 \nu_a x_0 \\ I_2 \simeq \frac{3}{2} f_{\text{max}} x_0 \left(\frac{\nu}{4\gamma^2 \nu_c x_0} \right)^{\frac{1}{3}}, & 4\gamma^2 \nu_a x_0 < \nu < 4\gamma^2 \nu_c x_0 \\ I_3 \simeq \frac{2}{3} f_{\text{max}} x_0 \left(\frac{\nu}{4\gamma^2 \nu_c x_0} \right)^{-\frac{1}{2}}, & 4\gamma^2 \nu_c x_0 < \nu < 4\gamma^2 \nu_m x_0 \\ I_4 \simeq \frac{2}{(p+2)} f_{\text{max}} x_0 \left(\frac{\nu_c}{\nu_m} \right)^{\frac{1}{2}} \left(\frac{\nu}{4\gamma^2 \nu_m x_0} \right)^{-\frac{p}{2}}, & \nu > 4\gamma^2 \nu_m x_0 \end{cases} \quad (3.13)$$

and the final SSC spectrum

$$f_\nu^{\text{IC}} \simeq R \sigma_T n f_{\text{max}} x_0 \quad (3.14)$$

$$\times \begin{cases} \frac{5}{6} \left(\frac{\nu_a}{\nu_c} \right)^{\frac{1}{3}} \left(\frac{\nu}{\nu_{ca}^{IC}} \right), & \nu < \nu_{ca}^{IC}; \\ \frac{9}{10} \left(\frac{\nu}{\nu_{cc}^{IC}} \right)^{\frac{1}{3}}, & \nu_{ca}^{IC} < \nu < \nu_{cc}^{IC}; \\ \frac{1}{3} \left(\frac{\nu}{\nu_{cc}^{IC}} \right)^{-\frac{1}{2}} \left[\frac{28}{15} + \ln \left(\frac{\nu}{\nu_{cc}^{IC}} \right) \right], & \nu_{cc}^{IC} < \nu < \nu_{cm}^{IC}; \\ \frac{1}{3} \left(\frac{\nu}{\nu_{cc}^{IC}} \right)^{-\frac{1}{2}} \left[\frac{2(p+5)}{(p+2)(p-1)} - \frac{2(p-1)}{3(p+2)} + \ln \left(\frac{\nu_{mm}^{IC}}{\nu} \right) \right], & \nu_{cm}^{IC} < \nu < \nu_{mm}^{IC}; \\ \frac{1}{(p+2)} \left(\frac{\nu_c}{\nu_m} \right) \left(\frac{\nu}{\nu_{mm}^{IC}} \right)^{-\frac{p}{2}} \left[\frac{2}{3} \frac{(p+5)}{(p-1)} - \frac{2}{3} \frac{(p-1)}{(p+2)} + \ln \left(\frac{\nu}{\nu_{mm}^{IC}} \right) \right], & \nu > \nu_{mm}^{IC}. \end{cases}$$

We note that Sari and Esin (2001) has an opposite sign in the term $\ln \left(\frac{\nu}{\nu_{cc}^{IC}} \right)$ in the third segment, which might be another typo in that paper.

We define ratio between the SSC luminosity and the synchrotron luminosity as the X parameter similar to Sari & Esin (2001), i.e.,

$$X \equiv \frac{L_{IC}}{L_{syn}} = \frac{U_{ph}}{U_B}, \quad (3.15)$$

where U_{ph} and U_B are the synchrotron photon energy density and magnetic field energy density, respectively.

For $\nu_a < \nu_m < \nu_c$ (case I) and $\nu_m < \nu_a < \nu_c$ (case II), the νf_ν peaks of the synchrotron and the SSC components are at ν_c and ν_{cc}^{IC} , respectively (see Figure 10). One can estimate

$$\begin{aligned} X = \frac{L_{IC}}{L_{syn}} &\sim \frac{\nu_{cc}^{IC} f_\nu^{IC}(\nu_{cc}^{IC})}{\nu_c f_\nu(\nu_c)} \\ &\sim \frac{\nu_{cc}^{IC} R \sigma_T n f_{max} x_0 \left(\frac{\nu_{cc}^{IC}}{\nu_{mm}^{IC}} \right)^{\frac{1-p}{2}}}{\nu_c f_{max} \left(\frac{\nu_c}{\nu_m} \right)^{\frac{1-p}{2}}} \\ &\sim 4x_0^2 \sigma_T n R \gamma_c^2 \left(\frac{\gamma_c}{\gamma_m} \right)^{1-p}, \end{aligned} \quad (3.16)$$

which is consistent with Sari & Esin (2001). Note that when calculating X , we did not include the coefficients in the analytical approximations of the SSC component,

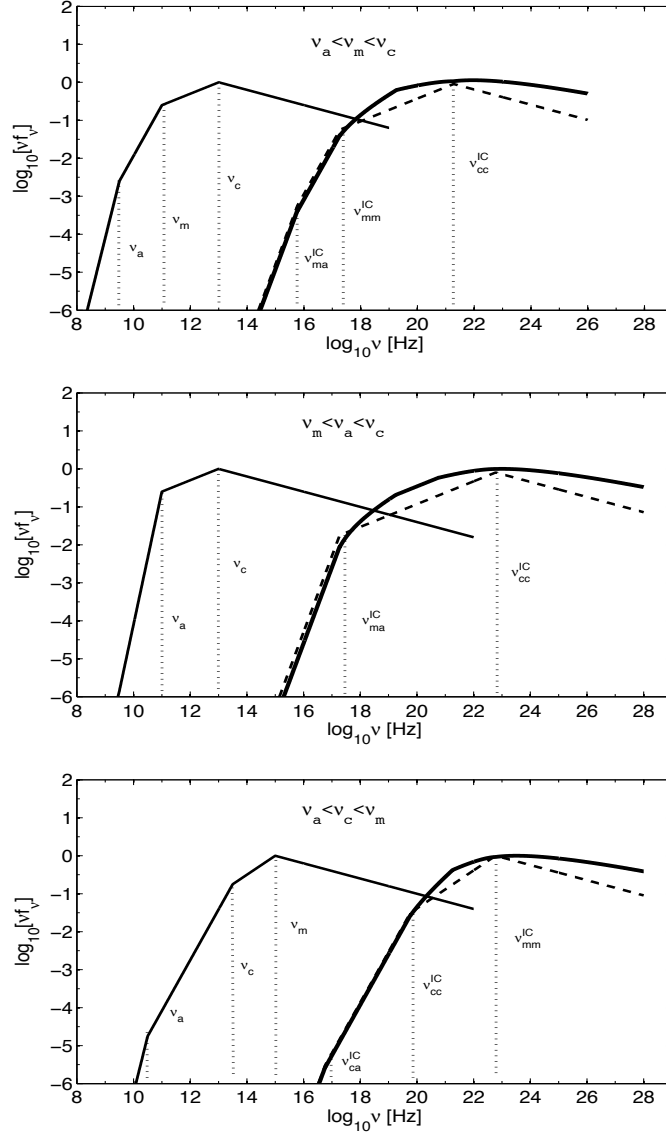


Figure 10 Total synchrotron + SSC spectra for weak synchrotron reabsorption cases ($\nu_a < \nu_c$). The top panel is for $\nu_a < \nu_m < \nu_c$ case; the middle panel is for $\nu_m < \nu_a < \nu_c$ case; and the bottom panel is for $\nu_a < \nu_c < \nu_m$ case. The thin solid line is synchrotron component. The thick solid line in the SSC component is drawn using the analytical approximations, while the dashed lines are the broken power-law approximation for comparison. In all the cases, the νF_ν peaks for both the synchrotron and the SSC components are normalized to unity.

which is of order unity.

For $\nu_a < \nu_c < \nu_m$ (case III), the νf_ν peaks of the synchrotron and SSC components are at ν_m , and $\nu_{\text{mm}}^{\text{IC}}$, respectively. One therefore has

$$\begin{aligned}
X = \frac{L_{\text{IC}}}{L_{\text{syn}}} &\sim \frac{\nu_{\text{mm}}^{\text{IC}} f_\nu^{\text{IC}}(\nu_{\text{mm}}^{\text{IC}})}{\nu_m f_\nu(\nu_m)} \\
&\sim \frac{\nu_{\text{mm}}^{\text{IC}} R \sigma_T n f_{\text{max}} x_0 \left(\frac{\nu_{\text{mm}}^{\text{IC}}}{\nu_c^{\text{IC}}}\right)^{-\frac{1}{2}}}{\nu_m f_{\text{max}} \left(\frac{\nu_m}{\nu_c}\right)^{-\frac{1}{2}}} \\
&\sim 4x_0^2 \sigma_T n R \gamma_c \gamma_m,
\end{aligned} \tag{3.17}$$

which is also consistent with Sari & Esin (2001).

Strong Synchrotron Self-Absorption Cases

When $\nu_a > \nu_c$, synchrotron/SSC cooling and self-absorption heating would reach a balance around a specific electron energy under certain conditions (see details in the last section of this chapter). For such cases, the electron energy distribution and the photon spectrum are coupled, a numerical iterative procedure is needed to obtain the self-consistent solution. Ghisellini et al. (1988) solved the kinetic equation and found that the electron energy distribution would include two components: a thermal component shaped by synchrotron self-absorption heating, and a non-thermal power-law component. Based on their results (Ghisellini et al., 1988), the electron distribution is close but not strictly Maxwellian. Strictly, one needs to use equation (3.2) to calculate the SSC spectral component numerically. In the following, we make an approximation to derive analytical results. For the quasi-thermal component, we take $N(\gamma) \propto \gamma^2$ for $\gamma < \gamma_a$ to denote the thermal component, and take a sharp cutoff at γ_a . Above this energy, the electron energy distribution is taken as the standard (broken) power law distribution.

In particular, for $\nu_c < \nu_a < \nu_m$, the electron distribution becomes

$$N(\gamma) = \begin{cases} n \frac{3\gamma^2}{\gamma_a^3}, & \gamma \leq \gamma_a, \\ n\gamma_c\gamma^{-2}, & \gamma_a < \gamma \leq \gamma_m. \\ n\gamma_m^{p-1}\gamma_c\gamma^{-p-1}, & \gamma > \gamma_m. \end{cases} \quad (3.18)$$

For $\nu_m < \nu_c < \nu_a$, one has

$$N(\gamma) = \begin{cases} n \frac{3\gamma^2}{\gamma_a^3}, & \gamma \leq \gamma_a, \\ n(p-1)\gamma_m^{p-1}\gamma_c\gamma^{-p-1}, & \gamma > \gamma_a. \end{cases} \quad (3.19)$$

For $\nu_c < \nu_m < \nu_a$, one has

$$N(\gamma) = \begin{cases} n \frac{3\gamma^2}{\gamma_a^3}, & \gamma \leq \gamma_a, \\ n\gamma_m^{p-1}\gamma_c\gamma^{-p-1}, & \gamma > \gamma_a. \end{cases} \quad (3.20)$$

Following these new shapes of the electron distribution, the synchrotron photon spectra can be calculated, which also contain a thermal component and a (broken) power-law component. Still applying equation (3.2), one can analytically calculate the SSC spectral component for another three cases in this regime. We note that due to the simple approximation to the complicated electron pile-up process, the analytical results presented below are not as precise as those in the weak absorption cases.

Case IV: $\nu_c < \nu_a < \nu_m$

In this case, the synchrotron photon spectrum reads

$$f_\nu = \begin{cases} f_{\max} \left(\frac{\nu}{\nu_a}\right)^2, & \nu \leq \nu_a; \\ f_{\max} \mathfrak{R} \left(\frac{\nu}{\nu_a}\right)^{-\frac{1}{2}}, & \nu_a < \nu \leq \nu_m; \\ f_{\max} \mathfrak{R} \left(\frac{\nu_m}{\nu_a}\right)^{-\frac{1}{2}} \left(\frac{\nu}{\nu_m}\right)^{-\frac{p}{2}}, & \nu > \nu_m; \end{cases} \quad (3.21)$$

where \mathfrak{R} is the discontinuity ratio in the electron distribution at γ_a ,

$$\mathfrak{R} = \frac{\gamma_c}{3\gamma_a}. \quad (3.22)$$

One can then derive

$$I = \begin{cases} I_1 \simeq f_{\max} x_0 \left(\frac{1}{2}\mathfrak{R} + 1\right) \left(\frac{\nu}{4\gamma^2 \nu_a x_0}\right), & \nu < 4\gamma^2 \nu_a x_0 \\ I_2 \simeq \frac{1}{2} f_{\max} x_0 \mathfrak{R} \left(\frac{\nu}{4\gamma^2 \nu_a x_0}\right)^{-\frac{1}{2}}, & 4\gamma^2 \nu_a x_0 < \nu < 4\gamma^2 \nu_m x_0 \\ I_3 \simeq \frac{3}{2(p+2)} f_{\max} x_0 \mathfrak{R} \left(\frac{\nu_a}{\nu_m}\right)^{\frac{1}{2}} \left(\frac{\nu}{4\gamma^2 \nu_m x_0}\right)^{-\frac{p}{2}}, & \nu > 4\gamma^2 \nu_m x_0 \end{cases} \quad (3.23)$$

and

$$f_{\nu}^{\text{IC}} \simeq R\sigma_{\text{T}} n f_{\max} x_0 \quad (3.24)$$

$$\times \begin{cases} \left(\frac{1}{2}\mathfrak{R} + 1\right) (\mathfrak{R} + 4) \left(\frac{\nu}{\nu_{\text{aa}}^{\text{IC}}}\right), \nu < \nu_{\text{aa}}^{\text{IC}}; \\ \mathfrak{R} \left(\frac{\nu}{\nu_{\text{aa}}^{\text{IC}}}\right)^{-\frac{1}{2}} \left[\frac{1}{6}\mathfrak{R} + \frac{9}{10} + \frac{1}{4}\mathfrak{R} \ln\left(\frac{\nu}{\nu_{\text{aa}}^{\text{IC}}}\right)\right], \nu_{\text{aa}}^{\text{IC}} < \nu < \nu_{\text{am}}^{\text{IC}}; \\ \mathfrak{R}^2 \left(\frac{\nu}{\nu_{\text{aa}}^{\text{IC}}}\right)^{-\frac{1}{2}} \left[\frac{3}{p-1} - \frac{1}{2} + \frac{3}{4} \ln\left(\frac{\nu_{\text{mm}}^{\text{IC}}}{\nu}\right)\right], \nu_{\text{am}}^{\text{IC}} < \nu < \nu_{\text{mm}}^{\text{IC}}; \\ \frac{9\mathfrak{R}^2}{2(p+2)} \left(\frac{\nu_a}{\nu_m}\right) \left(\frac{\nu}{\nu_{\text{mm}}^{\text{IC}}}\right)^{-\frac{p}{2}} \left[\frac{4}{p+3} \left(\frac{\gamma_a}{\gamma_m}\right)^{p-1} \frac{\gamma_a}{\gamma_c} + \frac{3(p+1)}{(p-1)(p+2)} + \frac{1}{2} \ln \frac{\nu}{\nu_{\text{mm}}^{\text{IC}}}\right], \nu > \nu_{\text{mm}}^{\text{IC}}. \end{cases}$$

In this case, there are two peaks in the νF_{ν} spectrum for the synchrotron and SSC components, respectively. For the synchrotron component, the thermal peak is at $(25/9)\nu_a \simeq 2.8\nu_a$, and the non-thermal peak is at ν_m . For the SSC component, the thermal peak is at $\nu_{\text{aa}}^{\text{IC}}$, and the non-thermal peak is at $\nu_{\text{mm}}^{\text{IC}}$. The relative importance of the two peaks depends on the relative location of ν_a with respect to ν_c and ν_m . More specifically, the spectrum is non-thermal-dominated when $\nu_a < \sqrt{\nu_m \nu_c}$, and is thermal-dominated when $\nu_a > \sqrt{\nu_m \nu_c}$.

In Figure 11, we compare the above simplified analytical approximation (solid) with a simplest power law prescription (dashed) of the SSC component. The non-thermal-dominated and the thermal-dominated cases are presented in Figures 11a and 11b, respectively. Below $\nu_{\text{mm}}^{\text{IC}}$, similar to the weak self-absorption regime (cases

I-III), the logarithmic terms make the analytical spectrum harder than the simple broken power-law approximation above the non-thermal νF_ν peak frequency. At high frequencies, the simple broken power-law approximation is not adequate to represent the true SSC spectrum.

Case V and VI: $\nu_a > \max(\nu_m, \nu_c)$

For these two cases ($\nu_m < \nu_c < \nu_a$ and $\nu_c < \nu_m < \nu_a$), the treatments and results are rather similar to each other. we take $\nu_m < \nu_c < \nu_a$ as an example. In this case, the synchrotron spectrum reads

$$f_\nu = \begin{cases} f_{\max} \left(\frac{\nu}{\nu_a}\right)^2, & \nu \leq \nu_a; \\ f_{\max} \mathfrak{R} \left(\frac{\nu}{\nu_a}\right)^{-\frac{p}{2}}, & \nu > \nu_a; \end{cases} \quad (3.25)$$

where

$$\mathfrak{R} = (p-1) \frac{\gamma_c}{3\gamma_a} \left(\frac{\gamma_m}{\gamma_a}\right)^{p-1}. \quad (3.26)$$

Applying equation (3.2), the inner integral I can be then approximated as

$$I = \begin{cases} I_1 \simeq f_{\max} x_0 \left(\frac{3\mathfrak{R}}{2(p+2)} + 1\right) \left(\frac{\nu}{4\gamma^2 \nu_a x_0}\right), & \nu < 4\gamma^2 \nu_a x_0 \\ I_2 \simeq \frac{3}{2(p+2)} f_{\max} x_0 \mathfrak{R} \left(\frac{\nu}{4\gamma^2 \nu_a x_0}\right)^{-\frac{p}{2}}, & \nu > 4\gamma^2 \nu_a x_0. \end{cases} \quad (3.27)$$

Integrating over the outer integral, one gets

$$f_\nu^{\text{IC}} \simeq R\sigma_{\text{T}} n f_{\max} x_0 \quad (3.28)$$

$$\times \begin{cases} \left(\frac{3\mathfrak{R}}{2(p+2)} + 1\right) \left(\frac{3\mathfrak{R}}{p+2} + 4\right) \left(\frac{\nu}{\nu_{\text{aa}}^{\text{IC}}}\right), & \nu < \nu_{\text{aa}}^{\text{IC}}; \\ \frac{1}{p+2} \left[\frac{6\mathfrak{R}}{p+3} + \mathfrak{R} \left(\frac{9\mathfrak{R}}{2(p+2)} + 1\right) + \frac{9\mathfrak{R}^2}{4} \ln \left(\frac{\nu}{\nu_{\text{aa}}^{\text{IC}}}\right)\right] \left(\frac{\nu}{\nu_{\text{aa}}^{\text{IC}}}\right)^{-\frac{p}{2}}, & \nu > \nu_{\text{aa}}^{\text{IC}}; \end{cases}$$

The case of $\nu_c < \nu_m < \nu_a$ is almost identical to the above $\nu_m < \nu_c < \nu_a$. The only

difference is that the expression of \mathfrak{R} is modified to

$$\mathfrak{R} = \frac{\gamma_c}{3\gamma_a} \left(\frac{\gamma_m}{\gamma_a} \right)^{p-1}. \quad (3.29)$$

This is reasonable, since in the fast cooling case, the electron energy spectral index is $p = 2$, so that the factor $(p-1)$ can be reduced to 1. The analytical results and simple broken power-law approximation in this regime is identical to Figure 11c. We note again that full numerical calculations are needed to obtain more accurate results.

Finally, we investigate the X parameter in the strong synchrotron self-absorption regime.

For $\nu_c < \nu_a < \nu_m$ (case IV), if the spectrum is non-thermal-dominated, the synchrotron and SSC emission components peak at ν_m and $\nu_{\text{mm}}^{\text{IC}}$, respectively. One thus has

$$\begin{aligned} X = \frac{L_{\text{IC}}}{L_{\text{syn}}} &\sim \frac{\nu_{\text{mm}}^{\text{IC}} f_{\nu}^{\text{IC}}(\nu_{\text{mm}}^{\text{IC}})}{\nu_m f_{\nu}(\nu_m)} \\ &\sim \frac{\nu_{\text{mm}}^{\text{IC}} R \sigma_{\text{T}} n f_{\text{max}} x_0 \mathfrak{R}^2 \left(\frac{\nu_{\text{mm}}^{\text{IC}}}{\nu_{\text{aa}}^{\text{IC}}} \right)^{-\frac{1}{2}}}{\nu_m \mathfrak{R} f_{\text{max}} \left(\frac{\nu_m}{\nu_a} \right)^{-\frac{1}{2}}} \\ &\sim 4x_0^2 \sigma_{\text{T}} n R \gamma_c \gamma_m. \end{aligned} \quad (3.30)$$

If the spectrum is thermal-dominated, the synchrotron and SSC emission components peak at ν_a and $\nu_{\text{aa}}^{\text{IC}}$, respectively. One has

$$\begin{aligned} X = \frac{L_{\text{IC}}}{L_{\text{syn}}} &\sim \frac{\nu_{\text{aa}}^{\text{IC}} f_{\nu}^{\text{IC}}(\nu_{\text{aa}}^{\text{IC}})}{\nu_a f_{\nu}(\nu_a)} \\ &\sim \frac{\nu_{\text{aa}}^{\text{IC}} R \sigma_{\text{T}} n f_{\text{max}} x_0}{\nu_a f_{\text{max}}} \\ &\sim 4x_0^2 \sigma_{\text{T}} n R \gamma_a^2. \end{aligned} \quad (3.31)$$

In general, the X parameter for $\nu_c < \nu_a < \nu_m$ (case IV) is $4x_0^2 \sigma_{\text{T}} n R \cdot \max(\gamma_a^2, \gamma_c \gamma_m)$.

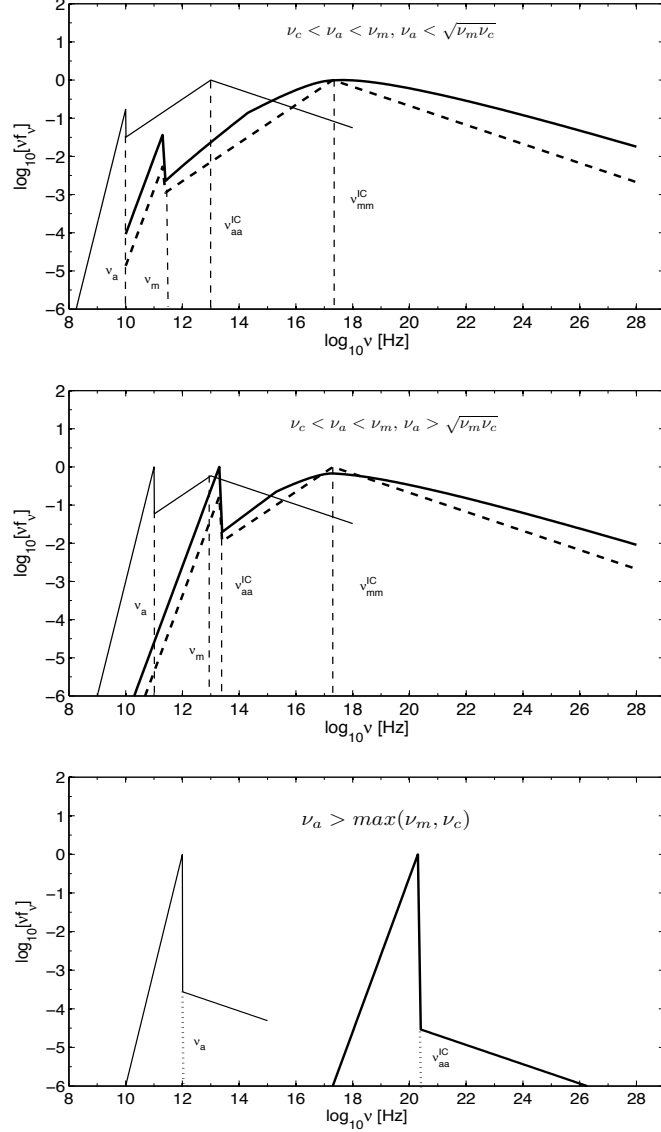


Figure 11 Same as Figure 10, but for strong synchrotron reabsorption cases . The top panel is for $\nu_c < \nu_a < \nu_m$ and $\nu_a < \sqrt{\nu_m \nu_c}$ case; the middle panel is for $\nu_c < \nu_a < \nu_m$ and $\nu_a > \sqrt{\nu_m \nu_c}$ case; and the bottom panel is for $\nu_a > \max(\nu_m, \nu_c)$ case. All the solid lines are analytical approximations and the dashed lines are broken power-law approximations.

For $\nu_m < \nu_c < \nu_a$ (case V) and $\nu_c < \nu_m < \nu_a$ (case VI), the synchrotron and SSC emission components peak at ν_a and ν_{aa}^{IC} , respectively. In this case, one has

$$\begin{aligned}
X = \frac{L_{IC}}{L_{syn}} &\sim \frac{\nu_{aa}^{IC} f_{\nu}^{IC}(\nu_{aa}^{IC})}{\nu_a f_{\nu}(\nu_a)} \\
&\sim \frac{\nu_{aa}^{IC} R \sigma_T n f_{max} x_0}{\nu_a f_{max}} \\
&\sim 4x_0^2 \sigma_T n R \gamma_a^2.
\end{aligned} \tag{3.32}$$

which is same as the thermal-dominated case for $\nu_c < \nu_a < \nu_m$ (case IV). So in general the expression of X is equation (3.32) only if the spectrum is thermal-dominated.

Conclusion and Discussion

We have extended the analysis of Sari and Esin (2001) and derived the analytical approximations of the SSC spectra of all possible orders of the three synchrotron characteristic frequencies ν_a , ν_m , and ν_c . Based on the relative order between ν_a and ν_c , we divide the six possible orders into two regimes.

In the weak self-absorption regime $\nu_a < \nu_c$, self-absorption does not affect the electron energy distribution. Two cases in this regime have been studied by Sari and Esin (2001). Our results are consistent with theirs (except the two typos in their paper). For the other regime $\nu_m < \nu_a < \nu_c$, we find that the SSC spectrum is linear to ν all the way to ν_{ma}^{IC} , and there is no break corresponding to ν_{mm}^{IC} .

In the strong self-absorption $\nu_a > \nu_c$ regime, synchrotron self-absorption heating balances synchrotron/SSC cooling, leading to pile-up of electrons at a certain energy, so that the electron energy distribution is significantly altered, with an additional thermal component besides the non-thermal power law component. Both the synchrotron and the SSC spectral components become two-hump shaped. To get an analytical approximation of the SSC spectrum, we simplified the quasi-thermal electron energy distribution as a power law with a sharp cutoff above the piling up energy,

and derived the analytical approximation results of the synchrotron and SSC spectral components. We suggest that for the thermal-dominated cases, i.e. $\nu_a > \sqrt{\nu_m \nu_c}$ in the $\nu_c < \nu_a < \nu_m$ regime or the $\nu_a > \max(\nu_m, \nu_c)$ regime, full numerical calculations are needed to get accurate results.

In general, the SSC component roughly tracks the shape of the seed synchrotron component, but is smoother and harder at high energies. For all the cases, we compare our analytical approximation results of SSC component with the simplest broken power-law prescription. We find that in general the presence of the logarithmic terms in the high energy range makes the SSC spectrum harder than the broken power-law approximation. One should consider these terms when studying high energy emission. The only exceptions are the $\nu_a > \max(\nu_m, \nu_c)$ regimes. However, in these regimes the analytical approximations may be no longer good, and one should appeal to full numerical calculations.

Our newly derived spectral regimes may find applications in astrophysical objects with high “compactness” (i.e. high luminosity, and small size). In these cases, ν_a can be higher than ν_c or ν_m , or even both (see last section in this chapter for the critical condition). For example, in the early afterglow phase of GRBs, slow cooling may be relevant, and the radio afterglow is self-absorbed with ν_a above ν_m (e.g. Chandra and Frail, 2012). In the prompt emission phase when fast cooling is more relevant, the self-absorption frequency can be above ν_c (e.g. Shen and Zhang, 2009).

An example of the extreme case $\nu_a > \max(\nu_m, \nu_c)$ can be identified for a GRB problem. For a dense circumburst medium with a wind-like ($n \propto r^{-2}$) structure, in the reverse shock region, the condition $\nu_a > \max(\nu_m, \nu_c)$ can be satisfied (e.g. Kobayashi et al., 2004). For a GRB with isotropic energy $E = 10^{52} E_{52}$, initial Lorentz factor $\Gamma_0 = 100 \Gamma_{0,2}$, initial shell width $\Delta = 10^{12} \Delta_{12}$ running into stellar wind with density $\rho = (5 \times 10^{11} \text{g cm}^{-3}) A_* r^{-2}$, one can derive following parameters at the shock crossing radius r_\times : The blastwave Lorentz factor $\Gamma_\times = 25.8 A_*^{-1/4} \Delta_{12}^{-1/4} E_{52}^{1/4}$, $\nu_m = 3.1 \times$

$10^{14} \text{ Hz } [g(p)/g(2.3)] A_* \Delta_{12}^{-1/2} E_{52}^{-1/2} \epsilon_{e,-1}^2 \epsilon_{B,-2}^{1/2} \Gamma_{0,2}^2$, $\nu_c = 1.2 \times 10^{12} \text{ Hz } A_*^{-2} \Delta_{12}^{1/2} E_{52}^{1/2} \epsilon_{B,-2}^{-3/2}$,
 $\nu_a = 4.6 \times 10^{14} \text{ Hz } A_*^{3/5} \Delta_{12}^{-11/10} E_{52}^{1/10} \epsilon_{B,-2}^{3/10} \Gamma_{0,2}^{-2/5}$. Here $\epsilon_e = 0.1 \epsilon_{e,-1}$ and $\epsilon_B = 0.01 \epsilon_{B,-2}$
are microphysics shock parameters for the internal energy fraction that goes to electrons and magnetic fields, p is the electron spectral index, and $g(p) = (p-2)/(p-1)$.
We can see that for typical parameters, $\nu_a > \max(\nu_c, \nu_m)$ is satisfied. In this regime, one should check whether the ‘‘Razin’’ plasma effect is important. At shock crossing time, the comoving number density of the shocked ejecta region is $n' = 2.3 \times 10^8 \text{ cm}^{-3} A_*^{5/4} \Delta_{12}^{-7/4} E_{52}^{-1/4} \Gamma_{0,1}^{-1}$. Noticing that the comoving plasma angular frequency is $\omega'_p = 5.63 \times 10^4 \text{ s}^{-1} n'^{1/2}$, one can write the plasma frequency in the observer frame as $\nu_p = 1.4 \times 10^{11} \text{ Hz } A_*^{3/8} \Delta_{12}^{-9/8} E_{52}^{1/8} \Gamma_{0,2}^{-1/2}$. Multiplying by $\gamma_a = 102 A_*^{1/20} \Delta_{12}^{-1/20} E_{52}^{1/20} \epsilon_{B,-2}^{-1/10} \Gamma_{0,2}^{-1/5}$, one gets $\gamma_a \nu_p = 1.4 \times 10^{13} \text{ Hz } A_*^{17/40} \Delta_{12}^{-47/40} E_{52}^{7/40} \epsilon_{B,-2}^{-1/10} \Gamma_{0,2}^{-7/10}$, which is much smaller than ν_a . This suggests that the Razin effect is not important (Rybicki and Lightman, 1979), and the dominant mechanism to suppress synchrotron emission at low energies is synchrotron self-absorption. Notice that for this particular problem, the second order Comptonization may not be suppressed by the Klein-Nishina effect, and one has to introduce it for a fully self-consistent treatment.

Condition of electron pile-up and strong absorption

By applying the Einstein coefficients and their relations to a system with three energy levels, Ghisellini et al. (1991) have derived one useful analytical expression of the cross section for synchrotron self-absorption:

$$\sigma_S(\gamma, \nu) = \begin{cases} \frac{2^{2/3} \sqrt{3} \pi \Gamma^2(4/3)}{5} \frac{\sigma_T}{\alpha_f} \frac{B_{\text{cr}}}{B} \left(\frac{\gamma \nu}{3\nu_L} \right)^{-5/3}, & \frac{\nu_L}{\gamma} < \nu \ll \frac{3}{2} \gamma^2 \nu_L, \\ \frac{\sqrt{3}}{2} \pi^2 \frac{\sigma_T}{\alpha_f} \frac{B_{\text{cr}}}{B} \frac{1}{\gamma^3} \left(\frac{\nu_L}{\nu} \right) \exp \left(\frac{-2\nu}{3\gamma^2 \nu_L} \right), & \nu \gg \frac{3}{2} \gamma^2 \nu_L. \end{cases} \quad (3.33)$$

where γ is the relevant electron Lorentz factor, ν is photon frequency being absorbed, α_f is the fine structure constant, $B_{\text{cr}} = \alpha_f (m_e c^2 / r_e^3)^{1/2} \approx 4.4 \times 10^{13} \text{ G}$ is the critical

magnetic field strength, r_e is the classical electron radius, and $\nu_L = eB/2\pi m_e c$ is the electron cyclotron frequency. All the parameters introduced in this section are in the comoving frame.

For a simple derivation of the electron pile-up condition, we take an approximate form

$$\sigma_S(\gamma, \nu) = \begin{cases} \frac{2^{2/3} \sqrt{3} \pi \Gamma^2(4/3)}{5} \frac{\sigma_T}{\alpha_f} \frac{B_{\text{cr}}}{B} \left(\frac{\gamma \nu}{3\nu_L} \right)^{-5/3}, & \frac{\nu_L}{\gamma} < \nu \leq \frac{3}{2} \gamma^2 \nu_L, \\ 0, & \nu > \frac{3}{2} \gamma^2 \nu_L. \end{cases} \quad (3.34)$$

For electrons with Lorentz factor γ , the heating rate due to synchrotron self-absorption can be estimated as

$$\dot{\gamma}^+(\gamma) = \int_0^\infty c \cdot n_\nu \cdot h\nu \cdot \sigma_S(\gamma, \nu) \cdot d\nu \quad (3.35)$$

where n_ν is the specific photon number density at frequency ν contributed by all the electrons.

The cooling rate for electrons with Lorentz factor of γ is

$$\begin{aligned} \dot{\gamma}^-(\gamma) &= (1 + Y) \cdot P_{\text{syn}} \\ &= (1 + Y) \times \frac{4}{3} \sigma_T c \gamma^2 \frac{B^2}{8\pi}, \end{aligned} \quad (3.36)$$

where $Y \equiv \frac{P_{\text{ssc}}}{P_{\text{syn}}}$ is the Compton parameter.

By balancing the heating and cooling rate, one can easily obtain the critical electron Lorentz factor γ_{cr} , which satisfies

$$\dot{\gamma}^+(\gamma_{\text{cr}}) = \dot{\gamma}^-(\gamma_{\text{cr}}) \quad (3.37)$$

Initially, the photon spectrum has not been revised through self-absorption, i.e., $n_\nu \propto$

$\nu^{1/3}$. One therefore has

$$\gamma_{\text{cr}} = 2.1 \times 10^4 B^{-3/5} \mathcal{F}_{\nu, \text{max}}^{3/10} \gamma_c^{-1/5} (1 + Y)^{-3/10} \quad (3.38)$$

The electron pile-up (strong absorption) condition can be expressed as

$$\gamma_{\text{cr}} > \gamma_c = \frac{6\pi m_e c}{\sigma_T B^2 t (1 + Y)}. \quad (3.39)$$

With equations 3.34 - 3.39, the pile-up condition can be expressed as

$$\left(\frac{B}{100\text{G}}\right)^2 \times \left(\frac{t}{100\text{s}}\right)^{4/3} \times \mathcal{F}_{\nu, \text{max}}^{1/3} \times \left(\frac{1 + Y}{2}\right) > 1 \quad (3.40)$$

where

$$\mathcal{F}_{\nu, \text{max}} = \frac{f_{\text{max}}}{\Gamma(1 + z)} \left(\frac{d_L}{R}\right)^2 = 1 \text{ erg cm}^{-2} \text{ s}^{-1} \text{ Hz}^{-1} \frac{f_{\text{max, mJy}}}{\Gamma_2(1 + z)} \left(\frac{d_{L, 28}}{R_{14}}\right)^2 \quad (3.41)$$

is the synchrotron peak flux in the emission region. Here d_L is the luminosity distance of the source, and R is the distance of the emission region from the central engine.

One can immediately see that this condition is very difficult to satisfy. It requires a strong magnetic field, long dynamical time scale and high synchrotron flux. In the GRB afterglow problem, for forward shock emission, B decreases with t rapidly, and there is essentially no parameter space to satisfy the condition. This condition may be realized in extreme conditions, e.g. the reverse shock emission during shock crossing phase for a wind medium, as discussed in the main text.

One interesting note is that SSC cooling only enhances the pile-up condition. Once the pile-up condition is satisfied for synchrotron cooling only, adding SSC cooling only makes the condition more easily satisfied (as shown in equation 3.40).

Once the electron pile-up process is triggered, both electron distribution and pho-

ton spectrum would be modified, so that the value of γ_{cr} is modified correspondingly. According to the numerical calculation results (Ghisellini et al., 1988, 1991, 1998a), the electron distribution is dominated by a quasi-thermal component until a “transition” Lorentz factor γ_t , above which the electrons go back to the optically-thin normal power law. In this case, γ_{cr} should be around the thermal peak, and γ_a should be around the “transition” Lorentz factor γ_t , which is slightly larger than γ_{cr} . Consequently, one would roughly have $\gamma_a \sim \gamma_{\text{cr}} \sim \gamma_t$, so that the assumption of a sharp cutoff in the electron distribution around this energy is justified. In the main text, we did not differentiate the three Lorentz factors, and only adopt γ_a in the expressions.

CHAPTER 4

A COMPLETE REFERENCE OF THE ANALYTICAL SYNCHROTRON EXTERNAL SHOCK MODELS OF GAMMA-RAY BURSTS

This chapter is part of the following published paper :

Gao H., Lei W.-H., Wu, X.-F., Zou, Y.-C., Zhang B., 2013, New Astronomy

Review 57, 141

Although the nature of the progenitor and central engine as well as the detailed physics of γ -ray emission are still rather uncertain (for reviews, see e.g. Zhang and Mészáros, 2004a; Piran, 2004; Mészáros, 2006; Zhang, 2007b; Kumar and Zhang, 2013), a generic synchrotron external shock model has been well established to interpret the prompt emission and the broad-band afterglow data (Rees and Mészáros, 1992, 1994; Mészáros and Rees, 1993, 1997a; Sari et al., 1998a; Chevalier and Li, 2000). This model delineates the interaction between the relativistic GRB jet and a circumburst medium. During the initial interaction, a pair of shocks (forward and reverse) propagate into the ambient medium and the ejecta, respectively. After the reverse shock crosses the shell, the blastwave enters a self-similar phase described by the Blandford-McKee self-similar solution (Blandford and McKee, 1976). In this phase, the dynamics of the blastwave is solely determined by a few parameters (e.g. the total energy of the system, the ambient density and its profile).

Electrons are accelerated in both forward and reverse shocks, which radiate synchrotron emission in the magnetic fields behind the shocks that are believed to be generated in situ due to plasma instabilities (e.g. Medvedev and Loeb, 1999). Introducing several notations to parameterize micro-scopic processes, i.e. the fractions of shock energy that go to electrons and magnetic fields (ϵ_e and ϵ_B), and the electron spectral index p , one can then calculate the instantaneous synchrotron spectrum at a given epoch, as well as the flux evolution with time (the lightcurve) for a given observed frequency.

Since the simplest external shock theory does not invoke details of a burst, and invokes only a limit number of model parameters, it is an elegant theory with falsifiable predictions. It turned out that the predicted power-law decay of lightcurves and broken power law instantaneous spectra are well consistent with many late time afterglow data in the pre-Swift era (e.g. Wijers et al., 1997; Waxman, 1997a; Wijers and Galama, 1999; Huang et al., 1999, 2000; Panaitescu and Kumar, 2001, 2002; Yost et al., 2003), suggesting that most of the observed multi-wavelength afterglows indeed originate from jet-medium interaction, and that synchrotron radiation is indeed the right radiation mechanism to power the observed emission. Later observations showed more complicated afterglow behaviors (e.g. Akerlof et al., 1999; Harrison et al., 1999; Berger et al., 2003; Fox et al., 2003; Li et al., 2003), which demand more complicated models (Mészáros et al., 1998) that invoke joint forward shock and reverse shock emission (Mészáros and Rees, 1997a; Mészáros and Rees, 1999; Sari and Piran, 1999a,b; Kobayashi and Zhang, 2003b; Zhang et al., 2003), non-uniform density medium (Dai and Lu, 1998b; Chevalier and Li, 1999, 2000), continuous energy injection into the blastwave (Dai and Lu, 1998a; Rees and Mészáros, 1998; Zhang and Mészáros, 2001a), collimation of the jet (Rhoads, 1999; Sari et al., 1999c; Zhang and Mészáros, 2002a; Rossi et al., 2002), hard electron injection spectrum (Dai and Cheng, 2001a), etc. Nonetheless, these more complicated models, by introducing one or more additional assumptions/parameters, still have clear testable predictions regarding the afterglow decaying index α , the spectral index β , and the relation between them (the so-called “closure relations”) (e.g. Zhang and Mészáros, 2004a; Zhang et al., 2006, for a collection of these models). The Swift mission (Gehrels et al., 2004) made it possible to systematically detect the early phase of the GRB X-ray afterglow, which shows some un-predicted features (Tagliaferri et al., 2005; Burrows et al., 2005a; Nousek et al., 2006; O’Brien et al., 2006; Evans et al., 2009) that demand multiple physical processes that shape the observed lightcurves (Zhang et al., 2006). Systematic data

analyses (Zhang et al., 2007a; Liang et al., 2007b, 2008, 2009; Butler and Kocevski, 2007; Kocevski et al., 2007; Chincarini et al., 2007, 2010; Margutti et al., 2010) suggest that the X-ray afterglow is a superposition of the conventional external shock component and a radiation component that is related to the late central engine activity (e.g. Zhang, 2007b, 2011b; Zou et al., 2013). Nonetheless, the data indicate that the low-energy (optical and radio) afterglows (Kann et al., 2010, 2011; Chandra and Frail, 2012) and the late-time X-ray afterglow is more likely of the external shock origin. Recent Fermi observations suggest that the GeV afterglow after the prompt emission phase is also dominated by the emission from the external shock (Kumar and Barniol Duran, 2010; Ghisellini et al., 2010; He et al., 2011; Liu and Wang, 2011; Maxham et al., 2011). Observations with EVLA and ALMA start to reveal the early phase of GRB afterglow in the radio and sub-mm regime, during which reverse shock and self-absorption effects are important. These are the regimes not fully covered by the already published materials. With new data flooding in, it is essential to systematically survey a complete list of external shock models in all possible temporal and spectral regimes.

This chapter aims at providing a complete reference to the analytical synchrotron external shock afterglow models. It includes all the published models and spectral regimes, but also includes new derivations in the previously not well-studied models or spectral regimes. All the models are surveyed systematically, with typical model parameters calculated, temporal and spectral indices and their closure relations summarized in tables. It is designated as a complete reference tool for GRB afterglow observers to quickly identify the relevant models to interpret their broad-band data. In the second 2, we provide a general description of the synchrotron external shock models, which lay the foundation to derive any model discussed later. The third section summarizes all the models in four different phases: the reverse and forward shock models during the reverse shock crossing phase, the forward shock models during the

isotropic self-similar deceleration phase, the forward shock models in the post-jet break phase, and the forward shock models in the non-relativistic phase. For each model, the expressions of key parameters, including the three characteristic frequencies ν_a (self-absorption frequency), ν_m (the characteristic synchrotron frequency of the electrons at the minimum injection energy), and ν_c (the cooling frequency), and the peak synchrotron flux density $F_{\nu, \max}$, are presented. The spectral index β and the temporal index α (with the convention $F_\nu \propto \nu^{-\beta} t^{-\alpha}$, as well as their closure relations are presented in Tables 5-25. Next, we describe how to make use of the models to calculate lightcurves, and derive all possible lightcurves (Fig.12-55) by allowing a wide range of parameters. We also draw typical lightcurves in the radio, optical and X-ray bands by adopting typical values of model parameters. Finally, we discuss the limitations of these simple analytical models.

General Description of the Synchrotron External Shock Models of GRBs

The synchrotron external shock models (Rees and Mészáros, 1992; Mészáros and Rees, 1993, 1997a; Sari et al., 1998a) describe the interaction between the GRB outflow and the circum-burst hydrogen medium (CBM). The physical parameters that enter the problem to determine the dynamics of blastwave deceleration include the “isotropic” energy E (the total energy assuming that the outflow is isotropic), the initial Lorentz factor Γ_0 , and the CBM density and its profile $n(R) \propto R^{-k}$, $0 \leq k < 4$ (Blandford and McKee, 1976) (and see Sari (2006) for a discussion for the cases with $k \geq 4$), where R is the radius from the central engine. As a result, these models are very generic, not depending on the details of the central engine activity and prompt γ -ray emission. There is another parameter, i.e. the magnetization of the outflow σ , that would slightly affect the dynamics of the system during the early phase of evolution (e.g. Zhang and Kobayashi, 2005; Mimica et al., 2009). In this chapter, we limit

ourselves to the regime of zero (or very low) magnetization. These matter-dominated ejecta are also called “fireballs”.

Assuming that a jet with opening angle θ_j is launched from the central engine, which lasts a duration T with constant Lorentz factor Γ_0 , the evolution of the a fireball jet includes four phases¹. The first phase is when a pair of shocks (forward and reverse) propagating into the CBM and the shell (with initial width $\Delta_0 = cT$), respectively (Sari and Piran, 1995). After the reverse shock crosses the shell, the blastwave quickly enters a self-similar deceleration phase described by the Blandford-McKee solution (Blandford and McKee, 1976). This is the second phase. Later, as the blastwave is decelerated enough, the $1/\Gamma$ cone becomes larger than the geometric cone defined by θ_j , the afterglow enters the post-jet-break phase. Finally, the blastwave enters the Newtonian phase when the velocity is much smaller than speed of light. The dynamics is then described by the well-known Sedov solution widely used to study supernova remnants.

During all the phases, particles are believed to be accelerated from the forward shock front via the 1st-order Fermi acceleration mechanism. For the reverse shock, particle acceleration occurs only during the shock crossing phase. No new particles are accelerated in the reverse-shocked region after the reverse shock crosses the ejecta shell. Assume a power-law distribution of the electrons $N(\gamma_e)d\gamma_e \propto \gamma_e^{-p}d\gamma_e$ (for $\gamma_m \leq \gamma_e \leq \gamma_M$) and consider radiative cooling of electrons and continuous injection of new electrons from the shock front, one can obtain a broken power-law electron spectrum, which leads to a multi-segment broken power-law photon spectrum at any epoch (Sari et al., 1998a; Mészáros et al., 1998).

Assuming that a constant fraction ϵ_e of the shock energy is distributed to electrons,

¹These simplified assumptions are certainly not the case in reality, but may be a good approximation after the prompt emission phase when the ejecta irregularities are smoothed out after energy dissipation through internal shocks (Rees and Mészáros, 1994; Kobayashi et al., 1997; Kumar and Piran, 2000b; Maxham and Zhang, 2009).

one can derive the minimum injected electron Lorentz factor

$$\gamma_m = g(p)\epsilon_e(\Gamma - 1)\frac{m_p}{m_e}, \quad (4.1)$$

where Γ is the relative Lorentz factor between the unshocked region and the shocked region, which is the Lorentz factor of the blastwave for the forward shock, m_p is proton mass, m_e is electron mass, and the function $g(p)$ takes the form

$$g(p) \simeq \begin{cases} \frac{p-2}{p-1}, & p > 2; \\ \ln^{-1}(\gamma_M/\gamma_m), & p = 2; \end{cases} \quad (4.2)$$

Here γ_M is the maximum electron Lorentz factor, which may be estimated by balancing the acceleration time scale and the dynamical time scale, i.e.

$$\gamma_M \sim \frac{\Gamma t q_e B}{\zeta m_p c}, \quad (4.3)$$

where ζ is a parameter of order unity that describes the details of acceleration, t is the observational time, q_e is the electron charge, and B is the comoving magnetic field strength. We also assume that the magnetic energy density behind the shock is a constant fraction ϵ_B of the shock energy density. This gives

$$B = (8\pi e\epsilon_B)^{1/2}, \quad (4.4)$$

where e is the energy density in the shocked region. If the electron energy has a harder spectral index $1 < p < 2$, the minimum electron Lorentz factor would be derived as (Dai and Cheng, 2001a; Bhattacharya, 2001)

$$\gamma_m = \left(\frac{2-p}{p-1} \frac{m_p}{m_e} \epsilon_e (\Gamma - 1) \gamma_M^{p-2} \right)^{1/(p-1)} \quad (4.5)$$

For synchrotron radiation, the observed radiation power and the characteristic frequency of an electron with Lorentz factor γ_e are given by (Rybicki and Lightman, 1979)

$$P(\gamma_e) \simeq \frac{4}{3} \sigma_T c \Gamma^2 \gamma_e^2 \frac{B^2}{8\pi}, \quad (4.6)$$

$$\nu(\gamma_e) \simeq \Gamma \gamma_e^2 \frac{q_e B}{2\pi m_e c}, \quad (4.7)$$

where the factors of Γ^2 and Γ are introduced to transform the values from the rest frame of the shocked fluid to the frame of the observer.

The spectral power of individual electron, P_ν (power per unit frequency, in unit of $\text{erg Hz}^{-1} \text{s}^{-1}$), varies as $\nu^{1/3}$ for $\nu < \nu(\gamma_e)$, and cuts off exponentially for $\nu > \nu(\gamma_e)$ (Rybicki and Lightman, 1979). The peak power occurs at $\nu(\gamma_e)$, where it has the approximate value

$$P_{\nu, \max} \approx \frac{P(\gamma_e)}{\nu(\gamma_e)} = \frac{m_e c^2 \sigma_T}{3q_e} \Gamma B. \quad (4.8)$$

Note that $P_{\nu, \max}$ does not depend on γ_e .

The life time of a relativistic electron with Lorentz factor γ_e in the observer frame can be estimated as

$$\tau(\gamma_e) = \frac{\Gamma \gamma_e m_e c^2}{\frac{4}{3} \sigma_T c \Gamma^2 \gamma_e^2 \frac{B^2}{8\pi}} = \frac{6\pi m_e c}{\Gamma \gamma_e \sigma_T B^2}. \quad (4.9)$$

One can define a critical electron Lorentz factor γ_c by setting $\tau(\gamma_e) = t$, i.e.,

$$\gamma_c = \frac{6\pi m_e c}{\Gamma \sigma_T B^2 t}, \quad (4.10)$$

where t refers to the time in the observer frame. Above γ_c , cooling by synchrotron

radiation becomes significant, so that the electron distribution shape is modified in the $\gamma_e > \gamma_c$ regime.

The electron Lorentz factors γ_m and γ_c defines two characteristic emission frequencies ν_m and ν_c in the synchrotron spectrum. A third characteristic frequency ν_a , is defined by synchrotron self-absorption, below which the synchrotron photons are self-absorbed. There are two methods to calculate this frequency. The first one is to define ν_a by the condition that the photon optical depth for self-absorption is unity (Rybicki and Lightman, 1979). A more convenient method (e.g. Sari and Piran, 1999b; Kobayashi and Zhang, 2003b) is to define ν_a by equating the synchrotron flux and the flux of a blackbody, i.e.

$$I_\nu^{syn}(\nu_a) = I_\nu^{bb}(\nu_a) \simeq 2kT \cdot \frac{\nu_a^2}{c^2}, \quad (4.11)$$

where the blackbody temperature is

$$kT = \max[\gamma_a, \min(\gamma_c, \gamma_m)]m_e c^2, \quad (4.12)$$

and γ_a is the corresponding electron Lorentz factor of ν_a for synchrotron radiation, i.e. $\gamma_a = (2\pi m_e c \nu_a / \Gamma q_e B)^{1/2}$ (derived from Eq. 4.7). One can prove (Shen and Zhang, 2009) that the two methods are equivalent to each other, even though the coefficient may slightly differ within a factor of two.

In the afterglow phase, ν_a is usually the smallest among the three frequencies. The broad-band synchrotron spectrum therefore falls into two broad categories depending on the order of γ_m and γ_c , namely the fast cooling regime ($\gamma_m > \gamma_c$) or the slow cooling regime $\gamma_m < \gamma_c$ (Sari et al., 1998a).

In the slow cooling regime, the electron energy distribution is

$$N(\gamma_e) = \begin{cases} C_1(p-1)\gamma_m^{p-1}\gamma_e^{-p}, & \gamma_m \leq \gamma_e \leq \gamma_c, \\ C_1(p-1)\gamma_m^{p-1}\gamma_c\gamma_e^{-p-1}, & \gamma_e > \gamma_c. \end{cases} \quad (4.13)$$

In the fast cooling regime, usually one has the approximation

$$N(\gamma) = \begin{cases} C_2\gamma_c\gamma_e^{-2}, & \gamma_c \leq \gamma_e \leq \gamma_m, \\ C_2\gamma_m^{p-1}\gamma_c\gamma_e^{-p-1}, & \gamma_e > \gamma_m. \end{cases} \quad (4.14)$$

where C_1 and C_2 are normalization factors².

For such an electron energy distribution, the observed synchrotron radiation flux density F_ν can be expressed as

I. $\nu_a < \nu_m < \nu_c$:

$$F_\nu = F_{\nu, \max} \begin{cases} \left(\frac{\nu_a}{\nu_m}\right)^{1/3} \left(\frac{\nu}{\nu_a}\right)^2, & \nu < \nu_a; \\ \left(\frac{\nu}{\nu_m}\right)^{1/3}, & \nu_a < \nu < \nu_m; \\ \left(\frac{\nu}{\nu_m}\right)^{-(p-1)/2}, & \nu_m < \nu < \nu_c; \\ \left(\frac{\nu_c}{\nu_m}\right)^{-(p-1)/2} \left(\frac{\nu}{\nu_c}\right)^{-p/2}, & \nu > \nu_c; \end{cases} \quad (4.15)$$

II. $\nu_a < \nu_c < \nu_m$:

$$F_\nu = F_{\nu, \max} \begin{cases} \left(\frac{\nu_a}{\nu_c}\right)^{1/3} \left(\frac{\nu}{\nu_a}\right)^2, & \nu < \nu_a; \\ \left(\frac{\nu}{\nu_c}\right)^{1/3}, & \nu_a < \nu < \nu_c; \\ \left(\frac{\nu}{\nu_c}\right)^{-1/2}, & \nu_c < \nu < \nu_m; \\ \left(\frac{\nu_m}{\nu_c}\right)^{-1/2} \left(\frac{\nu}{\nu_m}\right)^{-p/2}, & \nu > \nu_m. \end{cases} \quad (4.16)$$

²It is realized that the fast-cooling spectrum below injection can be harder than -2 in a decaying magnetic field, which is the case for GRB afterglow emission (Uhm and Zhang, 2013b,a). We will discuss this more in the fifth Section.

In general, there are six different orders among ν_a , ν_m and ν_c . Under extreme conditions they might be all possible. When $\nu_a > \nu_c$, the electron energy distribution may be significantly modified (Gao et al., 2013a), so that analytical models are no longer good approximations. Those cases are rare but not impossible, and we will leave out from this chapter. A detailed analysis can be found in Kobayashi et al. (2004) and Gao et al. (2013a).

For the $\nu_a < \nu_c$ regime, there is one more case, i.e.

III. $\nu_m < \nu_a < \nu_c$:

$$F_\nu = F_{\nu, \max} \begin{cases} \left(\frac{\nu_m}{\nu_a}\right)^{(p+4)/2} \left(\frac{\nu}{\nu_m}\right)^2, & \nu < \nu_m; \\ \left(\frac{\nu_a}{\nu_m}\right)^{-(p-1)/2} \left(\frac{\nu}{\nu_a}\right)^{5/2}, & \nu_m < \nu < \nu_a; \\ \left(\frac{\nu}{\nu_m}\right)^{-(p-1)/2}, & \nu_a < \nu < \nu_c; \\ \left(\frac{\nu_c}{\nu_m}\right)^{-(p-1)/2} \left(\frac{\nu}{\nu_c}\right)^{-p/2}, & \nu > \nu_c. \end{cases} \quad (4.17)$$

In all the above expressions, $F_{\nu, \max}$ is the observed peak flux at luminosity distance D from the source, which can be estimated as (Sari et al., 1998a):

$$F_{\nu, \max} \equiv N_e P_{\nu, \max} / 4\pi D^2, \quad (4.18)$$

where N_e is the total number of electrons in the emission region. For the forward shock emission, it is usually calculated as $N_e \sim \int_{R_0}^R 4\pi n(r) r^2 dr$, where R_0 is the central engine radius and R is the radius from the center of central engine.

The instantaneous spectra described above do not depend on the hydrodynamical evolution of the shocks. However, in order to calculate the light curve at a given frequency, we need to know the temporal evolution of various quantities, such as the break frequencies ν_a , ν_m and ν_c and the peak flux density $F_{\nu, \max}$, which depend on the dynamics of the system. For the forward shock, the emission essentially depends

on the temporal evolution of three quantities Γ , R and B (or the energy density e if ϵ_B is assumed to be constant). In the next section, we will derive how Γ , R and e evolve as a function of t for various systems and dynamical phases, and quantify the evolutions of the break frequencies ν_m , ν_c , ν_a , as well as the peak flux density $F_{\nu, \max}$. We will then present the spectral and temporal indices (β and α) for all the spectral regimes of all the models, as well as the closure relations between α and β .

Analytical Synchrotron External Shock Models

There are many variations of the external shock synchrotron models. First, during the reverse shock crossing phase, the dynamics of the blastwave is complicated, and there are rich features in the reverse shock and forward shock lightcurves. Second, even after reverse shock crossing and when the blastwave is in the self-similar deceleration phase, variations in the energy content of the blastwave (e.g. radiative loss or energy injection) or in the profile of the CBM (e.g. constant density ISM, a stratified wind, or a more general profile) would give very different lightcurves. Next, the collimation effect becomes important when the blastwave is decelerated enough so that the relativistic beaming $1/\Gamma$ cone is large enough to enclose a solid angle in which the anisotropic effect becomes significant. Finally, the blastwave eventually enters the Newtonian phase, when a different self-similar solution is reached. For each dynamical model, there could be many possible lightcurves in view of a range of initial spectral regime of the observing frequency, and the complicated evolutions of three characteristic frequencies and their relative orders.

In the following, we will discuss all these models based on the four dynamical phases outlined above: Phase 1: reverse shock crossing phase; Phase 2: relativistic, pre-jet-break self-similar deceleration phase; Phase 3: post-jet-break phase; Phase 4: Newtonian phase.

Phase 1: reverse shock crossing phase

We consider a uniform and cold relativistic shell with isotropic energy E , lab-frame width $\Delta_0 = cT$, coasting with an initial Lorentz factor Γ_0 . This shell sweeps into a circumburst hydrogen medium (CBM) with a proton number density profile $n = AR^{-k}$ ($0 \leq k < 4$). A pair of shocks are developed: a forward shock propagating into the CBM and a reverse shock propagating into the shell. The two shocks and the contact discontinuity separate the system into four regions: (1) the unshocked CBM (called Region 1 hereafter), (2) the shocked CBM (Region 2), (3) the shocked shell (Region 3), and (4) the unshocked shell (Region 4). Using the relativistic shock jump conditions (Blandford and McKee, 1976) and assuming equal pressure and velocity in the blastwave region (Regions 2 and 3)³, i.e., $e_2 = e_3$ and $\gamma_2 = \gamma_3$, the values of the bulk Lorentz factor Γ , the radius R , and the energy density e in the shocked regions can be estimated as functions of n_1 , n_4 , and $\Gamma_0 = \gamma_4$, where n_i , e_i and γ_i are the comoving number densities, energy density and Lorentz factors for Region i .

Analytical results can be obtained in both relativistic and Newtonian reverse shock limits. These two cases are defined by comparing a parameter $f \equiv n_4/n_1$ (ratio of the number densities between the unshocked shell and the unshocked CBM) and γ_4^2 (Sari and Piran, 1995). If $f \gg \gamma_4^2$, the reverse shock is Newtonian (NRS, thin shell case), and if $f \ll \gamma_4^2$, the reverse shock is relativistic (RRS, thick shell case). The strength of the reverse shock depends on the relative Lorentz factor between Region 3 and Region 4, i.e.

$$\bar{\gamma}_{34} = \gamma_3\gamma_4(1 - \sqrt{1 - 1/\gamma_3^2}\sqrt{1 - 1/\gamma_4^2}). \quad (4.19)$$

For $\gamma_2, \gamma_4 \gg 1$ and assuming $\gamma_2 = \gamma_3$, $\bar{\gamma}_{34}$ can be expressed as $\bar{\gamma}_{34} \simeq \frac{1}{\sqrt{2}}\gamma_4^{1/2}f^{-1/4}$ for

³Strictly speaking, such a situation cannot be achieved since it violates energy conservation (Uhm, 2011; Uhm et al., 2012). Nonetheless, for a short-lived reverse shock (finite width Δ_0 with constant Γ_0), such an approximation is good enough to delineate the dynamical evolution of the system.

a RRS, while $\bar{\gamma}_{34} - 1 \simeq \frac{4}{7}\gamma_4^2 f^{-1}$ for a NRS.

The Phase 1 ends at the reverse shock crossing time

$$t_{\times} = \max(t_{\text{dec}}, T), \quad (4.20)$$

where T is the duration of the burst, and

$$t_{\text{dec}} = \left[\frac{(3-k)E}{2^{4-k}\pi A m_p \Gamma_0^{8-2k} c^{5-k}} \right]^{\frac{1}{3-k}} \quad (4.21)$$

is the deceleration time of the ejecta for an impulsive injection of fireball with energy E and initial Lorentz factor Γ_0 , which corresponds to the time when the mass collected from the CBM is about $1/\Gamma$ of the rest mass entrained in the ejecta. For thin shells, one has $t_{\times} = t_{\text{dec}}$, while for thick shells, one has $t_{\times} = T$ (Kobayashi et al., 1999).

In the following, we discuss the synchrotron emission properties for four models: thin shell forward shock model, thin shell reverse shock model, thick shell forward shock model, and thick shell reverse shock model.

Thin Shell Forward Shock Model

In the thin shell models, the reverse shock is Newtonian, so that $\gamma_2 \simeq \gamma_4 = \Gamma_0$. We consider the dynamics of Region 2, i.e.

$$\gamma_2 = \Gamma_0, \quad R_2 = 2c\Gamma_0^2 t.$$

In general, the expressions for an arbitrary density profile index k can be derived. The two most commonly used models are the constant density interstellar medium (ISM) model ($k = 0$) and the free stratified wind model ($k = 2$). Hereafter we will explicitly derive the expressions for these two density profiles.

For the constant density case ($n_1 = n_0$) with electron energy spectral index $p > 2$,

one has

$$\begin{aligned}
\nu_m &= 3.1 \times 10^{16} \text{ Hz } \hat{z}^{-1} \frac{G(p)}{G(2.3)} \Gamma_{0,2}^4 n_{0,0}^{1/2} \epsilon_{e,-1}^2 \epsilon_{B,-2}^{1/2}, \\
\nu_c &= 4.1 \times 10^{16} \text{ Hz } \hat{z} \Gamma_{0,2}^{-4} n_{0,0}^{-3/2} \epsilon_{B,-2}^{-3/2} t_2^{-2}, \\
F_{\nu,\max} &= 1.1 \times 10^4 \text{ } \mu\text{Jy } \hat{z}^{-2} \Gamma_{0,2}^8 n_{0,0}^{3/2} \epsilon_{B,-2}^{1/2} D_{28}^{-2} t_2^3, \\
\nu_a &= 5.7 \times 10^9 \text{ Hz } \hat{z}^{-8/5} \frac{g^I(p)}{g^I(2.3)} \Gamma_{0,2}^{8/5} n_{0,0}^{4/5} \epsilon_{e,-1}^{-1} \epsilon_{B,-2}^{1/5} t_2^{3/5}, \quad \nu_a < \nu_m < \nu_c \\
\nu_a &= 8.3 \times 10^{12} \text{ Hz } \hat{z}^{-\frac{p+6}{p+4}} \frac{g^{II}(p)}{g^{II}(2.3)} \Gamma_{0,2}^{\frac{4(p+2)}{p+4}} n_{0,0}^{\frac{p+6}{2(p+4)}} \epsilon_{e,-1}^{\frac{2(p-1)}{p+4}} \epsilon_{B,-2}^{\frac{p+2}{2(p+4)}} t_2^{\frac{2}{p+4}}, \nu_m < \nu_a < \nu_c \\
\nu_a &= 4.9 \times 10^9 \text{ Hz } \hat{z}^{-13/5} \frac{g^{III}(p)}{g^{III}(2.3)} \Gamma_{0,2}^{28/5} n_{0,0}^{9/5} \epsilon_{B,-2}^{6/5} t_2^{8/5}, \quad \nu_a < \nu_c < \nu_m
\end{aligned} \tag{4.22}$$

where $G(p)$ and $g^i(p)$ are numerical constants related to p , and $\hat{z} = (1+z)/2$ is the redshift correction factor. The explicit expressions of $G(p)$ and $g^i(p)$ are complicated, and we present them (along with the p -dependent coefficients in all other models) in last section of this chapter.

When $1 < p < 2$, expressions of ν_c and $F_{\nu,\max}$ remain the same as the $p > 2$ case (also apply to other models discussed later). Other expressions are modified as follows

$$\begin{aligned}
\nu_m &= 3.2 \times 10^{14} \text{ Hz } \hat{z}^{-1} \frac{g^{IV}(p)}{g^{IV}(1.8)} \Gamma_{0,2}^{\frac{p+2}{p-1}} n_{0,0}^{\frac{1}{2(p-1)}} \zeta_0^{\frac{2-p}{p-1}} \epsilon_{e,-1}^{\frac{2}{p-1}} \epsilon_{B,-2}^{\frac{1}{2(p-1)}}, \\
\nu_a &= 4.6 \times 10^{10} \text{ Hz } \hat{z}^{-8/5} \frac{g^V(p)}{g^V(1.8)} \Gamma_{0,2}^{\frac{46-31p}{10(1-p)}} n_{0,0}^{\frac{26-21p}{20(1-p)}} \zeta_0^{\frac{p-2}{2(p-1)}} \epsilon_{e,-1}^{\frac{1}{1-p}} \epsilon_{B,-2}^{\frac{14-9p}{20(1-p)}} t_2^{3/5}, \nu_a < \nu_m < \nu_c \\
\nu_a &= 2.0 \times 10^{10} \text{ Hz } \hat{z}^{-\frac{p+6}{p+4}} \frac{g^{VI}(p)}{g^{VI}(1.8)} \Gamma_{0,2}^{\frac{p+14}{p+4}} n_{0,0}^{\frac{4}{p+4}} \zeta_0^{\frac{2-p}{p+4}} \epsilon_{e,-1}^{\frac{2}{p+4}} \epsilon_{B,-2}^{\frac{2}{p+4}} t_2^{\frac{2}{p+4}}, \quad \nu_m < \nu_a < \nu_c \\
\nu_a &= 4.0 \times 10^9 \text{ Hz } \hat{z}^{-13/5} \frac{g^{VII}(p)}{g^{VII}(1.8)} \Gamma_{0,2}^{28/5} n_{0,0}^{9/5} \epsilon_{B,-2}^{6/5} t_2^{8/5}, \quad \nu_a < \nu_c < \nu_m
\end{aligned} \tag{4.23}$$

For the wind model ($k = 2$), one can express the density profile as $n_1 = AR^{-2}$,

with $A = \dot{M}/4\pi m_p v_w = 3 \times 10^{35} A_* \text{cm}^{-1}$, $A_* = (\dot{M}/10^{-5} M_\odot \text{yr}^{-1})(v_w/10^3 \text{km s}^{-1})^{-1}$ (Dai and Lu, 1998b; Chevalier and Li, 1999, 2000). For $p > 2$, one has

$$\begin{aligned}
\nu_m &= 8.7 \times 10^{16} \text{ Hz} \frac{G(p)}{G(2.3)} A_{*, -1}^{1/2} \Gamma_{0,2}^2 \epsilon_{e,-1}^2 \epsilon_{B,-2}^{1/2} t_2^{-1}, \\
\nu_c &= 1.8 \times 10^{15} \text{ Hz} \hat{z}^{-2} \Gamma_{0,2}^2 A_{*, -1}^{-3/2} \epsilon_{B,-2}^{-3/2} t_2 \\
F_{\nu, \text{max}} &= 7.5 \times 10^5 \mu\text{Jy} \hat{z} A_{*, -1}^{3/2} \Gamma_{0,2}^2 \epsilon_{B,-2}^{1/2} D_{28}^{-2}, \\
\nu_a &= 5.9 \times 10^{10} \text{ Hz} \frac{g^{VIII}(p)}{g^{VIII}(2.3)} \Gamma_{0,2}^{-\frac{8}{5}} A_{*, -1}^{\frac{4}{5}} \epsilon_{e,-1}^{-1} \epsilon_{B,-2}^{\frac{1}{5}} t_2^{-1}, \quad \nu_a < \nu_m < \nu_c \\
\nu_a &= 4.7 \times 10^{13} \text{ Hz} \frac{g^{IX}(p)}{g^{IX}(2.3)} \Gamma_{0,2}^{\frac{2(p-2)}{p+4}} A_{*, -1}^{\frac{p+6}{2(p+4)}} \epsilon_{e,-1}^{\frac{2(p-1)}{p+4}} \epsilon_{B,-2}^{\frac{p+2}{2(p+4)}} t_2^{-1}, \nu_a < \nu_m < \nu_c \\
\nu_a &= 4.1 \times 10^{11} \text{ Hz} \hat{z} \frac{g^X(p)}{g^X(2.3)} \Gamma_{0,2}^{-8/5} A_{*, -1}^{9/5} \epsilon_{B,-2}^{6/5} t_2^{-2}, \quad \nu_a < \nu_c < \nu_m
\end{aligned} \tag{4.24}$$

For $1 < p < 2$, one has

$$\begin{aligned}
\nu_m &= 1.2 \times 10^{15} \text{ Hz} \hat{z}^{\frac{2-p}{p-1}} \frac{g^{XI}(p)}{g^{XI}(1.8)} A_{*, -1}^{\frac{1}{2(p-1)}} \Gamma_{0,2}^{\frac{p}{p-1}} \zeta_0^{\frac{2-p}{p-1}} \epsilon_{e,-1}^{\frac{2}{p-1}} \epsilon_{B,-2}^{\frac{1}{2(p-1)}} t_2^{\frac{1}{1-p}}, \\
\nu_a &= 4.2 \times 10^{11} \text{ Hz} \hat{z}^{\frac{p-2}{2(p-1)}} \frac{g^{XII}(p)}{g^{XII}(1.8)} \Gamma_{0,2}^{\frac{11p-6}{10(1-p)}} A_{*, -1}^{\frac{26-21p}{20(1-p)}} \zeta_0^{\frac{p-2}{2(p-1)}} \epsilon_{e,-1}^{\frac{1}{1-p}} \epsilon_{B,-2}^{\frac{14-9p}{20(1-p)}} t_2^{\frac{4-3p}{2(p-1)}}, \\
\nu_a &< \nu_m < \nu_c \\
\nu_a &= 1.2 \times 10^{13} \text{ Hz} \hat{z}^{\frac{2-p}{p+4}} \frac{g^{XIII}(p)}{g^{XIII}(1.8)} \Gamma_{0,2}^{\frac{p-2}{p+4}} A_{*, -1}^{\frac{4}{p+4}} \zeta_0^{\frac{2-p}{p+4}} \epsilon_{e,-1}^{\frac{2}{p+4}} \epsilon_{B,-2}^{\frac{2}{p+4}} t_2^{-\frac{6}{p+4}}, \nu_m < \nu_a < \nu_m \\
\nu_a &= 3.4 \times 10^{11} \text{ Hz} \hat{z} \frac{g^{XIV}(p)}{g^{XIV}(1.8)} \Gamma_{0,2}^{-8/5} A_{*, -1}^{9/5} \epsilon_{B,-2}^{6/5} t_2^{-2}, \quad \nu_a < \nu_c < \nu_m
\end{aligned} \tag{4.25}$$

The α and β values and their closure relations of the models described in this section (with convention $F_\nu \propto t^{-\alpha} \nu^{-\beta}$) are collected in Tables 5 and 6.

We note that the temporal evolution of the characteristic frequencies and the peak flux density are important to judge the relevant models. Hereafter at the end of each subsection, we summarize these dependences for easy identification.

		$p > 2$		$1 < p < 2$	
	β	α	$\alpha(\beta)$	α	$\alpha(\beta)$
ISM	slow cooling				
$\nu < \nu_a$	-2	-2	$\alpha = \beta$	-2	$\alpha = \beta$
$\nu_a < \nu < \nu_m$	$-\frac{1}{3}$	-3	$\alpha = 3\beta$	-3	$\alpha = 3\beta$
$\nu_m < \nu < \nu_c$	$\frac{p-1}{2}$	-3	--	-3	--
$\nu > \nu_c$	$\frac{p}{2}$	-2	--	-2	--
ISM	fast cooling				
$\nu < \nu_a$	-2	-1	$\alpha = \frac{\beta}{2}$	-1	$\alpha = \frac{\beta}{2}$
$\nu_a < \nu < \nu_c$	$-\frac{1}{3}$	$-\frac{11}{3}$	$\alpha = 11\beta$	$-\frac{11}{3}$	$\alpha = 11\beta$
$\nu_c < \nu < \nu_m$	$\frac{1}{2}$	-2	$\alpha = -4\beta$	-2	$\alpha = -4\beta$
$\nu > \nu_m$	$\frac{p}{2}$	-2	--	-2	--
Wind	slow cooling				
$\nu < \nu_a$	-2	-2	$\alpha = \beta$	$\frac{5p-6}{2(1-p)}$	--
$\nu_a < \nu < \nu_m$	$-\frac{1}{3}$	$-\frac{1}{3}$	$\alpha = \beta$	$-\frac{1}{3(p-1)}$	--
$\nu_m < \nu < \nu_c$	$\frac{p-1}{2}$	$\frac{p-1}{2}$	$\alpha = \beta$	$\frac{1}{2}$	--
$\nu > \nu_c$	$\frac{p}{2}$	$\frac{p-2}{2}$	$\alpha = \beta - 1$	0	--
Wind	fast cooling				
$\nu < \nu_a$	-2	-3	$\alpha = \frac{3\beta}{2}$	-3	$\alpha = \frac{3\beta}{2}$
$\nu_a < \nu < \nu_c$	$-\frac{1}{3}$	$\frac{1}{3}$	$\alpha = -\beta$	$\frac{1}{3}$	$\alpha = -\beta$
$\nu_c < \nu < \nu_m$	$\frac{1}{2}$	$-\frac{1}{2}$	$\alpha = -\beta$	$-\frac{1}{2}$	$\alpha = -\beta$
$\nu > \nu_m$	$\frac{p}{2}$	$\frac{p-2}{2}$	$\alpha = \beta - 1$	0	--

Table 5 The temporal decay index α and spectral index β in thin shell forward shock model with $\nu_a < \min(\nu_m, \nu_c)$.

For this regime (thin-shell forward shock model during shock crossing) and for $p > 2$, $\nu_m \propto t^0$ (t^{-1}), $\nu_c \propto t^{-2}$ (t^1), $F_{\nu, \max} \propto t^3$ (t^0) for the ISM (wind) models, respectively. The temporal evolution of ν_a depends on the relative orders between ν_a , ν_m and ν_c . For $1 < p < 2$, ν_c and $F_{\nu, \max}$ evolutions are the same as $p > 2$ cases, while $\nu_m \propto t^0$ ($t^{\frac{1}{1-p}}$) for the ISM (wind) models, respectively.

		$p > 2$		$1 < p < 2$	
	β	α	$\alpha(\beta)$	α	$\alpha(\beta)$
ISM	slow cooling				
$\nu < \nu_m$	-2	-2	$\alpha = \beta$	-2	$\alpha = \beta$
$\nu_m < \nu < \nu_a$	$-\frac{5}{2}$	-2	$\alpha = \frac{4\beta}{5}$	-2	$\alpha = \frac{4\beta}{5}$
$\nu_a < \nu < \nu_c$	$\frac{p-1}{2}$	-3	--	-3	--
$\nu > \nu_c$	$\frac{p}{2}$	-2	--	-2	--
Wind	slow cooling				
$\nu < \nu_m$	-2	-2	$\alpha = \beta$	$\frac{6-5p}{2(p-1)}$	--
$\nu_m < \nu < \nu_a$	$-\frac{5}{2}$	$-\frac{5}{2}$	$\alpha = \beta$	$-\frac{5}{2}$	$\alpha = \beta$
$\nu_a < \nu < \nu_c$	$\frac{p-1}{2}$	$\frac{p-1}{2}$	$\alpha = \beta$	$\frac{1}{2}$	--
$\nu > \nu_c$	$\frac{p}{2}$	$\frac{p-2}{2}$	$\alpha = \beta - 1$	0	--

Table 6 The temporal decay index α and spectral index β in thin shell forward shock model in the $\nu_m < \nu_a < \nu_c$ regime.

Thin Shell Reverse Shock Model

The scalings of this regime have been derived by Kobayashi (2000b). During the reverse shock crossing phase, the blastwave dynamics is same as the thin-shell forward shock case. However, the emission properties of the reverse shock depend on $\bar{\gamma}_{34}$ and n_4 , while those of the forward shock depend on γ_2 and n_1 . Following the similar procedure described above, one can derive the expressions of various parameters of this model. For the ISM model ($k = 0$) and $p > 2$, one has

$$\begin{aligned}
\nu_m &= 1.9 \times 10^{12} \text{ Hz } \hat{z}^{-7} \frac{G(p)}{G(2.3)} E_{52}^{-2} \Gamma_{0,2}^{18} n_{0,0}^{5/2} \epsilon_{e,-1}^2 \epsilon_{B,-2}^{1/2} t_2^6, \\
\nu_c &= 4.1 \times 10^{16} \text{ Hz } \hat{z} \Gamma_{0,2}^{-4} n_{0,0}^{-3/2} \epsilon_{B,-2}^{-3/2} t_2^{-2} \\
F_{\nu,\max} &= 9.1 \times 10^5 \text{ } \mu\text{Jy } \hat{z}^{-1/2} E_{52}^{1/2} \Gamma_{0,2}^5 n_{0,0}^{1/2} \epsilon_{B,-2}^{-2} t_2^{3/2}, \\
\nu_a &= 1.0 \times 10^{13} \text{ Hz } \hat{z}^{23/10} \frac{g^I(p)}{g^I(2.3)} E_{52}^{13/10} \Gamma_{0,2}^{-36/5} n_{0,0}^{-1/2} \epsilon_{e,-1}^{-1} \epsilon_{B,-2}^{1/5} t_2^{-33/10}, \quad \nu_a < \nu_m < \nu_c \\
\nu_a &= 4.7 \times 10^{12} \text{ Hz } \hat{z}^{\frac{3-7p}{p+4}} \frac{g^{II}(p)}{g^{II}(2.3)} E_{52}^{\frac{3-2p}{p+4}} \Gamma_0^{\frac{18p-12}{p+4}} n_{0,0}^{\frac{5p}{2(p+4)}} \epsilon_{e,-1}^{\frac{2(p-1)}{p+4}} \epsilon_{B,-2}^{\frac{p+2}{2(p+4)}} t_2^{\frac{6p-7}{p+4}}, \nu_m < \nu_a < \nu_c \\
\nu_a &= 7.0 \times 10^{10} \text{ Hz } \hat{z}^{-17/10} \frac{g^{III}(p)}{g^{III}(2.3)} E_{52}^{3/10} \Gamma_{0,2}^{19/5} n_{0,0}^{3/2} \epsilon_{B,-2}^{6/5} t_2^{7/10}. \quad \nu_a < \nu_c < \nu_m
\end{aligned} \tag{4.26}$$

For $1 < p < 2$, one has

$$\begin{aligned}
\nu_m &= 1.8 \times 10^9 \text{ Hz } \hat{z}^{\frac{p+5}{1-p}} \frac{g^{IV}(p)}{g^{IV}(1.8)} E_{52}^{-\frac{2}{p-1}} n_{0,0}^{\frac{5}{2(p-1)}} \Gamma_{0,2}^{\frac{p+16}{p-1}} \zeta_0^{\frac{2-p}{p-1}} \epsilon_{e,-1}^{\frac{2}{p-1}} \epsilon_{B,-2}^{\frac{1}{2(p-1)}} t_2^{\frac{6}{p-1}}, \\
\nu_a &= 2.7 \times 10^{14} \text{ Hz } \hat{z}^{\frac{37-7p}{10(p-1)}} \frac{g^V(p)}{g^V(1.8)} E_{52}^{\frac{3p+7}{10(p-1)}} \Gamma_{0,2}^{\frac{98-13p}{10(1-p)}} n_{0,0}^{\frac{8-3p}{4(1-p)}} \zeta_0^{\frac{p-2}{2(p-1)}} \epsilon_{e,-1}^{\frac{1}{1-p}} \epsilon_{B,-2}^{\frac{14-9p}{20(1-p)}} t_2^{-\frac{3(p+9)}{10(p-1)}}, \\
\nu_a &< \nu_m < \nu_c \\
\nu_a &= 1.7 \times 10^{12} \text{ Hz } \hat{z}^{-\frac{p+9}{p+4}} \frac{g^{VI}(p)}{g^{VI}(1.8)} E_{52}^{-\frac{1}{p+4}} \Gamma_{0,2}^{\frac{p+22}{p+4}} n_{0,0}^{\frac{5}{p+4}} \zeta_0^{\frac{2-p}{p+4}} \epsilon_{e,-1}^{\frac{2}{p+4}} \epsilon_{B,-2}^{\frac{2}{p+4}} t_2^{\frac{5}{p+4}}, \nu_m < \nu_a < \nu_c \\
\nu_a &= 5.8 \times 10^{10} \text{ Hz } \hat{z}^{-17/10} \frac{g^{VII}(p)}{g^{VII}(1.8)} E_{52}^{3/10} \Gamma_{0,2}^{19/5} n_{0,0}^{3/2} \epsilon_{B,-2}^{6/5} t_2^{7/10}, \quad \nu_a < \nu_c < \nu_m
\end{aligned} \tag{4.27}$$

For the wind model ($k = 2$) and $p > 2$, one has

$$\begin{aligned}
\nu_m &= 3.3 \times 10^{15} \text{ Hz } \hat{z}^{-2} \frac{G(p)}{G(2.3)} E_{52}^{-2} A_{*, -1}^{5/2} \Gamma_{0,2}^8 \epsilon_{e,-1}^2 \epsilon_{B,-2}^{1/2} t_2, \\
\nu_c &= 1.8 \times 10^{15} \text{ Hz } \hat{z}^{-2} \Gamma_{0,2}^2 A_{*, -1}^{-3/2} \epsilon_{B,-2}^{-3/2} t_2 \\
F_{\nu, \max} &= 1.3 \times 10^7 \text{ } \mu\text{Jy } \hat{z}^{3/2} E_{52}^{1/2} A_{*, -1} \Gamma_{0,2}^{1/2} D_{28}^{-2} t_2^{-1/2}, \\
\nu_a &= 1.7 \times 10^{12} \text{ Hz } \hat{z}^{13/10} \frac{g^{VIII}(p)}{g^{VIII}(2.3)} E_{52}^{13/10} \Gamma_{0,2}^{-26/5} A_{*, -1}^{-1/2} \epsilon_{e,-1}^{-1} \epsilon_{B,-2}^{1/5} t_2^{-23/10}, \nu_a < \nu_m < \nu_c \\
\nu_a &= 5.9 \times 10^{13} \text{ Hz } \hat{z}^{\frac{3-2p}{p+4}} \frac{g^{IX}(p)}{g^{IX}(2.3)} E_{52}^{\frac{3-2p}{p+4}} \Gamma_{0,2}^{\frac{8p-12}{p+4}} A_{*, -1}^{\frac{5p}{2(p+4)}} \epsilon_{e,-1}^{\frac{2(p-1)}{p+4}} \epsilon_{B,-2}^{\frac{p+2}{2(p+4)}} t_2^{\frac{p-7}{p+4}}, \nu_m < \nu_a < \nu_c \\
\nu_a &= 2.3 \times 10^{12} \text{ Hz } \hat{z}^{13/10} \frac{g^X(p)}{g^X(2.3)} E_{52}^{3/10} \Gamma_{0,2}^{-11/5} A_{*, -1}^{3/2} \epsilon_{B,-2}^{6/5} t_2^{-23/10}, \quad \nu_a < \nu_c < \nu_m
\end{aligned} \tag{4.28}$$

For $1 < p < 2$, one has

$$\begin{aligned}
\nu_m &= 2.0 \times 10^{13} \text{ Hz } \hat{z}^{\frac{p}{1-p}} \frac{g^{XI}(p)}{g^{XI}(1.8)} E_{52}^{-\frac{2}{p-1}} A_{*, -1}^{\frac{5}{2(p-1)}} \Gamma_{0,2}^{\frac{p+6}{p-1}} \zeta_0^{\frac{2-p}{p-1}} \epsilon_{e,-1}^{\frac{2}{p-1}} \epsilon_{B,-2}^{\frac{1}{2(p-1)}} t_2^{\frac{1}{p-1}}, \\
\nu_a &= 1.8 \times 10^{13} \text{ Hz } \hat{z}^{\frac{8p-3}{10(p-1)}} \frac{g^{XII}(p)}{g^{XII}(1.8)} E_{52}^{\frac{3p+7}{10(p-1)}} \Gamma_{0,2}^{\frac{17p+18}{10(1-p)}} A_{*, -1}^{\frac{8-3p}{4(1-p)}} \zeta_0^{\frac{p-2}{2(p-1)}} \epsilon_{e,-1}^{\frac{1}{1-p}} \epsilon_{B,-2}^{\frac{14-9p}{20(1-p)}} t_2^{\frac{13-18p}{10(p-1)}}, \\
\nu_a &< \nu_m < \nu_c \\
\nu_a &= 1.9 \times 10^{13} \text{ Hz } \hat{z}^{\frac{1-p}{p+4}} \frac{g^{XIII}(p)}{g^{XIII}(1.8)} E_{52}^{-\frac{1}{p+4}} \Gamma_{0,2}^{\frac{p+2}{p+4}} A_{*, -1}^{\frac{5}{p+4}} \zeta_0^{\frac{2-p}{p+4}} \epsilon_{e,-1}^{\frac{2}{p+4}} \epsilon_{B,-2}^{\frac{2}{p+4}} t_2^{-\frac{5}{p+4}}, \nu_m < \nu_a < \nu_c \\
\nu_a &= 1.9 \times 10^{12} \text{ Hz } \hat{z}^{13/10} \frac{g^{XIV}(p)}{g^{XIV}(1.8)} E_{52}^{3/10} \Gamma_{0,2}^{-11/5} A_{*, -1}^{3/2} \epsilon_{B,-2}^{6/5} t_2^{-23/10}, \quad \nu_a < \nu_c < \nu_m
\end{aligned} \tag{4.29}$$

After the NRS crosses the shell, the Lorentz factor of the shocked shell may be assumed to have a general power-law decay behavior $\gamma_3 \propto r^{-g}$ (Mészáros and Rees, 1999; Kobayashi and Sari, 2000a). The dynamical behavior in Region 3 could be expressed with some scaling-laws:

$$\gamma_3 \propto t^{-g/(1+2g)}, n_3 \propto t^{-6(3+g)/7(1+2g)},$$

$$e_3 \propto t^{-8(3+g)/7(1+2g)}, r \propto t^{1/(1+2g)}, N_{e,3} \propto t^0, \quad (4.30)$$

For the ISM case ($k = 0$), one may adopt $g \simeq 2$ (Kobayashi, 2000b; Zou et al., 2005). For $p > 2$, one has

$$\begin{aligned} \nu_m &= 8.5 \times 10^{11} \text{ Hz } \hat{z}^{19/35} \frac{G(p)}{G(2.3)} E_{52}^{18/35} \Gamma_{0,2}^{-74/35} n_{0,0}^{-1/70} \epsilon_{e,-1}^2 \epsilon_{B,-2}^{1/2} t_2^{-54/35}, \\ \nu_{\text{cut}} &= 4.3 \times 10^{16} \text{ Hz } \hat{z}^{19/35} E_{52}^{-16/105} \Gamma_{0,2}^{-292/105} n_{0,0}^{-283/210} \epsilon_{B,-2}^{-3/2} t_2^{-54/35} \\ F_{\nu,\text{max}} &= 7.0 \times 10^5 \mu\text{Jy } \hat{z}^{69/35} E_{52}^{139/105} \Gamma_{0,2}^{-167/105} n_{0,0}^{37/210} \epsilon_{B,-2}^{1/2} D_{28}^{-2} t_2^{-34/35}, \\ \nu_a &= 1.4 \times 10^{13} \text{ Hz } \hat{z}^{-73/175} \frac{g^{XV}(p)}{g^{XV}(2.3)} E_{52}^{69/175} \Gamma_{0,2}^{8/175} n_{0,0}^{71/175} \epsilon_{e,-1}^{-1} \epsilon_{B,-2}^{1/5} t_2^{-102/175}, \\ \nu_a &< \nu_m < \nu_c \\ \nu_a &= 3.7 \times 10^{12} \text{ Hz } \hat{z}^{\frac{19p-36}{35(p+4)}} \frac{g^{XVI}(p)}{g^{XVI}(2.3)} E_{52}^{\frac{2(9p+29)}{35(p+4)}} \Gamma_{0,2}^{\frac{-74p-44}{35(p+4)}} n_{0,0}^{\frac{94-p}{70(p+4)}} \epsilon_{e,-1}^{\frac{2(p-1)}{p+4}} \epsilon_{B,-2}^{\frac{p+2}{2(p+4)}} t_2^{-\frac{54p+104}{35(p+4)}}, \\ \nu_m &< \nu_a < \nu_c \end{aligned} \quad (4.31)$$

Here ν_{cut} is the cut-off frequency of the synchrotron spectrum, which is different from the traditional ν_c . After reverse shock crossing, no new electrons are accelerated. The maximum electron energy is defined by ν_{cut} , which is calculated by ν_c at the shock crossing time with correction due to adiabatic expansion (Kobayashi, 2000b). In this case, fast cooling is not relevant, so there are only two regimes, i.e., $\nu_a < \nu_m < \nu_{\text{cut}}$ and $\nu_m < \nu_a < \nu_{\text{cut}}$.

For $1 < p < 2$, again the expressions of ν_{cut} and $F_{\nu,\text{max}}$ remain the same, and other parameters are

$$\begin{aligned} \nu_m &= 6.8 \times 10^{11} \text{ Hz } \hat{z}^{19/35} \frac{g^{XVII}(p)}{g^{XVII}(1.8)} E_{52}^{\frac{18}{35}} \Gamma_{0,2}^{\frac{109p-144}{35(1-p)}} n_{0,0}^{\frac{71-36p}{70(p-1)}} \zeta_0^{\frac{2-p}{p-1}} \epsilon_{e,-1}^{\frac{2}{p-1}} \epsilon_{B,-2}^{\frac{1}{2(p-1)}} t_2^{-\frac{54}{35}}, \\ \nu_a &= 1.3 \times 10^{13} \text{ Hz } \hat{z}^{-73/175} \frac{g^{XVIII}(p)}{g^{XVIII}(1.8)} E_{52}^{\frac{69}{175}} \Gamma_{0,2}^{\frac{191p-366}{350(p-1)}} n_{0,0}^{\frac{459p-634}{700(p-1)}} \zeta_0^{\frac{p-2}{2(p-1)}} \epsilon_{e,-1}^{\frac{1}{1-p}} \\ &\quad \epsilon_{B,-2}^{\frac{14-9p}{20(1-p)} t_2^{-\frac{102}{175}}}, \nu_a < \nu_m < \nu_{\text{cut}} \end{aligned}$$

$$\nu_a = 3.7 \times 10^{12} \text{ Hz } \hat{z}^{\frac{19p-36}{35(p+4)}} \frac{g^{XIX}(p)}{g^{XIX}(1.8)} E_{52}^{\frac{2(9p+29)}{35(p+4)}} \Gamma_{0,2}^{\frac{26-109p}{35(p+4)}} n_{0,0}^{-\frac{2(9p-41)}{35(p+4)}} \zeta_0^{\frac{2-p}{p+4}} \epsilon_{e,-1}^{\frac{2}{p+4}}$$

$$\epsilon_{B,-2}^{\frac{2}{p+4}} t_2^{-\frac{54p+104}{35(p+4)}}, \nu_m < \nu_a < \nu_{\text{cut}}$$

(4.32)

For the wind model ($k = 2$), one could adopt $g \simeq 1$ (Zou et al., 2005). For $p > 2$, one has

$$\nu_m = 1.4 \times 10^{11} \text{ Hz } \hat{z}^{6/7} \frac{G(p)}{G(2.3)} E_{52}^{6/7} A_{*, -1}^{-5/14} \Gamma_{0,2}^{-24/7} \epsilon_{e,-1}^{1/2} \epsilon_{B,-2}^{-13/7},$$

$$\nu_{\text{cut}} = 7.4 \times 10^{10} \text{ Hz } \hat{z}^{6/7} E_{52}^{20/7} \Gamma_{0,2}^{-66/7} A_{*, -1}^{-61/14} \epsilon_{B,-2}^{-3/2} t_2^{-13/7}$$

$$F_{\nu, \text{max}} = 1.6 \times 10^6 \text{ } \mu\text{Jy } \hat{z}^{44/21} E_{52}^{23/21} A_{*, -1}^{17/42} \Gamma_{0,2}^{-29/21} \epsilon_{B,-2}^{1/2} D_{28}^{-2} t_2^{-23/21},$$

$$\nu_a = 5.5 \times 10^{14} \text{ Hz } \hat{z}^{-8/35} \frac{g^{XX}(p)}{g^{XX}(2.3)} E_{52}^{-12/35} \Gamma_{0,2}^{48/35} A_{*, -1}^{8/7} \epsilon_{e,-1}^{-1} \epsilon_{B,-2}^{1/5} t_2^{-23/35},$$

$$\nu_a < \nu_m < \nu_{\text{cut}}$$

$$\nu_a = 5.5 \times 10^{14} \text{ Hz } \hat{z}^{\frac{6p-4}{7(p+4)}} \frac{g^{XXI}(p)}{g^{XXI}(2.3)} E_{52}^{\frac{6p-4}{7(p+4)}} \Gamma_{0,2}^{\frac{16-24p}{7(p+4)}} A_{*, -1}^{\frac{50-5p}{14(p+4)}} \epsilon_{e,-1}^{\frac{2(p-1)}{p+4}} \epsilon_{B,-2}^{\frac{p+2}{2(p+4)}} t_2^{-\frac{13p+24}{7(p+4)}},$$

$$\nu_m < \nu_a < \nu_{\text{cut}}$$

(4.33)

For $1 < p < 2$, ν_{cut} and $F_{\nu, \text{max}}$ remain the same, and

$$\nu_m = 3.5 \times 10^{11} \text{ Hz } \hat{z}^{6/7} \frac{g^{XXII}(p)}{g^{XXII}(1.8)} E_{52}^{\frac{13p-20}{7(p-1)}} \Gamma_{0,2}^{\frac{45p-66}{7(1-p)}} A_{*, -1}^{\frac{47-26p}{14(p-1)}} \zeta_0^{\frac{2-p}{p-1}} \epsilon_{e,-1}^{\frac{2}{p-1}} \epsilon_{B,-2}^{\frac{1}{2(p-1)}} t_2^{-\frac{13}{7}},$$

$$\nu_a = 2.8 \times 10^{14} \text{ Hz } \hat{z}^{-8/35} \frac{g^{XXIII}(p)}{g^{XXIII}(1.8)} E_{52}^{\frac{94-59p}{70(p-1)}} \Gamma_{0,2}^{\frac{3(67p-102)}{70(p-1)}} A_{*, -1}^{\frac{74-53p}{28(1-p)}} \zeta_0^{\frac{p-2}{2(p-1)}} \epsilon_{e,-1}^{\frac{1}{1-p}}$$

$$\epsilon_{B,-2}^{\frac{14-9p}{20(1-p)}} t_2^{-\frac{23}{35}},$$

$$\nu_a < \nu_m < \nu_{\text{cut}}$$

$$\nu_a = 1.6 \times 10^{13} \text{ Hz } \hat{z}^{\frac{6p-4}{7(p+4)}} \frac{g^{XXIV}(p)}{g^{XXIV}(1.8)} E_{52}^{\frac{13p-18}{7(p+4)}} \Gamma_{0,2}^{\frac{58-45p}{7p+28}} A_{*, -1}^{\frac{46-13p}{7p+28}} \zeta_0^{\frac{2-p}{p+4}} \epsilon_{e,-1}^{\frac{2}{p+4}} \epsilon_{B,-2}^{\frac{2}{p+4}} t_2^{-\frac{13p+24}{7(p+4)}},$$

$$\nu_m < \nu_a < \nu_{\text{cut}}$$

(4.34)

		$p > 2$		$1 < p < 2$	
	β	α	$\alpha(\beta)$	α	$\alpha(\beta)$
ISM	slow cooling				
$\nu < \nu_a$	-2	-5	$\alpha = \frac{5\beta}{2}$	$-\frac{2p+1}{2}$	--
$\nu_a < \nu < \nu_m$	$-\frac{1}{3}$	$\frac{1}{2}$	$\alpha = \frac{3\beta}{2}$	$-\frac{3p-7}{2(p-1)}$	--
$\nu_m < \nu < \nu_c$	$\frac{p-1}{2}$	$-\frac{6p-3}{2}$	$\alpha = -\frac{3(4\beta+1)}{2}$	$-\frac{9}{2}$	--
$\nu > \nu_c$	$\frac{p}{2}$	$-\frac{6p-5}{2}$	$-\frac{11\beta+1}{2}$	$-\frac{7}{2}$	--
ISM	fast cooling				
$\nu < \nu_a$	-2	-1	$\alpha = \frac{\beta}{2}$	-1	$\alpha = \frac{\beta}{2}$
$\nu_a < \nu < \nu_c$	$-\frac{1}{3}$	$-\frac{13}{6}$	$\alpha = \frac{13\beta}{2}$	$-\frac{13}{6}$	$\alpha = \frac{13\beta}{2}$
$\nu_c < \nu < \nu_m$	$\frac{1}{2}$	$-\frac{1}{2}$	$\alpha = -\beta$	$-\frac{1}{2}$	$\alpha = -\beta$
$\nu > \nu_m$	$\frac{p}{2}$	$-\frac{6p-5}{2}$	$-\frac{12\beta-5}{2}$	$-\frac{7}{2}$	--
Wind	slow cooling				
$\nu < \nu_a$	-2	-3	$\alpha = \frac{3\beta}{2}$	$-\frac{5p-4}{2(p-1)}$	--
$\nu_a < \nu < \nu_m$	$-\frac{1}{3}$	$\frac{5}{6}$	$\alpha = \frac{5\beta}{2}$	$\frac{3p-1}{6(p-1)}$	--
$\nu_m < \nu < \nu_c$	$\frac{p-1}{2}$	$-\frac{p-2}{2}$	$\alpha = \frac{1-2\beta}{2}$	0	--
$\nu > \nu_c$	$\frac{p}{2}$	$-\frac{p-1}{2}$	$\alpha = \frac{1-2\beta}{2}$	$-\frac{1}{2}$	--
Wind	fast cooling				
$\nu < \nu_a$	-2	-3	$\alpha = \frac{3\beta}{2}$	-3	$\alpha = \frac{3\beta}{2}$
$\nu_a < \nu < \nu_c$	$-\frac{1}{3}$	$\frac{5}{6}$	$\alpha = -\frac{5\beta}{2}$	$\frac{5}{6}$	$\alpha = -\frac{5\beta}{2}$
$\nu_c < \nu < \nu_m$	$\frac{1}{2}$	0	--	0	--
$\nu > \nu_m$	$\frac{p}{2}$	$-\frac{p-1}{2}$	$\alpha = \frac{1-2\beta}{2}$	$-\frac{1}{2}$	--

Table 7 Temporal decay index α and spectral index β in the thin shell reverse shock model during the reverse shock crossing phase in the $\nu_a < \min(\nu_m, \nu_c)$ spectral regime.

The α and β values and their closure relations for the thin shell reverse shock models are presented in Tables 7 and 8 (for pre-shock-crossing), and Tables 9 and 10 (for post-shock-crossing).

For this regime (thin-shell reverse shock model during shock crossing), for $p > 2$, one has $\nu_m \propto t^6$ (t^1), $\nu_c \propto t^{-2}$ (t^1), $F_{\nu, \max} \propto t^{3/2}$ ($t^{-1/2}$) for the ISM (wind) models, respectively. For $1 < p < 2$, ν_c and $F_{\nu, \max}$ evolutions are the same as $p > 2$ cases, while $\nu_m \propto t^{\frac{6}{p-1}}$ ($t^{\frac{1}{p-1}}$) for the ISM (wind) models, respectively.

After shock crossing, $\nu_m \propto \nu_{\text{cut}} \propto t^{-54/35}$ ($t^{-13/7}$), $F_{\nu, \max} \propto t^{-34/35}$ ($t^{-23/21}$) for the ISM (wind) models, respectively.

Thick Shell Forward Shock Model

For the thick shell case, the reverse shock becomes relativistic early on during shock crossing. In this relativistic shock crossing phase, the blastwave dynamics can

		$p > 2$		$1 < p < 2$	
	β	α	$\alpha(\beta)$	α	$\alpha(\beta)$
ISM	slow cooling				
$\nu < \nu_m$	-2	-5	$\alpha = \frac{5\beta}{2}$	$-\frac{2p+1}{p-1}$	--
$\nu_m < \nu < \nu_a$	$-\frac{5}{2}$	-2	$\alpha = \frac{4\beta}{5}$	-2	$\alpha = \frac{4\beta}{5}$
$\nu_a < \nu < \nu_c$	$\frac{p-1}{2}$	$-\frac{6p-3}{2}$	$\alpha = -\frac{3(4\beta+1)}{2}$	$-\frac{9}{2}$	--
$\nu > \nu_c$	$\frac{p}{2}$	$-\frac{6p-5}{2}$	$-\frac{12\beta-5}{2}$	$-\frac{7}{2}$	--
Wind	slow cooling				
$\nu < \nu_m$	-2	-3	$\alpha = \frac{3\beta}{2}$	$-\frac{5p-4}{2(p-1)}$	--
$\nu_m < \nu < \nu_a$	$-\frac{5}{2}$	$-\frac{5}{2}$	$\alpha = \beta$	$-\frac{5}{2}$	$\alpha = \beta$
$\nu_a < \nu < \nu_c$	$\frac{p-1}{2}$	$-\frac{p-2}{2}$	$\alpha = \frac{1-2\beta}{2}$	0	--
$\nu > \nu_c$	$\frac{p}{2}$	$-\frac{p-1}{2}$	$\alpha = \frac{1-2\beta}{2}$	$-\frac{1}{2}$	--

Table 8 Temporal decay index α and spectral index β in the thin shell reverse shock model during the reverse shock crossing phase in the $\nu_m < \nu_a < \nu_c$ spectral regime.

		$p > 2$		$1 < p < 2$	
	β	α	$\alpha(\beta)$	α	$\alpha(\beta)$
ISM	slow cooling				
$\nu < \nu_a$	-2	$-\frac{18}{35}$	$\alpha = \frac{9\beta}{35}$	$-\frac{18}{35}$	$\alpha = \frac{9\beta}{35}$
$\nu_a < \nu < \nu_m$	$-\frac{1}{3}$	$\frac{16}{35}$	$\alpha = -\frac{16\beta}{105}$	$\frac{16}{35}$	$\alpha = -\frac{16\beta}{105}$
$\nu_m < \nu < \nu_{cut}$	$\frac{p-1}{2}$	$\frac{27p+7}{35}$	$\alpha = \frac{54\beta+34}{35}$	$\frac{27p+7}{35}$	$\alpha = \frac{54\beta+34}{35}$
Wind	slow cooling				
$\nu < \nu_a$	-2	$-\frac{13}{21}$	$\alpha = \frac{13\beta}{42}$	$-\frac{13}{21}$	$\alpha = \frac{13\beta}{42}$
$\nu_a < \nu < \nu_m$	$-\frac{1}{3}$	$\frac{10}{21}$	$\alpha = \frac{10\beta}{7}$	$\frac{10}{21}$	$\alpha = \frac{10\beta}{7}$
$\nu_m < \nu < \nu_{cut}$	$\frac{p-1}{2}$	$\frac{39p+7}{42}$	$\alpha = \frac{78\beta+46}{2}$	$\frac{39p+7}{42}$	$\alpha = \frac{78\beta+46}{2}$

Table 9 Temporal decay index α and spectral index β in thin shell reverse shock model after reverse shock crossing in the $\nu_a < \min(\nu_m, \nu_{cut})$ spectral regime.

		$p > 2$		$1 < p < 2$	
	β	α	$\alpha(\beta)$	α	$\alpha(\beta)$
ISM	slow cooling				
$\nu < \nu_m$	-2	$-\frac{18}{35}$	$\alpha = \frac{9\beta}{35}$	$-\frac{18}{35}$	$\alpha = \frac{9\beta}{35}$
$\nu_m < \nu < \nu_a$	$-\frac{5}{2}$	$-\frac{9}{7}$	$\alpha = \frac{18\beta}{35}$	$-\frac{9}{7}$	$\alpha = \frac{18\beta}{35}$
$\nu_a < \nu < \nu_{cut}$	$\frac{p-1}{2}$	$\frac{27p+7}{35}$	$\alpha = \frac{54\beta+34}{35}$	$\frac{27p+7}{35}$	$\alpha = \frac{54\beta+34}{35}$
Wind	slow cooling				
$\nu < \nu_m$	-2	$-\frac{13}{21}$	$\alpha = \frac{13\beta}{42}$	$-\frac{13}{21}$	$\alpha = \frac{13\beta}{42}$
$\nu_m < \nu < \nu_a$	$-\frac{5}{2}$	$-\frac{65}{42}$	$\alpha = \frac{13\beta}{24}$	$-\frac{65}{42}$	$\alpha = \frac{13\beta}{24}$
$\nu_a < \nu < \nu_{cut}$	$\frac{p-1}{2}$	$\frac{39p+7}{42}$	$\alpha = \frac{78\beta+46}{2}$	$\frac{39p+7}{42}$	$\alpha = \frac{78\beta+46}{2}$

Table 10 Temporal decay index α and spectral index β in thin shell reverse shock model after reverse shock crossing in the $\nu_m < \nu_a < \nu_{cut}$ spectral regime.

be characterized as

$$\gamma_2 = \gamma_3 = \frac{1}{\sqrt{2}} \left(\frac{l^{3-k}}{\Delta_0} \right)^{\frac{1}{2(4-k)}} \left(\frac{t}{T} \right)^{\frac{k-2}{2(k-4)}} \Delta_0^{\frac{k-2}{2(k-4)}}, \quad R = 2c\gamma_2^2 t \quad (4.35)$$

where $l = \left(\frac{(3-k)E}{4\pi A m_p c^2} \right)^{\frac{1}{3-k}}$ is the Sedov length, and $T = \frac{\Delta_0}{c}$ is the shock crossing time (Yi et al., 2013).

For the ISM model and when $p > 2$, the forward shock emission can be characterized by

$$\begin{aligned} \nu_m &= 1.0 \times 10^{16} \text{ Hz} \frac{G(p)}{G(2.3)} E_{52}^{1/2} \Delta_{0,13}^{-1/2} \epsilon_{e,-1}^2 \epsilon_{B,-2}^{1/2} t_2^{-1}, \\ \nu_c &= 1.2 \times 10^{17} \text{ Hz} E_{52}^{-1/2} \Delta_{0,13}^{1/2} n_{0,0}^{-1} \epsilon_{B,-2}^{-3/2} t_2^{-1} \\ F_{\nu,\max} &= 1.2 \times 10^3 \text{ } \mu\text{Jy} \hat{z} E_{52} \Delta_{0,13}^{-1} n_{0,0}^{1/2} \epsilon_{B,-2}^{1/2} D_{28}^{-2}, \\ \nu_a &= 3.6 \times 10^9 \text{ Hz} \hat{z}^{-6/5} \frac{g^I(p)}{g^I(2.3)} E_{52}^{1/5} \Delta_{0,13}^{-1/5} n_{0,0}^{3/5} \epsilon_{e,-1}^{-1} \epsilon_{B,-2}^{1/5} t_2^{1/5}, \nu_a < \nu_m < \nu_c \\ \nu_a &= 3.9 \times 10^{12} \text{ Hz} \hat{z}^{-\frac{4}{p+4}} \frac{g^{II}(p)}{g^{II}(2.3)} E_{52}^{\frac{p+2}{2(p+4)}} \Delta_{0,13}^{-\frac{p+2}{2(p+4)}} n_{0,0}^{\frac{2}{p+4}} \epsilon_{e,-1}^{\frac{2(p-1)}{p+4}} \epsilon_{B,-2}^{\frac{p+2}{2(p+4)}} t_2^{-\frac{p}{p+4}}, \\ &\hspace{15em} \nu_m < \nu_a < \nu_c \\ \nu_a &= 1.0 \times 10^9 \text{ Hz} \hat{z}^{-6/5} \frac{g^{III}(p)}{g^{III}(2.3)} E_{52}^{7/10} \Delta_{0,13}^{-7/10} n_{0,0}^{11/10} \epsilon_{B,-2}^{6/5} t_2^{1/5}, \nu_a < \nu_c < \nu_m \end{aligned} \quad (4.36)$$

For $1 < p < 2$, one has (ν_c and $F_{\nu,\max}$ remain the same)

$$\begin{aligned} \nu_m &= 8.6 \times 10^{13} \text{ Hz} \hat{z}^{\frac{6-3p}{4(p-1)}} \frac{g^{IV}(p)}{g^{IV}(1.8)} E_{52}^{\frac{p+2}{8(p-1)}} n_{0,0}^{\frac{2-p}{8(p-1)}} \Delta_{0,13}^{\frac{p+2}{8(1-p)}} \zeta_0^{\frac{2-p}{p-1}} \epsilon_{e,-1}^{\frac{2}{p-1}} \epsilon_{B,-2}^{\frac{1}{2(p-1)}} t_2^{\frac{p+2}{4(1-p)}}, \\ \nu_a &= 3.2 \times 10^{10} \text{ Hz} \frac{g^V(p)}{g^V(1.8)} \hat{z}^{\frac{18-33p}{40(p-1)}} E_{52}^{\frac{46-31p}{80(1-p)}} \Delta_{0,13}^{\frac{46-31p}{80(p-1)}} n_{0,0}^{\frac{58-53p}{80(1-p)}} \zeta_0^{\frac{p-2}{2(p-1)}} \epsilon_{e,-1}^{\frac{1}{1-p}} \epsilon_{B,-2}^{\frac{14-9p}{20(1-p)}} t_2^{\frac{22-7p}{40(p-1)}}, \\ &\hspace{15em} \nu_a < \nu_m < \nu_c \\ \nu_a &= 9.3 \times 10^{11} \text{ Hz} \hat{z}^{-\frac{3p+10}{4(p+4)}} \frac{g^{VI}(p)}{g^{VI}(1.8)} E_{52}^{\frac{p+14}{8(p+4)}} \Delta_{0,13}^{-\frac{p+14}{8(p+4)}} n_{0,0}^{\frac{18-p}{8(p+4)}} \zeta_0^{\frac{2-p}{p+4}} \epsilon_{e,-1}^{\frac{2}{p+4}} \epsilon_{B,-2}^{\frac{2}{p+4}} t_2^{-\frac{p+6}{4(p+4)}}, \\ &\hspace{15em} \nu_m < \nu_a < \nu_c \end{aligned}$$

$$\nu_a = 8.5 \times 10^8 \text{ Hz } \hat{z}^{-6/5} \frac{g^{VII}(p)}{g^{VII}(1.8)} E_{52}^{7/10} \Delta_{0,13}^{-7/10} n_{0,0}^{11/10} \epsilon_{B,-2}^{6/5} t_2^{1/5}, \nu_a < \nu_c < \nu_m \quad (4.37)$$

For the wind model and $p > 2$, one has

$$\begin{aligned} \nu_m &= 5.8 \times 10^{15} \text{ Hz } \frac{G(p)}{G(2.3)} E_{52}^{1/2} \Delta_{0,13}^{-1/2} \epsilon_{e,-1}^2 \epsilon_{B,-2}^{1/2} t_2^{-1}, \\ \nu_c &= 1.2 \times 10^{14} \text{ Hz } \hat{z}^{-2} E_{52}^{1/2} \Delta_{0,13}^{-1/2} A_{*,-1}^{-2} \epsilon_{B,-2}^{-3/2} t_2 \\ F_{\nu,\max} &= 5.0 \times 10^4 \text{ } \mu\text{Jy } \hat{z} E_{52}^{1/2} \Delta_{0,13}^{-1/2} A_{*,-1}^{1/2} D_{28}^{-2}, \\ \nu_a &= 5.1 \times 10^{11} \text{ Hz } \frac{g^{VIII}(p)}{g^{VIII}(2.3)} E_{52}^{-2/5} \Delta_{0,13}^{2/5} A_{*,-1}^{6/5} \epsilon_{e,-1}^{-1} \epsilon_{B,-2}^{1/5} t_2^{-1}, \quad \nu_a < \nu_m < \nu_c \\ \nu_a &= 4.2 \times 10^{13} \text{ Hz } \frac{g^{IX}(p)}{g^{IX}(2.3)} E_{52}^{\frac{p-2}{2(p+4)}} \Delta_{0,13}^{\frac{2-p}{2(p+4)}} A_{*,-1}^{\frac{4}{p+4}} \epsilon_{e,-1}^{\frac{2(p-1)}{p+4}} \epsilon_{B,-2}^{\frac{p+2}{2(p+4)}} t_2^{-1}, \quad \nu_m < \nu_a < \nu_c \\ \nu_a &= 3.6 \times 10^{12} \text{ Hz } \hat{z} \frac{g^X(p)}{g^X(2.3)} E_{52}^{-2/5} \Delta_{0,13}^{2/5} A_{*,-1}^{11/5} \epsilon_{B,-2}^{6/5} t_2^{-2}, \quad \nu_a < \nu_c < \nu_m \end{aligned} \quad (4.38)$$

For $1 < p < 2$, one has (ν_c and $F_{\nu,\max}$ remain the same)

$$\begin{aligned} \nu_m &= 5.6 \times 10^{13} \text{ Hz } \hat{z}^{\frac{2-p}{p-1}} \frac{g^{XI}(p)}{g^{XI}(1.8)} E_{52}^{\frac{p}{4(p-1)}} A_{*,-1}^{\frac{2-p}{4(p-1)}} \Delta_{0,13}^{\frac{p}{4(1-p)}} \zeta_0^{\frac{2-p}{p-1}} \epsilon_{e,-1}^{\frac{2}{p-1}} \epsilon_{B,-2}^{\frac{1}{2(p-1)}} t_2^{\frac{1}{1-p}}, \\ \nu_a &= 4.3 \times 10^{12} \text{ Hz } \hat{z}^{\frac{p-2}{2(p-1)}} \frac{g^{XII}(p)}{g^{XII}(1.8)} E_{52}^{\frac{6-11p}{40(p-1)}} \Delta_{0,13}^{\frac{11-6p}{40(p-1)}} A_{*,-1}^{\frac{58-53p}{40(1-p)}} \zeta_0^{\frac{p-2}{2(p-1)}} \epsilon_{e,-1}^{\frac{1}{1-p}} \epsilon_{B,-2}^{\frac{14-9p}{20(1-p)}} t_2^{\frac{4-3p}{2(p-1)}}, \\ \nu_a &< \nu_m < \nu_c \\ \nu_a &= 1.3 \times 10^{13} \text{ Hz } \hat{z}^{\frac{2-p}{p+4}} \frac{g^{XIII}(p)}{g^{XIII}(1.8)} E_{52}^{\frac{p-2}{4(p+4)}} \Delta_{0,13}^{\frac{2-p}{4(p+4)}} A_{*,-1}^{\frac{18-p}{4(p+4)}} \zeta_0^{\frac{2-p}{p+4}} \epsilon_{e,-1}^{\frac{2}{p+4}} \epsilon_{B,-2}^{\frac{2}{p+4}} t_2^{-\frac{6}{p+4}}, \\ \nu_m &< \nu_a < \nu_c \\ \nu_a &= 3.0 \times 10^{12} \text{ Hz } \hat{z} \frac{g^{XIV}(p)}{g^{XIV}(1.8)} E_{52}^{-2/5} \Delta_{0,13}^{2/5} A_{*,-1}^{11/5} \epsilon_{B,-2}^{6/5} t_2^{-2}, \nu_a < \nu_c < \nu_m \end{aligned} \quad (4.39)$$

The α and β values and their closure relations for the thick shell forward shock models are presented in Tables 11 and 12.

		$p > 2$		$1 < p < 2$	
	β	α	$\alpha(\beta)$	α	$\alpha(\beta)$
ISM	slow cooling				
$\nu < \nu_a$	-2	-1	$\alpha = \frac{\beta}{2}$	$\frac{11p-14}{8(1-p)}$	--
$\nu_a < \nu < \nu_m$	$-\frac{1}{3}$	$-\frac{4}{3}$	$\alpha = 4\beta$	$\frac{13p-10}{12(1-p)}$	--
$\nu_m < \nu < \nu_c$	$\frac{p-1}{2}$	$\frac{p-3}{2}$	$\alpha = \beta - 1$	$\frac{p-6}{8}$	$\alpha = \frac{2\beta-5}{8}$
$\nu > \nu_c$	$\frac{p}{2}$	$\frac{p-2}{2}$	$\alpha = \beta - 1$	$\frac{p-2}{8}$	$\alpha = \frac{\beta-1}{4}$
ISM	fast cooling				
$\nu < \nu_a$	-2	-1	$\alpha = \frac{\beta}{2}$	-1	$\alpha = \frac{\beta}{2}$
$\nu_a < \nu < \nu_c$	$-\frac{1}{3}$	$-\frac{4}{3}$	$\alpha = 4\beta$	$-\frac{4}{3}$	$\alpha = 4\beta$
$\nu_c < \nu < \nu_m$	$\frac{1}{2}$	$-\frac{1}{2}$	$\alpha = -\beta$	$-\frac{1}{2}$	$\alpha = -\beta$
$\nu > \nu_m$	$\frac{p}{2}$	$\frac{p-2}{2}$	$\alpha = \beta - 1$	0	--
Wind	slow cooling				
$\nu < \nu_a$	-2	-2	$\alpha = \beta$	$\frac{5p-6}{2(1-p)}$	--
$\nu_a < \nu < \nu_m$	$-\frac{1}{3}$	$-\frac{1}{3}$	$\alpha = \beta$	$-\frac{1}{3(p-1)}$	--
$\nu_m < \nu < \nu_c$	$\frac{p-1}{2}$	$\frac{p-1}{2}$	$\alpha = \beta$	$\frac{1}{2}$	--
$\nu > \nu_c$	$\frac{p}{2}$	$\frac{p-2}{2}$	$\alpha = \beta - 1$	0	--
Wind	fast cooling				
$\nu < \nu_a$	-2	-3	$\alpha = \frac{3\beta}{2}$	-3	$\alpha = \frac{3\beta}{2}$
$\nu_a < \nu < \nu_c$	$-\frac{1}{3}$	$\frac{1}{3}$	$\alpha = -\beta$	$\frac{1}{3}$	$\alpha = -\beta$
$\nu_c < \nu < \nu_m$	$\frac{1}{2}$	$-\frac{1}{2}$	$\alpha = -\beta$	$-\frac{1}{2}$	$\alpha = -\beta$
$\nu > \nu_m$	$\frac{p}{2}$	$\frac{p-2}{2}$	$\alpha = \beta - 1$	0	--

Table 11 The temporal decay index α and spectral index β of the thick shell forward shock model in the $\nu_a < \min(\nu_m, \nu_c)$ spectral regime.

For this regime (thick-shell forward shock model during shock crossing), for $p > 2$, one has $\nu_m \propto t^{-1}$ (t^{-1}), $\nu_c \propto t^{-1}$ (t^1), $F_{\nu, \max} \propto t^0$ (t^0) for the ISM (wind) models, respectively. For $1 < p < 2$, ν_c and $F_{\nu, \max}$ evolutions are the same as $p > 2$ cases, while $\nu_m \propto t^{\frac{p+2}{4(1-p)}}$ ($t^{\frac{1}{1-p}}$) for the ISM (wind) models, respectively.

		$p > 2$		$1 < p < 2$	
	β	α	$\alpha(\beta)$	α	$\alpha(\beta)$
ISM	slow cooling				
$\nu < \nu_a$	-2	-1	$\alpha = \frac{\beta}{2}$	$\frac{11p-14}{8(1-p)}$	--
$\nu_a < \nu < \nu_m$	$-\frac{1}{3}$	$-\frac{3}{2}$	$\alpha = \frac{9\beta}{2}$	$-\frac{3}{2}$	$\alpha = \frac{9\beta}{2}$
$\nu_m < \nu < \nu_c$	$\frac{p-1}{2}$	$\frac{p-3}{2}$	$\alpha = \beta - 1$	$\frac{p-6}{8}$	$\alpha = \frac{2\beta-5}{8}$
$\nu > \nu_c$	$\frac{p}{2}$	$\frac{p-2}{2}$	$\alpha = \beta - 1$	$\frac{p-2}{8}$	$\alpha = \frac{\beta-1}{4}$
Wind	slow cooling				
$\nu < \nu_a$	-2	-2	$\alpha = \beta$	$\frac{5p-6}{2(1-p)}$	--
$\nu_a < \nu < \nu_m$	$-\frac{1}{3}$	$-\frac{5}{2}$	$\alpha = \frac{15\beta}{2}$	$-\frac{5}{2}$	$\alpha = \frac{15\beta}{2}$
$\nu_m < \nu < \nu_c$	$\frac{p-1}{2}$	$\frac{p-1}{2}$	$\alpha = \beta$	$\frac{1}{2}$	--
$\nu > \nu_c$	$\frac{p}{2}$	$\frac{p-2}{2}$	$\alpha = \beta - 1$	0	--

Table 12 The temporal decay index α and spectral index β of the thick shell forward shock model in the $\nu_m < \nu_a < \nu_c$ spectral regime.

Thick Shell Reverse Shock Model

Using the same dynamics in Eq.(4.35), one can characterize the reverse shock emission during the shock crossing phase.

For the ISM model and $p > 2$, the reverse shock emission can be characterized by

$$\begin{aligned}
\nu_m &= 7.6 \times 10^{11} \text{ Hz } \hat{z}^{-1} \frac{G(p)}{G(2.3)} \Gamma_{0,2}^2 n_{0,0}^{1/2} \epsilon_{e,-1}^2 \epsilon_{B,-2}^{1/2}, \\
\nu_c &= 1.2 \times 10^{17} \text{ Hz } E_{52}^{-1/2} \Delta_{0,13}^{1/2} n_{0,0}^{-1} \epsilon_{B,-2}^{-3/2} t_2^{-1} \\
F_{\nu,\max} &= 1.3 \times 10^5 \text{ } \mu\text{Jy } \hat{z}^{1/2} E_{52}^{5/4} \Delta_{0,13}^{-5/4} \Gamma_{0,2}^{-1} n_{0,0}^{1/4} \epsilon_{B,-2}^{1/2} D_{28}^{-2} t_2^{1/2}, \\
\nu_a &= 7.2 \times 10^{12} \text{ Hz } \hat{z}^{-2/5} \frac{g^I(p)}{g^I(2.3)} E_{52}^{3/5} \Gamma_{0,2}^{-8/5} \Delta_{0,13}^{-3/5} n_{0,0}^{1/5} \epsilon_{e,-1}^{-1} \epsilon_{B,-2}^{1/5} t_2^{-3/5}, \nu_a < \nu_m < \nu_c \\
\nu_a &= 2.5 \times 10^{12} \text{ Hz } \hat{z}^{-\frac{p+2}{p+4}} \frac{g^{II}(p)}{g^{II}(2.3)} E_{52}^{\frac{2}{p+4}} \Gamma_{0,2}^{\frac{2(p-2)}{p+4}} \Delta_{0,13}^{-\frac{2}{p+4}} n_{0,0}^{\frac{p+2}{2(p+4)}} \epsilon_{e,-1}^{\frac{2(p-1)}{p+4}} \epsilon_{B,-2}^{\frac{p+2}{2(p+4)}} t_2^{-\frac{2}{p+4}}, \\
&\nu_m < \nu_a < \nu_c \\
\nu_a &= 1.8 \times 10^{10} \text{ Hz } \hat{z}^{-9/10} \frac{g^{III}(p)}{g^{III}(2.3)} E_{52}^{17/20} \Gamma_{0,2}^{-3/5} \Delta_{0,13}^{-17/20} n_{0,0}^{19/20} \epsilon_{B,-2}^{6/5} t_2^{-1/10}, \\
&\nu_a < \nu_c < \nu_m
\end{aligned} \tag{4.40}$$

For $1 < p < 2$, one has (ν_c and $F_{\nu,\max}$ remain the same)

$$\begin{aligned}
\nu_m &= 6.1 \times 10^8 \text{ Hz } \hat{z}^{\frac{2-3p}{4(p-1)}} \frac{g^{IV}(p)}{g^{IV}(1.8)} E_{52}^{\frac{p-2}{8(p-1)}} n_{0,0}^{\frac{6-p}{8(p-1)}} \Gamma_{0,2}^{\frac{2}{p-1}} \Delta_{0,13}^{\frac{p-2}{8(1-p)}} \zeta_0^{\frac{2-p}{p-1}} \epsilon_{e,-1}^{\frac{2}{p-1}} \epsilon_{B,-2}^{\frac{1}{2(p-1)}} t_2^{\frac{2-p}{4(p-1)}}, \\
\nu_a &= 2.1 \times 10^{14} \text{ Hz } \hat{z}^{\frac{26-21p}{40(p-1)}} \frac{g^V(p)}{g^V(1.8)} E_{52}^{\frac{38-43p}{80(1-p)}} \Gamma_{0,2}^{\frac{3p+2}{5(1-p)}} \Delta_{0,13}^{\frac{38-43p}{80(p-1)}} n_{0,0}^{\frac{66-41p}{80(1-p)}} \zeta_0^{\frac{p-2}{2(p-1)}} \epsilon_{e,-1}^{\frac{1}{1-p}}, \\
&\epsilon_{B,-2}^{\frac{14-9p}{20(1-p)}} t_2^{\frac{14-19p}{40(p-1)}}, \quad \nu_a < \nu_m < \nu_c \\
\nu_a &= 9.3 \times 10^{11} \text{ Hz } \hat{z}^{-\frac{3p+10}{4(p+4)}} \frac{g^{VI}(p)}{g^{VI}(1.8)} E_{52}^{\frac{p+14}{8(p+4)}} \Delta_{0,13}^{-\frac{p+14}{8(p+4)} - \frac{p-18}{8(p+4)}} \zeta_0^{\frac{2-p}{p+4}} \epsilon_{e,-1}^{\frac{2}{p+4}} \epsilon_{B,-2}^{\frac{2}{p+4}} t_2^{-\frac{p+6}{4(p+4)}}, \\
&\nu_m < \nu_a < \nu_c \\
\nu_a &= 1.5 \times 10^{10} \text{ Hz } \hat{z}^{-9/10} \frac{g^{VII}(p)}{g^{VII}(1.8)} E_{52}^{17/20} \Gamma_{0,2}^{-3/5} \Delta_{0,13}^{-17/20} n_{0,0}^{19/20} \epsilon_{B,-2}^{6/5} t_2^{-1/10}, \\
&\nu_a < \nu_c < \nu_m
\end{aligned} \tag{4.41}$$

For the wind model and $p > 2$, one has

$$\begin{aligned}
\nu_m &= 3.3 \times 10^{13} \text{ Hz} \frac{G(p)}{G(2.3)} E_{52}^{-1/2} A_{*, -1} \Gamma_{0,2}^2 \Delta_{0,13}^{1/2} \epsilon_{e,-1}^2 \epsilon_{B,-2}^{1/2} t_2^{-1}, \\
\nu_c &= 1.2 \times 10^{14} \text{ Hz} \hat{z}^{-2} E_{52}^{1/2} \Delta_{0,13}^{-1/2} A_{*, -1}^{-2} \epsilon_{B,-2}^{-3/2} t_2 \\
F_{\nu, \max} &= 6.7 \times 10^5 \mu\text{Jy} \hat{z} E_{52} A_{*, -1}^{1/2} \Gamma_{0,2}^{-1} \Delta_{0,13}^{-1} \epsilon_{B,-2}^{1/2} D_{28}^{-2}, \\
\nu_a &= 3.2 \times 10^{13} \text{ Hz} \frac{g^{VIII}(p)}{g^{VIII}(2.3)} E_{52}^{2/5} \Gamma_{0,2}^{-8/5} A_{*, -1}^{2/5} \Delta_{0,13}^{-2/5} \epsilon_{e,-1}^{1/5} \epsilon_{B,-2}^{-1} t_2^{-1}, \quad \nu_a < \nu_m < \nu_c \\
\nu_a &= 3.3 \times 10^{13} \text{ Hz} \frac{g^{IX}(p)}{g^{IX}(2.3)} E_{52}^{\frac{2-p}{2(p+4)}} \Gamma_{0,2}^{\frac{2(p-2)}{p+4}} \Delta_{0,13}^{\frac{p-2}{2(p+4)}} A_{*, -1}^{\frac{p+2}{p+4}} \epsilon_{e,-1}^{\frac{2(p-1)}{p+4}} \epsilon_{B,-2}^{\frac{p+2}{2(p+4)}} t_2^{-1}, \nu_m < \nu_a < \nu_c \\
\nu_a &= 1.7 \times 10^{13} \text{ Hz} \hat{z} \frac{g^X(p)}{g^X(2.3)} E_{52}^{-1/10} \Gamma_{0,2}^{-3/5} \Delta_{0,13}^{1/10} A_{*, -1}^{19/10} \epsilon_{B,-2}^{6/5} t_2^{-2}, \quad \nu_a < \nu_c < \nu_m
\end{aligned} \tag{4.42}$$

For $1 < p < 2$, one has (ν_c and $F_{\nu, \max}$ remain the same)

$$\begin{aligned}
\nu_m &= 8.7 \times 10^{10} \text{ Hz} \hat{z}^{\frac{2-p}{p-1}} \frac{g^{XI}(p)}{g^{XI}(1.8)} E_{52}^{\frac{p-4}{4(p-1)}} A_{*, -1}^{\frac{6-p}{4(p-1)}} \Gamma_{0,2}^{\frac{2}{p-1}} \Delta_{0,13}^{\frac{p-4}{4(1-p)}} \zeta_0^{\frac{2-p}{p-1}} \epsilon_{e,-1}^{\frac{2}{p-1}} \epsilon_{B,-2}^{\frac{1}{2(p-1)}} t_2^{\frac{1}{1-p}}, \\
\nu_a &= 5.2 \times 10^{14} \text{ Hz} \hat{z}^{\frac{p-2}{2(p-1)}} \frac{g^{XII}(p)}{g^{XII}(1.8)} E_{52}^{\frac{p+14}{40(p-1)}} \Gamma_{0,2}^{\frac{3p+2}{5(1-p)}} \Delta_{0,13}^{\frac{p+14}{40(p-1)}} A_{*, -1}^{\frac{66-41p}{40(1-p)}} \zeta_0^{\frac{p-2}{2(p-1)}} \epsilon_{e,-1}^{\frac{1}{1-p}} \\
&\quad \epsilon_{B,-2}^{\frac{14-9p}{20(1-p)}} t_2^{\frac{4-3p}{2(p-1)}}, \quad \nu_a < \nu_m < \nu_c \\
\nu_a &= 1.3 \times 10^{13} \text{ Hz} \hat{z}^{\frac{2-p}{p+4}} \frac{g^{XIII}(p)}{g^{XIII}(1.8)} E_{52}^{\frac{p-2}{4(p+4)}} \Delta_{0,13}^{\frac{2-p}{4(p+4)}} A_{*, -1}^{\frac{18-p}{4(p+4)}} \zeta_1^{\frac{2-p}{p+4}} \epsilon_{e,-1}^{\frac{2}{p+4}} \epsilon_{B,-2}^{\frac{2}{p+4}} t_2^{-\frac{6}{p+4}}, \\
&\quad \nu_m < \nu_a < \nu_c \\
\nu_a &= 1.4 \times 10^{13} \text{ Hz} \hat{z} \frac{g^{XIV}(p)}{g^{XIV}(1.8)} E_{52}^{-1/10} \Gamma_{0,2}^{-3/5} \Delta_{0,13}^{1/10} A_{*, -1}^{19/10} \epsilon_{B,-2}^{6/5} t_2^{-2}, \nu_a < \nu_c < \nu_m
\end{aligned} \tag{4.43}$$

After the reverse shock crosses the shell, the shocked shell can be roughly described by the BM solution (Kobayashi and Sari, 2000a; Wu et al., 2003; Kobayashi and Zhang, 2003a; Kobayashi et al., 2004),

$$\gamma_3 \propto t^{(2k-7)/4(4-k)}, e_3 \propto t^{(2k-13)/3(4-k)}, r \propto t^{1/(8-2k)}, N_{e,3} \propto t^0, \tag{4.44}$$

For the ISM case, one has

$$\gamma = \gamma_{3,\times} \left(\frac{t}{T} \right)^{-\frac{7}{16}}, \quad R = R_{\times} \left(\frac{t}{T} \right)^{\frac{1}{8}}$$

where $\gamma_{3,\times}$ and R_{\times} are the Lorentz factor and radius of Region 3 at the shock crossing time.

For $p > 2$, one has

$$\begin{aligned} \nu_m &= 4.8 \times 10^{12} \text{ Hz } \hat{z}^{25/48} \frac{G(p)}{G(2.3)} \Gamma_{0,2}^2 \Delta_{0,13}^{73/48} n_{0,0}^{1/2} \epsilon_{e,-1}^{1/2} \epsilon_{B,-2}^{-73/48}, \\ \nu_{\text{cut}} &= 2.3 \times 10^{17} \text{ Hz } \hat{z}^{25/48} E_{52}^{-1/2} \Delta_{0,13}^{49/48} n_{0,0}^{-1} \epsilon_{B,-2}^{-3/2} t_2^{-73/48} \\ F_{\nu,\text{max}} &= 7.9 \times 10^5 \text{ } \mu\text{Jy } \hat{z}^{95/48} E_{52}^{5/4} \Gamma_{0,2}^{-1} \Delta_{0,13}^{11/48} n_{0,0}^{1/4} \epsilon_{B,-2}^{1/2} D_{28}^{-2} t_2^{-47/48}, \\ \nu_a &= 6.6 \times 10^{12} \text{ Hz } \hat{z}^{-7/15} \frac{g^{XV}(p)}{g^{XV}(2.3)} E_{52}^{3/5} \Gamma_{0,2}^{-8/5} \Delta_{0,13}^{-2/3} n_{0,0}^{1/5} \epsilon_{e,-1}^{-1} \epsilon_{B,-2}^{1/5} t_2^{-8/15}, \\ &\quad \nu_a < \nu_m < \nu_{\text{cut}} \\ \nu_a &= 5.7 \times 10^{12} \text{ Hz } \hat{z}^{\frac{25p-58}{48(p+4)}} \frac{g^{XVI}(p)}{g^{XVI}(2.3)} E_{52}^{\frac{2}{p+4}} \Gamma_{0,2}^{\frac{2(p-2)}{p+4}} \Delta_{0,13}^{\frac{73p-58}{48(p+4)}} n_{0,0}^{\frac{p+2}{2(p+4)}} \epsilon_{e,-1}^{\frac{2(p-1)}{p+4}} \epsilon_{B,-2}^{\frac{p+2}{2(p+4)}} t_2^{-\frac{73p+134}{48(p+4)}}, \\ &\quad \nu_m < \nu_a < \nu_{\text{cut}} \end{aligned} \tag{4.45}$$

For $1 < p < 2$, one has (ν_c and $F_{\nu,\text{max}}$ remain the same)

$$\begin{aligned} \nu_m &= 4.2 \times 10^{12} \text{ Hz } \hat{z}^{25/48} \frac{g^{XVII}(p)}{g^{XVII}(1.8)} E_{52}^{\frac{p-2}{8(p-1)}} \Gamma_{0,2}^{\frac{2}{p-1}} n_{0,0}^{\frac{6-p}{8(p-1)}} \Delta_{0,13}^{\frac{55p-37}{48(p-1)}} \zeta_0^{\frac{2-p}{p-1}} \epsilon_{e,-1}^{\frac{2}{p-1}} \epsilon_{B,-2}^{\frac{1}{2(p-1)}} t_2^{-73/48}, \\ \nu_a &= 5.8 \times 10^{12} \text{ Hz } \hat{z}^{-7/15} \frac{g^{XVIII}(p)}{g^{XVIII}(1.8)} E_{52}^{\frac{43p-38}{80(p-1)}} \Gamma_{0,2}^{\frac{3p+2}{5(1-p)}} \Delta_{0,13}^{\frac{23p-14}{48(1-p)}} n_{0,0}^{\frac{66-41p}{80(1-p)}} \zeta_0^{\frac{p-2}{2(p-1)}} \epsilon_{e,-1}^{\frac{1}{1-p}} \\ &\quad \epsilon_{B,-2}^{\frac{14-9p}{20(1-p)}} t_2^{-8/15}, \quad \nu_a < \nu_m < \nu_{\text{cut}} \\ \nu_a &= 5.1 \times 10^{12} \text{ Hz } \hat{z}^{\frac{25p-58}{48(p+4)}} \frac{g^{XIX}(p)}{g^{XIX}(1.8)} E_{52}^{\frac{p+14}{8(p+4)}} \Delta_{0,13}^{\frac{11(5p-2)}{48(p+4)}} n_{0,0}^{\frac{18-p}{8(p+4)}} \zeta_0^{\frac{2-p}{p+4}} \epsilon_{e,-1}^{\frac{2}{p+4}} \epsilon_{B,-2}^{\frac{2}{p+4}} t_2^{-\frac{73p+134}{48(p+4)}}, \\ &\quad \nu_m < \nu_a < \nu_{\text{cut}} \end{aligned} \tag{4.46}$$

For the wind model and $p > 2$, one has

$$\begin{aligned}
\nu_m &= 9.4 \times 10^{13} \text{ Hz } \hat{z}^{7/8} \frac{G(p)}{G(2.3)} E_{52}^{-1/2} A_{*, -1} \Gamma_{0,2}^2 \Delta_{0,13}^{11/8} \epsilon_{e,-1}^2 \epsilon_{B,-2}^{1/2} t_2^{-15/8}, \\
\nu_{\text{cut}} &= 3.7 \times 10^{15} \text{ Hz } \hat{z}^{7/8} E_{52}^{1/2} \Delta_{0,13}^{19/8} A_{*, -1}^{-2} \epsilon_{B,-2}^{-3/2} t_2^{-15/8} \\
F_{\nu, \text{max}} &= 2.6 \times 10^6 \text{ } \mu\text{Jy } \hat{z}^{17/8} E_{52} A_{*, -1}^{1/2} \Gamma_{0,2}^{-1} \Delta_{0,13}^{1/8} \epsilon_{B,-2}^{1/2} D_{28}^{-2} t_2^{-9/8}, \\
\nu_a &= 1.9 \times 10^{13} \text{ Hz } \hat{z}^{-2/5} \frac{g^{XX}(p)}{g^{XX}(2.3)} E_{52}^{2/5} \Gamma_{0,2}^{-8/5} A_{*, -1}^{2/5} \Delta_{0,13}^{-4/5} \epsilon_{e,-1}^{1/5} \epsilon_{B,-2} t_2^{-3/5}, \\
&\quad \nu_a < \nu_m < \nu_{\text{cut}} \\
\nu_a &= 4.1 \times 10^{13} \text{ Hz } \hat{z}^{\frac{7p-6}{8(p+4)}} \frac{g^{XXI}(p)}{g^{XXI}(2.3)} E_{52}^{\frac{2-p}{2(p+4)}} \Gamma_{0,2}^{\frac{2(p-2)}{p+4}} \Delta_{0,13}^{\frac{11p-14}{8(p+4)}} A_{*, -1}^{\frac{p+2}{p+4}} \epsilon_{e,-1}^{\frac{2(p-1)}{p+4}} \epsilon_{B,-2}^{\frac{p+2}{2(p+4)}} t_2^{-\frac{15p+26}{8(p+4)}}, \\
&\quad \nu_m < \nu_a < \nu_{\text{cut}}
\end{aligned} \tag{4.47}$$

For $1 < p < 2$, one has (ν_c and $F_{\nu, \text{max}}$ remain the same)

$$\begin{aligned}
\nu_m &= 1.9 \times 10^{14} \text{ Hz } \hat{z}^{7/8} \frac{g^{XXII}(p)}{g^{XXII}(1.8)} E_{52}^{\frac{p-4}{4(p-1)}} \Gamma_{0,2}^{\frac{2}{p-1}} A_{*, -1}^{\frac{6-p}{4(p-1)}} \Delta_{0,13}^{\frac{13p-15}{8(p-1)}} \zeta_0^{\frac{2-p}{p-1}} \epsilon_{e,-1}^{\frac{2}{p-1}} \epsilon_{B,-2}^{\frac{1}{2(p-1)}} t_2^{-15/8}, \\
\nu_a &= 1.2 \times 10^{13} \text{ Hz } \hat{z}^{-2/5} \frac{g^{XXIII}(p)}{g^{XXIII}(1.8)} E_{52}^{\frac{p+14}{40(p-1)}} \Gamma_{0,2}^{\frac{3p+2}{5(1-p)}} A_{*, -1}^{\frac{66-41p}{40(1-p)}} \Delta_{0,13}^{\frac{42-37p}{40(p-1)}} \zeta_0^{\frac{2-p}{p-1}} \epsilon_{e,-1}^{\frac{2}{p-1}} \\
&\quad \epsilon_{B,-2}^{\frac{1}{2(p-1)}} t_2^{-3/5}, \quad \nu_a < \nu_m < \nu_{\text{cut}} \\
\nu_a &= 3.8 \times 10^{13} \text{ Hz } \hat{z}^{\frac{7p-6}{8(p+4)}} \frac{g^{XXIV}(p)}{g^{XXIV}(1.8)} E_{52}^{\frac{p-2}{4(p+4)}} \Delta_{0,13}^{\frac{13p-18}{8(p+4)}} A_{*, -1}^{\frac{18-p}{4(p+4)}} \zeta_0^{\frac{2-p}{p+4}} \epsilon_{e,-1}^{\frac{2}{p+4}} \epsilon_{B,-2}^{\frac{2}{p+4}} t_2^{-\frac{15p+26}{8(p+4)}}, \\
&\quad \nu_m < \nu_a < \nu_{\text{cut}}
\end{aligned} \tag{4.48}$$

The α and β values and their closure relations for the thick shell reverse shock models are presented in Tables 13 and 14 (for pre-shock-crossing), and Tables 15 and 16 (for post-shock-crossing).

For this regime (thick-shell reverse shock model during shock crossing), for $p > 2$, one has $\nu_m \propto t^0$ (t^{-1}), $\nu_c \propto t^{-1}$ (t^1), $F_{\nu, \text{max}} \propto t^{1/2}$ (t^0) for the ISM (wind) models, respectively. For $1 < p < 2$, ν_c and $F_{\nu, \text{max}}$ evolutions are the same as $p > 2$ cases,

		$p > 2$		$1 < p < 2$	
	β	α	$\alpha(\beta)$	α	$\alpha(\beta)$
ISM	slow cooling				
$\nu < \nu_a$	-2	$-\frac{3}{2}$	$\alpha = \frac{3\beta}{4}$	$\frac{11p-10}{8(1-p)}$	--
$\nu_a < \nu < \nu_m$	$-\frac{1}{3}$	$-\frac{1}{2}$	$\alpha = \frac{3\beta}{2}$	$\frac{7p-8}{12(1-p)}$	--
$\nu_m < \nu < \nu_c$	$\frac{p-1}{2}$	$-\frac{1}{2}$	--	$\frac{p-6}{8}$	$\alpha = \frac{2\beta-5}{8}$
$\nu > \nu_c$	$\frac{p}{2}$	0	--	$\frac{p-2}{8}$	$\frac{\beta-1}{4}$
ISM	fast cooling				
$\nu < \nu_a$	-2	-1	$\alpha = \frac{\beta}{2}$	-1	$\alpha = \frac{\beta}{2}$
$\nu_a < \nu < \nu_c$	$-\frac{1}{3}$	$-\frac{5}{6}$	$\alpha = \frac{5\beta}{2}$	$-\frac{5}{6}$	$\alpha = \frac{5\beta}{2}$
$\nu_c < \nu < \nu_m$	$\frac{1}{2}$	0	--	0	--
$\nu > \nu_m$	$\frac{p}{2}$	0	--	$\frac{p-2}{8}$	$\alpha = \frac{\beta-1}{4}$
Wind	slow cooling				
$\nu < \nu_a$	-2	-2	$\alpha = \beta$	$\frac{5p-6}{2(1-p)}$	--
$\nu_a < \nu < \nu_m$	$-\frac{1}{3}$	$-\frac{1}{3}$	$\alpha = \beta$	$-\frac{1}{3(p-1)}$	--
$\nu_m < \nu < \nu_c$	$\frac{p-1}{2}$	$\frac{p-1}{2}$	$\alpha = \beta$	$\frac{1}{2}$	--
$\nu > \nu_c$	$\frac{p}{2}$	$\frac{p-2}{2}$	$\alpha = \beta - 1$	0	--
Wind	fast cooling				
$\nu < \nu_a$	-2	-3	$\alpha = \frac{3\beta}{2}$	-3	$\alpha = \frac{3\beta}{2}$
$\nu_a < \nu < \nu_c$	$-\frac{1}{3}$	$\frac{1}{3}$	$\alpha = -\beta$	$\frac{1}{3}$	$\alpha = -\beta$
$\nu_c < \nu < \nu_m$	$\frac{1}{2}$	$-\frac{1}{2}$	$\alpha = -\beta$	$-\frac{1}{2}$	$\alpha = -\beta$
$\nu > \nu_m$	$\frac{p}{2}$	$\frac{p-2}{2}$	$\alpha = \beta - 1$	0	--

Table 13 The temporal decay index α and spectral index β of the thick shell reverse shock model during the shock crossing phase in the $\nu_a < \min(\nu_m, \nu_c)$ spectral regime.

while $\nu_m \propto t^{\frac{2-p}{4(p-1)}} (t^{\frac{1}{1-p}})$ for the ISM (wind) models, respectively.

After shock crossing, $\nu_m \propto \nu_{\text{cut}} \propto t^{-73/48} (t^{-15/8})$, $F_{\nu, \text{max}} \propto t^{-47/48} (t^{-9/8})$ for the ISM (wind) models, respectively.

Notice that in the above treatment, a relativistic reverse shock has been assumed. In reality, there is a brief epoch before the reverse shock becomes relativistic. There should be an additional dynamical change at R_N (the transition radius from Newtonian to relativistic reverse shock), which is much smaller than R_\times (Sari and Piran, 1995). The light curves may show an additional break at this epoch, before which the thin shell scalings apply.

Phase 2: relativistic, pre-jet-break, self-similar deceleration phase

After reverse shock crosses the shell, the blastwave would quickly adjust itself to a self-similar deceleration phase (Blandford and McKee, 1976)⁴. Early on, the

⁴This is the case for the idealized situation. In reality, there might be irregularities in the system (e.g. ambient density fluctuations or non-power-law energy injection). The blastwave is no

	β	$p > 2$ α	$\alpha(\beta)$	$1 < p < 2$ α	$\alpha(\beta)$
ISM	slow cooling				
$\nu < \nu_m$	-2	$-\frac{3}{2}$	$\alpha = \frac{3\beta}{4}$	$\frac{11p-10}{8(1-p)}$	--
$\nu_m < \nu < \nu_a$	$-\frac{5}{2}$	$-\frac{3}{2}$	$\alpha = \frac{3\beta}{5}$	$-\frac{3}{2}$	$\alpha = \frac{3\beta}{5}$
$\nu_a < \nu < \nu_c$	$\frac{p-1}{2}$	$-\frac{1}{2}$	--	$\frac{p-6}{8}$	$\alpha = \frac{2\beta-5}{8}$
$\nu > \nu_c$	$\frac{p}{2}$	0	--	$\frac{p-2}{8}$	$\frac{\beta-1}{4}$
Wind	slow cooling				
$\nu < \nu_m$	-2	-2	$\alpha = \beta$	$\frac{6-5p}{2(p-1)}$	--
$\nu_m < \nu < \nu_a$	$-\frac{5}{2}$	$-\frac{5}{2}$	$\alpha = \beta$	$-\frac{5}{2}$	$\alpha = \beta$
$\nu_a < \nu < \nu_c$	$\frac{p-1}{2}$	$\frac{p-1}{2}$	$\alpha = \beta$	$\frac{1}{2}$	--
$\nu > \nu_c$	$\frac{p}{2}$	$\frac{p-2}{2}$	$\alpha = \beta - 1$	0	--

Table 14 The temporal decay index α and spectral index β for the thick shell reverse shock model during the reverse shock crossing phase in the $\nu_m < \nu_a < \nu_c$ spectral regime.

	β	$p > 2$ α	$\alpha(\beta)$	$1 < p < 2$ α	$\alpha(\beta)$
ISM	slow cooling				
$\nu < \nu_a$	-2	$-\frac{5}{12}$	$\alpha = \frac{5\beta}{24}$	$-\frac{5}{12}$	$\alpha = \frac{5\beta}{24}$
$\nu_a < \nu < \nu_m$	$-\frac{1}{3}$	$\frac{17}{36}$	$-\alpha = \frac{17\beta}{12}$	$\frac{17}{36}$	$-\alpha = \frac{17\beta}{12}$
$\nu_m < \nu < \nu_{cut}$	$\frac{p-1}{2}$	$\frac{73p+21}{96}$	$\alpha = \frac{73\beta+47}{48}$	$\frac{73p+21}{96}$	$\alpha = \frac{73\beta+47}{48}$
Wind	slow cooling				
$\nu < \nu_a$	-2	$-\frac{1}{2}$	$\alpha = \frac{\beta}{4}$	$-\frac{1}{2}$	$\alpha = \frac{\beta}{4}$
$\nu_a < \nu < \nu_m$	$-\frac{1}{3}$	$\frac{1}{2}$	$\alpha = -\frac{3\beta}{2}$	$\frac{1}{2}$	$\alpha = -\frac{3\beta}{2}$
$\nu_m < \nu < \nu_{cut}$	$\frac{p-1}{2}$	$\frac{3(5p+1)}{16}$	$\alpha = \frac{3(5\beta+3)}{8}$	$\frac{3(5p+1)}{16}$	$\alpha = \frac{3(5\beta+3)}{8}$

Table 15 The temporal decay index α and spectral index β of the thick shell reverse shock model in the post-shock crossing phase in the $\nu_a < \min(\nu_m, \nu_{cut})$ spectral regime.

	β	$p > 2$ α	$\alpha(\beta)$	$1 < p < 2$ α	$\alpha(\beta)$
ISM	slow cooling				
$\nu < \nu_m$	-2	$-\frac{5}{12}$	$\alpha = \frac{5\beta}{24}$	$-\frac{5}{12}$	$\alpha = \frac{5\beta}{24}$
$\nu_m < \nu < \nu_a$	$-\frac{5}{2}$	$-\frac{113}{96}$	$\alpha = \frac{226\beta}{480}$	$-\frac{113}{96}$	$\alpha = \frac{226\beta}{480}$
$\nu_a < \nu < \nu_{cut}$	$\frac{p-1}{2}$	$\frac{73p+21}{96}$	$\alpha = \frac{73\beta+47}{48}$	$\frac{73p+21}{96}$	$\alpha = \frac{73\beta+47}{48}$
Wind	slow cooling				
$\nu < \nu_m$	-2	$-\frac{1}{2}$	$\alpha = \frac{\beta}{4}$	$-\frac{1}{2}$	$\alpha = \frac{\beta}{4}$
$\nu_m < \nu < \nu_a$	$-\frac{5}{2}$	$-\frac{23}{16}$	$\alpha = \frac{23\beta}{40}$	$-\frac{23}{16}$	$\alpha = \frac{23\beta}{40}$
$\nu_a < \nu < \nu_{cut}$	$\frac{p-1}{2}$	$\frac{3(5p+1)}{16}$	$\alpha = \frac{3(5\beta+3)}{8}$	$\frac{3(5p+1)}{16}$	$\alpha = \frac{3(5\beta+3)}{8}$

Table 16 The temporal decay index α and spectral index β of the thick shell reverse shock model in the post-shock crossing phase in the $\nu_m < \nu_a < \nu_{cut}$ spectral regime.

blastwave is ultra-relativistic with $1/\Gamma \ll \theta_j$. The closure relations in this phase have been reviewed previously (e.g. Zhang and Mészáros, 2004a; Zhang et al., 2006).

Adiabatic deceleration without energy injection

The simplest model invokes a constant energy in the blastwave. This requires that the blastwave is adiabatic (no radiative loss), and that there is no energy injection into the blastwave. The adiabatic approximation usually gives a reasonable description to the blastwave evolution. This is because the radiative loss fraction is at most ϵ_e (for fast cooling), which is constrained to be around 0.1 and lower (Panaitescu and Kumar, 2001, 2002; Yost et al., 2003)⁵.

For an arbitrary k density profile, the dynamics of the blast wave in the constant energy regime can be described as

$$\gamma = \left(\frac{(17 - 4k)E}{4^{5-k}(4 - k)^{3-k}\pi Am_p c^{5-k} t^{3-k}} \right)^{\frac{1}{2(4-k)}}, \quad R = \left(\frac{(17 - 4k)(4 - k)Et}{4\pi Am_p c} \right)^{\frac{1}{4-k}},$$

For the ISM model ($k = 0$) and $p > 2$, one has

$$\begin{aligned} \nu_m &= 4.3 \times 10^{10} \text{ Hz } \hat{z}^{1/2} \frac{G(p)}{G(2.3)} E_{52}^{1/2} \epsilon_{e,-1}^2 \epsilon_{B,-2}^{1/2} t_5^{-3/2}, \\ \nu_c &= 2.9 \times 10^{16} \text{ Hz } \hat{z}^{-1/2} E_{52}^{-1/2} n_{0,0}^{-1} \epsilon_{B,-2}^{-3/2} t_5^{-1/2} \\ F_{\nu,\max} &= 1.1 \times 10^4 \text{ } \mu\text{Jy } \hat{z} E_{52} n_{0,0}^{1/2} \epsilon_{B,-2}^{1/2} D_{28}^{-2}, \\ \nu_a &= 5.7 \times 10^9 \text{ Hz } \hat{z}^{-1} \frac{g^I(p)}{g^I(2.3)} E_{52}^{1/5} n_{0,0}^{3/5} \epsilon_{e,-1}^{-1} \epsilon_{B,-2}^{1/5}, \quad \nu_a < \nu_m < \nu_c \\ \nu_a &= 1.5 \times 10^{10} \text{ Hz } \hat{z}^{\frac{p-6}{2(p+4)}} \frac{g^{II}(p)}{g^{II}(2.3)} E_{52}^{\frac{p+2}{2(p+4)}} n_{0,0}^{\frac{2}{p+4}} \epsilon_{e,-1}^{\frac{2(p-1)}{p+4}} \epsilon_{B,-2}^{\frac{p+2}{2(p+4)}} t_5^{-\frac{3p+2}{2(p+4)}}, \quad \nu_m < \nu_a < \nu_c \\ \nu_a &= 6.9 \times 10^6 \text{ Hz } \hat{z}^{-1/2} \frac{g^{III}(p)}{g^{III}(2.3)} E_{52}^{7/10} n_{0,0}^{11/10} \epsilon_{B,-2}^{6/5} t_5^{-1/2}, \quad \nu_a < \nu_c < \nu_m \end{aligned}$$

longer self-similar. We limit ourselves to the self-similar assumption and derive the scalings in this subsection, and discuss more complicated simulations in the fifth section.

⁵Note that since the blast-wave energy is given again and again to newly heated material, the radiative energy loss may become important after several orders of magnitude of deceleration time (Sari, 1997).

(4.49)

For $1 < p < 2$, one has (ν_c and $F_{\nu, \max}$ remain the same)

$$\begin{aligned}
\nu_m &= 3.6 \times 10^7 \text{ Hz } \hat{z}^{\frac{14-5p}{8(p-1)}} \frac{g^{IV}(p)}{g^{IV}(1.8)} E_{52}^{\frac{p+2}{8(p-1)}} n_{0,0}^{\frac{2-p}{8(p-1)}} \zeta_0^{\frac{2-p}{p-1}} \epsilon_{e,-1}^{\frac{2}{p-1}} \epsilon_{B,-2}^{\frac{1}{2(p-1)}} t_5^{\frac{3p+6}{8(1-p)}}, \\
\nu_a &= 1.6 \times 10^{11} \text{ Hz } \hat{z}^{-\frac{7p+2}{16(p-1)}} \frac{g^V(p)}{g^V(1.8)} E_{52}^{\frac{46-31p}{80(1-p)}} n_{0,0}^{\frac{58-53p}{80(1-p)}} \zeta_0^{\frac{p-2}{2(p-1)}} \epsilon_{e,-1}^{\frac{1}{1-p}} \epsilon_{B,-2}^{\frac{14-9p}{20(1-p)}} t_5^{-\frac{9(p-2)}{16(p-1)}}, \\
\nu_a &< \nu_m < \nu_c \\
\nu_a &= 4.5 \times 10^9 \text{ Hz } \hat{z}^{-\frac{5p+6}{8(p+4)}} \frac{g^{VI}(p)}{g^{VI}(1.8)} E_{52}^{\frac{p+14}{8(p+4)}} n_{0,0}^{\frac{18-p}{8(p+4)}} \zeta_0^{\frac{2-p}{p+4}} \epsilon_e^{\frac{2}{p+4}} \epsilon_B^{\frac{2}{p+4}} t_d^{-\frac{3p+26}{8(p+4)}}, \\
\nu_m &< \nu_a < \nu_c \\
\nu_a &= 5.7 \times 10^6 \text{ Hz } \hat{z}^{-1/2} \frac{g^{VII}(p)}{g^{VII}(1.8)} E_{52}^{7/10} n_{0,0}^{11/10} \epsilon_{B,-2}^{6/5} t_5^{-1/2}, \nu_a < \nu_c < \nu_m
\end{aligned} \tag{4.50}$$

For the wind model ($k = 2$) and $p > 2$, one has

$$\begin{aligned}
\nu_m &= 2.2 \times 10^{10} \text{ Hz } \hat{z}^{1/2} \frac{G(p)}{G(2.3)} E_{52}^{1/2} \epsilon_{e,-1}^2 \epsilon_{B,-2}^{1/2} t_5^{-3/2}, \\
\nu_c &= 1.8 \times 10^{18} \text{ Hz } \hat{z}^{-3/2} E_{52}^{1/2} A_{*, -1}^{-2} \epsilon_{B,-2}^{-3/2} t_5^{1/2} \\
F_{\nu, \max} &= 1.5 \times 10^3 \text{ } \mu\text{Jy } \hat{z}^{3/2} E_{52}^{1/2} A_{*, -1}^{1/2} D_{28}^{-2} t_5^{-1/2}, \\
\nu_a &= 1.0 \times 10^9 \text{ Hz } \hat{z}^{-2/5} \frac{g^{VIII}(p)}{g^{VIII}(2.3)} E_{52}^{-2/5} A_{*, -1}^{6/5} \epsilon_{e,-1}^{-1} \epsilon_{B,-2}^{1/5} t_5^{-3/5}, \quad \nu_a < \nu_m < \nu_c \\
\nu_a &= 4.4 \times 10^9 \text{ Hz } \hat{z}^{\frac{p-2}{2(p+4)}} \frac{g^{IX}(p)}{g^{IX}(2.3)} E_{52}^{\frac{p-2}{2(p+4)}} A_{*, -1}^{\frac{4}{p+4}} \epsilon_{e,-1}^{\frac{2(p-1)}{p+4}} \epsilon_{B,-2}^{\frac{p+2}{2(p+4)}} t_5^{-\frac{3(p+2)}{2(p+4)}}, \nu_m < \nu_a < \nu_c \\
\nu_a &= 1.2 \times 10^5 \text{ Hz } \hat{z}^{3/5} \frac{g^X(p)}{g^X(2.3)} E_{52}^{-2/5} A_{*, -1}^{11/5} \epsilon_{B,-2}^{6/5} t_5^{-8/5}, \quad \nu_a < \nu_c < \nu_m
\end{aligned} \tag{4.51}$$

For $1 < p < 2$, one has (ν_c and $F_{\nu, \max}$ remain the same)

$$\nu_m = 1.5 \times 10^7 \text{ Hz } \hat{z}^{\frac{8-3p}{4(p-1)}} \frac{g^{XI}(p)}{g^{XI}(1.8)} E_{52}^{\frac{p}{4(p-1)}} A_{*, -1}^{\frac{2-p}{4(p-1)}} \zeta_0^{\frac{2-p}{p-1}} \epsilon_{e,-1}^{\frac{2}{p-1}} \epsilon_{B,-2}^{\frac{1}{2(p-1)}} t_5^{\frac{p+4}{4(1-p)}},$$

$$\begin{aligned}
\nu_a &= 3.3 \times 10^{10} \text{ Hz } \hat{z}^{\frac{9p-34}{40(p-1)}} \frac{g^{XII}(p)}{g^{XII}(1.8)} E_{52}^{\frac{6-11p}{40(p-1)}} A_{*, -1}^{\frac{58-53p}{40(1-p)}} \zeta_0^{\frac{p-2}{2(p-1)}} \epsilon_{e, -1}^{\frac{1}{1-p}} \epsilon_{B, -2}^{\frac{14-9p}{20(1-p)}} t_5^{\frac{74-49p}{40(p-1)}}, \\
\nu_a &< \nu_m < \nu_c \\
\nu_a &= 1.3 \times 10^9 \text{ Hz } \hat{z}^{\frac{6-3p}{4(p+4)}} \frac{g^{XIII}(p)}{g^{XIII}(1.8)} E_{52}^{\frac{p-2}{4(p+4)}} A_{*, -1}^{\frac{18-p}{4(p+4)}} \zeta_0^{\frac{2-p}{p+4}} \epsilon_{e, -1}^{\frac{2}{p+4}} \epsilon_{B, -2}^{\frac{2}{p+4}} t_5^{-\frac{22+p}{4(p+4)}}, \\
\nu_m &< \nu_a < \nu_c \\
\nu_a &= 9.5 \times 10^4 \text{ Hz } \hat{z}^{3/5} \frac{g^{XIV}(p)}{g^{XIV}(1.8)} E_{52}^{-2/5} A_{*, -1}^{11/5} \epsilon_{B, -2}^{6/5} t_5^{-8/5}, \nu_a < \nu_c < \nu_m
\end{aligned} \tag{4.52}$$

The α and β values and their closure relations of these models are presented in Tables 17 to 20.

For this model (adiabatic deceleration without energy injection), for $p > 2$, one has $\nu_m \propto t^{-3/2}$ ($t^{-3/2}$), $\nu_c \propto t^{-1/2}$ ($t^{1/2}$), $F_{\nu, \max} \propto t^0$ ($t^{-1/2}$) for the ISM (wind) models, respectively. For $1 < p < 2$, ν_c and $F_{\nu, \max}$ evolutions are the same as $p > 2$ cases, while $\nu_m \propto t^{\frac{3p+6}{8(1-p)}}$ ($t^{\frac{p+4}{4(1-p)}}$) for the ISM (wind) models, respectively.

Adiabatic deceleration with energy injection

In some central engines models, such as the millisecond magnetar model (Dai and Lu, 1998c; Zhang and Mészáros, 2001a), significant energy injection into the blastwave is possible. Assume that the central engine has a power-law luminosity history $L(t) = L_0 \left(\frac{t}{t_0}\right)^{-q}$, the injected energy is $E_{inj} = \frac{L_0 t_0^q}{1-q} t^{1-q}$. If the injected energy is in the form of a Poynting flux so that a reverse shock does not exist or is weak, one can approximately treat the blastwave as a system with continuous energy increase. The energy injection effect becomes significant when $E_{inj} > E_{imp}$, where E_{imp} is the impulsively injected energy during the prompt emission phase (Zhang and Mészáros, 2001a). The dynamics of the system can be described by

$$\gamma = \left(\frac{(17-4k)E}{4^{5-k}(4-k)^{3-k}\pi Am_p c^{5-k} t^{q+2-k}} \right)^{\frac{1}{2(4-k)}}, \quad R = \left(\frac{((17-4k)(4-k)Et^{2-q})}{4\pi Am_p c} \right)^{\frac{1}{4-k}}.$$

There is an alternative type of energy injection, which does not invoke a long lasting central engine, but rather invokes a Lorentz factor stratification of the ejecta (Rees and Mészáros, 1998; Sari and Mészáros, 2000), e.g.

$$M(> \gamma) \propto \gamma^{-s} \quad (4.53)$$

As the blastwave decelerates, ejecta with lower γ gradually piles up onto the blastwave so that the energy of the blastwave is increased. Since energy is injected when $\Gamma \sim \gamma$, the reverse shock is very weak, one can treat the blastwave as a system with continuous energy injection.

The two energy injection mechanisms can be considered equivalent when bridging the two injection parameter s and q , i.e.,

$$s = \frac{10 - 3k - 7q + 2kq}{2 + q - k}, \quad q = \frac{10 - 2s - 3k + ks}{7 + s - 2k} \quad (4.54)$$

for general density profile $n_1 = AR^{-k}$. For the ISM model and wind model, it becomes $s = \frac{10-7q}{2+q}$, $q = \frac{10-2s}{7+s}$ and $s = \frac{4-3q}{q}$, $q = \frac{4}{3+s}$ respectively (Zhang et al., 2006).

In the following, we derive all the expressions using the parameter q . For the ISM model ($k = 0$) and $p > 2$, one has

$$\begin{aligned} \nu_m &= 1.37 \times 10^{18} \text{ Hz } \hat{z}^{q/2} E_{52}^{1/2} \epsilon_{e,-1}^2 \epsilon_{B,-2}^{1/2} t^{-1-q/2}, \\ \nu_c &= 9.2 \times 10^{18} \text{ Hz } \hat{z}^{-q/2} E_{52}^{-1/2} n_{0,0}^{-1} \epsilon_{B,-2}^{-3/2} t^{-1+q/2}, \\ F_{\nu,\max} &= 1.1 \times 10^4 \text{ } \mu\text{Jy } \hat{z}^q E_{52} n_{0,0}^{1/2} \epsilon_{B,-2}^{1/2} D_{28}^{-2} t^{1-q}, \\ \nu_a &= 5.7 \times 10^9 \text{ Hz } \hat{z}^{\frac{q-6}{5}} \frac{g^I(p)}{g^I(2.3)} E_{52}^{1/5} n_{0,0}^{3/5} \epsilon_{e,-1} \epsilon_{B,-2}^{1/5} t^{\frac{1-q}{5}}, \quad \nu_a < \nu_m < \nu_c \\ \nu_a &= 5.0 \times 10^{13} \text{ Hz } \hat{z}^{\frac{(p+2)q-8}{2(p+4)}} \frac{g^{II}(p)}{g^{II}(2.3)} E_{52}^{\frac{p+2}{2(p+4)}} n_{0,0}^{\frac{2}{p+4}} \epsilon_{e,-1}^{\frac{2(p-1)}{p+4}} \epsilon_{B,-2}^{\frac{p+2}{2(p+4)}} t^{-\frac{2p+(p+2)q}{2(p+4)}}, \quad \nu_m < \nu_a < \nu_c \\ \nu_a &= 2.2 \times 10^9 \text{ Hz } \hat{z}^{\frac{7q-12}{10}} \frac{g^{III}(p)}{g^{III}(2.3)} E_{52}^{7/10} n_{0,0}^{11/10} \epsilon_{e,-1}^{6/5} \epsilon_{B,-2} t^{-\frac{7q-2}{10}}, \quad \nu_a < \nu_c < \nu_m \end{aligned} \quad (4.55)$$

For $1 < p < 2$, one has (ν_c and $F_{\nu, \max}$ remain the same)

$$\begin{aligned}
\nu_m &= 2.9 \times 10^{16} \text{ Hz } \hat{z}^{\frac{pq-6p+2q+12}{8(p-1)}} \frac{g^{IV}(p)}{g^{IV}(1.8)} E_{52}^{\frac{p+2}{8(p-1)}} n_{0,0}^{\frac{2-p}{8(p-1)}} \zeta_0^{\frac{2-p}{p-1}} \epsilon_{e,-1}^{\frac{2}{p-1}} \epsilon_{B,-2}^{\frac{1}{2(p-1)}} t^{-\frac{(q+2)(p+2)}{8(p-1)}}, \\
\nu_a &= 3.2 \times 10^{10} \text{ Hz } \hat{z}^{\frac{31pq-66p-46q+36}{8(p-1)}} \frac{g^V(p)}{g^V(1.8)} E_{52}^{\frac{46-31p}{80(1-p)}} n_{0,0}^{\frac{58-53p}{80(1-p)}} \zeta_0^{\frac{p-2}{2(p-1)}} \epsilon_{e,-1}^{\frac{1}{1-p}} \epsilon_{B,-2}^{\frac{14-9p}{20(1-p)}}, \\
&\quad t^{\frac{44-14p+46q-31pq}{80(p-1)}}, \quad \nu_a < \nu_m < \nu_c \\
\nu_a &= 1.1 \times 10^{13} \text{ Hz } \hat{z}^{\frac{pq-6p+14q-20}{8(p+4)}} \frac{g^{VI}(p)}{g^{VI}(1.8)} E_{52}^{\frac{p+14}{8(p+4)}} n_{0,0}^{\frac{18-p}{8(p+4)}} \zeta_0^{\frac{2-p}{p+4}} \epsilon_{e,-1}^{\frac{2}{p+4}} \epsilon_{B,-2}^{\frac{2}{p+4}} t^{-\frac{p(q+2)+2(7q+6)}{8(p+4)}}, \\
&\quad \nu_m < \nu_a < \nu_c \\
\nu_a &= 1.8 \times 10^9 \text{ Hz } \hat{z}^{\frac{7q-12}{10}} \frac{g^{VII}(p)}{g^{VII}(1.8)} E_{52}^{7/10} n_{0,0}^{11/10} \epsilon_{B,-2}^{6/5} t^{-\frac{7q-2}{10}}, \nu_a < \nu_c < \nu_m
\end{aligned} \tag{4.56}$$

For the wind model ($k = 2$) and $p > 2$, one has

$$\begin{aligned}
\nu_m &= 7.0 \times 10^{17} \text{ Hz } \hat{z}^{q/2} E_{52}^{1/2} \epsilon_{e,-1}^2 \epsilon_{B,-2}^{1/2} t^{-1-q/2}, \\
\nu_c &= 5.8 \times 10^{15} \text{ Hz } \hat{z}^{q/2-2} E_{52}^{1/2} A_{*, -1}^{-2} \epsilon_{B,-2}^{-3/2} t^{1-q/2} \\
F_{\nu, \max} &= 4.9 \times 10^5 \text{ } \mu\text{Jy } \hat{z}^{\frac{q+2}{2}} E_{52}^{1/2} A_{*, -1}^{1/2} D_{28}^{-2} t^{-q/2}, \\
\nu_a &= 1.0 \times 10^{12} \text{ Hz } \hat{z}^{-\frac{2q}{5}} \frac{g^{VIII}(p)}{g^{VIII}(2.3)} E_{52}^{-2/5} A_{*, -1}^{6/5} \epsilon_{e,-1}^{-1} \epsilon_{B,-2}^{1/5} t^{-1+2q/5}, \quad \nu_a < \nu_m < \nu_c \\
\nu_a &= 5.8 \times 10^{14} \text{ Hz } \hat{z}^{\frac{(p-2)q}{2(p+4)}} \frac{g^{IX}(p)}{g^{IX}(2.3)} E_{52}^{\frac{p-2}{2(p+4)}} A_{*, -1}^{\frac{4}{p+4}} \epsilon_{e,-1}^{\frac{2(p-1)}{p+4}} \epsilon_{B,-2}^{\frac{p+2}{2(p+4)}} t^{-1-\frac{(p-2)q}{2(p+4)}}, \nu_m < \nu_a < \nu_c \\
\nu_a &= 1.2 \times 10^{13} \text{ Hz } \hat{z}^{\frac{5-2q}{5}} \frac{g^X(p)}{g^X(2.3)} E_{52}^{-2/5} A_{*, -1}^{11/5} \epsilon_{B,-2}^{6/5} t^{2q/5-2}, \quad \nu_a < \nu_c < \nu_m
\end{aligned} \tag{4.57}$$

For $1 < p < 2$, one has (ν_c and $F_{\nu, \max}$ remain the same)

$$\begin{aligned}
\nu_m &= 1.7 \times 10^{16} \text{ Hz } \hat{z}^{\frac{pq-4p+8}{4(p-1)}} \frac{g^{XI}(p)}{g^{XI}(1.8)} E_{52}^{\frac{p}{4(p-1)}} A_{*, -1}^{\frac{2-p}{4(p-1)}} \zeta_0^{\frac{2-p}{p-1}} \epsilon_{e,-1}^{\frac{2}{p-1}} \epsilon_{B,-2}^{\frac{1}{2(p-1)}} t^{\frac{4+pq}{4(1-p)}}, \\
\nu_a &= 5.5 \times 10^{12} \text{ Hz } \hat{z}^{\frac{120-100p-6q+11pq}{40(p-1)}} \frac{g^{XII}(p)}{g^{XII}(1.8)} E_{52}^{\frac{6-11p}{40(p-1)}} A_{*, -1}^{\frac{58-53p}{40(1-p)}} \zeta_0^{\frac{p-2}{2(p-1)}} \epsilon_{e,-1}^{\frac{1}{1-p}} \epsilon_{B,-2}^{\frac{14-9p}{20(1-p)}}, \\
&\quad t^{\frac{20p-40+6q-11pq}{40(p-1)}}, \nu_a < \nu_m < \nu_c
\end{aligned}$$

	no injection		injection		
	β	α	$\alpha(\beta)$	α	$\alpha(\beta)$
ISM	slow cooling				
$\nu < \nu_a$	-2	$-\frac{1}{2}$	$\alpha = \frac{\beta}{4}$	$\frac{q}{2} - 1$	--
$\nu_a < \nu < \nu_m$	$-\frac{1}{3}$	$-\frac{1}{2}$	$\alpha = \frac{3\beta}{2}$	$\frac{5q-8}{6}$	--
$\nu_m < \nu < \nu_c$	$\frac{p-1}{2}$	$\frac{3(p-1)}{4}$	$\alpha = \frac{3\beta}{2}$	$\frac{(2p-6)+(p+3)q}{6}$	$\alpha = (q-1) + \frac{(2+q)\beta}{2}$
$\nu > \nu_c$	$\frac{p}{2}$	$\frac{3p-2}{4}$	$\alpha = \frac{3\beta-1}{2}$	$\frac{(2p-4)+(p+2)q}{4}$	$\alpha = \frac{q-2}{2} + \frac{(2+q)\beta}{2}$
ISM	fast cooling				
$\nu < \nu_a$	-2	-1	$\alpha = \frac{\beta}{2}$	-1	$\alpha = \frac{\beta}{2}$
$\nu_a < \nu < \nu_c$	$-\frac{1}{3}$	$-\frac{1}{6}$	$\alpha = \frac{\beta}{2}$	$\frac{7q-8}{6}$	--
$\nu_c < \nu < \nu_m$	$\frac{1}{2}$	$\frac{1}{4}$	$\alpha = \frac{\beta}{2}$	$\frac{3q-2}{4}$	--
$\nu > \nu_m$	$\frac{p}{2}$	$\frac{3p-2}{4}$	$\alpha = \frac{3\beta-1}{2}$	$\frac{(2p-4)+(p+2)q}{4}$	$\alpha = \frac{q-2}{2} + \frac{(2+q)\beta}{2}$
Wind	slow cooling				
$\nu < \nu_a$	-2	-1	$\alpha = \frac{\beta}{2}$	$q-2$	--
$\nu_a < \nu < \nu_m$	$-\frac{1}{3}$	0	0	--	--
$\nu_m < \nu < \nu_c$	$\frac{p-1}{2}$	$\frac{3p-1}{4}$	$\alpha = \frac{3\beta+1}{2}$	$\frac{(2p-2)+(p+1)q}{4}$	$\alpha = \frac{q}{2} + \frac{(2+q)\beta}{2}$
$\nu > \nu_c$	$\frac{p}{2}$	$\frac{3p-2}{4}$	$\alpha = \frac{3\beta-1}{2}$	$\frac{(2p-4)+(p+2)q}{4}$	$\alpha = \frac{q-2}{2} + \frac{(2+q)\beta}{2}$
Wind	fast cooling				
$\nu < \nu_a$	-2	-2	$\alpha = \beta$	$q-3$	--
$\nu_a < \nu < \nu_c$	$-\frac{1}{3}$	$\frac{2}{3}$	$\alpha = -2\beta$	$\frac{(1+q)}{3}$	--
$\nu_c < \nu < \nu_m$	$\frac{1}{2}$	$\frac{1}{4}$	$\alpha = \frac{\beta}{2}$	$\frac{3q-2}{4}$	--
$\nu > \nu_m$	$\frac{p}{2}$	$\frac{3p-2}{4}$	$\alpha = \frac{3\beta-1}{2}$	$\frac{(2p-4)+(p+2)q}{4}$	$\alpha = \frac{q-2}{2} + \frac{(2+q)\beta}{2}$

Table 17 The temporal decay index α and spectral index β in relativistic, isotropic, self-similar deceleration phase for $\nu_a < \min(\nu_m, \nu_c)$ and $p > 2$.

$$\begin{aligned}
\nu_a &= 1.7 \times 10^{14} \text{ Hz } \hat{z}^{\frac{(p-2)q-4p+8}{4(p+4)}} \frac{g^{XIII}(p)}{g^{XIII}(1.8)} E_{52}^{\frac{p-2}{4(p+4)}} A_{*, -1}^{\frac{18-p}{4(p+4)}} \zeta_0^{\frac{2-p}{p+4}} \epsilon_{e, -1}^{\frac{2}{p+4}} \epsilon_{B, -2}^{\frac{2}{p+4}} t^{-\frac{(p-2)q+24}{4(p+4)}}, \\
\nu_m &< \nu_a < \nu_c \\
\nu_a &= 9.5 \times 10^{12} \text{ Hz } \hat{z}^{\frac{5-2q}{5}} \frac{g^{XIV}(p)}{g^{XIV}(1.8)} E_{52}^{-2/5} A_{*, -1}^{11/5} \epsilon_{B, -2}^{6/5} t^{2q/5-2}, \nu_a < \nu_c < \nu_m
\end{aligned} \tag{4.58}$$

The α and β values and their closure relations for these models are also presented in Tables 17 to 20.

For this model (adiabatic deceleration without energy injection), for $p > 2$, one has $\nu_m \propto t^{-1-q/2}$ ($t^{-1-q/2}$), $\nu_c \propto t^{-1+q/2}$ ($t^{-1+q/2}$), $F_{\nu, \max} \propto t^{-q}$ ($t^{-q/2}$) for the ISM (wind) models, respectively. For $1 < p < 2$, ν_c and $F_{\nu, \max}$ evolutions are the same as $p > 2$ cases, while $\nu_m \propto t^{\frac{(q+2)(p+2)}{8(1-p)}}$ ($t^{\frac{4+pq}{4(1-p)}}$) for the ISM (wind) models, respectively.

	no injection			injection	
	β	α	$\alpha(\beta)$	α	$\alpha(\beta)$
ISM	slow cooling				
$\nu < \nu_m$	-2	$-\frac{1}{2}$	$\alpha = \frac{\beta}{4}$	$\frac{q}{2} - 1$	--
$\nu_m < \nu < \nu_a$	$-\frac{5}{2}$	$-\frac{5}{4}$	$\alpha = \frac{\beta}{2}$	$\frac{q-6}{4}$	--
$\nu_a < \nu < \nu_c$	$\frac{p-1}{2}$	$\frac{3(p-1)}{4}$	$\alpha = \frac{3\beta}{2}$	$\frac{(2p-6)+(p+3)q}{4}$	$\alpha = (q-1) + \frac{(2+q)\beta}{2}$
$\nu > \nu_c$	$\frac{p}{2}$	$\frac{3p-2}{4}$	$\alpha = \frac{3\beta-1}{2}$	$\frac{(2p-4)+(p+2)q}{4}$	$\alpha = \frac{q-2}{2} + \frac{(2+q)\beta}{2}$
Wind	slow cooling				
$\nu < \nu_m$	-2	-1	$\alpha = \frac{\beta}{2}$	$q-2$	--
$\nu_m < \nu < \nu_a$	$-\frac{5}{2}$	$-\frac{7}{4}$	$\alpha = \frac{7\beta}{10}$	$\frac{3q-10}{4}$	--
$\nu_a < \nu < \nu_c$	$\frac{p-1}{2}$	$\frac{3p-1}{4}$	$\alpha = \frac{3\beta+1}{2}$	$\frac{(2p-2)+(p+1)q}{4}$	$\alpha = \frac{q}{2} + \frac{(2+q)\beta}{2}$
$\nu > \nu_c$	$\frac{p}{2}$	$\frac{3p-2}{4}$	$\alpha = \frac{3\beta-1}{2}$	$\frac{(2p-4)+(p+2)q}{4}$	$\alpha = \frac{q-2}{2} + \frac{(2+q)\beta}{2}$

Table 18 The temporal decay index α and spectral index β in relativistic, isotropic, self-similar deceleration phase for $\nu_m < \nu_a < \nu_c$ and $p > 2$.

	no injection			injection	
	β	α	$\alpha(\beta)$	α	$\alpha(\beta)$
ISM	slow cooling				
$\nu < \nu_a$	-2	$\frac{26-17p}{16(p-1)}$	--	$\frac{28-22p-2q+5pq}{16(p-1)}$	--
$\nu_a < \nu < \nu_m$	$-\frac{1}{3}$	$-\frac{p+2}{8(p-1)}$	--	$\frac{20-26p-26q+23pq}{24(p-1)}$	--
$\nu_m < \nu < \nu_c$	$\frac{p-1}{2}$	$\frac{3(p+2)}{16}$	$\alpha = \frac{6\beta+9}{16}$	$-\frac{12-18q-p(q+2)}{16}$	$\alpha = \frac{19q-10}{16} + \frac{(2+q)\beta}{8}$
$\nu > \nu_c$	$\frac{p}{2}$	$\frac{3p+10}{16}$	$\alpha = \frac{3\beta+5}{8}$	$\frac{14q+p(q+2)-4}{16}$	$\alpha = \frac{7q-2}{8} + \frac{(2+q)\beta}{8}$
ISM	fast cooling				
$\nu < \nu_a$	-2	-1	$\alpha = \frac{\beta}{2}$	-1	$\alpha = \frac{\beta}{2}$
$\nu_a < \nu < \nu_c$	$-\frac{1}{3}$	$-\frac{1}{6}$	$\alpha = \frac{\beta}{2}$	$\frac{7q-8}{6}$	--
$\nu_c < \nu < \nu_m$	$\frac{1}{2}$	$\frac{1}{4}$	$\alpha = \frac{\beta}{2}$	$\frac{3q-2}{4}$	--
$\nu > \nu_m$	$\frac{p}{2}$	$\frac{3p+10}{16}$	$\alpha = \frac{3\beta+5}{8}$	$\frac{14q+p(q+2)-4}{16}$	$\alpha = \frac{7q-2}{8} + \frac{(2+q)\beta}{8}$
Wind	slow cooling				
$\nu < \nu_a$	-2	$\frac{13p-18}{8(1-p)}$	--	$\frac{20p+6q-7pq-24}{8(1-p)}$	--
$\nu_a < \nu < \nu_m$	$-\frac{1}{3}$	$\frac{5(p-2)}{12(1-p)}$	--	$\frac{4+6q-5pq}{12(1-p)}$	--
$\nu_m < \nu < \nu_c$	$\frac{p-1}{2}$	$\frac{p+8}{8}$	$\alpha = \frac{2\beta+9}{8}$	$\frac{4+(p+4)q}{8}$	$\alpha = \frac{5q+4}{8} + \frac{\beta q}{4}$
$\nu > \nu_c$	$\frac{p}{2}$	$\frac{p+6}{8}$	$\alpha = \frac{2\beta+7}{8}$	$\frac{(6+p)q}{8}$	$\alpha = \frac{(\beta+3)q}{4}$
Wind	fast cooling				
$\nu < \nu_a$	-2	-2	$\alpha = \beta$	$q-3$	--
$\nu_a < \nu < \nu_c$	$-\frac{1}{3}$	$\frac{2}{3}$	$\alpha = -2\beta$	$\frac{1+q}{3}$	--
$\nu_c < \nu < \nu_m$	$\frac{1}{2}$	$\frac{1}{4}$	$\alpha = \frac{\beta}{2}$	$\frac{3q-2}{4}$	--
$\nu > \nu_m$	$\frac{p}{2}$	$\frac{p+6}{8}$	$\alpha = \frac{2\beta+7}{8}$	$\frac{(6+p)q}{8}$	$\alpha = \frac{(\beta+3)q}{4}$

Table 19 The temporal decay index α and spectral index β in relativistic, isotropic, self-similar deceleration phase for $\nu_a < \min(\nu_m, \nu_c)$ and $1 < p < 2$.

		no injection		injection	
	β	α	$\alpha(\beta)$	α	$\alpha(\beta)$
ISM	slow cooling				
$\nu < \nu_m$	-2	$\frac{26-1/p}{16(p-1)}$	--	$\frac{28-22p-2q+5pq}{16(p-1)}$	--
$\nu_m < \nu < \nu_a$	$-\frac{5}{2}$	$-\frac{5}{4}$	$\alpha = \frac{\beta}{2}$	$\frac{q-6}{4}$	--
$\nu_a < \nu < \nu_c$	$\frac{p-1}{2}$	$\frac{3(p+2)}{16}$	$\alpha = \frac{6\beta+9}{16}$	$\frac{18q+p(q+2)-12}{16}$	$\alpha = \frac{19q-10}{16} + \frac{(2+q)\beta}{8}$
$\nu > \nu_c$	$\frac{p}{2}$	$\frac{3p+10}{16}$	$\alpha = \frac{3\beta+5}{8}$	$\frac{14q+p(q+2)-4}{16}$	$\alpha = \frac{7q-2}{8} + \frac{(2+q)\beta}{8}$
Wind	slow cooling				
$\nu < \nu_m$	-2	$\frac{13p-18}{8(1-p)}$	--	$\frac{20p+6q-(pq-24)}{8(1-p)}$	-
$\nu_m < \nu < \nu_a$	$-\frac{5}{2}$	$-\frac{7}{4}$	$\alpha = \frac{7\beta}{10}$	$\frac{3q-10}{4}$	--
$\nu_a < \nu < \nu_c$	$\frac{p-1}{2}$	$\frac{p+8}{8}$	$\alpha = \frac{2\beta+9}{8}$	$\frac{4+(p+4)q}{8}$	$\alpha = \frac{5q+4}{8} + \frac{\beta q}{4}$
$\nu > \nu_c$	$\frac{p}{2}$	$\frac{6+p}{8}$	$\alpha = \frac{2\beta+7}{8}$	$\frac{(6+p)q}{8}$	$\alpha = \frac{(\beta+3)q}{4}$

Table 20 The temporal decay index α and spectral index β in relativistic, isotropic, self-similar deceleration phase for $\nu_m < \nu_a < \nu_c$ and $1 < p < 2$.

Phase 3: post jet break phase

The above calculations are based on the assumption of a spherical expansion. However, achromatic breaks seen in many afterglow lightcurves suggest that GRB outflows are collimated. For a simplified conical jet model with an opening angle θ_j , the jet effect becomes important when $1/\Gamma > \theta_j$. The lightcurve shows a steepening break around this time.

In the literature, two effects have been discussed to steepen the lightcurve. The first is the pure edge effect (e.g. Panaitescu et al., 1998a). Since an observer sees emission within the $1/\Gamma$ cone for a blastwave moving with bulk Lorentz factor Γ , he/she would feel the deficit of flux outside the θ_j cone when $1/\Gamma > \theta_j$ is satisfied. Assuming that the dynamics does not change, the flux reduction factor would be $\theta_j^2/(1/\Gamma)^2 = \Gamma^2\theta_j^2$. This defines the degree of steepening at the jet break.

The second effect discussed in the literature is the sideways expansion effect. According to (Rhoads, 1999; Sari et al., 1999c), when $\Gamma \sim \theta_j^{-1}$ is satisfied, sound waves in the jet would cross the jet in the transverse direction and lead to its sideways expansion. This leads to an exponential deceleration of the jet. However, later numerical simulations, and more sophisticated analytical treatments suggest that sideways expansion is not important until Γ drops below a few (Kumar and Panaitescu, 2003a; Cannizzo et al., 2004; Zhang and MacFadyen, 2009; Granot and Piran, 2012). We

therefore do not discuss this effect.

For the edge effect only, in the post-jet-break phase the expressions of the break frequencies ν_a , ν_m and ν_c and the peak flux density $F_{\nu, \max}$ all remain the same as the isotropic phase. The temporal decay indices are changed with the extra steepening correction factor. In rare cases, continuous energy injection may extend to the post-jet-break phase. For completeness, we also discuss these cases. After shock crossing, the reverse shocked region decelerates with a different dynamics from the forward shocked region. Given a same jet opening angle, it corresponds to an earlier jet break time. In Table 21, we present the expressions of jet break time and the temporal indices changes ($\Delta\alpha$ defined as post-jet-break α_2 minus pre-jet-break α_1) for all the models in different regimes.

In Tables 22 and 23, we present α and β values and their closure relations for the jet model. Since the reverse shock jet break is usually undetectable, only forward shock models are presented.

	t_{jet}	$\Delta\alpha$
ThinRS _{post} (ISM)	$2.8 \times 10^4 \text{ s } \hat{z} E_{52}^{1/3} \theta_{j,-1}^{5/2} n_0^{-1/3} \Gamma_{0.2}^{-1/6}$	4/5
ThinRS _{post} (wind)	$2.9 \times 10^3 \text{ s } \hat{z} E_{52} \theta_{j,-1}^3 A_{*, -1}^{-1} \Gamma_{0.2}^{-1}$	2/3
ThickRS _{post} (ISM)	$1.2 \times 10^4 \text{ s } \hat{z} E_{52}^{2/7} \theta_{j,-1}^{16/7} n_0^{-2/7} \Delta_{0.12}^{1/7}$	7/8
ThickRS _{post} (Wind)	$1.9 \times 10^3 \text{ s } \hat{z} E_{52}^{2/3} \theta_{j,-1}^{8/3} A_{*, -1}^{-2/3} \Delta_{0.12}^{1/3}$	3/4
FS (ISM, no injection)	$5.8 \times 10^3 \text{ s } \hat{z} E_{52}^{1/3} \theta_{j,-1}^{8/3} n_0^{-1/3}$	3/4
FS (wind, no injection)	$1.7 \times 10^4 \text{ s } \hat{z} E_{52} \theta_{j,-1}^4 A_{*, -1}^{-1}$	1/2
FS (ISM, injection)	$2.0 \times 10^{\frac{11}{2+q}} \text{ s } \hat{z} E_{52}^{\frac{1}{2+q}} \theta_{j,-1}^{\frac{8}{2+q}} n_0^{-\frac{1}{2+q}}$	$(2+q)/4$
FS (wind, injection)	$1.7 \times 10^{\frac{4}{q}} \text{ s } \hat{z} E_{52}^{\frac{1}{q}} \theta_{j,-1}^{\frac{4}{q}} A_{*, -1}^{-\frac{1}{q}}$	$q/2$

Table 21 Collection of jet break time and temporal indices changes $\Delta\alpha = \alpha_2 - \alpha_1$ for different regimes.

Phase 4: newtonian phase

The blastwave eventually enters the Newtonian phase when it has swept up a CBM mass comparable to the initial mass entrained in the ejecta. In the deep Newtonian

	β	$p > 2$ α	$\alpha(\beta)$	$1 < p < 2$ α	$\alpha(\beta)$
ISM	no injection				
$\nu < \nu_a$	-2	$\frac{1}{4}$	$\alpha = \frac{\beta}{8}$	$\frac{14-5p}{16(p-1)}$	--
$\nu_a < \nu < \nu_m$	$-\frac{1}{3}$	$\frac{1}{4}$	$\alpha = \frac{3\beta}{4}$	$\frac{5p-8}{8(p-1)}$	--
$\nu_m < \nu < \nu_c$	$\frac{p-1}{2}$	$\frac{3p}{4}$	$\alpha = \frac{6\beta+3}{4}$	$\frac{3(p+6)}{16}$	$\alpha = \frac{3(2\beta+7)}{16}$
$\nu > \nu_c$	$\frac{p}{2}$	$\frac{3p+1}{4}$	$\alpha = \frac{6\beta+1}{4}$	$\frac{3p+22}{16}$	$\alpha = \frac{3\beta+11}{8}$
Wind	no injection				
$\nu < \nu_a$	-2	$-\frac{1}{2}$	$\alpha = \frac{\beta}{4}$	$\frac{14-9p}{8(p-1)}$	--
$\nu_a < \nu < \nu_m$	$-\frac{5}{2}$	$\frac{1}{2}$	$\alpha = \frac{\beta}{5}$	$\frac{11p-16}{12(p-1)}$	--
$\nu_m < \nu < \nu_c$	$\frac{p-1}{2}$	$\frac{3p+1}{4}$	$\alpha = \frac{3\beta+2}{2}$	$\frac{p+12}{8}$	$\alpha = \frac{2\beta+13}{8}$
$\nu > \nu_c$	$\frac{p}{2}$	$\frac{3p}{4}$	$\alpha = \frac{3\beta}{2}$	$\frac{p+10}{8}$	$\alpha = \frac{\beta+5}{4}$
ISM	injection				
$\nu < \nu_a$	-2	$\frac{3q-2}{4}$	--	$\frac{20-14p-6q+9pq}{16(p-1)}$	--
$\nu_a < \nu < \nu_m$	$-\frac{1}{3}$	$\frac{13q-10}{12}$	--	$\frac{8-14p-32q+29pq}{24(p-1)}$	--
$\nu_m < \nu < \nu_c$	$\frac{p-1}{2}$	$\frac{p(q+2)-4(1-q)}{4}$	$\alpha = \frac{5q-2}{4} + \frac{(2+q)\beta}{2}$	$\frac{22q-4+p(q+2)}{16}$	$\alpha = \frac{11q-2}{8} + \frac{(2+q)\beta}{8}$
$\nu > \nu_c$	$\frac{p}{2}$	$\frac{3q-2+p(q+2)}{4}$	$\alpha = \frac{3q-2+2\beta(q+2)}{4}$	$\frac{18q+4+p(q+2)}{16}$	$\alpha = \frac{9q+2+\beta(q+2)}{8}$
Wind	injection				
$\nu < \nu_a$	-2	$\frac{3q-4}{2}$	--	$\frac{24-20p-10q+11pq}{8(p-1)}$	--
$\nu_a < \nu < \nu_m$	$-\frac{5}{2}$	$\frac{5q-2}{6}$	--	$\frac{11pq-12q-4}{12(p-1)}$	--
$\nu_m < \nu < \nu_c$	$\frac{p-1}{2}$	$\frac{3q-2+p(q+2)}{4}$	$\alpha = q + \frac{(2+q)\beta}{2}$	$\frac{pq+8q+4}{8}$	$\alpha = \frac{1}{2} + \frac{2\beta+9}{8}$
$\nu > \nu_c$	$\frac{p}{2}$	$\frac{p(q+2)-4(1-q)}{4}$	$\alpha = \frac{\beta(q+2)-2(1-q)}{2}$	$\frac{(p+10)q}{8}$	$\alpha = \frac{(\beta+5)q}{4}$

Table 22 The temporal decay index α and spectral index β after jet break for $\nu_a < \min(\nu_m, \nu_c)$, considering edge effect only.

	β	$p > 2$ α	$\alpha(\beta)$	$1 < p < 2$ α	$\alpha(\beta)$
ISM	no injection				
$\nu < \nu_m$	-2	$\frac{1}{4}$	$\alpha = \frac{\beta}{8}$	$\frac{14-5p}{16(p-1)}$	--
$\nu_m < \nu < \nu_a$	$-\frac{1}{3}$	$-\frac{1}{2}$	$\alpha = \frac{3\beta}{2}$	$-\frac{1}{2}$	$\alpha = \frac{3\beta}{2}$
$\nu_a < \nu < \nu_c$	$\frac{p-1}{2}$	$\frac{3p}{4}$	$\alpha = \frac{6\beta+3}{4}$	$\frac{3(p+6)}{16}$	$\alpha = \frac{3(2\beta+7)}{16}$
$\nu > \nu_c$	$\frac{p}{2}$	$\frac{3p+1}{4}$	$\alpha = \frac{6\beta+1}{4}$	$\frac{3p+22}{16}$	$\alpha = \frac{3\beta+11}{8}$
Wind	no injection				
$\nu < \nu_m$	-2	$-\frac{1}{2}$	$\alpha = \frac{\beta}{4}$	$\frac{14-9p}{8(p-1)}$	--
$\nu_m < \nu < \nu_a$	$-\frac{5}{2}$	$-\frac{5}{4}$	$\alpha = \frac{\beta}{2}$	$-\frac{5}{4}$	$\alpha = \frac{\beta}{2}$
$\nu_a < \nu < \nu_c$	$\frac{p-1}{2}$	$\frac{3p+1}{4}$	$\alpha = \frac{3\beta+2}{2}$	$\frac{p+12}{8}$	$\alpha = \frac{2\beta+13}{8}$
$\nu > \nu_c$	$\frac{p}{2}$	$\frac{3p}{4}$	$\alpha = \frac{3\beta}{2}$	$\frac{p+10}{8}$	$\alpha = \frac{\beta+5}{4}$
ISM	injection				
$\nu < \nu_m$	-2	$\frac{3q-2}{4}$	--	$\frac{20-14p-6q+9pq}{16(p-1)}$	--
$\nu_m < \nu < \nu_a$	$-\frac{1}{3}$	$\frac{q-2}{2}$	--	$\frac{q-2}{2}$	--
$\nu_a < \nu < \nu_c$	$\frac{p-1}{2}$	$\frac{p(q+2)-4(1-q)}{4}$	$\alpha = \frac{5q-2}{4} + \frac{(2+q)\beta}{2}$	$\frac{22q-4+p(q+2)}{16}$	$\alpha = \frac{11q-2}{8} + \frac{(2+q)\beta}{8}$
$\nu > \nu_c$	$\frac{p}{2}$	$\frac{3q-2+p(q+2)}{4}$	$\alpha = \frac{3q-2+2\beta(q+2)}{4}$	$\frac{18q+4+p(q+2)}{16}$	$\alpha = \frac{9q+2+\beta(q+2)}{8}$
Wind	injection				
$\nu < \nu_m$	-2	$\frac{3q-4}{2}$	--	$\frac{24-20p-10q+11pq}{8(p-1)}$	--
$\nu_m < \nu < \nu_a$	$-\frac{5}{2}$	$\frac{5(q-2)}{4}$	--	$\frac{5(q-2)}{4}$	--
$\nu_a < \nu < \nu_c$	$\frac{p-1}{2}$	$\frac{3q-2+p(q+2)}{4}$	$\alpha = q + \frac{(2+q)\beta}{2}$	$\frac{pq+8q+4}{8}$	$\alpha = \frac{1}{2} + \frac{2\beta+9}{8}$
$\nu > \nu_c$	$\frac{p}{2}$	$\frac{p(q+2)-4(1-q)}{4}$	$\alpha = \frac{\beta(q+2)-2(1-q)}{2}$	$\frac{(p+10)q}{8}$	$\alpha = \frac{(\beta+5)q}{4}$

Table 23 The temporal decay index α and spectral index β after jet break for $\nu_m < \nu_a < \nu_c$, considering edge effect only.

phase, the dynamics is described by the well known Sedov-Taylor solution:

$$R = \left(\frac{5-k}{2} \right)^{\frac{2}{5-k}} \left[\frac{(3-k)E}{2\pi Am_p} \right]^{\frac{1}{5-k}} t^{\frac{2}{5-k}}, \quad v = \left(\frac{5-k}{2} \right)^{\frac{k-3}{5-k}} \left[\frac{(3-k)E}{2\pi Am_p} \right]^{\frac{1}{5-k}} t^{\frac{k-3}{5-k}} \quad (4.59)$$

This phase has been studied extensively in the literature (Wijers et al., 1997; Dai and Lu, 1999a; Huang et al., 1999, 2000; Livio and Waxman, 2000; Huang and Cheng, 2003).

In this phase, for an ISM medium and $p > 2$, one has

$$\begin{aligned} \nu_m &= 2.0 \times 10^{14} \text{ Hz } \hat{z}^2 \frac{G(p)}{G(2.3)} E_{52} n_{0,0}^{-1/2} \epsilon_{e,-1}^2 \epsilon_{B,-2}^{1/2} t_5^{-3}, \\ \nu_c &= 7.0 \times 10^{15} \text{ Hz } \hat{z}^{-4/5} E_{52}^{-3/5} n_{0,0}^{-9/10} \epsilon_{B,-2}^{-3/2} t_5^{-1/5} \\ F_{\nu,\max} &= 2.3 \times 10^2 \text{ } \mu\text{Jy } \hat{z}^{2/5} E_{52}^{4/5} n_{0,0}^{7/10} \epsilon_{B,-2}^{1/2} D_{28}^{-2} t_5^{3/5}, \\ \nu_a &= 1.4 \times 10^7 \text{ Hz } \hat{z}^{-11/5} \frac{g^I(p)}{g^I(2.3)} E_{52}^{-1/5} n_{0,0} \epsilon_{e,-1}^{-1} \epsilon_{B,-2}^{1/5} t_5^{6/5}, \quad \nu_a < \nu_m < \nu_c \\ \nu_a &= 3.3 \times 10^{10} \text{ Hz } \hat{z}^{\frac{2p-6}{p+4}} \frac{g^{II}(p)}{g^{II}(2.3)} E_{52}^{\frac{p}{p+4}} n_{0,0}^{\frac{6-p}{2(p+4)}} \epsilon_{e,-1}^{\frac{2(p-1)}{p+4}} \epsilon_{B,-2}^{\frac{p+2}{2(p+4)}} t_5^{-\frac{3p-2}{p+4}}, \nu_m < \nu_a < \nu_c \end{aligned} \quad (4.60)$$

For $1 < p < 2$, one has (ν_c and $F_{\nu,\max}$ remain the same)

$$\begin{aligned} \nu_m &= 1.9 \times 10^{12} \text{ Hz } \hat{z}^{\frac{4-p}{p-1}} \frac{g^{III}(p)}{g^{III}(1.8)} E_{52}^{\frac{1}{p-1}} n_{0,0}^{\frac{1}{2(1-p)}} \zeta_0^{\frac{2-p}{p-1}} \epsilon_{e,-1}^{\frac{2}{p-1}} \epsilon_{B,-2}^{\frac{1}{2(p-1)}} t_5^{-\frac{3}{p-1}}, \\ \nu_a &= 1.2 \times 10^8 \text{ Hz } \frac{g^{IV}(p)}{g^{IV}(1.8)} \hat{z}^{\frac{7p+8}{10(p-1)}} E_{52}^{\frac{8-3p}{10(1-p)}} n_{0,0}^{\frac{2-3p}{4(1-p)}} \zeta_0^{\frac{p-2}{2(p-1)}} \epsilon_{e,-1}^{\frac{1}{1-p}} \epsilon_{B,-2}^{\frac{14-9p}{20(1-p)}} t_5^{-\frac{3(p-6)}{10(p-1)}}, \\ \nu_a &< \nu_m < \nu_c \\ \nu_a &= 7.4 \times 10^9 \text{ Hz } \hat{z}^{-\frac{p}{p+4}} \frac{g^V(p)}{g^V(1.8)} E_{52}^{\frac{2}{p+4}} n_{0,0}^{\frac{2}{p+4}} \zeta_0^{\frac{2-p}{p+4}} \epsilon_{e,-1}^{\frac{2}{p+4}} \epsilon_{B,-2}^{\frac{2}{p+4}} t_5^{-\frac{4}{p+4}}, \nu_m < \nu_a < \nu_c \end{aligned} \quad (4.61)$$

For the wind model and $p > 2$, one has

$$\begin{aligned}
\nu_m &= 1.6 \times 10^{14} \text{ Hz } \hat{z}^{4/3} \frac{G(p)}{G(2.3)} E_{52}^{4/3} A_{*, -1}^{-5/6} \epsilon_{e, -1}^2 \epsilon_{B, -2}^{1/2} t_5^{-7/3}, \\
\nu_c &= 1.7 \times 10^{15} \text{ Hz } \hat{z}^{-2} A_{*, 1}^{-3/2} \epsilon_{B, -2}^{-3/2} t_5 \\
F_{\nu, \max} &= 5.3 \times 10^2 \text{ } \mu\text{Jy } \hat{z}^{4/3} E_{52}^{1/3} A_{*, -1}^{7/6} \epsilon_{B, -2}^{1/2} D_{28}^{-2} t_5^{-1/3}, \\
\nu_a &= 6.9 \times 10^7 \text{ Hz } \hat{z}^{-13/15} \frac{g^{VI}(p)}{g^{VI}(2.3)} E_{52}^{-13/15} A_{*, -1}^{5/3} \epsilon_{e, -1}^{-1} \epsilon_{B, -2}^{1/5} t_5^{-2/15}, \quad \nu_a < \nu_m < \nu_c \\
\nu_a &= 6.9 \times 10^{10} \text{ Hz } \hat{z}^{\frac{4p-6}{3(p+4)}} \frac{g^{VII}(p)}{g^{VII}(2.3)} E_{52}^{\frac{2(2p-3)}{3(p+4)}} A_{*, -1}^{\frac{5(6-p)}{6(p+4)}} \epsilon_{e, -1}^{\frac{2(p-1)}{p+4}} \epsilon_{B, -2}^{\frac{p+2}{2(p+4)}} t_5^{-\frac{7p+6}{3(p+4)}}, \nu_m < \nu_a < \nu_c
\end{aligned} \tag{4.62}$$

For $1 < p < 2$, one has (ν_c and $F_{\nu, \max}$ remain the same)

$$\begin{aligned}
\nu_m &= 1.4 \times 10^{12} \text{ Hz } \hat{z}^{\frac{10-3p}{3(p-1)}} \frac{g^{VIII}(p)}{g^{VIII}(1.8)} E_{52}^{\frac{4}{3(p-1)}} A_{*, -1}^{\frac{5}{6(1-p)}} \zeta_0^{\frac{2-p}{p-1}} \epsilon_{e, -1}^{\frac{2}{p-1}} \epsilon_{B, -2}^{\frac{1}{2(p-1)}} t_5^{-\frac{7}{3(p-1)}}, \\
\nu_a &= 6.0 \times 10^8 \text{ Hz } \hat{z}^{\frac{9p-44}{30(p-1)}} \frac{g^{IX}(p)}{g^{IX}(1.8)} E_{52}^{\frac{3p+7}{15(1-p)}} A_{*, -1}^{\frac{5(3p-2)}{12(p-1)}} \zeta_0^{\frac{p-2}{2(p-1)}} \epsilon_{e, -1}^{\frac{1}{1-p}} \epsilon_{B, -2}^{\frac{14-9p}{20(1-p)}} t_5^{\frac{74-39p}{30(p-1)}}, \\
\nu_a &< \nu_m < \nu_c \\
\nu_a &= 1.6 \times 10^{10} \text{ Hz } \hat{z}^{\frac{8-3p}{3p+4}} \frac{g^X(p)}{g^X(1.8)} E_{52}^{\frac{2}{3(p+4)}} A_{*, -1}^{\frac{10}{3(p+4)}} \zeta_0^{\frac{2-p}{p+4}} \epsilon_{e, -1}^{\frac{2}{p+4}} \epsilon_{B, -2}^{\frac{2}{p+4}} t_5^{-\frac{20}{3(p+4)}}, \nu_m < \nu_a < \nu_c
\end{aligned} \tag{4.63}$$

The α and β values and their closure relations in this phase are presented in Tables 24 and 25.

For this model (newtonian Phase), for $p > 2$, one has $\nu_m \propto t^{-3}$ ($t^{-7/3}$), $\nu_c \propto t^{-1/5}$ (t^1), $F_{\nu, \max} \propto t^{3/5}$ ($t^{-1/3}$) for the ISM (wind) models, respectively. For $1 < p < 2$, ν_c and $F_{\nu, \max}$ evolutions are the same as $p > 2$ cases, while $\nu_m \propto t^{\frac{3}{1-p}}$ ($t^{\frac{7}{3(1-p)}}$) for the ISM (wind) models, respectively.

	β	no injection		injection	
		α	$\alpha(\beta)$	α	$\alpha(\beta)$
ISM	slow cooling				
$\nu < \nu_a$	-2	$\frac{2}{5}$	$\alpha = \frac{\beta}{5}$	$\frac{26-11p}{10(p-1)}$	--
$\nu_a < \nu < \nu_m$	$-\frac{1}{3}$	$-\frac{8}{5}$	$\alpha = \frac{24\beta}{5}$	$-\frac{3p+2}{5(p-1)}$	--
$\nu_m < \nu < \nu_c$	$\frac{p-1}{2}$	$\frac{3(5p-7)}{10}$	$\alpha = \frac{3(5\beta-1)}{5}$	$\frac{9}{10}$	--
$\nu > \nu_c$	$\frac{p}{2}$	$\frac{3p-4}{2}$	$\alpha = 3\beta - 2$	1	--
Wind	slow cooling				
$\nu < \nu_a$	-2	$-\frac{2}{3}$	$\alpha = \frac{\beta}{3}$	$\frac{18-11p}{6(p-1)}$	--
$\nu_a < \nu < \nu_m$	$-\frac{1}{3}$	$-\frac{4}{9}$	$\alpha = \frac{4\beta}{3}$	$\frac{3p-10}{9(p-1)}$	--
$\nu_m < \nu < \nu_c$	$\frac{p-1}{2}$	$\frac{7p-5}{6}$	$\alpha = \frac{7\beta+1}{3}$	$\frac{3}{2}$	--
$\nu > \nu_c$	$\frac{p}{2}$	$\frac{7p-8}{6}$	$\alpha = \frac{7\beta-4}{3}$	1	--

Table 24 The temporal decay index α and spectral index β in the Newtonian phase for $\nu_a < \min(\nu_m, \nu_c)$.

	β	no injection		injection	
		α	$\alpha(\beta)$	α	$\alpha(\beta)$
ISM	slow cooling				
$\nu < \nu_m$	-2	$\frac{2}{5}$	$\alpha = \frac{\beta}{5}$	$\frac{26-11p}{10(p-1)}$	--
$\nu_m < \nu < \nu_a$	$-\frac{5}{2}$	$-\frac{11}{10}$	$\alpha = \frac{11\beta}{25}$	$-\frac{11}{10}$	$\alpha = \frac{33\beta}{10}$
$\nu_a < \nu < \nu_c$	$\frac{p-1}{2}$	$\frac{3(5p-7)}{10}$	$\alpha = \frac{3(5\beta-1)}{5}$	$\frac{9}{10}$	--
$\nu > \nu_c$	$\frac{p}{2}$	$\frac{3p-4}{2}$	$\alpha = 3\beta - 2$	1	--
Wind	slow cooling				
$\nu < \nu_m$	-2	$-\frac{2}{3}$	$\alpha = \frac{\beta}{3}$	$\frac{18-11p}{6(p-1)}$	--
$\nu_m < \nu < \nu_a$	$-\frac{5}{2}$	$-\frac{11}{6}$	$\alpha = \frac{11\beta}{15}$	$-\frac{11}{6}$	$\alpha = \frac{11\beta}{2}$
$\nu_a < \nu < \nu_c$	$\frac{p-1}{2}$	$\frac{7p-5}{6}$	$\alpha = \frac{7\beta+1}{3}$	$\frac{3}{2}$	--
$\nu > \nu_c$	$\frac{p}{2}$	$\frac{7p-8}{6}$	$\alpha = \frac{7\beta-4}{3}$	1	--

Table 25 The temporal decay index α and spectral index β in the Newtonian phase for $\nu_m < \nu_a < \nu_c$.

Applications of the Models

The third section gives a complete reference of all the possible analytical synchrotron external shock models. There are two opposite ways of applying this reference tool. First, one can fit the observational data to get both temporal decay index α and spectral index β , and then identify which spectral regime the observational frequency lies in. One can then constrain related afterglow parameters. To fully determine the parameters, one needs multi-wavelength, multi-epoch observational data. In any case, for the relativistic deceleration phase before the jet break, from which most data are collected, usually a closure relation study could give a quick judgement about the possible spectral regime and medium type. Alternatively, one can start to assign reasonable ranges of a set of model parameters, and apply the models to draw predicted light curves. By varying parameters, one can use the model to fit the observational data.

Since the three characteristic frequencies ν_a , ν_m , and ν_c all evolve with time, the order among them may change during the evolution. The characteristic frequencies may also pass the observed band, so that the observational spectral regime may also change. These factors introduce complications in drawing theoretical lightcurves. First, one needs to estimate how spectral regimes evolve with time, using the related expressions of the characteristic frequencies; Second, one needs to use the closure relation tables to find out the temporal decay index for each segment of the light curve, and then connect all the segments. Lightcurves can differ for different dynamical models, different initial ordering of the characteristic frequencies, and different spectral regimes.

In order to make readers more conveniently use this reference tool, we plot all the possible lightcurve shapes that can be derived analytically⁶, and present spectral

⁶The only spectral regimes that are not included are all the spectral orders that invoke $\nu_a > \nu_c$. For such combinations, the power-law description of electron energy distribution is no longer valid, and pile up of electrons near γ_a is expected (Kobayashi et al., 2004). Since the exact shape of

and temporal indices for each temporal segment for all the phases discussed in the third section. These are presented in Figures 12 to 55. Some of these lightcurves may demand extreme afterglow parameters. However, since we aim at a complete reference of the models and keep a wide open range of the observational frequency and model parameters, we have included all the possible frequency regime transitions for all the phases. In reality, one could use the observational data to narrow down the possibilities to identify the most relevant lightcurve segments. For easy identification, Table 4 summarizes the corresponding figure numbers for different dynamical models and spectral regimes.

It is worth emphasizing that a critical time to separate Phase 1 (reverse shock crossing phase) and Phase 2 (self-similar deceleration phase) is the shock crossing time t_\times (Eq.4.20). At t_\times , the ratios of the forward and reverse shock quantities $F_{\nu,max}$, ν_m , ν_c etc. can be coasted into some simple forms (Zhang et al., 2003). Practically, one can derive the forward shock scaling first (which is easier), and extrapolate to t_\times . Then applying the reverse-to-forward shock ratios of critical parameters (Zhang et al., 2003; Harrison and Kobayashi, 2013), one can derive the reverse shock parameters at t_\times . One can then apply the reverse shock scaling laws to derive reverse shock quantities. By comparing the reverse-to-forward shock flux ratio at t_\times , one can determine which component dominates for a specific frequency, see Figure 56 for example.

The numerous possible lightcurves in each phase make it impossible to draw all possible overall lightcurves. We therefore only draw a set of example lightcurves based on a standard set of parameters. In Figure 56, we present the “standard” afterglow light curves in radio (10^9 Hz), optical (10^{15} Hz) and X-ray (10^{17} Hz) bands, by adopting a set of typical parameter values: the total energy $E \sim 10^{52}$ erg, initial Lorentz factor $\Gamma_0 = 100$, width of ejecta $\Delta_0 = 10^{12}$ cm, jet opening angle $\theta_j = 0.1$,

electron distribution cannot be obtained analytically, we do not include these cases in the figures. Such electron pile-up condition is usually not satisfied in most models reviewed in this work. The only relevant model is the reverse shock model during the shock crossing phase for a wind medium, when A_* is large enough (Kobayashi et al., 2004; Gao et al., 2013a).

microphysics shock parameters $\epsilon_e = 0.1$, $\epsilon_B = 0.01$ and electron index $p = 2.3$ for both forward and reverse shocks. For the ISM model, we take $n_0 = 1 \text{ cm}^{-3}$, so that the reverse shock is non-relativistic and the system is in the thin-shell approximation. For the wind model, we take $A_* = 0.1$, the reverse shock is relativistic and the system is in the thick-shell approximation. More detailed studies on the standard models can be found in the literature (e.g. Sari et al., 1998a; Chevalier and Li, 2000; Granot and Sari, 2002; Wu et al., 2003; Kobayashi and Zhang, 2003a; Zou et al., 2005).

Several remarks regarding Fig.45 are worth addressing. 1. Only external shock afterglow light curves are plotted. If one includes the internal-origin “prompt” emission also, one would expect another component before t_x . There has been no observations in the radio band in this time frame. In the optical and X-ray band, this component is usually brighter than the external shock component, and hence, would mask the early phase of the lightcurves. After the cessation of the prompt emission, the lightcurve usually transits to the afterglow emission through a “steep decay” likely due to the high-latitude emission (e.g. as observed in the early X-ray afterglow detected with *Swift*, Tagliaferri et al., 2005; Zhang et al., 2006, 2007a). 2. The lightcurves are plotted with identical microphysics parameters ϵ_e and ϵ_B in the forward and reverse shocks. For the particular set of parameters adopted, the reverse shock flux is usually lower than that of forward shock in both radio and X-ray band, and it only dominates the forward shock emission in the optical band early on for a brief time. Observational data, on the other hand, require different microphysics parameters in the two shocks, in particular, a more magnetized reverse shock than the forward shock (Fan et al., 2002; Zhang et al., 2003; Kumar and Panaitescu, 2003a; Harrison and Kobayashi, 2013). This corresponds to the ISM models with enhanced reverse shock peaks in the optical and radio bands. Specifically, in the radio lightcurve (top-left panel), the reverse shock flux at t_{a+} is much brighter than the forward shock flux; in the optical band (mid-left panel), the reverse shock flux at t_x way exceeds the forward shock

flux, and even at t_{m+} the reverse shock flux is higher than that of forward shock, so that the optical flux shows a “flattening” behavior (Zhang et al., 2003). These are the “radio flares” and “optical flashes” as observed in some GRBs, such as GRB 990123 (Akerlof et al., 1999; Kulkarni et al., 1999; Kobayashi and Sari, 2000a). 3. Combining lightcurve features and spectral properties is essential to diagnose the physical origins of the afterglow emission. For example, the peaks of the light curves could be due to a hydro-dynamical origin (shock crossing or jet break) or crossing of a spectral break (ν_m or ν_a). The former should not be accompanied by a color change while the latter should. Taking spectral observations before and after a certain break time is therefore crucial to identify the correct model to interpret the data. The hydrodynamical breaks are also expected to be “achromatic”, i.e. occurring in all wavelengths, while the frequency crossing breaks should be chromatic. So simultaneous observations in all wavelengths are also important to diagnose the physics of afterglow emission. 4. Some light curve properties can be quickly applied to diagnose the properties of the ambient medium. For example, in the pre-jet-break phase, the wind model has a steeper slope than the ISM model. In the optical band, a fast-rising optical flash would point towards an ISM origin. In the radio band, a forward shock peak due to jet break (achromatic break with other bands such as optical) would point towards an ISM origin.

Limitations of the Analytical Models

Despite their great success, the analytical synchrotron external shock models are known to have certain limitations that hinder a precise description of GRB afterglows. In many situations, numerical calculations are needed. In this section we itemize all the limitations of the analytical approach, which serve as a caution to readers to apply the analytical models reviewed in this work.

- Swift observations suggest that X-ray flares observed in the afterglow phase can

be best modeled as internal emission of late central engine activities (Burrows et al., 2005a; Zhang et al., 2006; Fan and Wei, 2005a; Ioka et al., 2005; Lazzati and Perna, 2007; Maxham and Zhang, 2009). It is likely that some X-ray plateaus followed by steep decays (internal plateaus) are also caused by late central engine activities (Troja et al., 2007; Liang et al., 2007b; Lyons et al., 2010). A more extreme view interprets all the X-ray afterglow as emission from the central engine (Ghisellini et al., 2007; Kumar et al., 2008b,a). Therefore the external shock model discussed in this chapter is not relevant to interpret X-ray flares and internal X-ray plateaus, and possibly even the entire X-ray emission.

- A relativistic ejecta moving towards the observer has a complicated equal arrival time effect (Waxman, 1997c; Sari, 1998b; Panaitescu and Meszaros, 1998b; Granot et al., 1999), which smooths the spectral and temporal breaks (Granot and Sari, 2002). The sharp transition in the blastwave dynamics adopted in analytical models is also an approximation. As a result, the sharp breaks predicted in the analytical models usually do not exist.
- Since the strength of the shock is continuously decreasing as the blastwave decelerates, the magnetic field strengths continuously decay in the shocked region. Electrons therefore cool in a varying magnetic field, which leads to a very smooth or non-existence of ν_c (Uhm and Zhang, 2013b), see also van Eerten and Wijers (2009). In the fast cooling regime, exactly the same effect makes the fast cooling spectrum harder (Uhm and Zhang, 2013a) than $F_\nu \propto \nu^{-1/2}$ proposed by Sari et al. (1998a). In view of this, a sharp temporal or spectral break observed in GRB afterglow lightcurve or spectrum must not be associated with electron cooling (Uhm and Zhang, 2013b).
- All the analytical models reviewed in this article consider synchrotron radiation only. Synchrotron self-Compton (SSC) effect may be important in the

afterglow phase (Wei and Lu, 1998; Dermer et al., 2000b; Zhang and Mészáros, 2001b). Invoking synchrotron self-Compton (SSC) would complicate the matter. In particular, it would enhance cooling by a factor of $(1 + Y)$, where $Y = L_{\text{IC}}/L_{\text{syn}} = U_{\text{ph}}/U_{\text{B}}$, L_{IC} and L_{syn} are the luminosities of the SSC and synchrotron components, respectively, and U_{ph} and U_{B} are the energy densities of the synchrotron photons and magnetic fields, respectively. The detailed treatments of the SSC effect can be found in Sari and Esin (2001) and Gao et al. (2013a). During the reverse shock crossing phase, besides SSC in the reverse shock and forward shock regions, scattering of photons from the other shock by electrons from both shocked regions can be also important, which make more complicated spectra and lightcurves (Wang et al., 2001a,b).

- Only adiabatic models are reviewed in this work. In the literature, radiative models have been also discussed (e.g. Sari, 1997; Böttcher and Dermer, 2000). However, since ϵ_e is usually small, a GRB blastwave cannot be fully radiative even if electrons are in the fast cooling regime. A partially radiative fireball and its dynamical evolution have been discussed by various authors (e.g. Huang et al., 1999, 2000; Pe’er, 2012; Nava et al., 2012) and the detailed lightcurves of these cases have been calculated by Wu et al. (2005).
- Numerical simulations are needed to well describe the transitions among various phases. For example, the analytical models in Phase 1 (reverse shock crossing phase) and Phase 2 (self-similar phase) do not match exactly. After reverse shock crossing, how the blastwave self-adjusts itself to the Blandford-McKee profile can be only addressed by numerical simulations (e.g. Kobayashi and Sari, 2000a). Sideway expansion after the “jet break” phase and the transition from the ultra-relativistic phase to deep Newtonian phase all need numerical simulations to resolve the details (Cannizzo et al., 2004; Zhang and MacFadyen,

2009; van Eerten and MacFadyen, 2012).

- The lightcurves involving collimated jets are complicated and usually require numerical treatments. Even for a uniform jet, the shape of the jet break may depend on the viewing angle from the jet axis (Granot et al., 2002; van Eerten and MacFadyen, 2012). If the viewing angle is outside the jet cone, one expects a variety of lightcurves for the so-called “orphan afterglows”, which cannot be properly addressed analytically. More complicated jets invoke angular structure with decreasing luminosity and Lorentz factor with respect to the jet axis (Mészáros et al., 1998). The commonly discussed jet structures include power law (Mészáros et al., 1998), Gaussian (Zhang et al., 2004b), and two-component conical jets (Berger et al., 2003; Racusin et al., 2008). An on-axis observer would see a steeper lightcurve than the isotropic case (Mészáros et al., 1998; Dai and Gou, 2001b; Panaitescu, 2005). For an off-axis observer (Rossi et al., 2002; Zhang and Mészáros, 2002a), the lightcurve may show a jet-break-like feature as the jet axis enters the field of view, but the exact shape of the break depends on the angular structure of the jet and the viewing angle (Kumar and Granot, 2003b; Granot and Kumar, 2003). The two-component jets can show more complicated lightcurve behaviors (Huang et al., 2004; Peng et al., 2005).
- It is possible that due to continuous energy injection or ejecta Lorentz factor stratification, a long-lived reverse shock may continue to exist, and the blastwave never enters the Blandford-McKee phase. The long-lasting reverse shock can show rich afterglow lightcurve features (Uhm et al., 2012), which may show up above the forward shock contribution if the reverse shock emission is enhanced. A more extreme view is that the entire observed afterglow is of a reverse shock origin (Uhm and Beloborodov, 2007; Genet et al., 2007).

- Analyses of early afterglow data (Fan et al., 2002; Zhang et al., 2003; Kumar and Panaitescu, 2003a) and theoretical considerations (Usov, 1992; Mészáros and Rees, 1997b; Metzger et al., 2011; Lei et al., 2013) suggest that the GRB central engine is likely magnetized. The GRB ejecta therefore likely carries a certain degree of magnetization. The reverse shock models presented here apply to low-magnetization cases. For moderate to high magnetization, the shock jump conditions and the strength of reverse shock are modified (Zhang and Kobayashi, 2005; Fan et al., 2004), and numerical simulations are needed to achieve precise results (Mimica et al., 2009). Also numerical simulations (Sironi and Spitkovsky, 2009) suggest that electron acceleration becomes suppressed in a magnetized shock, which would also affect the predicted synchrotron radiation flux.
- All the models invoke constant microphysics parameters ϵ_e and ϵ_B . In principle, these parameters may evolve with time also, and some authors have considered such more complicated models (e.g. Ioka et al., 2006; Fan and Piran, 2006a).
- More complicated afterglow models invoke density bumps (Dai and Lu, 2002; Dai and Wu, 2003; Nakar and Granot, 2007), violent energy injection into the blastwave via collision from a fast shell ejected at late times (Zhang and Mészáros, 2002b; Geng et al., 2013), and patchy jets (Kumar and Piran, 2000b; Ioka et al., 2005).
- Finally, in the early afterglow phase, additional physical processes may modify the blastwave dynamics. These include pair loading effect caused by interaction between radiation front and ambient medium (Madau and Thompson, 2000; Mészáros et al., 2001; Beloborodov, 2002) and neutron decay effect from a neutron-rich ejecta (Derishev et al., 2001; Beloborodov, 2003; Fan et al., 2005b).

Initial characteristic frequency order	Phase 1						Phase 2	Phase 4
	Thin shell			Thick shell				
	FS	RS _{pre}	RS _{post}	FS	RS _{pre}	RS _{post}		
$\nu_a < \nu_m < \nu_c$ (ISM)	1 – 2	5	8	10	13	16	18	22
$\nu_a < \nu_c < \nu_m$ (ISM)	3	6	--	11	14	--	19 – 20	--
$\nu_m < \nu_a < \nu_c$ (ISM)	4	7	9	12	15	17	21	23
$\nu_a < \nu_m < \nu_c$ (Wind)	24	27	30	32	35	38	40	43
$\nu_a < \nu_c < \nu_m$ (Wind)	25	28	--	33	36	--	41	--
$\nu_m < \nu_a < \nu_c$ (Wind)	26	29	31	34	37	39	42	44

Table 26 Collection of figure numbers corresponding to different dynamical models and initial spectra regimes.

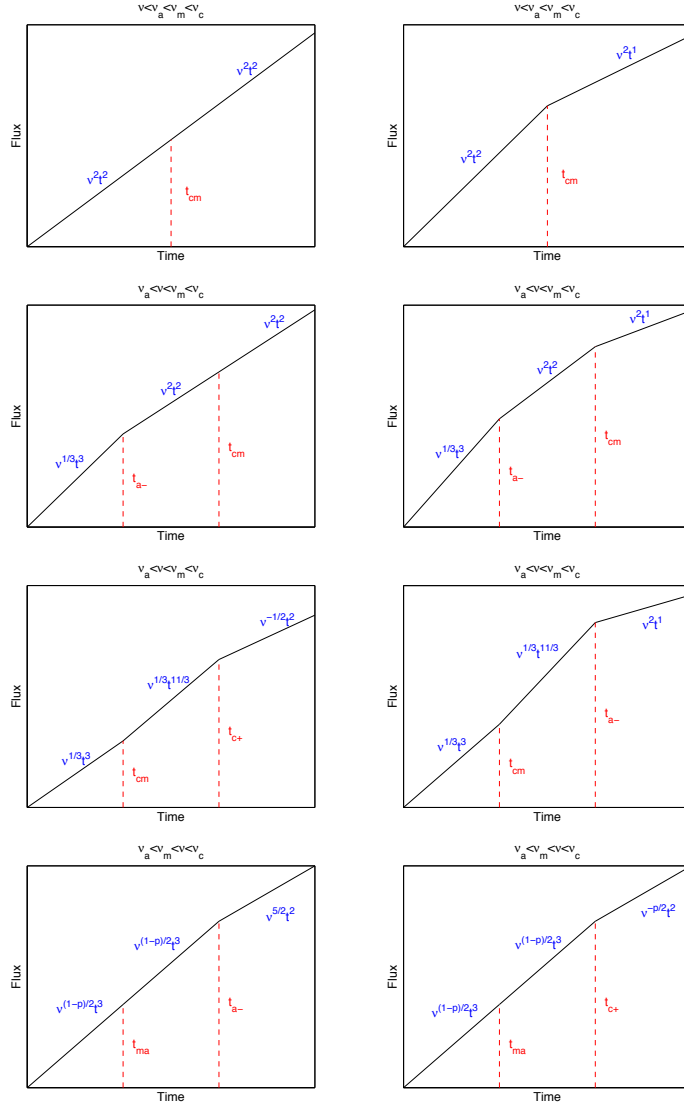


Figure 12 All possible forward shock lightcurves during Phase 1 (reverse shock crossing phase), for thin shell ISM model and the initial characteristic frequency order $\nu_a < \nu_m < \nu_c$. The notations t_{i+} , $i = a, m, c$ denote frequency regime change from $\nu_i > \nu$ to $\nu_i < \nu$; t_{i-} , $i = a, m, c$ denote frequency regime change from $\nu_i < \nu$ to $\nu_i > \nu$; t_{ij} , $\{i, j\} = a, m, c$ denote frequency regime change from $\nu_i > \nu_j$ to $\nu_i < \nu_j$. The title for each sub-figure is the initial spectral regime of the observed frequency ν .

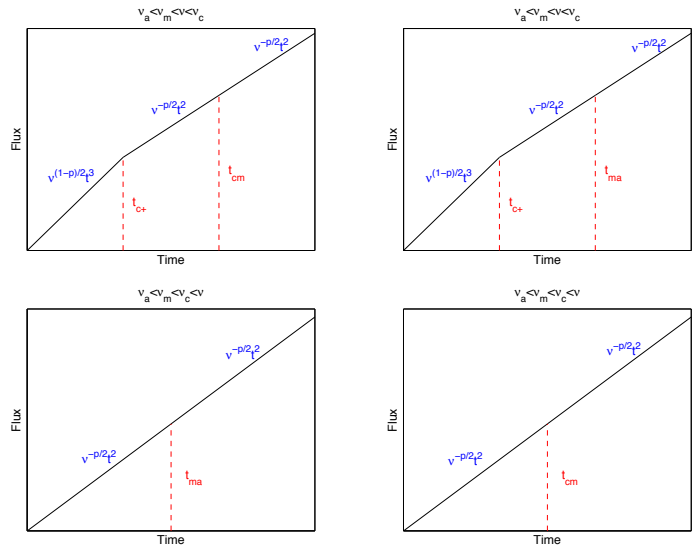


Figure 13 Figure 12 continued.

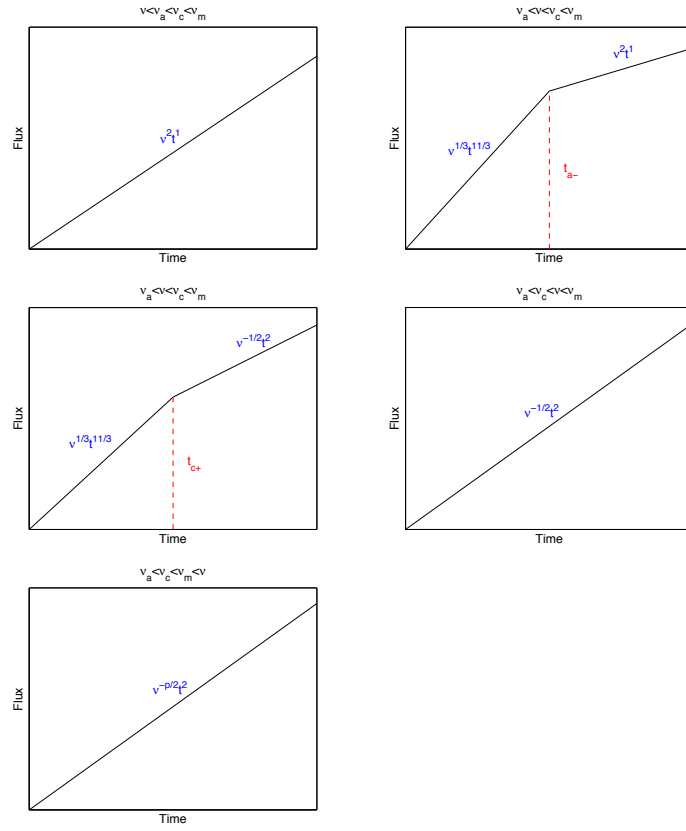


Figure 14 Same as Fig. 12, but with the initial characteristic frequency order $\nu_a < \nu_c < \nu_m$.

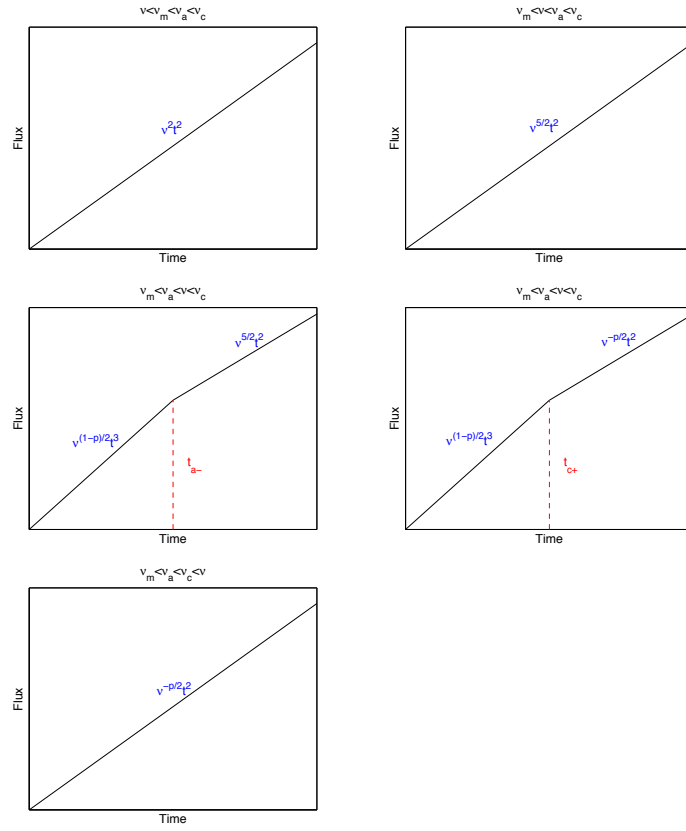


Figure 15 Same as Fig. 12, but with the initial characteristic frequency order $\nu_m < \nu_a < \nu_c$.

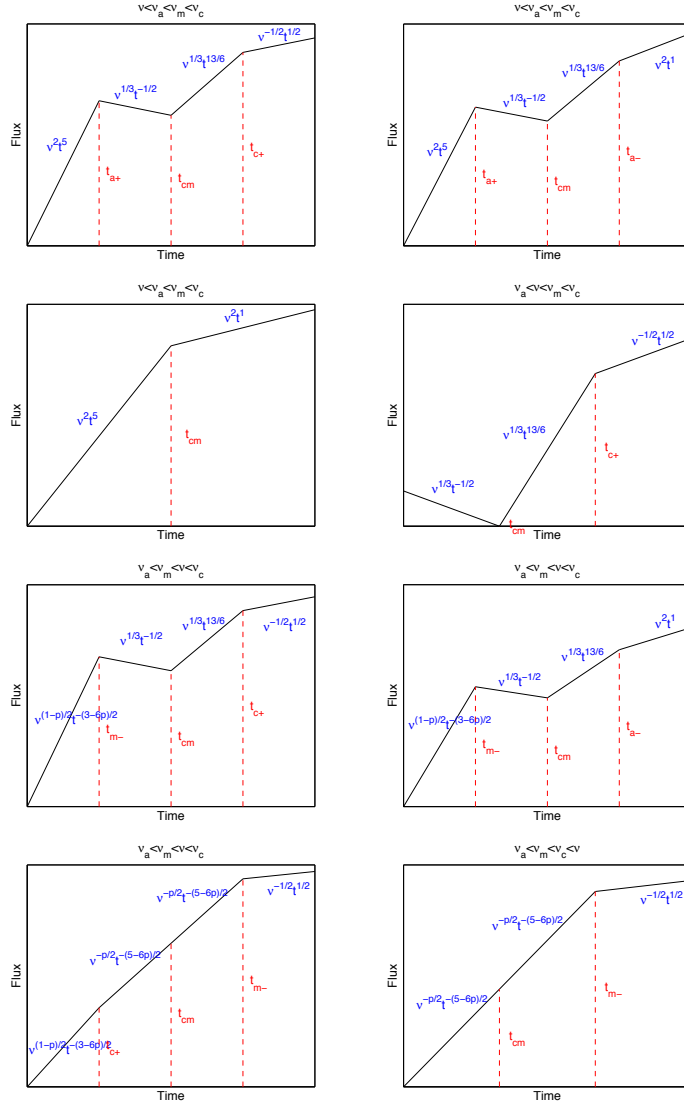


Figure 16 All possible reverse shock lightcurves during Phase 1 (reverse shock crossing phase), for thin shell ISM model and the initial characteristic frequency order $\nu_a < \nu_m < \nu_c$.

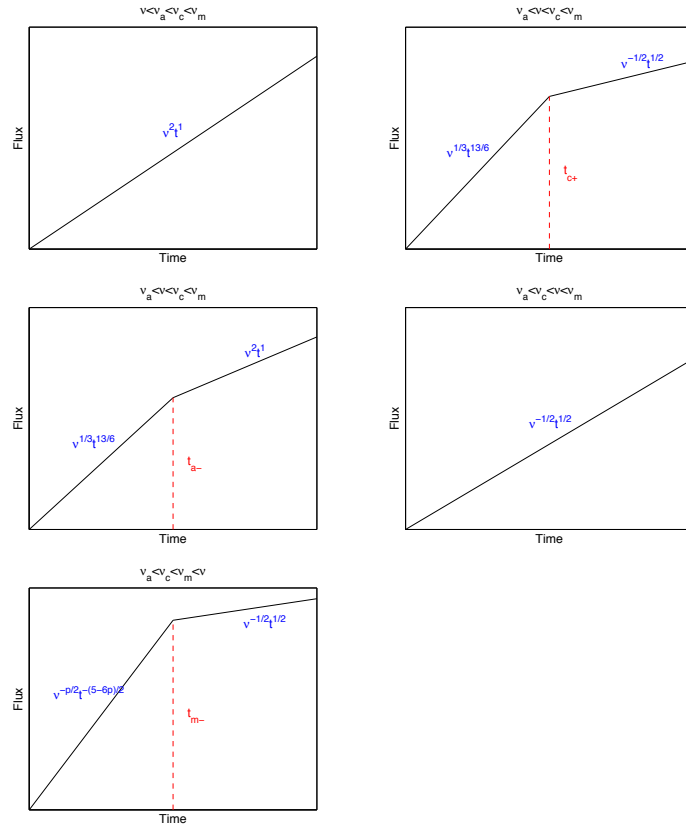


Figure 17 Same as Fig. 16, but with the initial characteristic frequency order $\nu_a < \nu_c < \nu_m$.

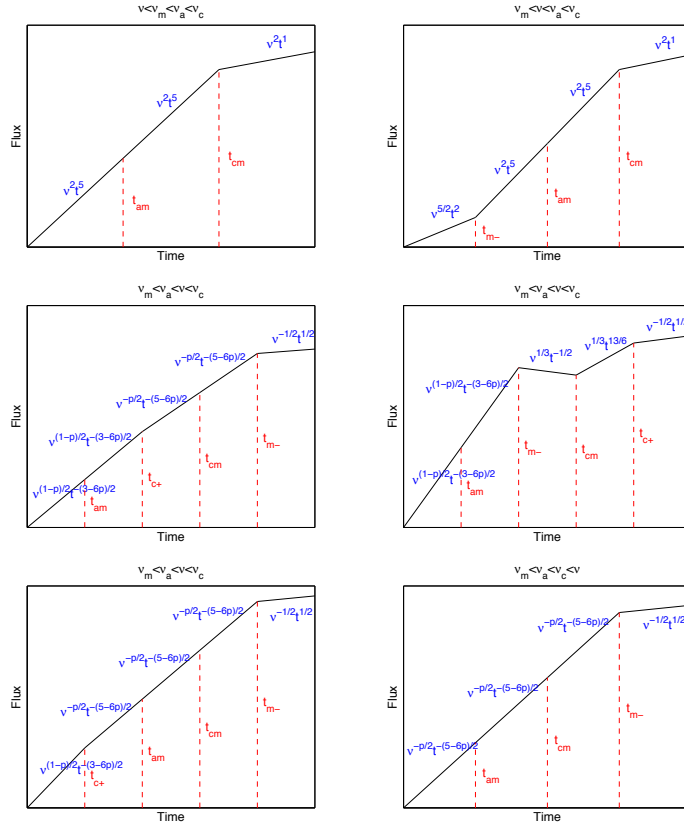


Figure 18 Same as Fig. 16, but with the initial characteristic frequency order $\nu_m < \nu_a < \nu_c$.

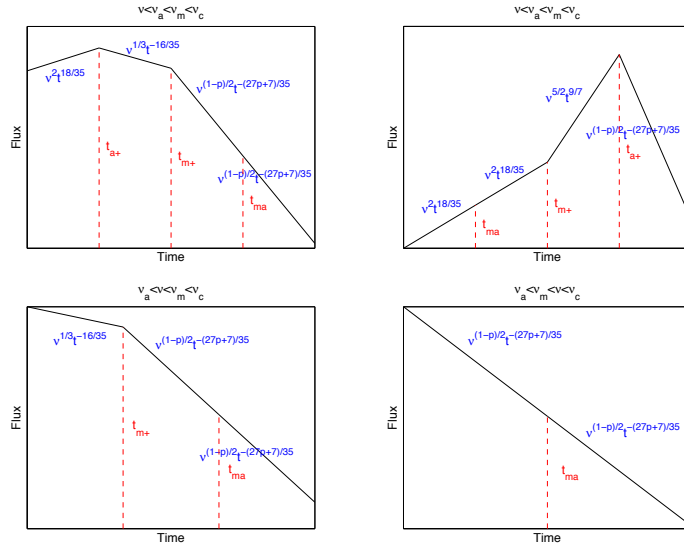


Figure 19 All possible reverse shock lightcurves after reverse shock crossing the shell, for thin shell ISM model and the initial characteristic frequency order $\nu_a < \nu_m < \nu_c$.

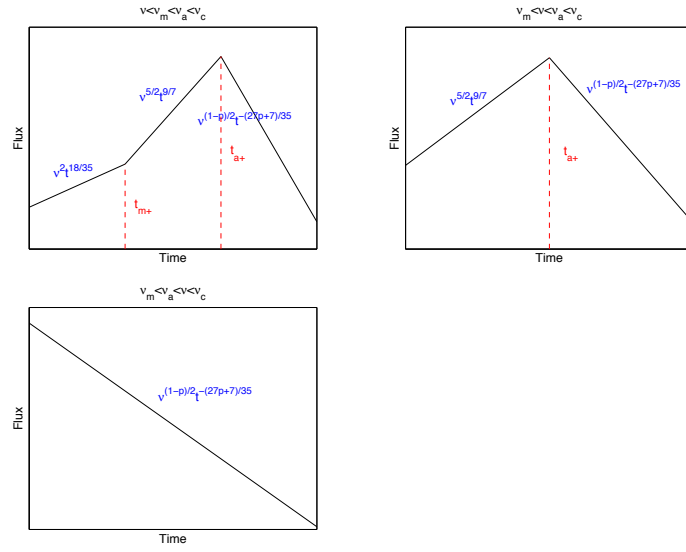


Figure 20 Same as Fig. 19, but with the initial characteristic frequency order $\nu_m < \nu_a < \nu_c$.

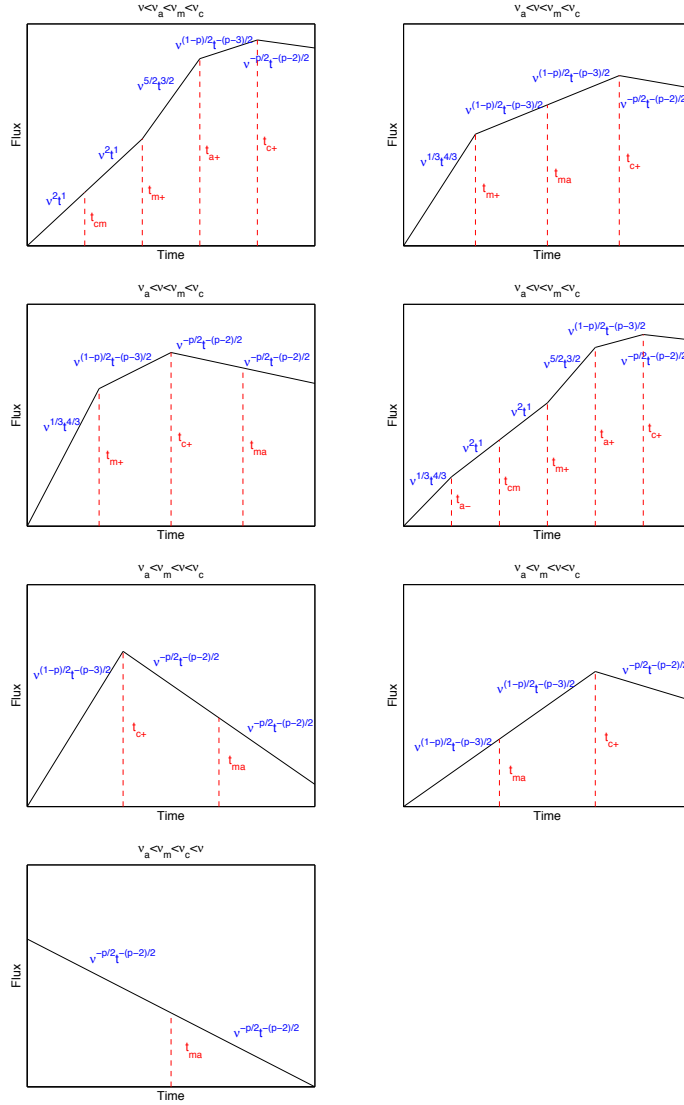


Figure 21 All possible forward shock lightcurves during Phase 1 (reverse shock crossing phase), for thick shell ISM model and the initial characteristic frequency order $\nu_a < \nu_m < \nu_c$.

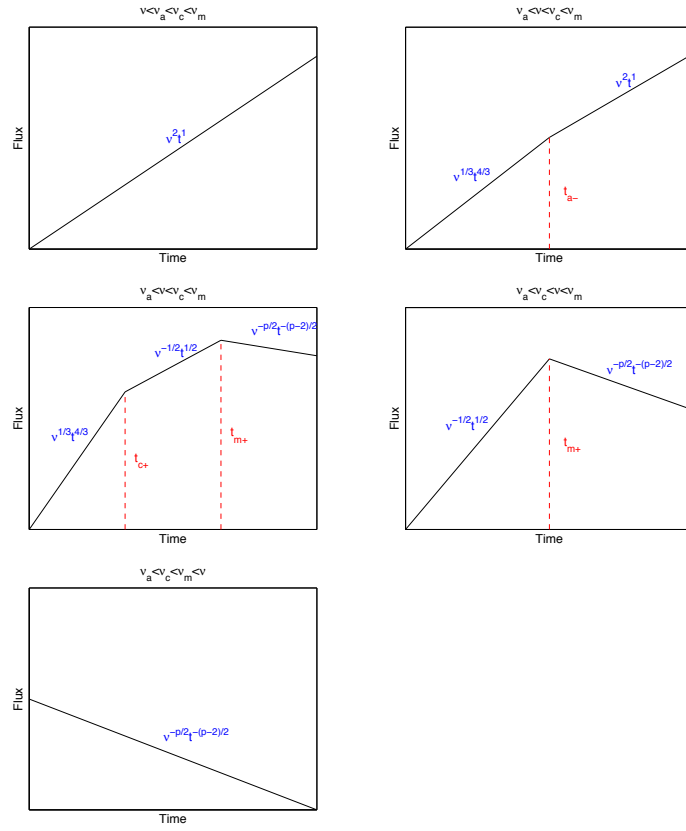


Figure 22 Same as Fig. 21, but with the initial characteristic frequency order $\nu_a < \nu_c < \nu_m$.

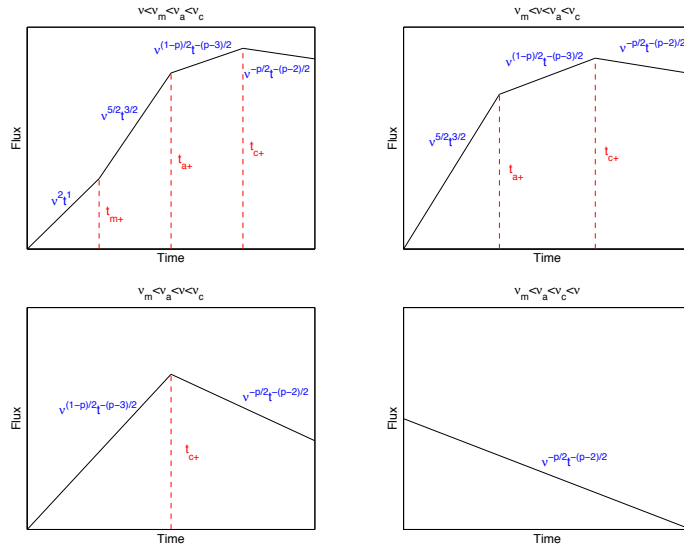


Figure 23 Same as Fig. 21, but with the initial characteristic frequency order $\nu_m < \nu_a < \nu_c$.

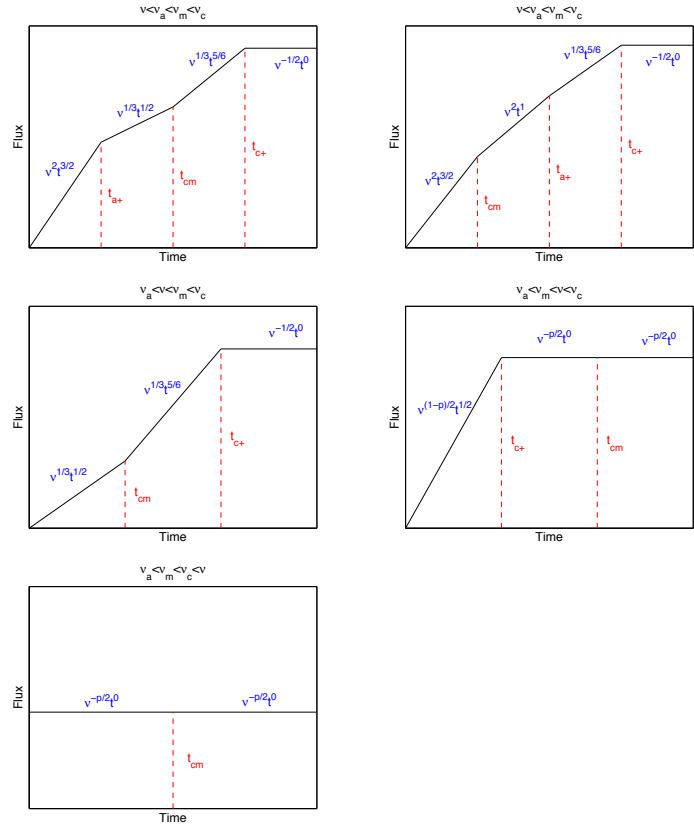


Figure 24 All possible reverse shock lightcurves during Phase 1 (reverse shock crossing phase), for thick shell ISM model and the initial characteristic frequency order $\nu_a < \nu_m < \nu_c$.

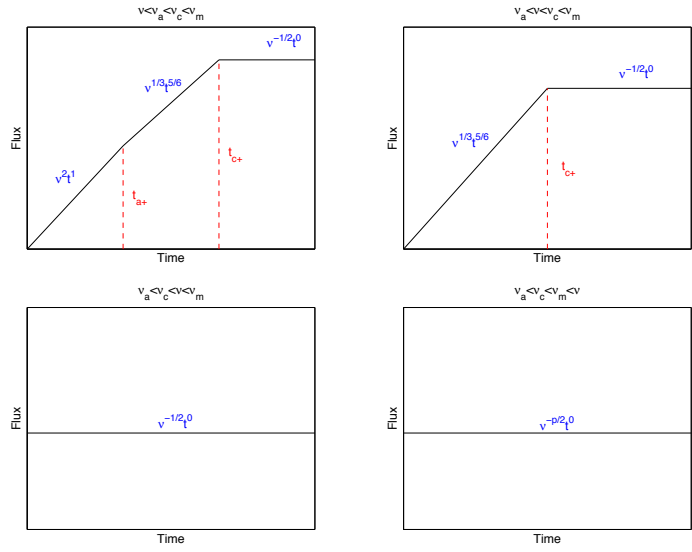


Figure 25 Same as Fig. 24, but with the initial characteristic frequency order $\nu_a < \nu_c < \nu_m$.

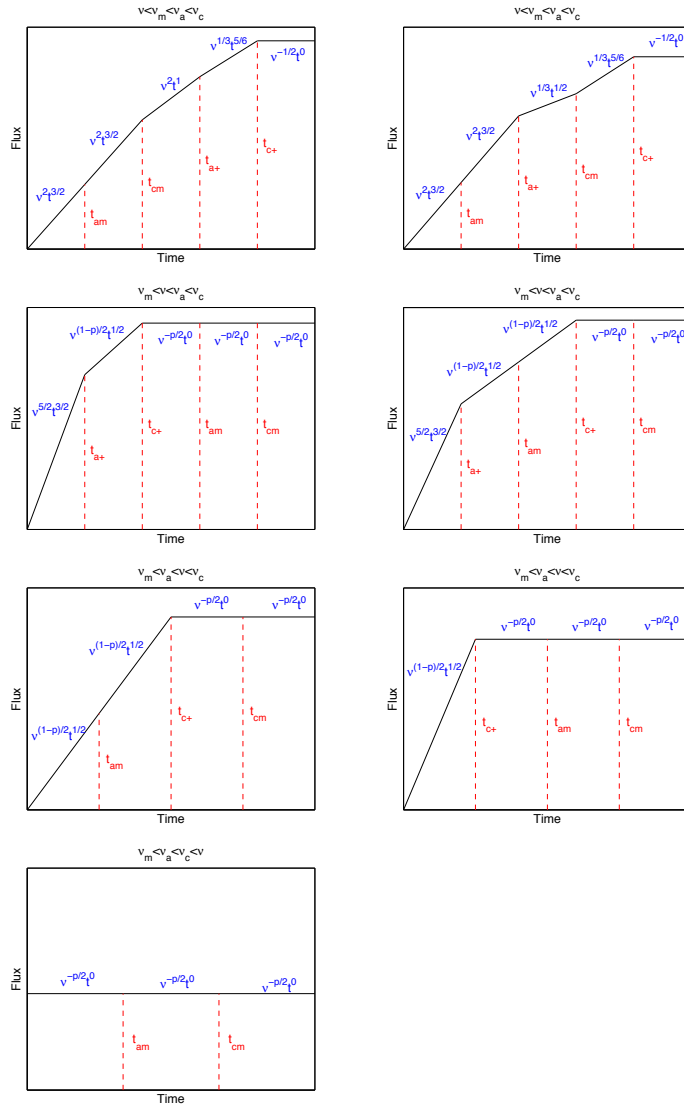


Figure 26 Same as Fig. 24, but with the initial characteristic frequency order $\nu_m < \nu_a < \nu_c$.

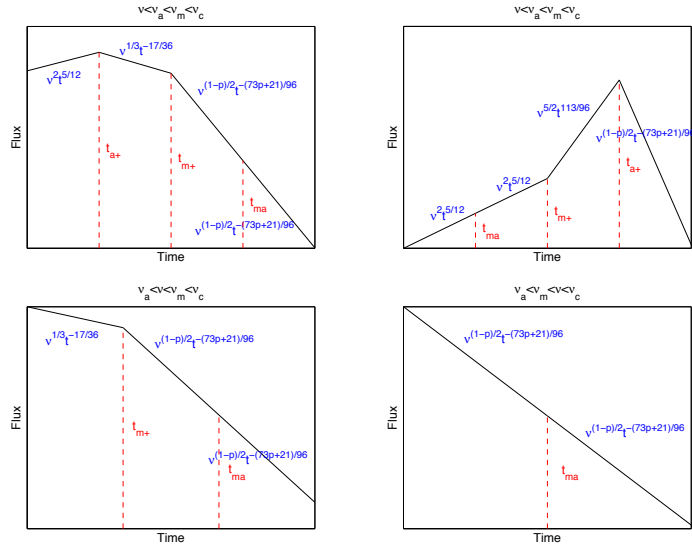


Figure 27 All possible reverse shock lightcurves after reverse shock crosses the shell, for thick shell ISM model and the initial characteristic frequency order $\nu_a < \nu_m < \nu_c$.

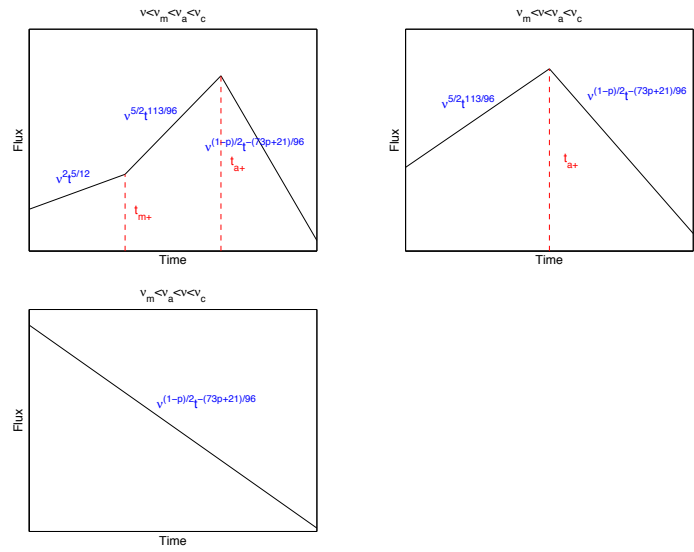


Figure 28 Same as Fig. 27, but with the initial characteristic frequency order $\nu_m < \nu_a < \nu_c$.

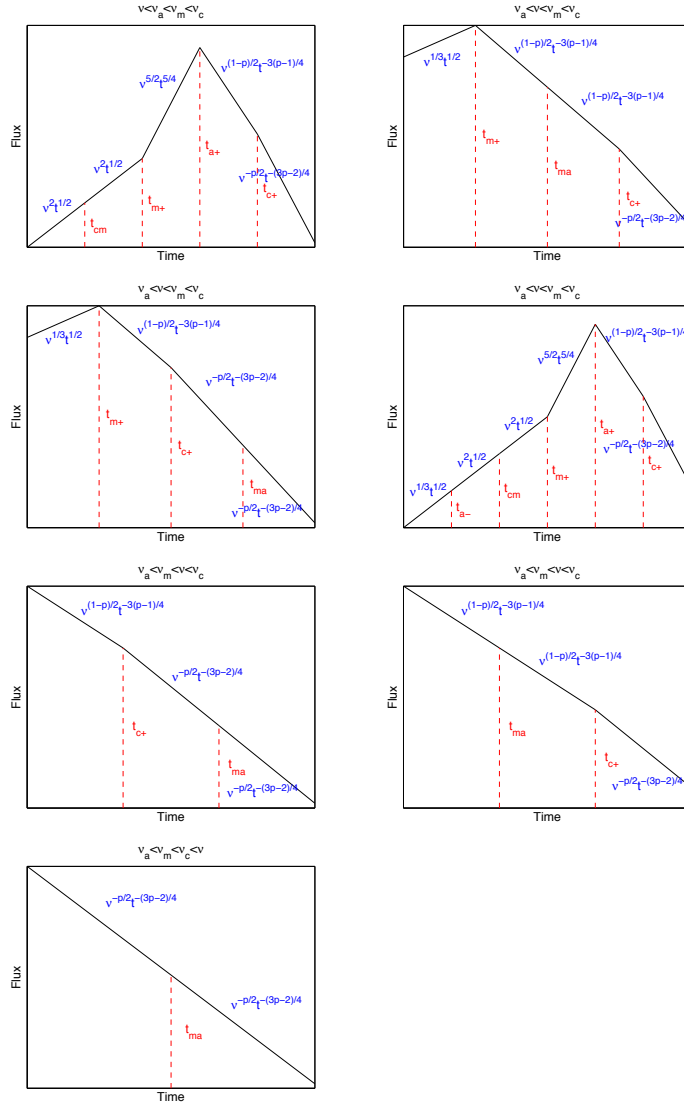


Figure 29 All possible forward shock lightcurves during Phase 2 (relativistic, isotropic, self-similar deceleration phase), with an ISM medium and initial characteristic frequency order $\nu_a < \nu_m < \nu_c$.

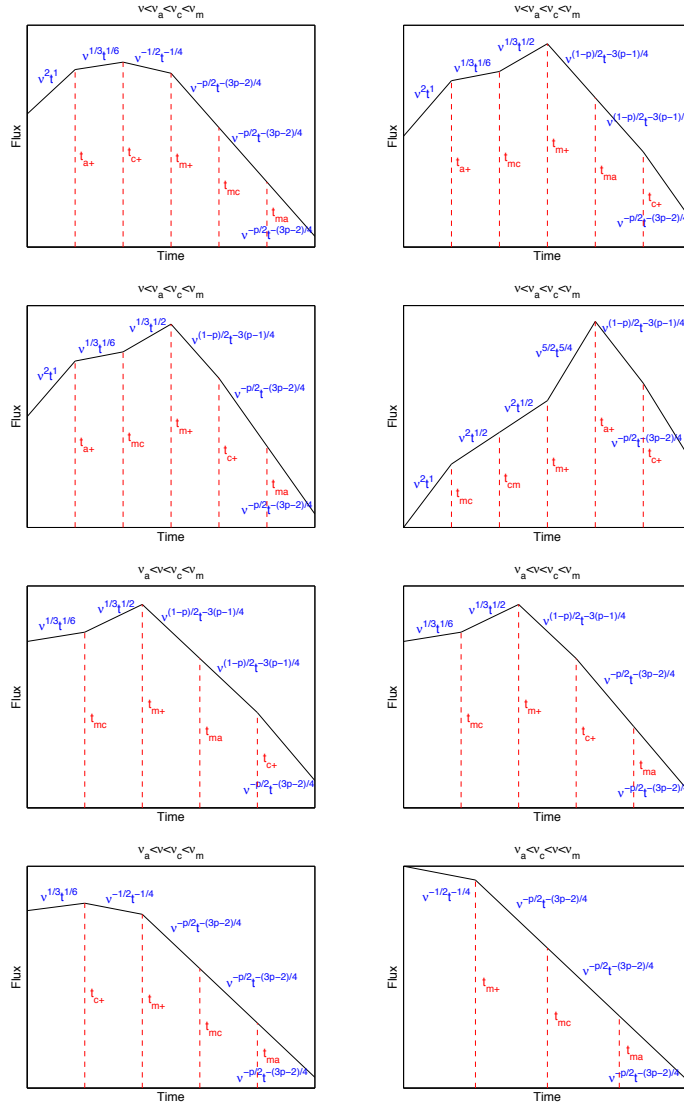


Figure 30 Same as Fig. 29, but with the initial characteristic frequency order $\nu_a < \nu_c < \nu_m$.

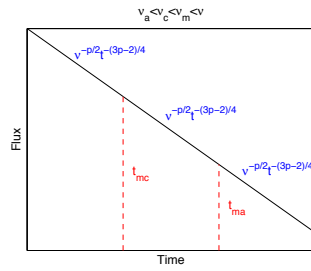


Figure 31 Figure 30 continued.

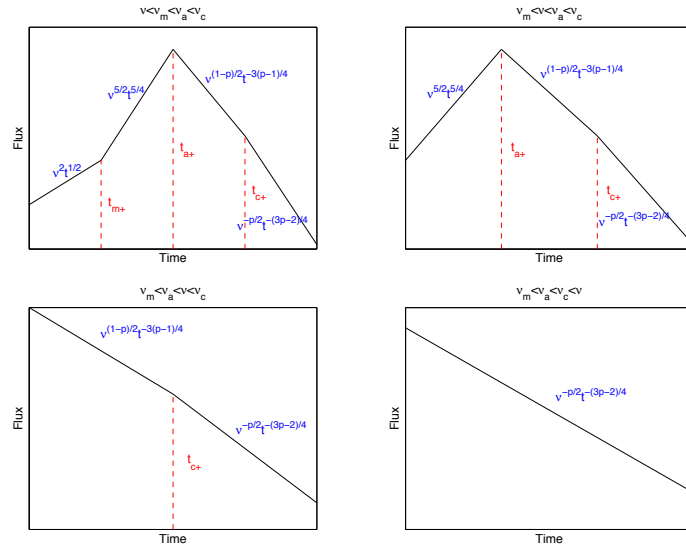


Figure 32 Same as Fig. 29, but with the initial characteristic frequency order $\nu_m < \nu_a < \nu_c$.

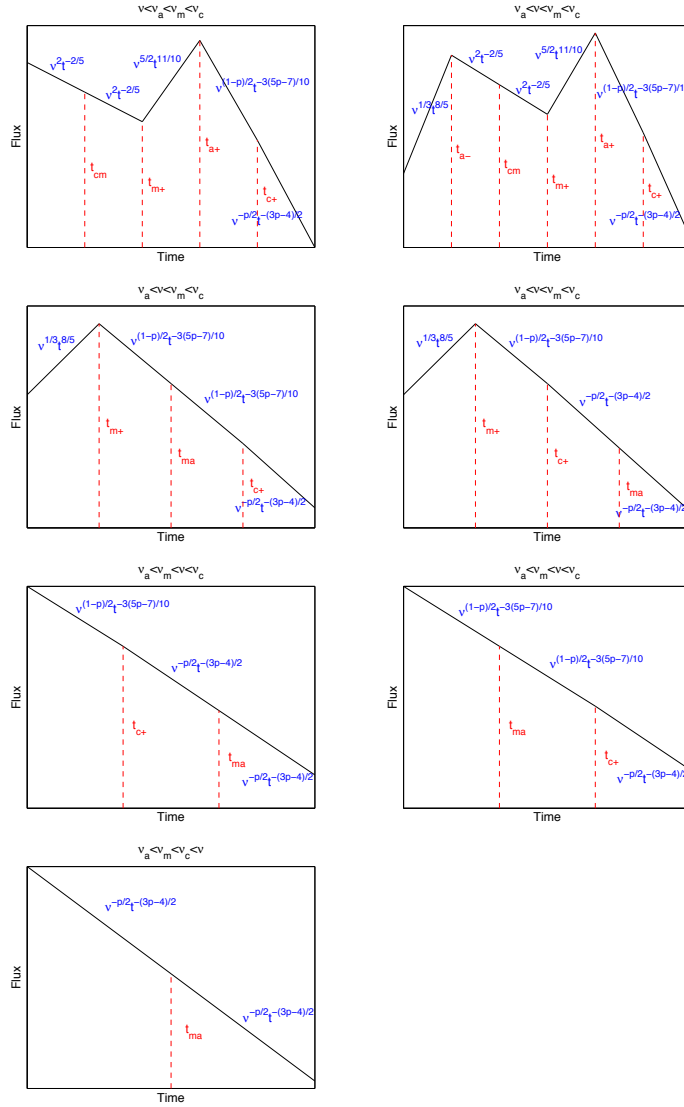


Figure 33 All possible forward shock lightcurves during Phase 4 (Newtonian phase), with an ISM medium and initial characteristic frequency order $\nu_a < \nu_m < \nu_c$.

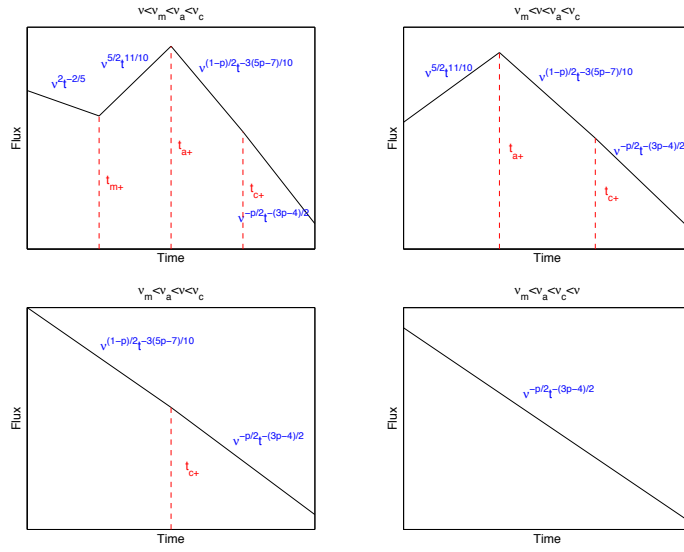


Figure 34 Same as Fig. 33, but with the initial characteristic frequency order $\nu_m < \nu_a < \nu_c$.

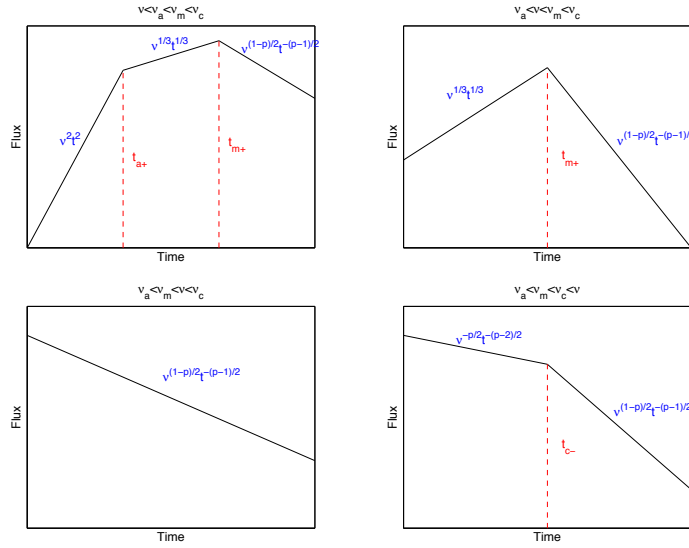


Figure 35 All possible forward shock lightcurves during Phase 1 (reverse shock crossing phase), for thin shell wind model and the initial characteristic frequency order $\nu_a < \nu_m < \nu_c$.

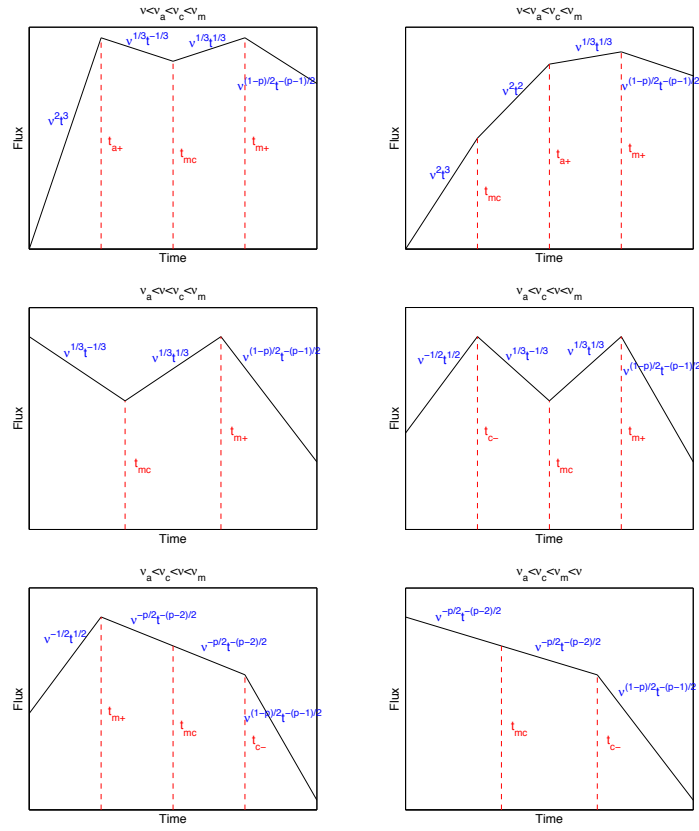


Figure 36 Same as Fig. 35, but with the initial characteristic frequency order $\nu_a < \nu_c < \nu_m$.

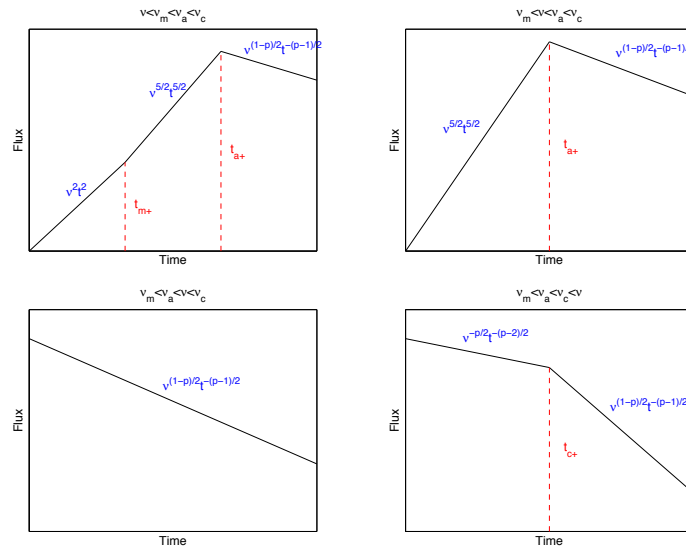


Figure 37 Same as Fig. 35, but with the initial characteristic frequency order $\nu_m < \nu_a < \nu_c$.

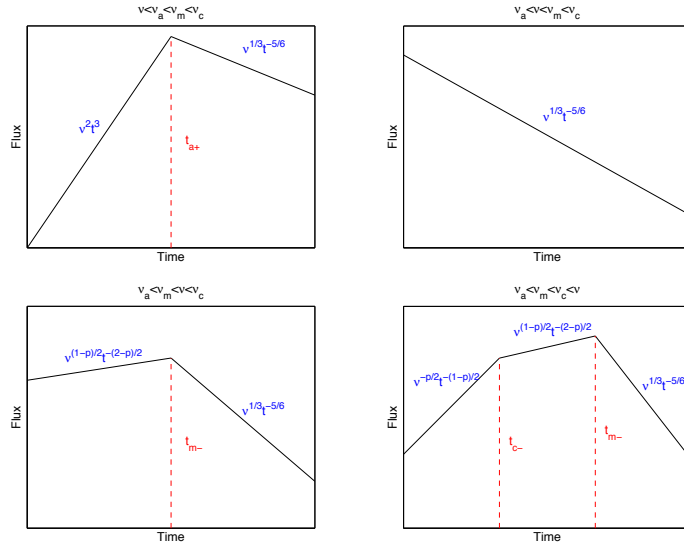


Figure 38 All possible reverse shock lightcurves during Phase 1 (reverse shock crossing phase), for thin shell wind model and the initial characteristic frequency order $\nu_a < \nu_m < \nu_c$.

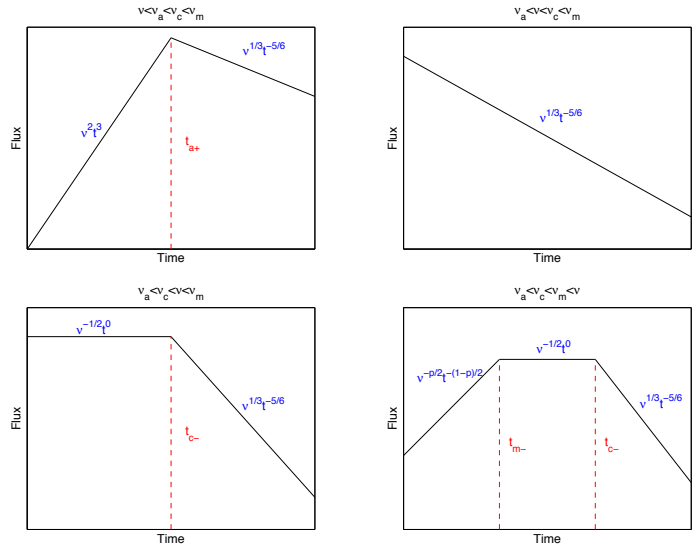


Figure 39 Same as Fig. 38, but with the initial characteristic frequency order $\nu_a < \nu_c < \nu_m$.

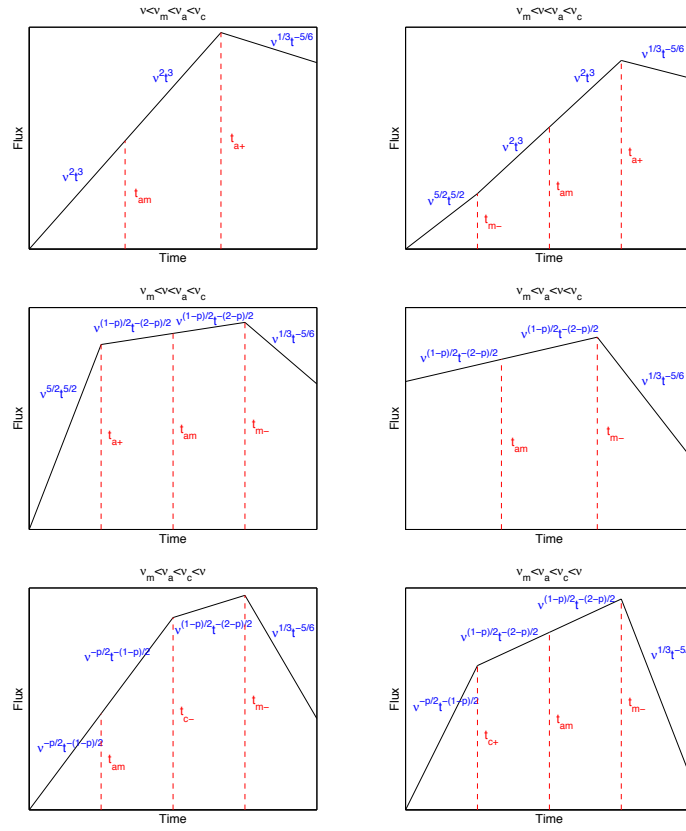


Figure 40 Same as Fig. 38, but with the initial characteristic frequency order $\nu_m < \nu_a < \nu_c$.

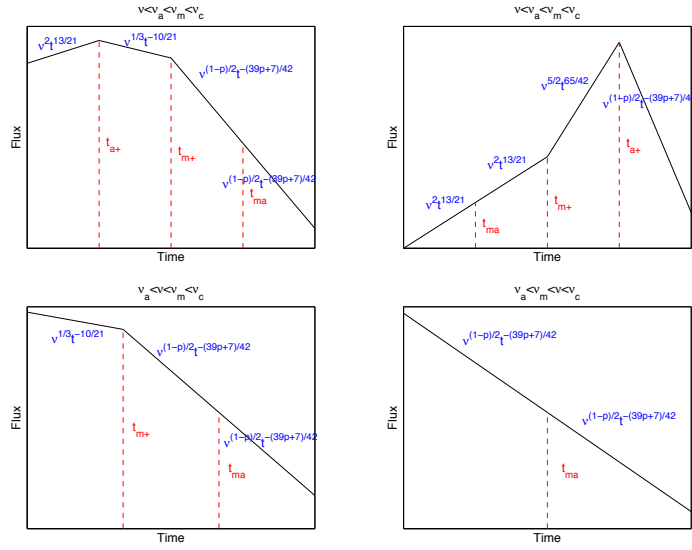


Figure 41 All possible reverse shock lightcurves after reverse shock crossing, for thin shell wind model and the initial characteristic frequency order $\nu_a < \nu_m < \nu_c$.

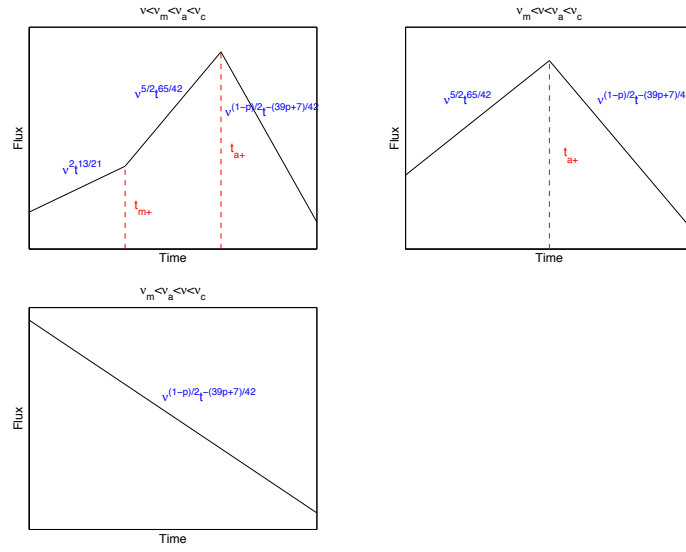


Figure 42 Same as Fig. 41, but with the initial characteristic frequency order $\nu_m < \nu_a < \nu_c$.

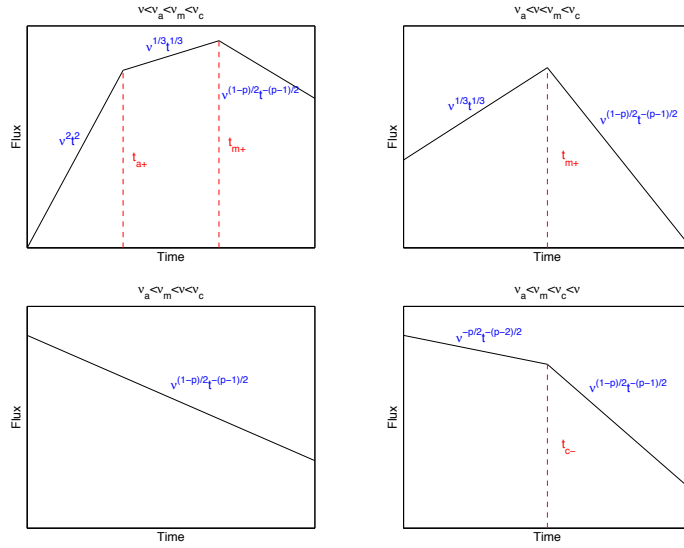


Figure 43 All possible forward shock lightcurves during Phase 1 (reverse shock crossing phase), for thick shell wind model and the initial characteristic frequency order $\nu_a < \nu_m < \nu_c$.

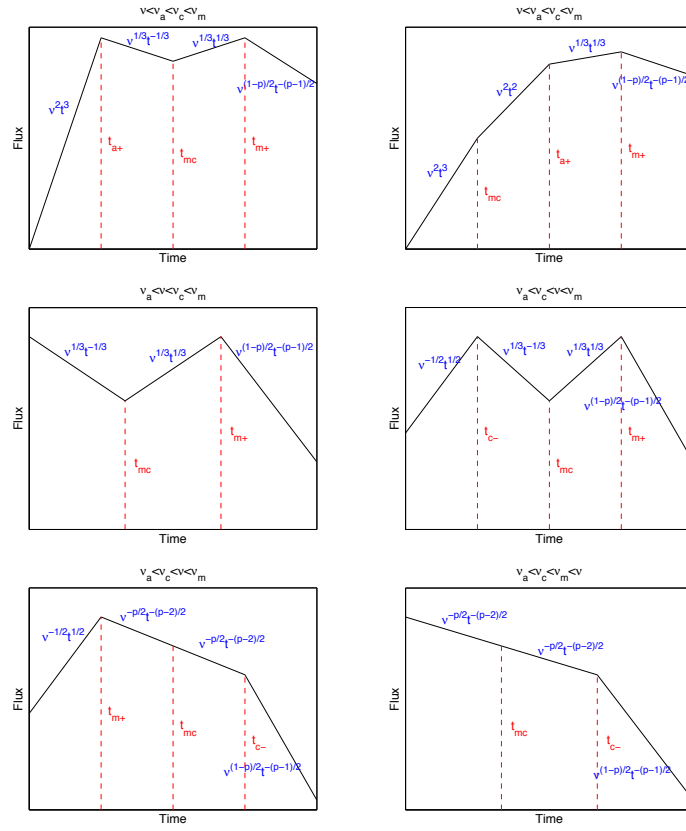


Figure 44 Same as Fig. 43, but with the initial characteristic frequency order $\nu_a < \nu_c < \nu_m$.

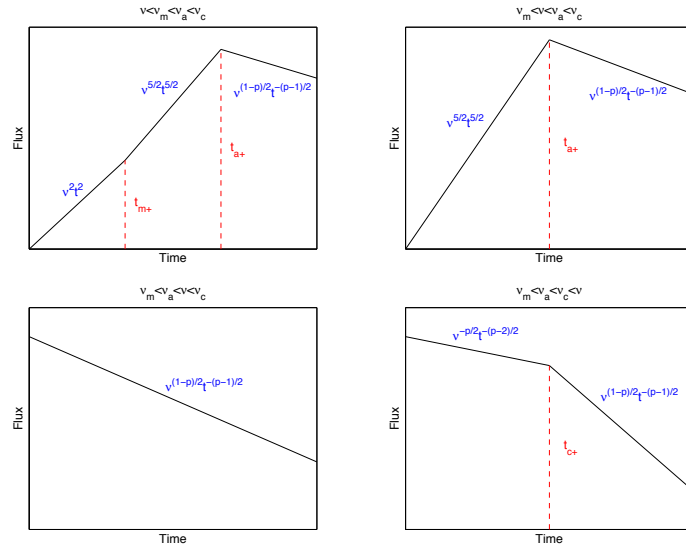


Figure 45 Same as Fig. 43, but with the initial characteristic frequency order $\nu_m < \nu_a < \nu_c$.

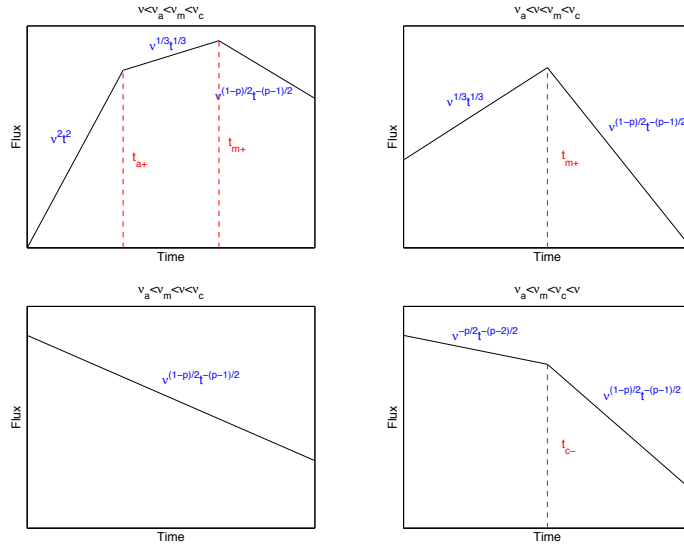


Figure 46 All possible reverse shock lightcurves during Phase 1 (reverse shock crossing phase), for thick shell wind model and the initial characteristic frequency order $\nu_a < \nu_m < \nu_c$.

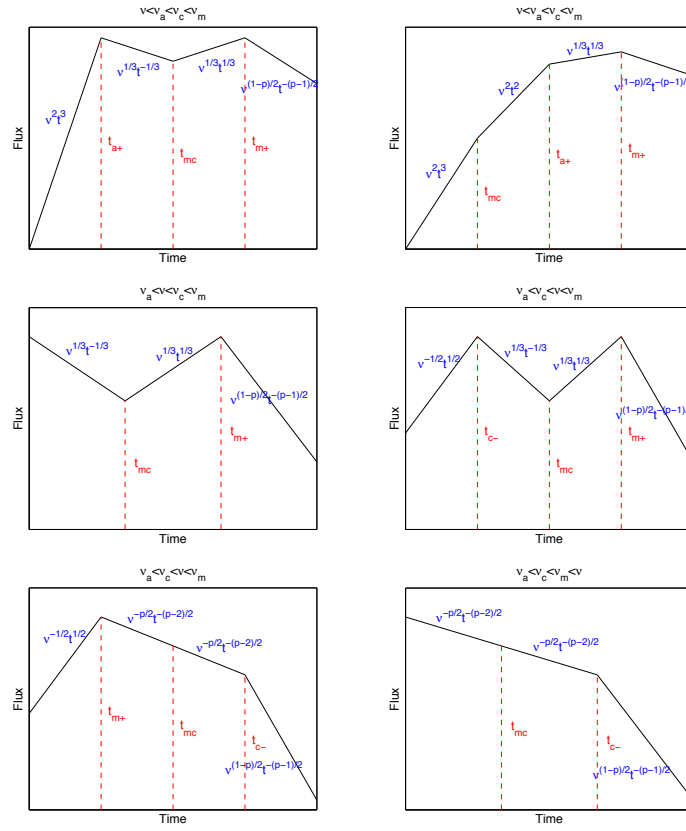


Figure 47 Same as Fig. 46, but with the initial characteristic frequency order $\nu_a < \nu_c < \nu_m$.

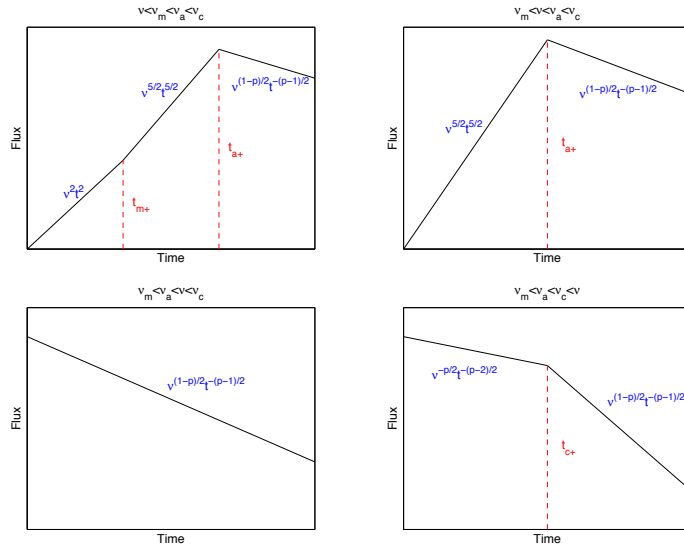


Figure 48 Same as Fig. 46, but with the initial characteristic frequency order $\nu_m < \nu_a < \nu_c$.

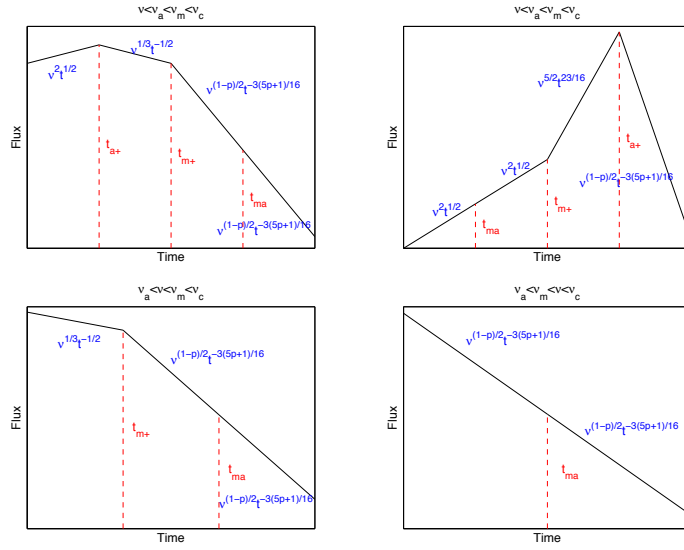


Figure 49 All possible reverse shock lightcurves after reverse shock crossing, for thick shell wind model and the initial characteristic frequency order $\nu_a < \nu_m < \nu_c$.

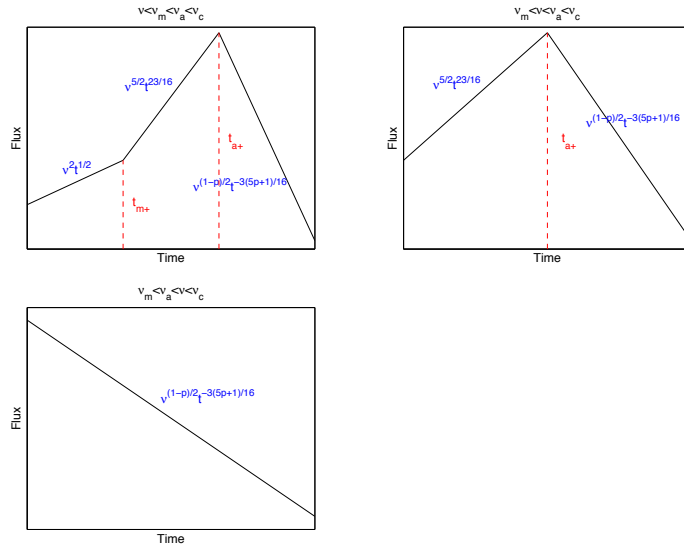


Figure 50 Same as Fig. 49, but with the initial characteristic frequency order $\nu_m < \nu_a < \nu_c$.

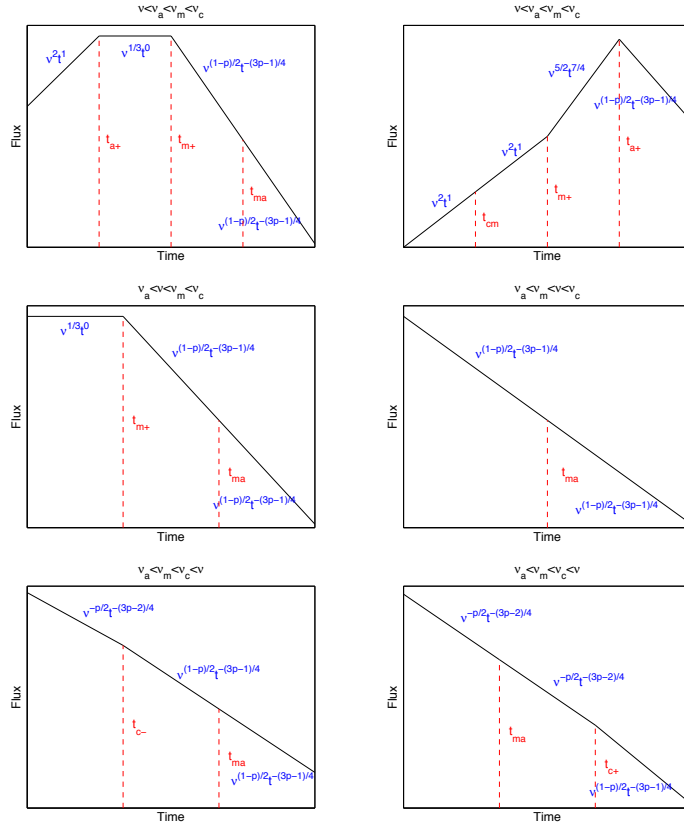


Figure 51 All possible forward shock lightcurves during Phase 2 (relativistic, isotropic, self-similar deceleration phase), for a wind medium and the initial characteristic frequency order $\nu_a < \nu_m < \nu_c$.

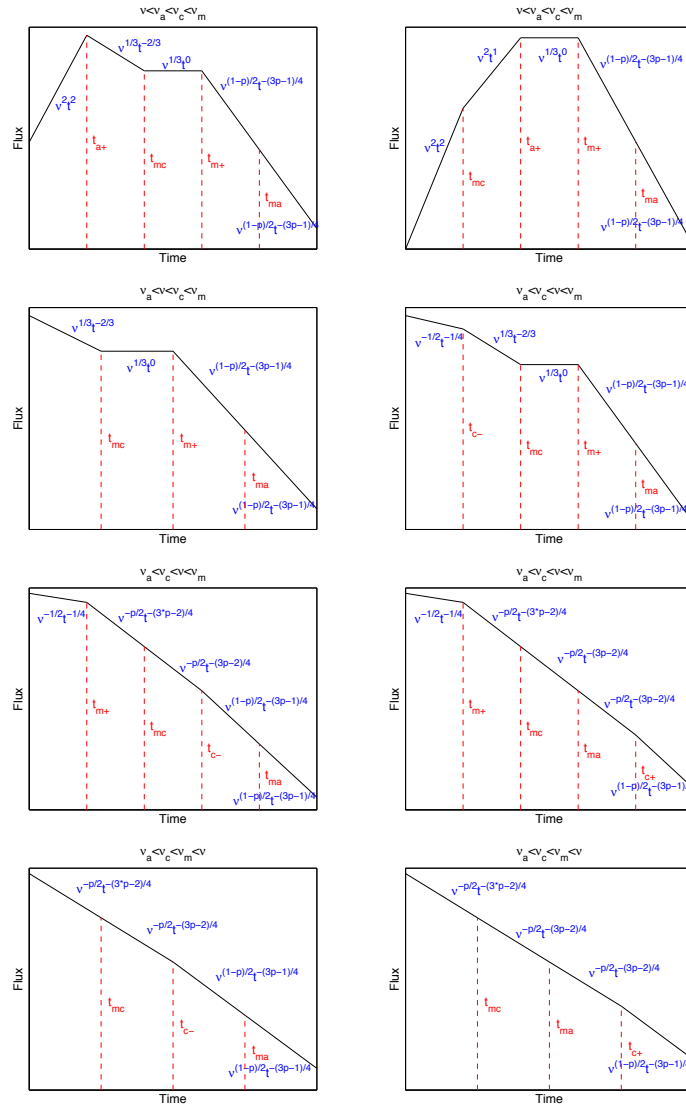


Figure 52 Same as Fig. 51, but with the initial characteristic frequency order $\nu_a < \nu_c < \nu_m$.

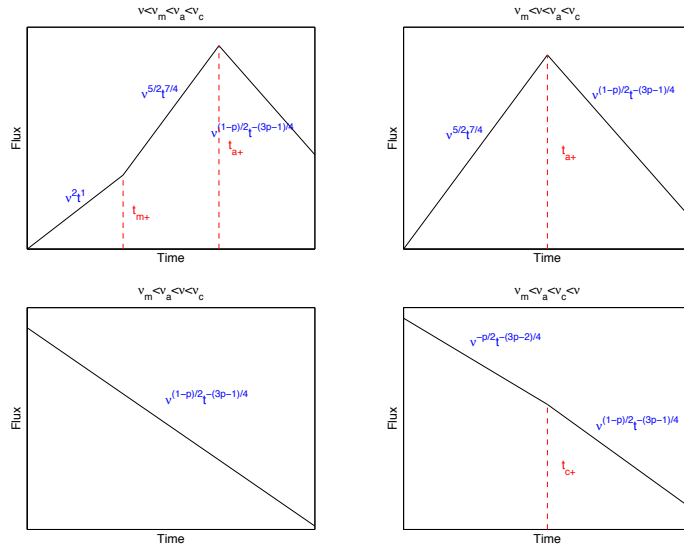


Figure 53 Same as Fig. 51, but with the initial characteristic frequency order $\nu_m < \nu_a < \nu_c$.

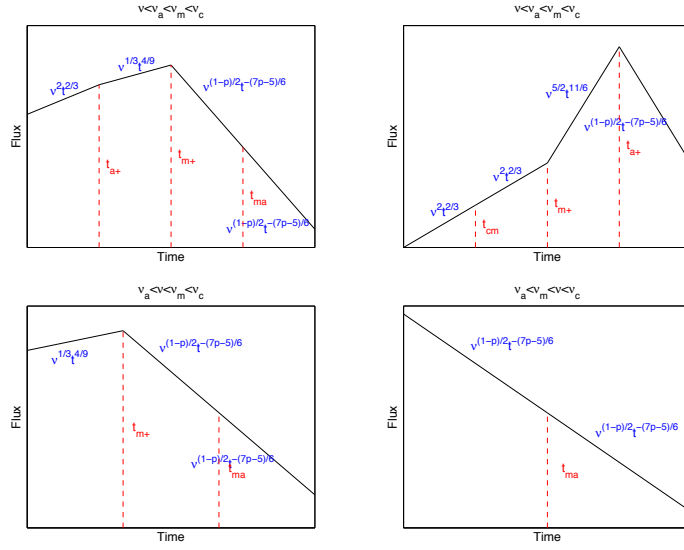


Figure 54 All possible forward shock lightcurves during Phase 4 (Newtonian phase), for a wind medium and the initial characteristic frequency order $\nu_a < \nu_m < \nu_c$.

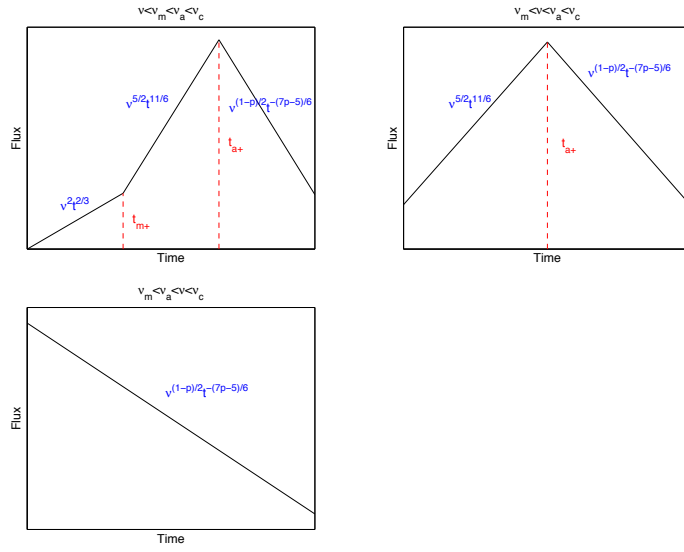


Figure 55 Same as Fig. 54, but with the initial characteristic frequency order $\nu_m < \nu_a < \nu_c$.

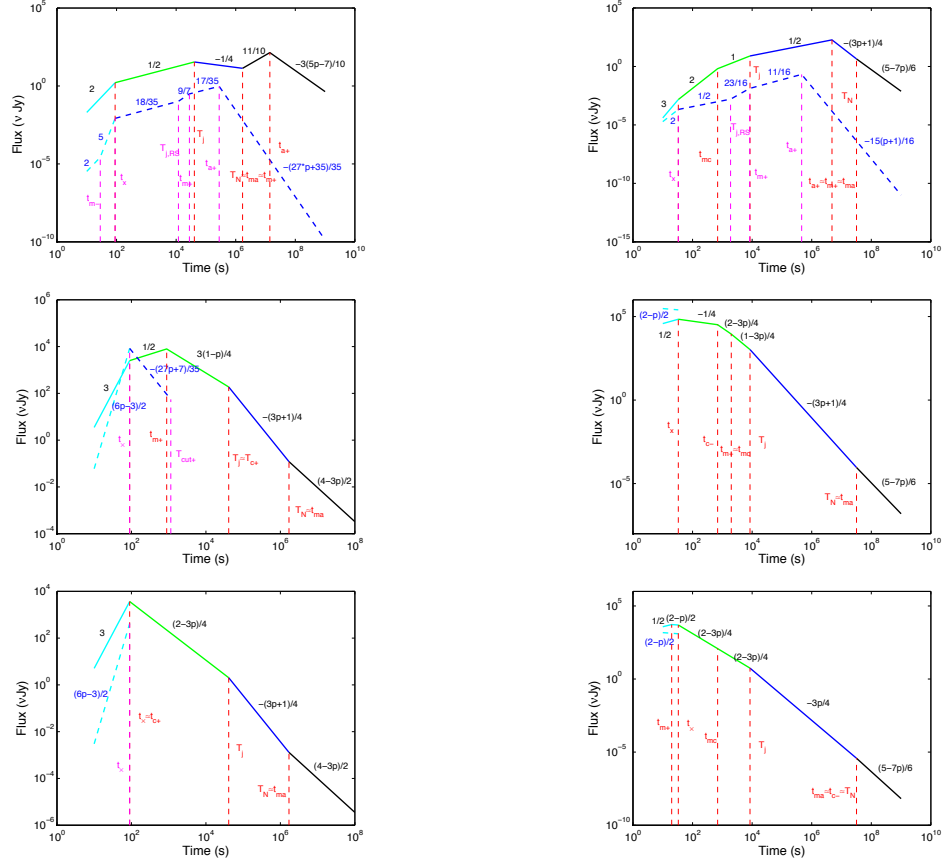


Figure 56 Example light curves in the radio, optical and X-ray bands for a set of typical parameter values (see text). The left and right panels are for the ISM and wind medium, respectively. In each panel, from top to bottom are the lightcurves in the radio, optical and X-ray band, respectively. Notations are the same with other Figures. The parameters T_{cut+}, t_x, T_j and T_N denote ν_{cut} crossing time, the shock crossing time, jet break time, and the transition time to the Newtonian phase, respectively. The solid and dashed lightcurves denote contributions from the forward and reverse shock, respectively. The 4 different phases of forward shock emission are marked with 4 different colors. Notice that the reverse shock light curves have a sharp ending, which corresponds to time beyond which no on-axis electron radiation contributes to the band (i.e. after shock crossing and $\nu > \nu_{cut}$). In reality, there should be emission from high latitudes during these phases, so in these regimes there should be a steeply-decaying lightcurve with slope $-(2 + \beta)$, where β is the flux density spectra index in the band (Kumar and Panaitescu, 2000a).

p -dependent Coefficients in Analytical Solutions

$G(p) = \left(\frac{p-2}{p-1}\right)^2$. For convenience, we define $f(p) = \frac{\Gamma(\frac{3p+22}{12})\Gamma(\frac{3p+2}{12})}{\Gamma(\frac{3p+19}{12})\Gamma(\frac{3p-1}{12})}$.

Thin Shell Forward shock

$$\begin{aligned}
 g^I(p) &= \left(\frac{p-1}{p-2}\right) (p+1)^{3/5} f(p)^{3/5} \\
 g^{II}(p) &= 1.5 \times 10^{-\frac{30}{p+4}} \left(\frac{p-2}{p-1}\right)^{\frac{2(p-1)}{p+4}} (p+1)^{\frac{2}{p+4}} f(p)^{\frac{2}{p+4}} \\
 g^{III}(p) &= (p+1)^{3/5} f(p)^{3/5} \\
 g^{IV}(p) &= e^{\frac{38p-76}{p-1}} (3736 - 1868p)^{\frac{2}{p-1}} (p-1)^{-\frac{2}{p-1}} \\
 g^V(p) &= e^{\frac{38-19p}{p-1}} (3736 - 1868p)^{\frac{1}{1-p}} (p-1)^{\frac{1}{p-1}} (p+1)^{3/5} f(p)^{3/5} \\
 g^{VI}(p) &= 1.9 \times 10^{\frac{16(p-2)}{p+4}} e^{\frac{7}{p+4}} (3736 - 1868p)^{\frac{2}{p+4}} (p-1)^{-\frac{2}{p+4}} (p+1)^{\frac{2}{p+4}} f(p)^{\frac{2}{p+4}} \\
 g^{VII}(p) &= (p+1)^{3/5} f(p)^{3/5} \\
 g^{VIII}(p) &= \left(\frac{p-1}{p-2}\right) (p+1)^{3/5} f(p)^{3/5} \\
 g^{IX}(p) &= 4.0 \times 10^{-\frac{16}{p+4}} \left(\frac{p-2}{p-1}\right)^{\frac{2(p-1)}{p+4}} (p+1)^{\frac{2}{p+4}} f(p)^{\frac{2}{p+4}} \\
 g^X(p) &= (p+1)^{3/5} f(p)^{3/5} \\
 g^{XI}(p) &= 2^{\frac{11(p-2)}{p-1}} 3^{\frac{p-2}{p-1}} e^{\frac{13p-27}{p-1}} (3736 - 1868p)^{\frac{2}{p-1}} (p-1)^{-\frac{2}{p-1}} \\
 g^{XII}(p) &= 2^{-\frac{11(p-2)}{2(p-1)}} 3^{\frac{2-p}{2(p-1)}} e^{\frac{13-7p}{p-1}} (3736 - 1868p)^{\frac{1}{1-p}} (p-1)^{\frac{1}{p-1}} (p+1)^{3/5} f(p)^{3/5} \\
 g^{XIII}(p) &= 2^{\frac{11(p-2)}{p+4}} 3^{\frac{2-p}{p+4}} e^{\frac{41}{p+4}} (3736 - 1868p)^{\frac{2}{p+4}} (p-1)^{-\frac{2}{p+4}} (p+1)^{\frac{2}{p+4}} f(p)^{\frac{2}{p+4}} \\
 g^{XIV}(p) &= (p+1)^{3/5} f(p)^{3/5}
 \end{aligned} \tag{4.64}$$

Thin Shell Reverse shock

$$\begin{aligned}
 g^I(p) &= \left(\frac{p-1}{p-2}\right) (p+1)^{3/5} f(p)^{3/5} \\
 g^{II}(p) &= 4.1 \times 10^{-\frac{360}{p+4}} \left(\frac{p-2}{p-1}\right)^{\frac{2(p-1)}{p+4}} (p+1)^{\frac{2}{p+4}} f(p)^{\frac{2}{p+4}}
 \end{aligned}$$

$$\begin{aligned}
g^{III}(p) &= (p+1)^{3/5} f(p)^{3/5} \\
g^{IV}(p) &= e^{\frac{38p-76}{p-1}} (3.0 \times 10^{33} - 1.5 \times 10^{33} p)^{\frac{2}{p-1}} (p-1)^{-\frac{2}{p-1}} \\
g^V(p) &= e^{\frac{38-19p}{p-1}} (3.0 \times 10^{33} - 1.5 \times 10^{33} p)^{\frac{1}{1-p}} (p-1)^{\frac{1}{p-1}} (p+1)^{3/5} f(p)^{3/5} \\
g^{VI}(p) &= 5.5 \times 10^{\frac{16p-60}{p+4}} (3.0 \times 10^{33} - 1.5 \times 10^{33} p)^{\frac{2}{p+4}} (p-1)^{-\frac{2}{p+4}} (p+1)^{\frac{2}{p+4}} f(p)^{\frac{2}{p+4}} \\
g^{VII}(p) &= (p+1)^{3/5} f(p)^{3/5} \\
g^{VIII}(p) &= \left(\frac{p-1}{p-2} \right) (p+1)^{3/5} f(p)^{3/5} \\
g^{IX}(p) &= 1.3 \times 10^{-\frac{486}{p+4}} 3^{-\frac{25}{p+4}} \pi^{-\frac{9}{p+4}} \left(\frac{p-2}{p-1} \right)^{\frac{2(p-1)}{p+4}} (p+1)^{\frac{2}{p+4}} f(p)^{\frac{2}{p+4}} \\
g^X(p) &= (p+1)^{3/5} f(p)^{3/5} \\
g^{XI}(p) &= 2^{\frac{11(p+6)}{p-1}} 3^{\frac{p+4}{p-1}} e^{\frac{13p-27}{p-1}} (1.5 \times 10^{33} - 7.6 \times 10^{32} p)^{\frac{1}{1-p}} (p-1)^{-\frac{2}{p-1}} \\
g^{XII}(p) &= 2^{-\frac{11(p+6)}{p-1}} 3^{\frac{p+4}{2(1-p)}} e^{\frac{13-7p}{p-1}} (1.5 \times 10^{33} - 7.6 \times 10^{32} p)^{\frac{1}{1-p}} (p-1)^{\frac{1}{p-1}} (p+1)^{3/5} \\
&\quad f(p)^{3/5} \\
g^{XIII}(p) &= 1.8 \times 10^{-\frac{30}{p+4}} 787^{\frac{2(p-2)}{p+4}} 2^{\frac{11(p+6)}{p+4}} 3^{\frac{p+9}{p+4}} \pi^{\frac{1}{p+4}} (1.5 \times 10^{33} - 7.6 \times 10^{32} p)^{\frac{1}{1-p}} \\
&\quad (p-1)^{-\frac{2}{p+4}} (p+1)^{\frac{2}{p+4}} f(p)^{\frac{2}{p+4}} \\
g^{XIV}(p) &= (p+1)^{3/5} f(p)^{3/5} \\
g^{XV}(p) &= \left(\frac{p-1}{p-2} \right) (p+1)^{3/5} f(p)^{3/5} \\
g^{XVI}(p) &= 8.3 \times 10^{-\frac{22}{p+4}} \left(\frac{p-2}{p-1} \right)^{\frac{2(p-1)}{p+4}} (p+1)^{\frac{2}{p+4}} f(p)^{\frac{2}{p+4}} \\
g^{XVII}(p) &= 5.2 \times 10^{-10} e^{\frac{38p-76}{p-1}} (1068p - 1068)^{\frac{2}{p-1}} (2-p)^{-\frac{2}{p-1}} \\
g^{XVIII}(p) &= 1.8 \times 10^{-5} e^{\frac{38-19p}{p-1}} (1068p - 1068)^{\frac{1}{1-p}} (2-p)^{\frac{1}{p-1}} (p+1)^{3/5} f(p)^{3/5} \\
g^{XIX}(p) &= 9.6 \times 10^{\frac{6p-72}{p+4}} e^{\frac{35}{p+4}} (1068p - 1068)^{\frac{2}{p+4}} (2-p)^{-\frac{2}{p+4}} (p+1)^{\frac{2}{p+4}} f(p)^{\frac{2}{p+4}} \\
g^{XX}(p) &= \left(\frac{p-1}{p-2} \right) (p+1)^{3/5} f(p)^{3/5} \\
g^{XXI}(p) &= 1.8 \times 10^{-\frac{26}{p+4}} \pi^{\frac{6}{p+4}} \left(\frac{p-2}{p-1} \right)^{\frac{2(p-1)}{p+4}} (p+1)^{\frac{2}{p+4}} f(p)^{\frac{2}{p+4}} \\
g^{XXII}(p) &= 1.0 \times 10^{-25} 2^{\frac{33(p-2)}{(1-p)}} e^{\frac{113-56p}{p-1}} \pi^{\frac{p-2}{(1-p)}} (1068p - 1068)^{\frac{2}{p-1}} (2-p)^{-\frac{2}{p-1}} \\
g^{XXIII}(p) &= 3.6 \times 10^{\frac{47p-60}{p-1}} 2^{\frac{33(p-2)}{2(p-1)}} \pi^{\frac{2-p}{2(p-1)}} (1068p - 1068)^{\frac{1}{1-p}} (2-p)^{\frac{1}{p-1}}
\end{aligned}$$

$$\begin{aligned}
& (p+1)^{3/5} f(p)^{3/5} \\
g^{XXIV}(p) &= 1.8 \times 10^{-\frac{49p+52}{p+4}} 2^{-\frac{33(p-2)}{p+4}} e^{\frac{445}{p+4}} \pi^{\frac{8-p}{p+4}} (1068p - 1068)^{\frac{2}{p+4}} (2-p)^{-\frac{2}{p+4}} \\
& (p+1)^{\frac{2}{p+4}} f(p)^{\frac{2}{p+4}}
\end{aligned} \tag{4.65}$$

Thick Shell Forward shock

$$\begin{aligned}
g^I(p) &= \left(\frac{p-1}{p-2} \right) (p+1)^{3/5} f(p)^{3/5} \\
g^{II}(p) &= 1.4 \times 10^{-\frac{10}{p+4}} \left(\frac{p-1}{p-2} \right)^{\frac{2(1-p)}{p+4}} (p+1)^{\frac{2}{p+4}} f(p)^{\frac{2}{p+4}} \\
g^{III}(p) &= (p+1)^{3/5} f(p)^{3/5} \\
g^{IV}(p) &= e^{\frac{44p-88}{p-1}} (12-6p)^{\frac{2}{p-1}} (p-1)^{-\frac{2}{p-1}} \\
g^V(p) &= e^{\frac{44-22p}{p-1}} (12-6p)^{\frac{1}{1-p}} (p-1)^{\frac{1}{p-1}} (p+1)^{3/5} f(p)^{3/5} \\
g^{VI}(p) &= 1.9 \times 10^{\frac{16(p-2)}{p+4}} 0.003^{\frac{2-p}{p+4}} 0.1^{\frac{2}{p+4}} (12-6p)^{\frac{2}{p+4}} (p-1)^{-\frac{2}{p+4}} (p+1)^{\frac{2}{p+4}} f(p)^{\frac{2}{p+4}} \\
g^{VII}(p) &= (p+1)^{3/5} f(p)^{3/5} \\
g^{VIII}(p) &= \left(\frac{p-1}{p-2} \right) (p+1)^{3/5} f(p)^{3/5} \\
g^{IX}(p) &= 2^{\frac{105}{p+4}} e^{\frac{127}{p+4}} \pi^{\frac{3}{p+4}} \left(\frac{p-1}{p-2} \right)^{\frac{2(1-p)}{p+4}} (p+1)^{\frac{2}{p+4}} f(p)^{\frac{2}{p+4}} \\
g^X(p) &= (p+1)^{3/5} f(p)^{3/5} \\
g^{XI}(p) &= 2^{\frac{88-9p}{4(1-p)}} 3^{\frac{p-4}{2(p-1)}} \pi^{\frac{p}{4(1-p)}} (0.009 - 0.005p)^{\frac{2}{p-1}} (p-1)^{-\frac{2}{p-1}} \\
g^{XII}(p) &= 0.005^{\frac{2}{p-1}} 2^{\frac{88-9p}{8(p-1)}} 3^{\frac{4-p}{4(p-1)}} \pi^{\frac{p}{8(p-1)}} (2-p)^{\frac{1}{1-p}} (p-1)^{\frac{1}{p-1}} (p+1)^{3/5} f(p)^{3/5} \\
g^{XIII}(p) &= 1.3^{\frac{2(p-2)}{p+4}} 2^{\frac{9p-106}{2(p+4)}} 3^{\frac{p-6}{2(p+4)}} 25^{-\frac{10(p+3)}{(p+4)(p-1)}} e^{\frac{106p+23}{(p+4)(p-1)}} \pi^{\frac{2-p}{2(p+4)}} (2+p-p^2)^{\frac{2}{p+4}} \\
& (p-1)^{-\frac{2}{p+4}} (p+1)^{\frac{2}{p+4}} f(p)^{\frac{2}{p+4}} \\
g^{XIV}(p) &= (p+1)^{3/5} f(p)^{3/5}
\end{aligned} \tag{4.66}$$

Thick Shell Reverse shock

$$\begin{aligned}
g^I(p) &= \left(\frac{p-1}{p-2}\right) (p+1)^{3/5} f(p)^{3/5} \\
g^{II}(p) &= 1.0 \times 10^{12} e^{-\frac{66}{p+4}} \left(\frac{p-2}{p-1}\right)^{\frac{2(p-1)}{p+4}} (p+1)^{\frac{2}{p+4}} f(p)^{\frac{2}{p+4}} \\
g^{III}(p) &= (p+1)^{3/5} f(p)^{3/5} \\
g^{IV}(p) &= e^{\frac{44(p-2)}{p-1}} (5.8 \times 10^5 - 2.9 \times 10^5 p)^{\frac{2}{p-1}} (p-1)^{-\frac{2}{p-1}} \\
g^V(p) &= e^{\frac{22(2-p)}{p-1}} (5.8 \times 10^5 - 2.9 \times 10^5 p)^{\frac{1}{1-p}} (p-1)^{\frac{1}{p-1}} (p+1)^{3/5} f(p)^{3/5} \\
g^{VI}(p) &= 4.2 \times 10^{\frac{16p-44}{p+4}} 0.003^{\frac{2-p}{p+4}} (5.8 \times 10^5 - 2.9 \times 10^5 p)^{\frac{2}{p+4}} (p-1)^{-\frac{2}{p+4}} \\
&\quad (p+1)^{\frac{2}{p+4}} f(p)^{\frac{2}{p+4}} \\
g^{VII}(p) &= (p+1)^{3/5} f(p)^{3/5} \\
g^{VIII}(p) &= \left(\frac{p-1}{p-2}\right) (p+1)^{3/5} f(p)^{3/5} \\
g^{IX}(p) &= 1.6 \times 10^{-\frac{100}{p+4}} 2^{-\frac{47}{p+4}} \pi^{-\frac{1}{p+4}} \left(\frac{p-2}{p-1}\right)^{\frac{2(p-1)}{p+4}} (p+1)^{\frac{2}{p+4}} f(p)^{\frac{2}{p+4}} \\
g^X(p) &= (p+1)^{3/5} f(p)^{3/5} \\
g^{XI}(p) &= 2^{\frac{9p+44}{4(p-1)}} 3^{\frac{p}{2(p-1)}} \pi^{\frac{4-p}{4(p-1)}} (1.5 \times 10^9 - 7.3 \times 10^8)^{\frac{2}{p-1}} (p-1)^{-\frac{2}{p-1}} \\
g^{XII}(p) &= 2^{-\frac{9p+44}{8(p-1)}} 3^{-\frac{p}{4(p-1)}} \pi^{\frac{p-4}{8(p-1)}} (1.5 \times 10^9 - 7.3 \times 10^8)^{\frac{1}{1-p}} (p-1)^{\frac{1}{p-1}} \\
&\quad (p+1)^{3/5} f(p)^{3/5} \\
g^{XIII}(p) &= 2.9 \times 10^{\frac{114-43p-21p^2}{(p+4)(p-1)}} e^{\frac{15p-144}{(p+4)(p-1)}} 2^{\frac{9p+166}{4(p+4)}} 3^{\frac{p+2}{2(p+4)}} \pi^{\frac{10-p}{4(p+4)}} (2+p-p^2)^{\frac{2}{p+4}} \\
&\quad (p-1)^{-\frac{2}{p+4}} (p+1)^{\frac{2}{p+4}} f(p)^{\frac{2}{p+4}} \\
g^{XIV}(p) &= (p+1)^{3/5} f(p)^{3/5} \\
g^{XV}(p) &= 4.29 \times 10^{21} \left(\frac{p-1}{p-2}\right) (p+1)^{3/5} f(p)^{3/5} \\
g^{XVI}(p) &= 5.2 \times 10^{-12} e^{\frac{253}{p+4}} \left(\frac{p-2}{p-1}\right)^{\frac{2(p-1)}{p+4}} (p+1)^{\frac{2}{p+4}} f(p)^{\frac{2}{p+4}} \\
g^{XVII}(p) &= 3.4 \times 10^{-10} 0.5^{\frac{p}{p-1}} e^{\frac{38p-77}{p-1}} (1321p - 1321)^{\frac{2}{p-1}} (2-p)^{-\frac{2}{p-1}} \\
g^{XVIII}(p) &= 8.2 \times 10^{-5} e^{\frac{38-19p}{p-1}} (1321p - 1321)^{\frac{1}{1-p}} (2-p)^{\frac{1}{p-1}} (p+1)^{3/5} f(p)^{3/5}
\end{aligned}$$

$$\begin{aligned}
g^{XIX}(p) &= 7.3 \times 10^{-\frac{24p+72}{p+4}} 0.5^{\frac{p}{p+4}} e^{\frac{43}{p+4}} (1321p - 1321)^{\frac{2}{p+4}} (2-p)^{-\frac{2}{p+4}} \\
&\quad (p+1)^{\frac{2}{p+4}} f(p)^{\frac{2}{p+4}} \\
g^{XX}(p) &= \left(\frac{p-1}{p-2}\right) (p+1)^{3/5} f(p)^{3/5} \\
g^{XXI}(p) &= 5.7 \times 10^{-\frac{82}{p+4}} 2^{\frac{19}{2(p+4)}} 3^{\frac{9}{4(p+4)}} 5^{\frac{21}{2(p+4)}} \pi^{-\frac{1}{p+4}} \left(\frac{p-2}{p-1}\right)^{\frac{2(p-1)}{p+4}} (p+1)^{\frac{2}{p+4}} f(p)^{\frac{2}{p+4}} \\
g^{XXII}(p) &= 1.0 \times 10^4 0.3^{\frac{2(p-2)}{p-1}} 2^{\frac{33(4-p)}{4(p-1)}} 625^{\frac{8-2p}{p-1}} \pi^{\frac{4-p}{4(p-1)}} (1321p - 1321)^{\frac{2}{p-1}} (2-p)^{-\frac{2}{p-1}} \\
g^{XXIII}(p) &= 5.9 \times 10^{17} 0.3^{\frac{2-p}{p-1}} 2^{\frac{33(p-4)}{8(p-1)}} 625^{\frac{p-4}{p-1}} \pi^{\frac{p-4}{8(p-1)}} (1321p - 1321)^{\frac{1}{1-p}} (2-p)^{\frac{1}{p-1}} \\
&\quad (p+1)^{3/5} f(p)^{3/5} \\
g^{XXIV}(p) &= 1.6 \times 10^{\frac{4p+22}{p+4}} 0.3^{\frac{2(p-2)}{p+4}} 2^{\frac{33(4-p)}{4(p+4)}} 3^{\frac{37-2p}{4(p+4)}} 5^{\frac{245-16p}{2(p+4)}} \pi^{\frac{10-p}{4(p+4)}} (1321p - 1321)^{\frac{2}{p+4}} \\
&\quad (2-p)^{-\frac{2}{p+4}} (p+1)^{\frac{2}{p+4}} f(p)^{\frac{2}{p+4}}
\end{aligned} \tag{4.67}$$

Adiabatic Deceleration With(or Without) Energy Injection

$$\begin{aligned}
g^I(p) &= \left(\frac{p-1}{p-2}\right) (p+1)^{3/5} f(p)^{3/5} \\
g^{II}(p) &= e^{\frac{11}{p+4}} \left(\frac{p-2}{p-1}\right)^{\frac{2(p-1)}{p+4}} (p+1)^{\frac{2}{p+4}} f(p)^{\frac{2}{p+4}} \\
g^{III}(p) &= (p+1)^{3/5} f(p)^{3/5} \\
g^{IV}(p) &= e^{\frac{47p-95}{p-1}} (0.3 - 0.15p)^{\frac{2}{p-1}} (p-1)^{-\frac{2}{p-1}} \\
g^V(p) &= e^{\frac{47-24p}{p-1}} (0.3 - 0.15p)^{\frac{1}{1-p}} (p-1)^{\frac{1}{p-1}} (p+1)^{3/5} f(p)^{3/5} \\
g^{VI}(p) &= 1.8 \times 10^{\frac{2(p-2)}{p+4}} 0.00008^{\frac{2-p}{p+4}} 0.02^{\frac{2}{p+4}} e^{\frac{11}{p+4}} (0.3 - 0.15p)^{\frac{2}{p+4}} \\
&\quad (p-1)^{-\frac{2}{p+4}} (p+1)^{\frac{2}{p+4}} f(p)^{\frac{2}{p+4}} \\
g^{VII}(p) &= (p+1)^{3/5} f(p)^{3/5} \\
g^{VIII}(p) &= \left(\frac{p-1}{p-2}\right) (p+1)^{3/5} f(p)^{3/5} \\
g^{IX}(p) &= e^{\frac{273}{p+4}} \left(\frac{p-2}{p-1}\right)^{\frac{2(p-1)}{p+4}} (p+1)^{\frac{2}{p+4}} f(p)^{\frac{2}{p+4}} \\
g^X(p) &= (p+1)^{3/5} f(p)^{3/5}
\end{aligned}$$

$$\begin{aligned}
g^{XI}(p) &= 0.3^{\frac{2(p-2)}{p-1}} 2^{\frac{56-3p}{2(1-p)}} 3^{\frac{8-3p}{4(1-p)}} 5^{\frac{p+40}{2(1-p)}} \pi^{\frac{p}{4(1-p)}} (3736 - 1868p)^{\frac{2}{p-1}} (p-1)^{-\frac{2}{p-1}} \\
g^{XII}(p) &= 0.3^{\frac{2-p}{p-1}} 2^{\frac{56-3p}{4(p-1)}} 3^{\frac{8-3p}{8(p-1)}} 5^{\frac{p+40}{4(p-1)}} \pi^{\frac{p}{8(p-1)}} (3736 - 1868p)^{\frac{1}{1-p}} (p-1)^{\frac{1}{p-1}} \\
&\quad (p+1)^{3/5} f(p)^{3/5} \\
g^{XIII}(p) &= 0.3^{\frac{2(p-2)}{p+4}} 2^{\frac{3(p-2)}{2(p+4)}} 3^{\frac{3(p-2)}{4(p+4)}} 5^{\frac{2-p}{2(p+4)}} e^{\frac{41}{p+4}} (3736 - 1868p)^{\frac{2}{p+4}} \\
&\quad (p-1)^{-\frac{2}{p+4}} (p+1)^{\frac{2}{p+4}} f(p)^{\frac{2}{p+4}} \\
g^{XIV}(p) &= (p+1)^{3/5} f(p)^{3/5}
\end{aligned} \tag{4.68}$$

Newtonian Phase

$$\begin{aligned}
g^I(p) &= \left(\frac{p-1}{p-2}\right) (p+1)^{3/5} f(p)^{3/5} \\
g^{II}(p) &= e^{\frac{219}{p+4}} \left(\frac{p-2}{p-1}\right)^{\frac{2(p-1)}{p+4}} (p+1)^{\frac{2}{p+4}} f(p)^{\frac{2}{p+4}} \\
g^{III}(p) &= e^{\frac{53p-106}{p-1}} (1.6 \times 10^{-9} - 8.3 \times 10^{-10} p)^{\frac{2}{p-1}} (p-1)^{-\frac{2}{p-1}} \\
g^{IV}(p) &= e^{\frac{53-26p}{p-1}} (1.6 \times 10^{-9} - 8.3 \times 10^{-10} p)^{\frac{1}{1-p}} (p-1)^{\frac{1}{p-1}} (p+1)^{3/5} f(p)^{3/5} \\
g^V(p) &= 5.4 \times 10^{\frac{26(p-2)}{p+4}} 28245^{\frac{2-p}{p+4}} e^{\frac{10}{p+4}} (0.3 - 0.15p)^{\frac{2}{p+4}} (p-1)^{-\frac{2}{p+4}} (p+1)^{\frac{2}{p+4}} f(p)^{\frac{2}{p+4}} \\
g^{VI}(p) &= \left(\frac{p-1}{p-2}\right) (p+1)^{3/5} f(p)^{3/5} \\
g^{VII}(p) &= 2^{\frac{842}{3(p+4)}} e^{\frac{509}{p+4}} \left(\frac{p-2}{p-1}\right)^{\frac{2(p-1)}{p+4}} (p+1)^{\frac{2}{p+4}} f(p)^{\frac{2}{p+4}} \\
g^{VIII}(p) &= 2^{\frac{3p+158}{3(1-p)}} 3^{\frac{10-3p}{3(1-p)}} \pi^{\frac{p}{3(1-p)}} e^{\frac{22p-45}{p-1}} (5.6 \times 10^{-18} - 2.8 \times 10^{-18} p)^{\frac{2}{p-1}} (p-1)^{-\frac{2}{p-1}} \\
g^{IX}(p) &= 2.8 \times 10^{-\frac{36}{p-1}} 2^{\frac{3p+158}{5(p-1)}} 3^{\frac{10-3p}{6(p-1)}} e^{\frac{144-11p}{p-1}} \pi^{\frac{2}{3(p-1)}} (2-p)^{\frac{1}{1-p}} (p-1)^{\frac{1}{p-1}} \\
&\quad (p+1)^{3/5} f(p)^{3/5} \\
g^X(p) &= 2.8 \times 10^{-\frac{36}{p-1}} 2^{-\frac{3p+136}{3(p+4)}} 3^{\frac{3p-8}{3(p+4)}} 73399^{\frac{2(p-2)}{p+4}} e^{\frac{104p+300}{(p+4)(p-1)}} \pi^{-\frac{2}{3(p+4)}} (2+p-p^2)^{\frac{2}{p+4}} \\
&\quad (p-1)^{-\frac{2}{p+4}} (p+1)^{\frac{2}{p+4}} f(p)^{\frac{2}{p+4}}
\end{aligned} \tag{4.69}$$

CHAPTER 5

INTRODUCTION OF PART II

The next generation gravitational-wave (GW) detectors, such as Advanced LIGO (Abbott et al., 2009), Advanced VIRGO (Acernese et al., 2008) and KAGRA (Kuroda et al., 2010) interferometers, are expected to detect GW signals from mergers of two compact objects. The primary sources for such ground-based gravitational-wave detectors are coalescence of neutron-star (NS) binaries. The detection of GW signals would represent a great breakthrough for both fundamental physics and astrophysics. However, due to the faint nature of GWs, an associated electromagnetic (EM) emission signal in coincidence with a GW in both trigger time and direction becomes essential for its identification. As the new generation GW detectors are coming online, the study of double neutron star (DNS) system becomes more and more attractive to astrophysics. In this part of my dissertation, I will firstly give a general introduction to DNS merger scenario and then present some of my study work that contribute to this exciting field.

General Introduction for Neutron-Star Binary System

The first observed DNS binary was PSR B1913+16 (Hulse & Taylor, 1975). The measurement of its orbit decay provided strong indirect evidence for Einstein's general theory of relativity (GR; see, e.g., Taylor & Weisberg (1989); Weisberg et al. (2010)), leading to the 1993 Nobel Prize in physics for Hulse and Taylor. After a few decades accumulating, totally ten DNS binary systems have been observed, as collected in Table 27.

Object	Mass (M_{\odot})	References	Object	Mass (M_{\odot})	References
J1829+2456	$1.25^{+0.11}_{-0.35}$	Champion et al. (2005)	Companion	$1.34^{+0.37}_{-0.10}$	Champion et al. (2005)
J1811-1736	$1.53^{+0.22}_{-0.63}$	Corongiu et al. (2007)	Companion	$1.04^{+0.73}_{-0.12}$	Corongiu et al. (2007)
J1906+0746	$1.248^{+0.018}_{-0.018}$	Kasian (2008)	Companion	$1.365^{+0.018}_{-0.018}$	Kasian (2008)
J1518+4904	$1.23^{+0.00}_{-0.33}$	Janssen et al. (2008)	Companion	$1.49^{+0.33}_{-0.00}$	Janssen et al. (2008)
B1534+12	$1.3332^{+0.0010}_{-0.0010}$	Stairs et al. (2002)	Companion	$1.3452^{+0.0010}_{-0.0010}$	Stairs et al. (2002)
B1913+16	$1.4398^{+0.0002}_{-0.0002}$	Weisberg et al. (2010)	Companion	$1.3886^{+0.0002}_{-0.0002}$	Weisberg et al. (2010)
B2127+11C	$1.358^{+0.010}_{-0.010}$	Jacoby et al. (2006)	Companion	$1.354^{+0.010}_{-0.010}$	Jacoby et al. (2006)
J0737-3039A	$1.3381^{+0.0007}_{-0.0007}$	Kramer et al. (2006)	J0737-3039B	$1.2489^{+0.0007}_{-0.0007}$	Kramer et al. (2006)
J1756-2251	$1.312^{+0.017}_{-0.017}$	Ferdman et al. (2008)	Companion	$1.258^{+0.017}_{-0.017}$	Ferdman et al. (2008)
J1807-2500B	$1.3655^{+0.0020}_{-0.0020}$	Lynch et al. (2012)	Companion ?	$1.2064^{+0.0020}_{-0.0020}$	Lynch et al. (2012)

Table 27 List of observed double neutron star binaries.

In the standard channel, the progenitor of DNS system is a high-mass binary, where both stars are with mass $M \gtrsim 8 - 10 M_{\odot}$, ensuring that a pair of supernova explosion could happen (Bhattacharya & van den Heuvel, 1991). Over a few million years, the primary star (the one with higher mass) would pass through its giant phase, and undergoes a Type Ib, Ic, or II supernova, leaving behind the more massive NS in the final binary. Later, when the secondary star also evolves off the main sequence to giant phase, the binary would enter the common-envelope phase. Dynamical friction shrinks the binary separation dramatically, until sufficient energy is released to expel the envelope. The exposed Helium-rich core of the secondary would then go through another supernova, giving birth to the other NS. If the second supernova kick is not large enough to unbind the system, a tight DNS binary system is formed. Figure 57 is an illustration for this process (Faber & Rasio, 2012).

The newly formed tight DNS binary could maintain a stable stage, i.e., *inspiral* phase, for tens of Myr to much longer than a Hubble time (e.g., Burgay et al. (2003); Champion et al. (2004)), until the point where the gravitational radiation timescale becomes comparable to the dynamical timescale. During *inspiral* phase, the orbital separation decays over long timescales through GW emission. The binary separation

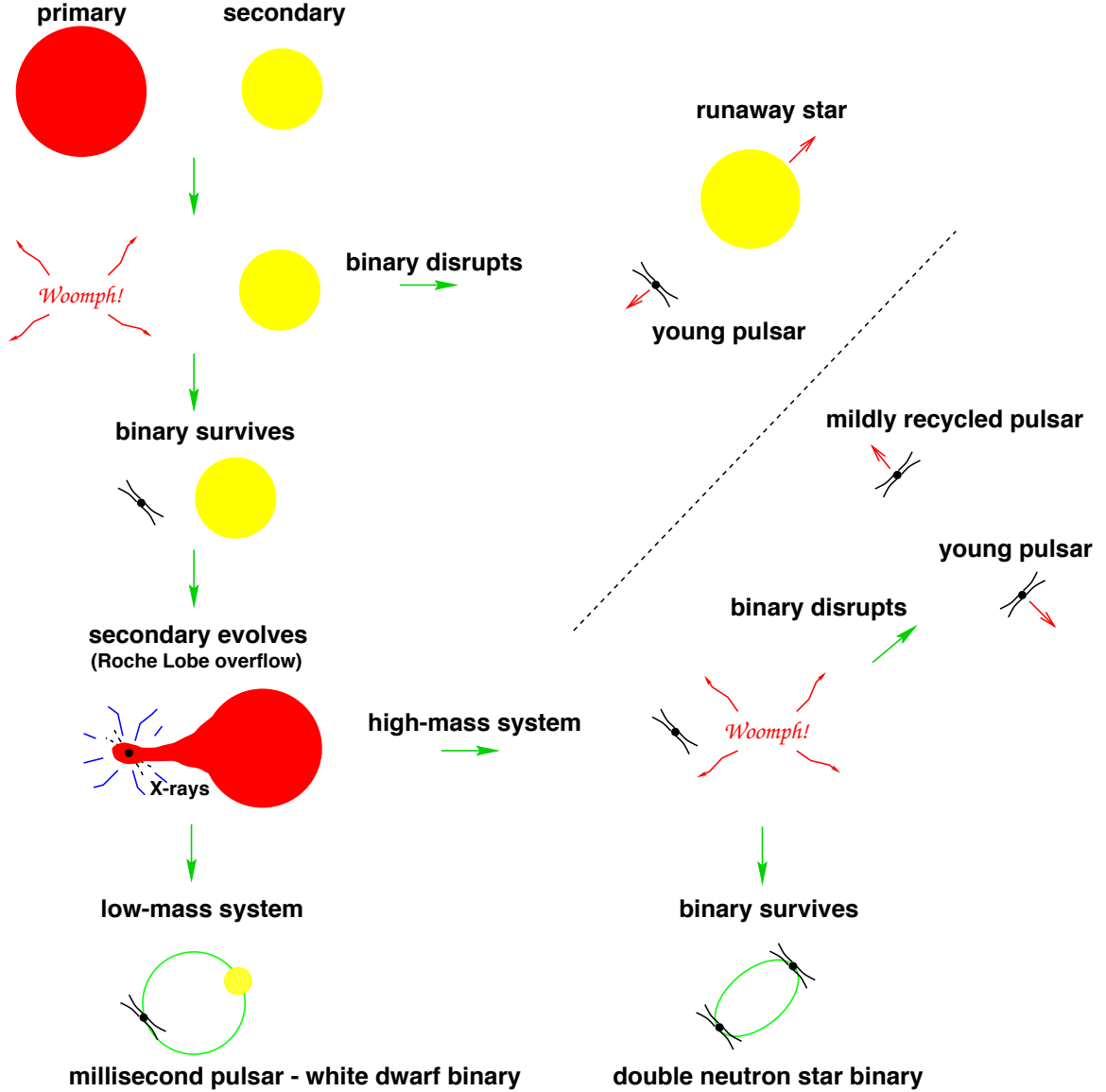


Figure 57 Cartoon showing standard formation channels for close NS–NS binaries through binary stellar evolution, taken from Lorimer (2008)

decaying rate is $da/dt = -a/\tau_{\text{GW}}$, where a is the binary separation and τ_{GW} is merger timescale causing by gravitational wave radiation. According to the lowest-order dissipative contribution from GR, τ_{GW} could be given by (Faber & Rasio, 2012)

$$\begin{aligned}
 \tau_{\text{GW}} &= \frac{5}{64} \frac{a^4}{\mu M^2} = \frac{5}{64} \frac{a^4}{q(1+q)M_1^3} \\
 &= 2.2 \times 10^8 q^{-1} (1+q)^{-1} \left(\frac{a}{R_\odot} \right)^4 \left(\frac{M_1}{1.4 M_\odot} \right)^{-3} \text{ yr}, \quad (5.1)
 \end{aligned}$$

where M_1 , M_2 , and $M \equiv M_1 + M_2$ are the individual NS masses and the total mass of the binary, $\mu = M_1 M_2 / M$ is the reduced mass, $q = M_2 / M_1$ is the binary mass ratio ($G = c = 1$ was assumed here).

DNS binaries would rapidly become unstable when its separation approaches comparable with the radii of the two NSs. *coalescence* phase would be triggered through the onset of dynamical instability. For equal or nearly equal masses system, the merger resembles a slow collision. Otherwise the secondary would be tidally disrupted during the plunge and essentially accrete onto the primary. On the other hand, numerical simulations show that binary neutron star mergers could eject a fraction of the materials, forming a mildly anisotropic outflow with a typical velocity about $0.1 - 0.3c$ (where c is the speed of light), and a typical mass about $10^{-4} \sim 10^{-2} M_\odot$ (e.g. Rezzolla et al., 2011; Rosswog et al., 2012; Hotokezaka et al., 2013).

After the short standing *coalescence* phase, the system will again settle into a new, dynamically stable configuration through a phase of *ringdown*, with a particular GW signal form that depends on the remnant's mass and rotational profile. Usually, the merger product is assumed to be a black hole or a temporal hyper-massive neutron star which survives 10-100 ms before collapsing into the black hole (e.g. Rosswog et al., 2003; Aloy et al., 2005; Shibata et al., 2005; Rezzolla et al., 2011; Rosswog et al., 2012). Nonetheless, recent observations of Galactic neutron stars and NS-NS binaries suggest that the maximum NS mass can be high, which is close to the total mass of the NS-NS systems (Dai et al., 2006; Zhang, 2013b, and references therein). Indeed, for the measured parameters of 6 known Galactic NS binaries and a range of equations of state, the majority of mergers of the known binaries will form a massive millisecond pulsar and survive for an extended period of time (Morrison et al., 2004). When the equation of state of nuclear matter is stiff (see arguments in Dai et al. (2006) and Zhang (2013b) and references therein), a stable massive neutron star would form after the merger. This newborn massive neutron star would be differentially rotating.

The dynamo mechanism may operate and generate an ultra-strong magnetic field (Duncan & Thompson, 1992; Kluźniak & Ruderman, 1998; Dai and Lu, 1998c), so that the product is very likely a millisecond magnetar. Evidence of a magnetar following some SGRBs has been collected in the Swift data (Rowlinson et al., 2010; Rowlinson & O’Brien, 2012), and magnetic activities of such a post-merger massive neutron star have been suggested to interpret several X-ray flares and plateau phase in SGRBs (Dai et al., 2006; Gao & Fan, 2006; Fan & Xu, 2006b).

By extrapolating the observed sample of NS binaries, or performing population-synthesis simulation, the NS-NS merger event rate could be very roughly estimated as $(10 - 5 \times 10^4) \text{ Gpc}^{-3} \text{ yr}^{-1}$ (Phinney, 1991; Kalogera et al., 2004; Abadie et al., 2010).

On the other hand, for the relative location of DNS system to their host galaxy, the population-synthesis simulation predicts relatively larger radial offsets (Wang et al., 2006; Wong et al., 2010), but all observed Galactic neutron-star binaries reside within the Galactic disk. Therefore, the circum number density of ISM is expected to vary significantly, from $n \sim 1 \text{ cm}^{-3}$, in galactic disks, to $n \sim 10^{-6} \text{ cm}^{-3}$, for mergers taking place outside their host galaxies (Nakar & Piran, 2011).

Gravitational Wave Signal

The form of the GW signal from DNS system varies with different undergoing phases. The most clear and detectable waveform is during *inspiral* phase, often called a *chirp* waveform, given by (Allen et al., 2012)

$$h_+(t) = -\frac{1 + \cos^2 \iota}{2} \left(\frac{GM}{c^2 D} \right) \left(\frac{t_c - t}{5GM/c^3} \right)^{-1/4} \times \cos[2\phi_c + 2\phi(t - t_c; M, \mu)], \quad (5.2)$$

$$h_\times(t) = -\cos \iota \left(\frac{GM}{c^2 D} \right) \left(\frac{t_c - t}{5GM/c^3} \right)^{-1/4} \times \sin[2\phi_c + 2\phi(t - t_c; M, \mu)], \quad (5.3)$$

where D is the distance from the source, ι is the angle between the direction to the observer and the angular momentum axis of the binary system, $\mathcal{M} = \mu^{3/5} M^{2/5}$ is the *chirp mass*, and $\phi(t - t_c; M, \mu)$ is the orbital phase of the binary (Blanchet et al., 1995, 1996). Here, t_c and ϕ_c are *coalescence time* and *coalescence phase*, when the waveform is terminated.

Entering the *coalescence* phase, full GR simulations is required to shown the GW signal form. And it turns out this phase yields the maximum GW amplitude but with a signal much simpler and more quasi-periodic than in the original cartoon version. In *ringdown* phase, GW signal is even complicate and depends on the remnant mass and rotational profile. Please refer to Faber & Rasio (2012) and reference therein for detailed GW signal discussion.

Electromagnetic Signal

Depending on different central merger product (essentially different equation of state of nuclear matter), the EM signals could be totally different: if the merger product is a black hole, the EM signals could include a short gamma-ray burst (SGRB) (Eichler et al., 1989; Rosswog et al., 2012; Gehrels et al., 2005; Barthelmy et al., 2005b; Berger, 2011), an optical “macronova” powered by the radioactivity of the ejecta (Li & Paczyński, 1998; Kulkarni, 2005; Metzger et al., 2010), and a long lasting radio afterglow (Nakar & Piran, 2011; Metzger & Berger, 2012) raising from the interaction between the ejecta and the ambient medium; on the other hand, if a stable massive neutron star would form after the merger (Dai et al., 2006; Zhang, 2013b; Giacomazzo & Perna, 2013), besides SGRB (SGRB may be not relevant in this case), the proto-magnetar would eject a near-isotropic Poynting-flux-dominated outflow, the dissipation of which would power a bright early X-ray afterglow (Zhang, 2013b); the ejecta launched during the merger would firstly be heated up by the magnetar wind to produce a bright ”merger-nova” peaking in the UV band (Yu et

al., 2013; Metzger & Piro, 2013) and be accelerated even into relativistic regime, giving rise to broad band afterglow emission through strong external shock between the ejecta and the ISM (Gao et al., 2013b).

Figure 58 and 59 present the physical pictures for different EM emission components for black hole remnant and megnetar remnant, respectively.

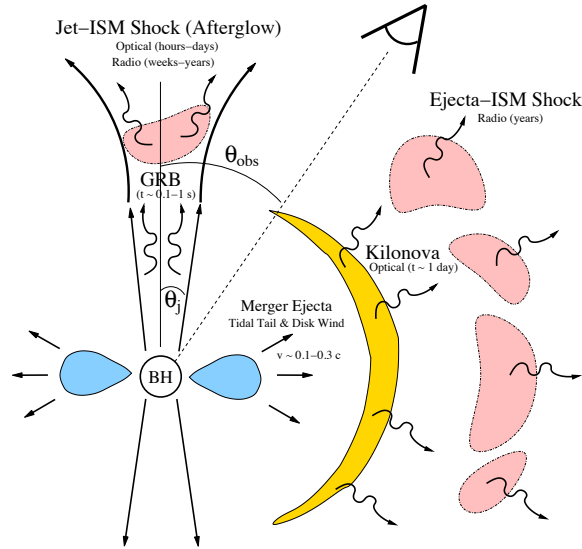


Figure 58 A physical picture for several EM emission components appearing after the merger, black hole as the remnant. Following the merger a centrifugally supported disk (*blue*) remains around the black hole. Rapid accretion powers a collimated relativistic jet, producing a SGRB. Non-thermal afterglow emission results from the interaction of the jet with the surrounding circumburst medium (*red*). Short-lived isotropic optical emission lasting \sim few days (kilonova; *yellow*) can also accompany the merger, powered by the radioactive decay of heavy elements synthesized in the ejecta. Figure produced by Metzger & Berger (2012).

Short gamma-ray bursts

Short GRBs is the most commonly discussed EM counterpart of DNS merger, since it provides detectable signal all the way from γ -ray to radio bands. However, two issues need to be claimed if we count on SGRBs for the joint detection of GW and EM signals:

Firstly, NS-NS/NS-BH mergers were proposed as SGRB progenitors for a long

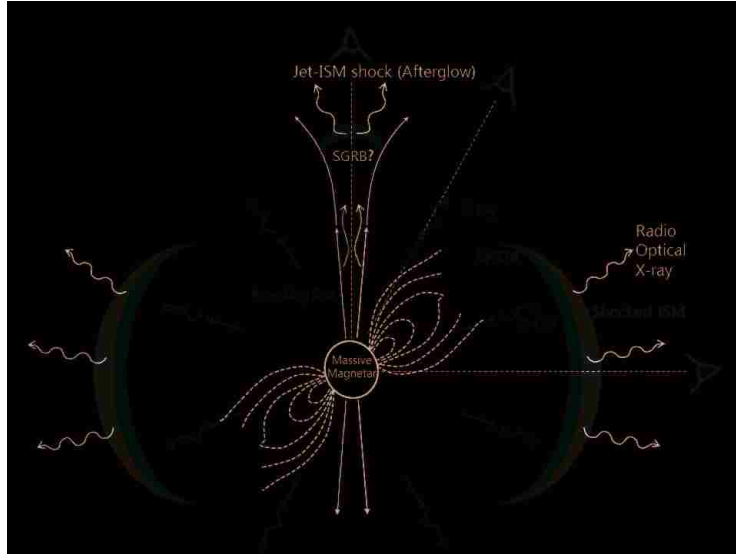


Figure 59 A physical picture for several EM emission components appearing after the merger, magnetar as the remnant. Near the spin axis, there might be a SGRB jet. An observer towards this jet (red observer) would see a SGRB. At larger angles (yellow observer), a free magnetar wind may be released, whose dissipation would power a bright X-ray afterglow (Zhang, 2013b). At even larger angles (orange observer), the magnetar wind is confined by the ejecta (green shell). The interaction between the magnetar wind and ejecta would trigger magnetic dissipation of the wind and also power a bright X-ray afterglow (Zhang, 2013b). After releasing some dissipated energy, a significant fraction of the spinning energy would push the ejecta and shock into the ambient medium (Dai and Lu, 1998a; Zhang and Mészáros, 2001a). Synchrotron emission from the shocked medium (red shell) would power brighter X-ray, optical and radio afterglow emission. Taken from Gao et al. (2013b)

time (Paczynski 1986; Eichler et al. 1989; Narayan et al. 1992; Rezzolla et al. 2011), even prior to the discovery of the duration bimodality (Berger, 2013). From theoretical point of view, DNS merger scenario could provided a roughly correct event rate, rapid release enough energy, and a clean environment to avoid significant baryon loading; from observational point of view, the observed properties of SGRBs tends to be consistent with the observational predictions of DNS merger scenario, such as short bursts will occur in both early- and late-type galaxies, offset distribution of SGRBs are in good agreement with compact object population synthesis predictions that include kicks, and the SGRBs are not accompanied by supernova explosions

(Berger, 2013). But one need to be cautious that, the *smoking gun* is still lacking to firmly establish the connection between DNS merger and SGRBs.

Secondly, even if there is a SGRBs and DNS merger association, the prompt γ -ray signal, X-ray afterglow signal and optical afterglow signal of SGRBs are non-detectable for the majority of cases, due to relativistic beaming effect. For example, for SGRBs with jet half-opening angle as $\theta_j \lesssim \pi/2$, only a fraction $f_{b,\gamma} \approx 1 - \cos \theta_j \approx \theta_j^2/2 \ll 1$ of viewers with observing angles $\theta_{\text{obs}} \lesssim \theta_j$ will detect bright γ -ray signal (the fraction could be relatively larger for X-ray and optical afterglow signal by a very limited factor). Observations have provided evidence for collimation in at least one case (GRB 051221A), with a jet half-opening angle of $\theta_j \approx 0.12$ (Burrows et al., 2006; Soderberg et al., 2006). Taking this value as the best-bet beaming factor for all SGRBs, we only have $f_{b,\gamma} \sim 0.01$. Radio afterglow emission can in principle be detected at all observer angles, but it is usually dim due to relatively low energy budget and circumburst density (the study of SGRBs afterglows provide a scale for the energy release and circumburst density, with $E \lesssim 10^{51}$ erg and $n \lesssim 0.1 \text{ cm}^{-3}$ (Berger et al., 2005; Soderberg et al., 2006; Berger, 2007)).

Li-Paczyński Nova/macro-nova/kilo-nova

As mentioned above, a fraction of the materials would be ejected during the coalescence process, forming a mildly anisotropic outflow with a typical velocity about $0.1 - 0.3c$, and a typical mass about $10^{-4} \sim 10^{-2}M_{\odot}$ (e.g. Rezzolla et al., 2011; Rosswog et al., 2012; Hotokezaka et al., 2013). The ejecta from NS-NS mergers is primarily neutron-rich. Thus radioactive elements (mass number $A \gtrsim 130$) are expected to form as neutrons capture onto nuclei (r -process nucleosynthesis) (e.g., Lattimer & Schramm 1974; Eichler et al. 1989; Freiburghaus et al. 1999). The resulting energy release will power a brief transient in the UV-Optical band with brightness approximately one thousand times brighter than novae but dimmer than supernova. With

a simple one zone model, Li & Paczyński (1998) firstly propose a simple analytical formula to estimate the peak luminosity and peak timescale of such transient as a function free parameters f , i.e., the fraction of the rest mass converting into radioactive decay energy budget. Back to that date, $f \sim 0.001$ was adopt as a prior. Most recently, Metzger et al. (2010) uses a nuclear physics reaction network to define the value of f and found that provided that one adopts a value of $f_{\text{nuc}} \approx 3 \times 10^{-6}$ for the dimensionless parameter quantifying the amount of nuclear heating on a timescale of $\sim 1\text{d}$, the resulting transient peaks on a timescale of $\sim 0.5 - 5\text{d}$, with an optical luminosity in the range $\sim 10^{41} - 10^{42.5}\text{ erg s}^{-1}$, corresponding to $\approx 19 - 22.5\text{ mag}$ at the edge of the ALIGO/Virgo volume. Following the peak, the luminosity declines as $L_\nu \propto t^{-\alpha}$, with $\alpha \approx 1 - 1.4$, due to the declining radioactive power.

Long lasting radio afterglow

Similar with GRB afterglow scenario, the ejected material would interact with the ambient medium, giving rise to synchrotron emission photons through external shock. One can easily estimate this signal with results shown in Chapter 4. According to estimation of Nakar & Piran (2011), such signal would mainly emerge in radio band, with peak flux

$$F_{\nu,p} \approx 40 E_{j,50} n_0^{7/8} \beta_{0.2}^{11/4} d_{L,200}^{-2} \nu_1^{-3/4} \mu\text{Jy}, \quad (5.4)$$

where $\beta_{0.2} = v_{\text{ej}}/0.2c$, ν_1 is the observing frequency in GHz; and $d_L = 200d_{L,200}$ Mpc is the luminosity distance. $p = 2.5$ and $\epsilon_e = \epsilon_B = 0.1$ is assumed here. The radio emission peaks at the deceleration time:

$$t_{\text{dec}} \approx 2.6 E_{j,50}^{1/3} n_0^{-1/3} \beta_{0.2}^{-5/3} \text{ yr}. \quad (5.5)$$

Dissipated early x-ray afterglow

If the merger product is millisecond magnetar instead of black hole, the proto-NS would quick cool down and a Poynting-flux-dominated outflow can be launched (Usov, 1992; Metzger et al., 2011). Two mechanisms could dissipate the magnetar wind energy into radiation. (1) In the free wind zone with solid angle $\Delta\Omega_{w,1}$, the magnetar wind would undergo strong self-dissipation, for instance, through internal-collision-induced magnetic reconnection and turbulence (ICMART) process (Zhang & Yan, 2011a) beyond self-dissipation radius; (2) One can also consider the confined magnetar wind zone with solid angle $\Delta\Omega_{w,2}$ where the magnetar wind is expanding into a heavy ejecta launched during the merger process. The magnetic energy may be rapidly discharged upon interaction between the wind and the ejecta. Zhang (2013b) carefully calculate these two situations and found that in both mechanism, radiation is peaked in X-ray band.

On the other hand, since before the merger the two NSs are in the Keplerian orbits, the post-merger product should be near the break-up limit, i.e., $P_0 = 1 \text{ ms}$ $P_{0,-3}$ could be taken as the typical value of the initial spin period of the proto-magnetar. Given nearly the same amount of the total rotation energy $E_{\text{rot}} = (1/2)I\Omega_0^2 \sim 2 \times 10^{52} \text{ erg}$ ($\Omega_0 = 2\pi/P$), the luminosity, and hence, the afterglow flux critically depend on the dipole magnetic field B_p . Applying dipole spindown formula and correcting for the beaming factor f_w and the efficiency factor η_x to convert the spin down luminosity to the observed X-ray luminosity in the detector band, Zhang (2013b) gives a rough estimation to this dissipation X-ray flux,

$$\begin{aligned}
 F_x &= \frac{\eta_x L_{sd}}{4\pi f_{b,w} D_L^2} \simeq 2 \times 10^{-8} \text{ erg s}^{-1} \text{ cm}^{-2} \\
 &\times \eta_{x,-2} f_{b,w}^{-1} \left(\frac{D_L}{300 \text{ Mpc}} \right)^{-2} I_{45} P_{0,3}^{-2} T_{sd,3}^{-1}, \quad (5.6)
 \end{aligned}$$

where $L_{sd} = I\Omega_0^2/(2T_{sd})$ is the characteristic spindown luminosity, and

$$T_{sd} \simeq 2 \times 10^3 \text{ s } I_{45} B_{p,15}^{-2} P_{0,-3}^2 R_6^{-6} \quad (5.7)$$

is the characteristic spindown time scale.

Merger-nova

In the confined magnetar wind zone, dissipation X-ray photons will heat up the the merger ejecta, which is much stronger than heating from r -process. Yu et al. (2013) develop a generic dynamic model for the merger ejecta with energy injection from the central magnetar and find that the ejecta emission (the “merger-nova”) powered by the magnetar peaks in the UV band and the peak of the light curve progressively shifts to an earlier epoch with increasing frequency. A magnetar-powered mergernova could have an optical peak brightness comparable to a supernova, which is a few tens or hundreds times brighter than the radioactive-powered merger-novae (the so-called macro-nova or kilo-nova). And such a merger-nova would peak earlier and have a significantly shorter duration than that of a supernova.

Double neutron star merger afterglow

On the other hand, through absorbing magnetar wind energy, the merger ejecta would essentially got accelerated, and under certain conditions, would reach a relativistic speed. Such a magnetar-powered ejecta, when interacting with the ambient medium, would develop a bright broad-band afterglow due to synchrotron radiation. In Chapter 6, we study this physical scenario in detail, and present the predicted X-ray, optical and radio light curves for a range of magnetar and ejecta parameters. We show that the X-ray and optical lightcurves usually peak around the magnetar spindown time scale ($\sim 10^3 - 10^5$ s), reaching brightness readily detectable by wide-field X-ray and optical telescopes, and remain detectable for an extended period.

The radio afterglow peaks later, but is much brighter than the case without a magnetar energy injection. Therefore, such bright broad-band afterglows, if detected and combined with GW signals in the future, would be a probe of massive millisecond magnetars and stiff equation-of-state for nuclear matter. Hereafter, we define such a model as the “double neutron star (DNS) merger” afterglow model.

Palomar Transient Factory (PTF) team recently reported the discovery of a rapidly fading optical transient source, PTF11agg. A long-lived scintillating radio counterpart was identified, but the search for a high energy counterpart showed negative results. The PTF team speculated that PTF11agg may represent a new class of relativistic outbursts. It turns out that the PTF11agg data could be explained well with above DNS merger afterglow model, suggesting that at least some GW signal from DNS mergers may be associated with such a bright electromagnetic counterpart without a γ -ray trigger (see Chapter 7 for detail).

Possible High-Energy Neutrino and Photon Signals

For the scenario with magnetar as central product of DNS merger, protons accelerated in the forward shock powered by a magnetar wind pushing the ejecta launched during the merger process would interact with photons generated in the dissipating magnetar wind and emit high energy neutrinos and photons. In Chapter 8, we estimate the typical energy and fluence of the neutrinos from such a scenario. We find that \sim PeV neutrinos could be emitted from the shock front as long as the ejecta could be accelerated to a relativistic speed. The diffuse neutrino flux from these events, even under the most optimistic scenarios, is too low to account for the two events announced by the IceCube Collaboration, but it is only slightly lower than the diffuse flux of GRBs, making it an important candidate for the diffuse background of \sim PeV neutrinos. The neutron-pion decay of these events make them a moderate contributor to the sub-TeV gamma-ray diffuse background.

CHAPTER 6

BRIGHT BROD-BAND AFTERGLOWS OF GRAVITATIONAL WAVE BRSTS OF BINARY NEUTRON STARS

This chapter is part of the following published paper :

*Gao H., Ding, X., Wu, X.-F., Zhang B., Dai, Z.-G., 2013, Astrophysics Journal
771,86*

The Double Neutron Star Merger Afterglow Model

The postmerger hyper-massive neutron star may be near the break up limit, so that the total spin energy $E_{\text{rot}} = (1/2)I\Omega_0^2 \simeq 2 \times 10^{52} I_{45} P_{0,-3}^{-2}$ erg (with $I_{45} \sim 1.5$ for a massive neutron star) may be universal. Here $P_0 \sim 1$ ms is the initial spin period of the proto-magnetar. Throughout this chapter, the convention $Q = 10^n Q_n$ is used for cgs units, except for the ejecta mass M_{ej} , which is in unit of solar mass M_{\odot} . Given nearly the same total energy, the spin-down luminosity and the characteristic spin down time scale critically depend on the polar-cap dipole magnetic field strength B_p (Zhang and Mészáros, 2001a), i.e. $L_{\text{sd}} = L_{\text{sd},0}/(1 + t/T_{\text{sd}})^2$, where $L_{\text{sd},0} \simeq 10^{49} \text{ erg s}^{-1} B_{p,15}^2 R_6^6 P_{0,-3}^{-4}$, and the spin down time scale $T_{\text{sd}} \simeq 2 \times 10^3 \text{ s } I_{45} B_{p,15}^{-2} P_{0,-3}^2 R_6^{-6} \simeq E_{\text{rot}}/L_{\text{sd},0}$, where $R = 10^6 R_6$ cm is the stellar radius¹.

After the internal dissipation of the magnetar wind that powers the early X-ray afterglow (Zhang, 2013b), the remaining spin energy would be added to the blastwave. The dynamics of the blastwave depends on the magnetization parameter σ of the magnetar wind after the internal dissipation. Since for the confined wind, magnetic dissipation occurs upon interaction between the wind and the ejecta, in this work, we assume that the wind is still magnetized (moderately high σ), so that there is no strong reverse shock into the magnetar wind (Zhang and Kobayashi, 2005; Mimica

¹In principle, besides dipole spindown, the proto-magnetar may also lose spin energy via gravitational radiation (Zhang and Mészáros, 2001a; Corsi & Mészáros, 2009; Fan et al., 2013). This effect is neglected in the following modeling for simplicity.

et al., 2009)². As a result, the remaining spin energy is continuously injected into the blastwave with a luminosity $L_0 = \xi L_{\text{sd},0}$, where $\xi < 1$ denotes the fraction of the spin down luminosity that is added to the blastwave. The evolution of the blastwave can be described by a system with continuous energy injection (Dai and Lu, 1998a; Zhang and Mészáros, 2001a).

The newly formed massive magnetar is initially hot. A Poynting flux dominated outflow is launched ~ 10 s later, when the neutrino-driven wind is clean enough (Metzger et al., 2011). At this time, the front of the ejecta traveled a distance $\sim 6 \times 10^{10}$ cm (for $v \sim 0.2c$), with a width $\Delta \sim 10^7$ cm. The ultra-relativistic magnetar wind takes ~ 2 s to catch up the ejecta, and drives a forward shock into the ejecta. Balancing the magnetic pressure and the ram pressure of shocked fluid in the ejecta, one can estimate the shocked fluid speed as $v_s \sim 10^{-4} c L_{0,47}^{1/2} \Delta_7^{1/2} M_{\text{ej},-3}^{-1/2}$, which is in the same order of forward shock speed. So the forward shock would cross the ejecta in around $t_\Delta \sim \Delta/v_s \sim 3$ s $L_{0,47}^{-1/2} \Delta_7^{1/2} M_{\text{ej},-3}^{1/2}$. Note that when calculating magnetic pressure, we have assumed a toroidal magnetic field configuration in the Poynting flux, but adopting a different magnetic configuration would not significantly affect the estimate of t_Δ .

After the forward shock crosses the ejecta, the forward shock ploughs into the ambient medium. The dynamics of the blastwave during this stage is defined by energy conservation³

$$L_0 t = (\gamma - 1) M_{\text{ej}} c^2 + (\gamma^2 - 1) M_{\text{sw}} c^2, \quad (6.1)$$

where $M_{\text{sw}} = \frac{4\pi}{3} R^3 n m_p$ is the swept mass from the interstellar medium. Initially, $(\gamma - 1) M_{\text{ej}} c^2 \gg (\gamma^2 - 1) M_{\text{sw}} c^2$, so the kinetic energy of the ejecta would increase

²If, on the other hand, the wind is already leptonic matter dominated, a reverse shock can be developed, which would predict additional radiation signatures (Dai, 2004).

³The accurate expression for Eq.8.4 should be $L_0 t = (\gamma - \gamma_{\text{ej},0}) M_{\text{ej}} c^2 + (\gamma^2 - 1) M_{\text{sw}} c^2$, where $\gamma_{\text{ej},0}$ is the initial Lorenz factor for the ejecta, which we take as unity for convenience.

linearly with time until $t = \min(T_{\text{sd}}, T_{\text{dec}})$, where the deceleration timescale T_{dec} is defined by the condition $(\gamma - 1)M_{\text{ej}}c^2 = (\gamma^2 - 1)M_{\text{sw}}c^2$. By setting $T_{\text{dec}} \sim T_{\text{sd}}$, we can derive a critical ejecta mass

$$\begin{aligned} M_{\text{ej},c,1} &\sim 10^{-3} M_{\odot} n^{1/8} I_{45}^{5/4} L_{0,47}^{-3/8} P_{0,-3}^{-5/2} \xi^{5/4} \\ &\sim 10^{-3} M_{\odot} n^{1/8} I_{45}^{5/4} B_{p,14}^{-3/4} R_6^{-9/4} P_{0,-3}^{-1} \xi^{7/8} \end{aligned} \quad (6.2)$$

which separate regimes with different blastwave dynamics. For a millisecond massive magnetar, the parameters I_{45} , R_6 , $P_{0,-3}$ are all essentially fixed values. The dependence on n is very weak (1/8 power), so the key parameters that determine the blastwave parameters are the ejecta mass M_{ej} and the magnetar injection luminosity L_0 (or the magnetic field strength B_p). If $M_{\text{ej}} < M_{\text{ej},c,1}$ (or $T_{\text{dec}} < T_{\text{sd}}$), the ejecta can be accelerated linearly until the deceleration radius, after which the blastwave decelerates, but still with continuous energy injection until T_{sd} . Conversely, in the opposite regime ($M_{\text{ej}} > M_{\text{ej},c,1}$ or $T_{\text{sd}} < T_{\text{dec}}$), the blastwave is only accelerated to T_{sd} , after which it coasts before decelerating at T_{dec} . In the intermediate regime of $M_{\text{ej}} \sim M_{\text{ej},c,1}$ (or $T_{\text{dec}} \sim T_{\text{sd}}$), the blastwave shows a decay after being linearly accelerated.

There is another critical ejecta mass, which defines whether the blastwave can reach a relativistic speed. This is defined by $E_{\text{rot}}\xi = 2(\gamma - 1)M_{\text{ej}}c^2$. Defining a relativistic ejecta as $\gamma - 1 > 1$, this second critical ejecta mass is

$$M_{\text{ej},c,2} \sim 6 \times 10^{-3} M_{\odot} I_{45} P_{0,-3}^{-2} \xi. \quad (6.3)$$

An ejecta heavier than this would not be accelerated to a relativistic speed.

Below we discuss four dynamical regimes.

Case I: $M_{\text{ej}} < M_{\text{ej},c,1}$ or $T_{\text{sd}} > T_{\text{dec}}$. This requires both a small L_0 (or low B_p) and a small M_{ej} . We take an example with $L_0 \sim 10^{47}$ erg s $^{-1}$ ($B_p \sim 10^{14}$ G) and $M_{\text{ej}} \sim 10^{-4} M_{\odot}$. To describe the dynamics in such a case, besides the spin down

timescale T_{sd} , we need three more characteristic time scales and the Lorentz factor value at the deceleration time

$$\begin{aligned}
T_{\text{dec}} &\sim 4.4 \times 10^4 \text{ s } L_{0,47}^{-7/10} M_{\text{ej},-4}^{4/5} n^{-1/10} \\
T_{\text{N1}} &\sim 3.6 \times 10^3 \text{ s } L_{0,47}^{-1} M_{\text{ej},-4} \\
T_{\text{N2}} &\sim 4.5 \times 10^7 \text{ s } L_{0,47}^{1/3} n^{-1/3} T_{\text{sd},5}^{1/3} \\
\gamma_{\text{dec}} &\sim 12.2 L_{0,47}^{3/10} M_{\text{ej},-4}^{-1/5} n^{-1/10} + 1
\end{aligned} \tag{6.4}$$

where $T_{\text{N1}}, T_{\text{N2}}$ are the two time scales when the blastwave passes the non-relativistic to relativistic transition line $\gamma - 1 = 1$ during the acceleration and deceleration phases. With these parameters, one can characterize the dynamical evolution of the blastwave (Fig.60a), as shown in Table 28. Based on the dynamics, we can quantify the temporal evolution of synchrotron radiation characteristic frequencies $\nu_{\text{a}}, \nu_{\text{m}}, \nu_{\text{c}}$, and the peak flux, $F_{\nu, \text{max}}$. The evolutions of the characteristic frequencies are presented in Fig.60b and collected in Table 29.

Following the standard procedure in Sari et al. (1998a), we derive the synchrotron radiation characteristic frequencies and the peak flux density at T_{dec} ,

$$\begin{aligned}
\nu_{\text{a,dec}} &\sim 5.0 \times 10^8 \text{ Hz } L_{0,47}^{3/50} M_{\text{ej},-4}^{4/25} n^{29/50} \epsilon_{e,-1}^{-1} \epsilon_{B,-2}^{1/5} \\
&\quad \times \left(\frac{p-1}{p-2} \right) (p+1)^{3/5} f(p)^{3/5} \\
\nu_{\text{m,dec}} &\sim 1.3 \times 10^{14} \text{ Hz } L_{0,47}^{6/5} M_{\text{ej},-4}^{-4/5} n^{1/10} \epsilon_{e,-1}^2 \epsilon_{B,-2}^{1/2} \left(\frac{p-2}{p-1} \right)^2 \\
\nu_{\text{c,dec}} &\sim 9.6 \times 10^{14} \text{ Hz } L_{0,47}^{1/5} M_{\text{ej},-4}^{-4/5} n^{-9/10} \epsilon_{B,-2}^{-3/2} \\
F_{\nu, \text{max,dec}} &\sim 1.7 \times 10^5 \text{ } \mu\text{Jy } L_{0,47}^{3/10} M_{\text{ej},-4}^{4/5} n^{2/5} \epsilon_{B,-2}^{1/2} D_{27}^{-2}
\end{aligned} \tag{6.5}$$

where $f(p) = \frac{\Gamma(\frac{3p+22}{12})\Gamma(\frac{3p+2}{12})}{\Gamma(\frac{3p+19}{12})\Gamma(\frac{3p-1}{12})}$. With the temporal evolution power law indices of these parameters (Table 29), one can calculate the X-ray, optical and radio afterglow lightcurves. Notice that there are two more temporal segments listed in Table

29, since ν_a crosses ν_m twice at

$$\begin{aligned}
T_{\text{ma1}} &\sim 1.4 \times 10^2 \text{ s } L_{0,47}^{-5/4} M_{\text{ej},-4}^{5/4} n^{1/8} \epsilon_{e,-1}^{-5/4} \epsilon_{B,-2}^{-1/8} \left(\frac{p-2}{p-1} \right)^{-5/4} \\
&\quad \times (p+1)^{1/4} f(p)^{1/4}, \\
T_{\text{ma2}} &\sim 1.9 \times 10^8 \text{ s } L_{0,47}^{1/5} n^{-2/5} T_{\text{sd},5}^{1/5} \epsilon_{e,-1}^2 \epsilon_{B,-2}^{1/5} \left(\frac{p-2}{p-1} \right)^2 \\
&\quad \times (p+1)^{-2/5} f(p)^{-2/5}, \tag{6.6}
\end{aligned}$$

respectively. We present the light curves in X-ray (Fig.60d), optical and radio (10GHz) band (Fig.60c). The distance is taken as 300 Mpc, the detection horizon of Advanced LIGO.

Case II: $M_{\text{ej}} \sim M_{\text{ej},c,1}$ or $T_{\text{sd}} \sim T_{\text{dec}}$. The dynamics and the expressions of the characteristic parameters become simpler:

$$\begin{aligned}
T_{\text{dec}} &\sim T_{\text{sd}} \\
T_{\text{N1}} &\sim 12 \text{ s } \xi^{-1} M_{\text{ej},-4} T_{\text{sd},3} \\
T_{\text{N2}} &\sim 1.3 \times 10^8 \text{ s } \xi^{8/3} M_{\text{ej},-4}^{-8/3} T_{\text{sd},3} \\
\gamma_{\text{sd}} &\sim 83.3 \xi M_{\text{ej},-4}^{-1} + 1 \tag{6.7}
\end{aligned}$$

The temporal indices of the evolutions of $\nu_a, \nu_m, \nu_c, F_{\nu, \text{max}}$ are listed in Table 29, and the expressions of γ and R are shown in Table 28.

As examples, we consider $L_0 \sim 10^{49} \text{ erg s}^{-1}$ ($B_p \sim 10^{15} \text{ G}$) vs. $M_{\text{ej}} \sim 10^{-4} M_{\odot}$, which satisfies $T_{\text{sd}} \sim T_{\text{dec}}$.

Similarly to Case I, we have

$$\begin{aligned}
\nu_{a,\text{sd}} &\sim 2.2 \times 10^9 \text{ Hz } \xi^{11/5} L_{0,49}^{-3/5} M_{\text{ej},-4}^{-8/5} n^{4/5} \epsilon_{e,-1}^{-1} \epsilon_{B,-2}^{1/5} \\
&\quad \times \left(\frac{p-1}{p-2} \right) (p+1)^{3/5} f(p)^{3/5}
\end{aligned}$$

$$\begin{aligned}
\nu_{\text{m,sd}} &\sim 2.7 \times 10^{17} \text{ Hz } \xi^4 M_{\text{ej},-4}^{-4} n^{1/2} \epsilon_{e,-1}^2 \epsilon_{B,-2}^{1/2} \left(\frac{p-2}{p-1} \right)^2 \\
\nu_{\text{c,sd}} &\sim 8.6 \times 10^{14} \text{ Hz } \xi^{-4} M_{\text{ej},-4}^4 n^{-3/2} T_{\text{sd},3}^{-2} \epsilon_{B,-2}^{-3/2} \\
F_{\nu,\text{max,sd}} &\sim 2.4 \times 10^8 \text{ } \mu\text{Jy } \xi^{11} L_{0,49}^{-3} M_{\text{ej},-4}^{-8} n^{3/2} \epsilon_{B,-2}^{1/2} D_{27}^{-2} \\
T_{\text{ma1}} &\sim 1.4 \times 10^{-1} \text{ s } \xi^{-1} L_{0,49}^{-1/4} M_{\text{ej},-4}^{5/4} n^{1/8} T_{\text{sd},3}^{-5/4} \epsilon_{e,-1}^{-1/8} \epsilon_{B,-2}^{-1/8} \\
&\quad \times \left(\frac{p-2}{p-1} \right)^{-5/4} (p+1)^{1/4} f(p)^{1/4} \\
T_{\text{ma2}} &\sim 2.5 \times 10^8 \text{ s } \xi^{6/5} L_{0,49}^{2/5} M_{\text{ej},-4}^{-8/5} n^{-1/5} T_{\text{sd},3}^2 \epsilon_{e,-1}^2 \epsilon_{B,-2}^{1/5} \\
&\quad \times \left(\frac{p-2}{p-1} \right)^2 (p+1)^{-2/5} f(p)^{-2/5} \tag{6.8}
\end{aligned}$$

The expressions of γ and R as well as the power-law indices for this case are also presented in Table 28 and Table 29, respectively. The dynamics typical frequency evolution, and the light curves are presented in Fig.61. We note that in this case (and case III), the synchrotron radiation properties are very sensitive to M_{ej} and ξ .

Case III: $M_{\text{ej},c,1} < M_{\text{ej}} < M_{\text{ej},c,2}$ ($T_{\text{sd}} < T_{\text{dec}}$). As an example, we take $B_p \sim 10^{15}$ G, and $M_{\text{ej}} \sim 10^{-3} M_{\odot}$.

For this example, the dynamics and the expressions of the characteristic parameters become

$$\begin{aligned}
T_{\text{dec}} &\sim 1.5 \times 10^4 \text{ s } \xi^{-7/3} M_{\text{ej},-3}^{8/3} n^{-1/3} \\
T_{\text{N1}} &\sim 59.9 \text{ s } \xi^{-1} M_{\text{ej},-3} T_{\text{sd},3} \\
T_{\text{N2}} &\sim 2.7 \times 10^7 \text{ s } \xi^{1/3} n^{-1/3} \\
\gamma_{\text{sd}} &\sim 16.7 \xi M_{\text{ej},-3}^{-1} + 1 \tag{6.9}
\end{aligned}$$

and

$$\begin{aligned}
\nu_{\text{a,sd}} &\sim 1.6 \times 10^8 \text{ Hz } \xi^{8/5} M_{\text{ej},-3}^{-8/5} n^{4/5} T_{\text{sd},3}^{3/5} \epsilon_{e,-1}^{-1} \epsilon_{B,-2}^{1/5} \left(\frac{p-1}{p-2} \right) \\
&\quad \times (p+1)^{3/5} f(p)^{3/5}
\end{aligned}$$

$$\begin{aligned}
\nu_{\text{m,sd}} &\sim 4.5 \times 10^{14} \text{ Hz } \xi^4 M_{\text{ej},-3}^{-4} n^{1/2} \epsilon_{e,-1}^2 \epsilon_{B,-2}^{1/2} \left(\frac{p-2}{p-1} \right)^2 \\
\nu_{\text{c,sd}} &\sim 5.3 \times 10^{17} \text{ Hz } \xi^{-4} M_{\text{ej},-3}^4 n^{-3/2} T_{\text{sd},3}^{-2} \epsilon_{B,-2}^{-3/2} \\
F_{\nu,\text{max,sd}} &\sim 6.5 \times 10^2 \text{ } \mu\text{Jy } \xi^8 M_{\text{ej},-3}^{-8} n^{3/2} T_{\text{sd},3}^3 \epsilon_{B,-2}^{1/2} D_{27}^{-2} \\
T_{\text{ma1}} &\sim 1.0 \text{ s } \xi^{-5/4} M_{\text{ej},-3}^{5/4} n^{1/8} T_{\text{sd},3}^{5/4} \epsilon_{e,-1}^{-5/4} \epsilon_{B,-2}^{-1/8} \left(\frac{p-2}{p-1} \right)^{-5/4} \\
&\quad \times (p+1)^{1/4} f(p)^{1/4} \\
T_{\text{ma2}} &\sim 9.9 \times 10^7 \text{ s } \xi^{1/5} n^{-2/5} \epsilon_{e,-1}^2 \epsilon_{B,-2}^{1/5} \left(\frac{p-2}{p-1} \right)^2 \\
&\quad \times (p+1)^{-2/5} f(p)^{-2/5}
\end{aligned} \tag{6.10}$$

The power-law indices of various parameters for this case are also collected in Table 29, and the dynamics, frequency evolutions, and light curves are presented in Fig. 62.

Case IV: $M_{\text{ej}} > M_{\text{ej},c,2}$. In this case, the blast wave never reaches a relativistic speed. The dynamics is similar to Case III, with the coasting regime in the non-relativistic phase. The dynamics for a non-relativistic ejecta and its radio afterglow emission have been discussed in Nakar & Piran (2011). Our Case IV resembles what is discussed in Nakar & Piran (2011), but the afterglow flux is much enhanced because of a larger total energy involved.

Detectability and Implications

For all the cases, bright broadband EM afterglow emission signals are predicted. The light curves typically show a sharp rise around T_{sd} , which coincides the ending time of the X-ray afterglow signal discussed by Zhang (2013b) due to internal dissipation of the magnetar wind. The X-ray afterglow luminosity predicted in our model is generally lower than that of the internal dissipation signal, but the optical and radio signals are much brighter. In some cases, the R-band magnitude can reach 11th at the 300 Mpc, if M_{ej} is small enough (so that the blastwave has a high Lorentz factor)

and the medium density is not too low. The duration of detectable optical emission ranges from 10^3 seconds to year time scale. The radio afterglow can reach the Jy level for an extended period of time, with peak reached in the year time scale. These signals can be readily picked up by all-sky optical monitors, and radio surveys. The X-ray afterglow can be also picked up by large field-of-view imaging telescopes such as ISS-Lobster.

Since these signals are originated from interaction between the magnetar wind and the ejecta in the equatorial directions, they are not supposed to be accompanied with short GRBs, and some internal-dissipation X-ray afterglows (Zhang, 2013b) in the free wind zone. Due to a larger solid angle, the event rate for this geometry (orange observer in Fig.59) should be higher than the other two geometries (red and yellow observers in Fig.59). However, the brightness of the afterglow critically depends on the unknown parameters such as M_{ej} , B_p (and hence L_0), and n . The event rate also crucially depends on the event rate of NS-NS mergers and the fraction of mergers that leave behind a massive magnetar rather than a black hole.

This afterglow signal is much stronger than the afterglow signal due to ejecta-medium interaction with a black hole as the post-merger product (Nakar & Piran, 2011). The main reason is the much larger energy budget involved in the magnetar case. Since the relativistic phase can be achieved, both X-ray and optical afterglows are detectable, which peak around the magnetar spindown time scale ($10^3 - 10^5$ s). The radio peak is later similar to the black hole case (Nakar & Piran, 2011), but the radio afterglow flux is also much brighter (reaching Jy level) due to a much larger energy budget involved. The current event rate limit of > 350 mJy radio transients in the minutes-to-days time scale at 1.4 GHz is $< 6 \times 10^{-4}$ degree $^{-2}$ yr $^{-1}$ (Bower & Saul, 2011), or < 20 yr all sky. In view of the large uncertainties in the NS-NS merger rate and the fraction of millisecond magnetar as the post-merger product, our prediction is entirely consistent with this upper limit. Because of their brightness, these radio

transients can be detected outside the Advanced LIGO horizon, which may account for some sub-mJy radio transients discovered by VLA (Bower et al., 2007).

Recently, Kyutoku et al. (2012) proposed another possible EM counterpart of GW signal with a wide solid angle. They did not invoke a long-lasting millisecond magnetar as the merger product, but speculated that during the merger process, a breakout shock from the merging neutron matter would accelerate a small fraction of surface material, which reaches a relativistic speed. Such an outflow would also emit broad-band synchrotron emission by shocking the surrounding medium. Within that scenario, the predicted peak flux is lower and the duration is shorter than the electro-magnetic signals predicted in (Zhang, 2013b) and this work, due to a much lower energy carried by the outflow.

Detecting the GW-associated bright signals as discussed in this work would unambiguously confirm the astrophysical origin of GW signals. Equally importantly, it would suggest that NS-NS mergers leave behind a hyper-massive neutron star, which gives an important constraint on the neutron star equation of state. With the GW data, one can infer the information of the two NSs involved in the merger. Modeling afterglow emission can give useful constraints on the ejected mass M_{ej} and the properties of the postmerger compact objects. Therefore, a combination of GW and afterglow information would shed light into the detailed merger physics, and in particular, provide a probe of massive millisecond magnetars and stiff equations of state for neutron matter.

	γ	R	
Case I	$t < T_{N1}$	$0.28L_{0,47}M_{ej,-4}^{-1}t_3 + 1$	$3.2 \times 10^{13}L_{0,47}^{1/2}M_{ej,-4}^{-1/2}t_3^{3/2}$
	$T_{N1} < t < T_{dec}$	$2.8L_{0,47}M_{ej,-4}^{-1}t_4 + 1$	$4.6 \times 10^{15}L_{0,47}^2M_{ej,-4}^{-2}t_4^3$
	$T_{dec} < t < T_{sd}$	$9.9L_{0,47}^{1/8}n^{-1/8}t_5^{-1/4} + 1$	$5.9 \times 10^{17}L_{0,47}^{1/4}n^{-1/4}t_5^{1/2}$
	$T_{sd} < t < T_{N2}$	$4.2L_{0,47}^{1/8}T_{sd,5}^{1/8}n^{-1/8}t_6^{-3/8} + 1$	$1.1 \times 10^{18}L_{0,47}^{1/4}T_{sd,5}^{1/4}n^{-1/4}t_6^{1/4}$
	$t > T_{N2}$	$0.4L_{0,47}^{2/5}T_{sd,5}^{2/5}n^{-2/5}t_8^{-6/5} + 1$	$3.7 \times 10^{18}L_{0,47}^{1/5}T_{sd,5}^{1/5}n^{-1/5}t_8^{2/5}$
Case II	$t < T_{N1}$	$0.08\xi M_{ej,-4}^{-1}T_{sd,3}^{-1}t + 1$	$1.7 \times 10^{10}\xi^{1/2}M_{ej,-4}^{-1/2}T_{sd,3}^{-1/2}t^{3/2}$
	$T_{N1} < t < T_{sd}$	$83.3\xi M_{ej,-4}^{-1}T_{sd,3}^{-1}t_3 + 1$	$4.2 \times 10^{17}\xi^2M_{ej,-4}^{-2}T_{sd,3}^{-2}t_3^3$
	$T_{sd} < t < T_{N2}$	$14.8\xi M_{ej,-4}^{-1}T_{sd,3}^{3/8}t_5^{-3/8} + 1$	$1.3 \times 10^{18}\xi^2M_{ej,-4}^{-2}T_{sd,3}^{3/4}t_5^{1/4}$
	$t > T_{N2}$	$1.4\xi^{16/5}M_{ej,-4}^{-16/5}T_{sd,3}^{6/5}t_8^{-6/5} + 1$	$7.1 \times 10^{18}\xi^{8/5}M_{ej,-4}^{-8/5}T_{sd,3}^{3/5}t_8^{2/5}$
Case III	$t < T_{N1}$	$0.02\xi M_{ej,-3}^{-1}T_{sd,3}^{-1}t + 1$	$7.8 \times 10^9\xi^{1/2}M_{ej,-3}^{-1/2}T_{sd,3}^{-1/2}t^{3/2}$
	$T_{N1} < t < T_{sd}$	$16.7\xi M_{ej,-3}^{-1}T_{sd,3}^{-1}t_3 + 1$	$1.7 \times 10^{16}\xi^2M_{ej,-3}^{-2}T_{sd,3}^{-2}t_3^3$
	$T_{sd} < t < T_{dec}$	$16.7\xi M_{ej,-3}^{-1} + 1$	$1.7 \times 10^{17}\xi^2M_{ej,-3}^{-2}t_4$
	$T_{dec} < t < T_{N2}$	$3.5\xi^{1/8}n^{-1/8}t_6^{-3/8} + 1$	$7.2 \times 10^{17}\xi^{1/4}n^{-1/4}t_6^{1/4}$
	$t > T_{N2}$	$0.2\xi^{2/5}n^{-2/5}t_8^{-6/5} + 1$	$2.8 \times 10^{18}\xi^{1/5}n^{-1/5}t_8^{2/5}$

Table 28 Expression of the Lorentz factor and radius as a function of model parameters in different temporal regimes for all dynamical cases.

	$\gamma - 1$	R	ν_a	ν_m	ν_c	$F_{\nu, \max}$
Case I: $L_0 \sim 10^{47} \text{ erg s}^{-1}, M_{\text{ej}} \sim 10^{-4} M_{\odot}$						
$t < T_{\text{ma1}}$	1	$\frac{3}{2}$	$\frac{5p+4}{2(p+4)}$	$\frac{5}{2}$	$-\frac{7}{2}$	5
$T_{\text{ma1}} < t < T_{\text{N1}}$	1	$\frac{3}{2}$	$\frac{1}{10}$	$\frac{5}{2}$	$-\frac{7}{2}$	5
$T_{\text{N1}} < t < T_{\text{dec}}$	1	3	$\frac{11}{5}$	4	-6	11
$T_{\text{dec}} < t < T_{\text{sd}}$	$-\frac{1}{4}$	$\frac{1}{2}$	$\frac{1}{5}$	-1	-1	1
$T_{\text{sd}} < t < T_{\text{ma2}}$	$-\frac{3}{4}$	$\frac{1}{4}$	0	$-\frac{3}{2}$	$-\frac{1}{2}$	0
$T_{\text{ma2}} < t < T_{\text{N2}}$	$-\frac{3}{4}$	$\frac{1}{4}$	$-\frac{3p+2}{2(p+4)}$	$-\frac{3}{2}$	$-\frac{1}{2}$	0
$t > T_{\text{N2}}$	$-\frac{6}{5}$	$\frac{2}{5}$	$\frac{2-3p}{p+4}$	-3	$-\frac{1}{5}$	$\frac{3}{5}$
Case II: $L_0 \sim 10^{49} \text{ erg s}^{-1}, M_{\text{ej}} \sim 10^{-4} M_{\odot}$						
$t < T_{\text{ma1}}$	1	$\frac{3}{2}$	$\frac{5p+4}{2(p+4)}$	$\frac{5}{2}$	$-\frac{7}{2}$	5
$T_{\text{ma1}} < t < T_{\text{N1}}$	1	$\frac{3}{2}$	$\frac{1}{10}$	$\frac{5}{2}$	$-\frac{7}{2}$	5
$T_{\text{N1}} < t < T_{\text{sd}}$	1	3	$\frac{11}{5}$	4	-6	11
$T_{\text{sd}} < t < T_{\text{ma2}}$	$-\frac{1}{4}$	$\frac{1}{4}$	0	$-\frac{3}{2}$	$-\frac{1}{2}$	0
$T_{\text{ma2}} < t < T_{\text{N2}}$	$-\frac{3}{4}$	$\frac{1}{4}$	$-\frac{3p+2}{2(p+4)}$	$-\frac{3}{2}$	$-\frac{1}{2}$	0
$t > T_{\text{N2}}$	$-\frac{6}{5}$	$\frac{2}{5}$	$\frac{2-3p}{p+4}$	-3	$-\frac{1}{5}$	$\frac{3}{5}$
Case III: $L_0 \sim 10^{49} \text{ erg s}^{-1}, M_{\text{ej}} \sim 10^{-3} M_{\odot}$						
$t < T_{\text{ma1}}$	1	$\frac{3}{2}$	$\frac{5p+4}{2(p+4)}$	$\frac{5}{2}$	$-\frac{7}{2}$	5
$T_{\text{ma1}} < t < T_{\text{N1}}$	1	$\frac{3}{2}$	$\frac{1}{10}$	$\frac{5}{2}$	$-\frac{7}{2}$	5
$T_{\text{N1}} < t < T_{\text{sd}}$	1	3	$\frac{11}{5}$	4	-6	11
$T_{\text{sd}} < t < T_{\text{dec}}$	0	1	$\frac{5}{5}$	0	-2	3
$T_{\text{dec}} < t < T_{\text{ma2}}$	$-\frac{3}{4}$	$\frac{1}{4}$	0	$-\frac{3}{2}$	$-\frac{1}{2}$	0
$T_{\text{ma2}} < t < T_{\text{N2}}$	$-\frac{3}{4}$	$\frac{1}{4}$	$-\frac{3p+2}{2(p+4)}$	$-\frac{3}{2}$	$-\frac{1}{2}$	0
$t > T_{\text{N2}}$	$-\frac{6}{5}$	$\frac{2}{5}$	$\frac{2-3p}{p+4}$	-3	$-\frac{1}{5}$	$\frac{3}{5}$

Table 29 Temporal scaling indices of various parameters in different temporal regimes for all dynamical cases.

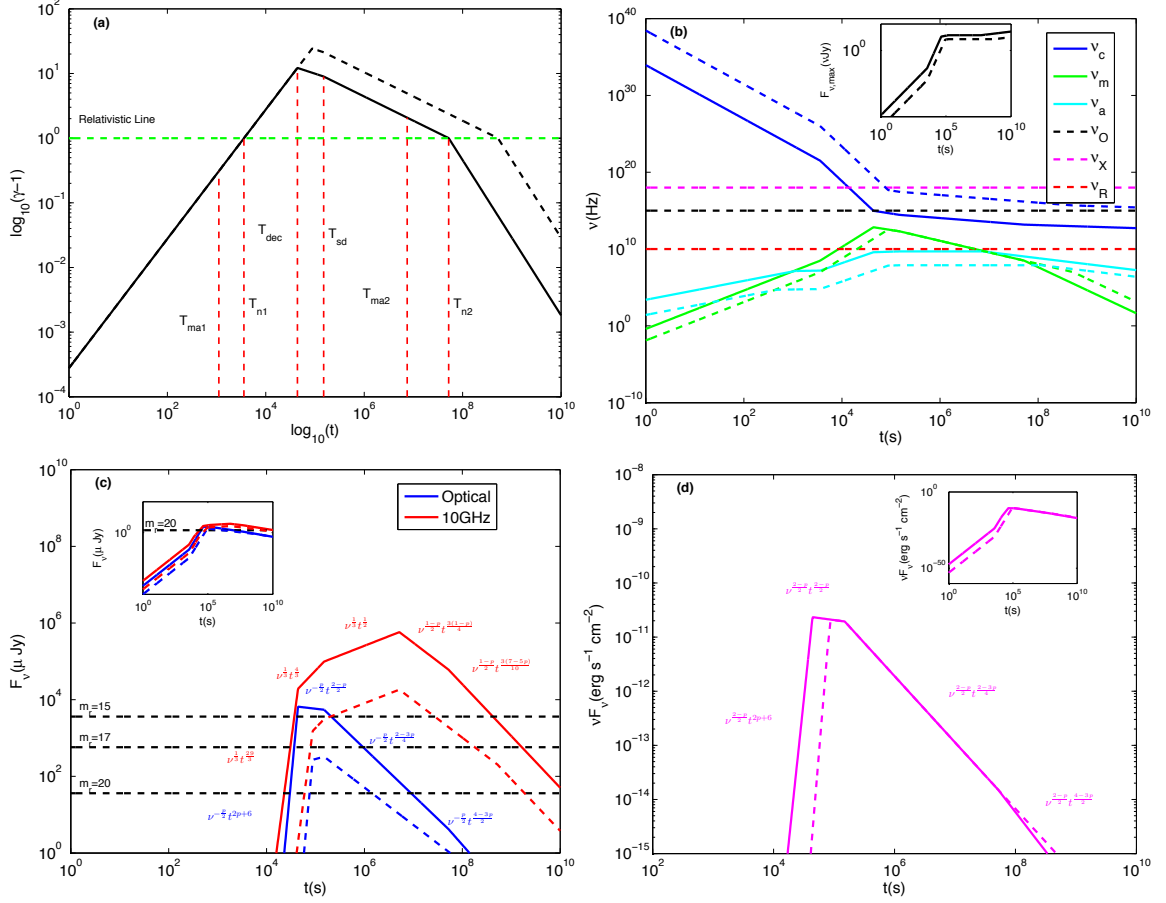


Figure 60 Calculation results for Case I: $L_0 \sim 10^{47}$ erg s $^{-1}$ and $M_{ej} \sim 10^{-4}M_\odot$ (for all the examples, we adopt $\xi = 0.5$, $p = 2.3$). (a) The dynamical evolution of the parameter $(\gamma - 1)$; (b) Temporal evolutions of the characteristic frequencies ν_a , ν_m , and ν_c , and the peak flux density $F_{\nu,max}$; (c) Analytical light curve in R-band (blue) and 10 GHz radio band (red); (d) Analytical light curve in X-ray band. The solid and dashed lines are for $n = 1$ cm $^{-3}$ and $n = 10^{-3}$ cm $^{-3}$, respectively. In (c) and (d), we mark the spectral and temporal indices for each segment of the light curves for $n = 1$ cm $^{-3}$. The main figures denote the time regimes when the light curves are detectable. The insets show the full light curves for completeness. Both X-ray and optical light curves reach their peaks around 10^4 s, and remain detectable in years. The radio light curve peaks around 10^7 s, and lasts even longer. The peak flux for X-ray, optical and radio could be as bright as 10^{-11} erg s $^{-1}$ cm $^{-2}$, 10 mJy and Jy, respectively.

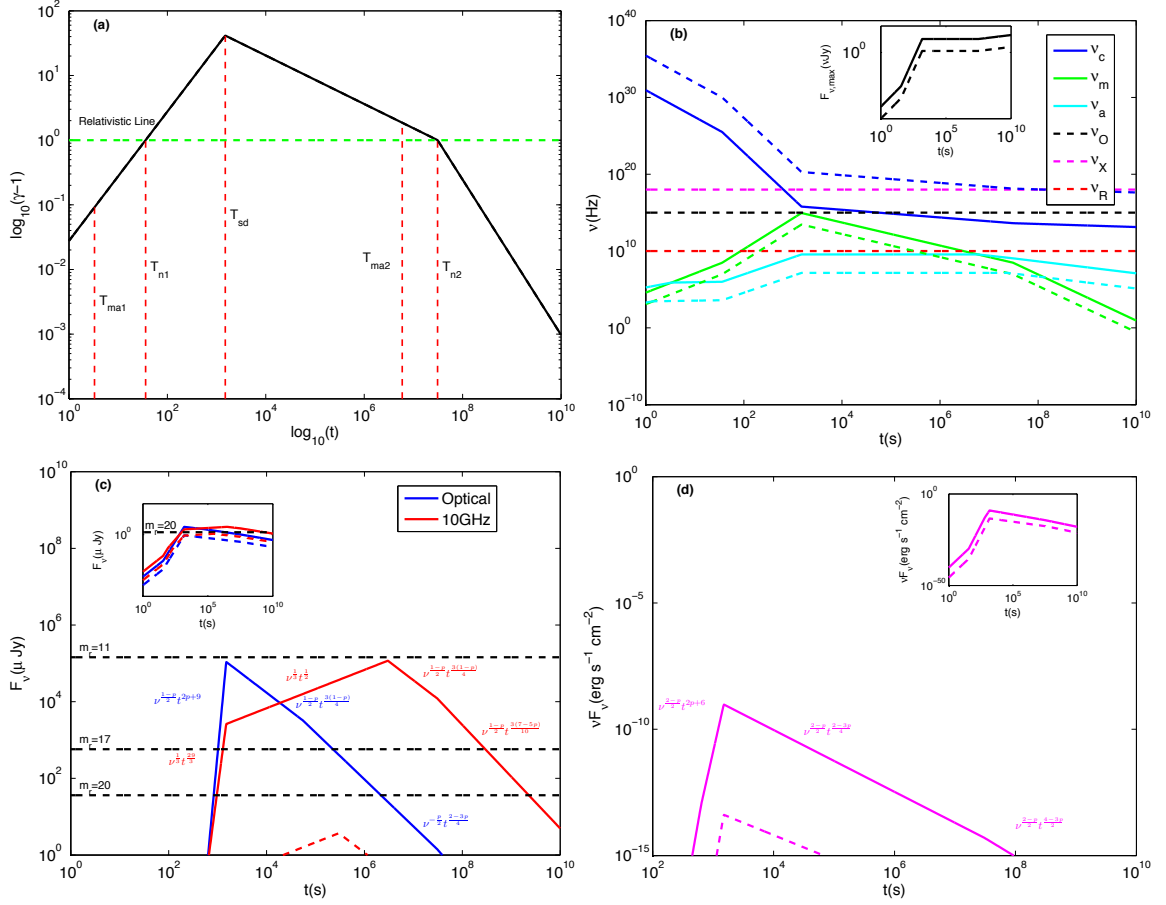


Figure 61 Calculation results for Case II: $L_0 \sim 10^{49}$ erg s $^{-1}$ and $M_{ej} \sim 10^{-4} M_{\odot}$. Captions are the same with Figure 60. For $n = 1$ cm $^{-3}$, both X-ray and optical light curve reach their peaks around 10^3 s, and the radio light curve peaks around 10^7 s. The peak flux of X-ray, optical, and radio is 10^{-9} erg s $^{-1}$ cm $^{-2}$, 100 mJy and 100 mJy, respectively. Taking R-band magnitude 20 and 10^{-15} erg s $^{-1}$ cm $^{-2}$ as the detection limit, the durations of the detectable optical and X-ray afterglow are $\sim 10^6$ s and $\sim 10^8$ s respectively. The radio afterglow lasts even longer. For $n = 10^{-3}$ cm $^{-3}$, the signals for X-ray is still detectable, but with shorter durations, $\sim 10^5$ s.

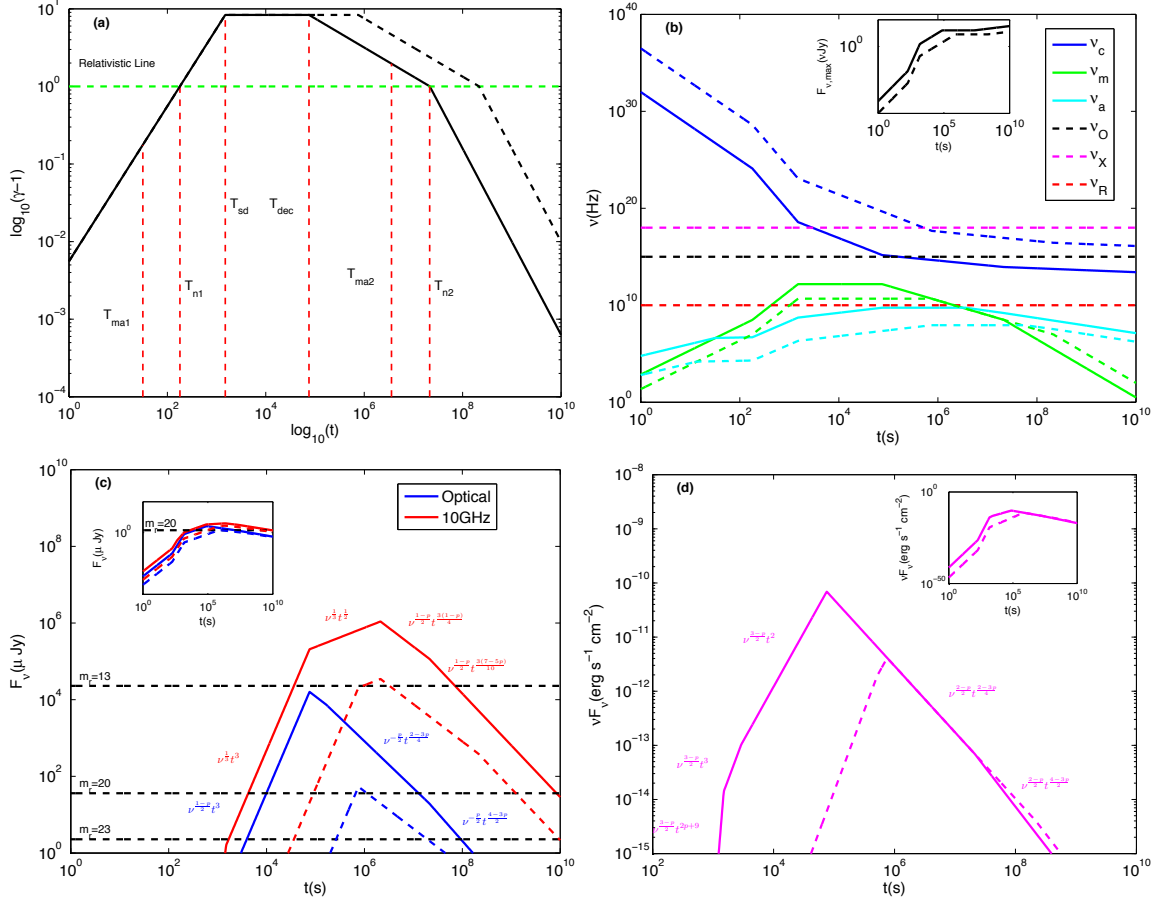


Figure 62 Calculation results for Case III: $L_0 \sim 10^{49} \text{ erg s}^{-1}$ and $M_{ej} \sim 10^{-3} M_{\odot}$. Captions are the same with Figure 61. For $n = 1 \text{ cm}^{-3}$, both X-ray and optical light curve reach their peaks around 10^5 s , and the radio light curve peaks around 10^6 s . The peak flux for X-ray, optical and radio is $10^{-10} \text{ erg s}^{-1} \text{ cm}^{-2}$, 10 mJy and Jy , respectively. Taking R-band magnitude 20 and $10^{-15} \text{ erg s}^{-1} \text{ cm}^{-2}$ as the detection limit, the durations of the observable optical and X-ray afterglows are $\sim 10^7 \text{ s}$ and $\sim 10^8 \text{ s}$ respectively. The radio duration lasts even longer. If $n = 10^{-3} \text{ cm}^{-3}$, the optical signal just reaches R-band magnitude 20 around $\sim 10^6 \text{ s}$, while the X-ray afterglow is detectable with a duration $\sim 10^8 \text{ s}$.

CHAPTER 7

A DOUBLE NEUTRON STAR MERGER ORIGIN FOR THE COSMOLOGICAL RELATIVISTIC FADING SOURCE PTF11AGG?

This chapter is part of the following published paper :

Wu, X.-F., Gao H., Ding, X., Zhang B., Dai, Z.-G., Wei, J.-Y., 2013, Astrophysics Journal 771,86

Statement of coauthorship: This chapter is based on the published paper mentioned above. This paper (Wu, X.-F., Gao H., Ding, X., Zhang B., Dai, Z.-G., Wei, J.-Y., 2013, Astrophysics Journal 771,86) was led by Xue-Feng Wu, who first propose to use DNS merger afterglow model to explain PTF11agg. Since the main calculation in this work was carried out by me and I also contribute to the writing part of this paper, I put this work as part of my dissertation.

Introduction

Recently, Cenko et al. (2013) (hereafter C13) reported a new discovery from the Palomar Transient Factory (PTF), named as PTF11agg. A multi-wavelength counterpart search was performed for this rapidly fading optical transient. While a year-long scintillating radio counterpart was identified, no high energy counterpart was found. Based on a late-time, deep optical observation which revealed a faint, quiescent source at the transient location, C13 suggested a cosmological origin for this transient. If so, a relativistic ejecta is required in order to explain the incoherent radio emission.

Many cosmological sources have been known (or proposed) to be able to generate relativistic ejecta, such as active galactic nuclei (Ghisellini et al. 1993; Krawczynski & Treister 2013), gamma-ray bursts (GRBs; Zhang & Mészáros 2004; Mészáros 2006; Gehrels & Razzaque 2013), tidal disruption of a star by a supermassive black hole (Burrows et al., 2011; Bloom et al., 2011; Cenko et al., 2012; Lei & Zhang, 2011; Lei et al., 2013), as well as core-collapse supernova without GRB association (Soderberg et

al., 2010). Among these sources, the GRB afterglows have the most similar observed properties to PTF11agg, regardless of the fact that PTF11agg has no high energy counterparts. If PTF11agg is indeed a GRB afterglow, the lack of a high energy signature could be explained in two ways: an on-axis burst but without a high energy band trigger due to a lack of satellite coverage; or an off-axis burst that gives rise to an “orphan” afterglow emerging due to a viewing-angle effect (Rhoads, 1997; Nakar & Piran, 2002). C13 considered both possibilities: it turns out the likelihood of an “untriggered” on-axis long GRB being discovered by PTF is quite small ($\sim 2.6\%$), and the off-axis afterglow model fails to interpret both the optical and radio data. They therefore speculated that PTF11agg may represent a new class of relativistic outburst. We suggest that PTF11agg might be the first recognized detection of MDNSM afterglow emission.

Observations of PTF11agg

PTF11agg was first detected by the Palomar 48 inch Oschin telescope at 5:17:11 on 2011 January 30, and is located at R.A.(J2000.0) = $08^{\text{h}}22^{\text{m}}17.195^{\text{s}}$, decl.(J2000.0) = $+21^{\circ}37'38''.26$. In the R band, the source shows decay behavior from the very beginning, with $R = 18.26 \pm 0.05$ mag in the first detection image and a faint last detection $R = 22.15 \pm 0.33$ mag on 2011 February 1. Checking back to 2009 November, no optical emission was reported at this location. Late-time ($\Delta t > 1$ month) deep optical observation revealed a faint, unresolved source in g' and R bands at R.A.(J2000.0) = $08^{\text{h}}22^{\text{m}}17.202^{\text{s}}$, decl.(J2000.0) = $+21^{\circ}37'38''.26$. Based on this detection, C13 speculated that the redshift of PTF11agg should fall somewhere in the range $0.5 \lesssim z \lesssim 3.0$. The R band light curve of PTF11agg could be fitted well by a power-law with a best-fit index $\alpha = 1.66 \pm 0.35$, if $t_0 = 23:34$ UT (± 1.7 hr) on 2011 January 29 is taken as the onset time.

Besides optical observation, the Karl G. Jansky Very Large Array (Perley et al.

2011) was also employed to observe the radio counterpart of PTF11agg, starting from 2011 March 11, with a total bandwidth 8 GHz and local oscillator frequency 93.6 GHz. The spectral energy distribution in the radio band was constructed at two epochs on 2011 March 14 and 2011 April 7, and both can be fitted with a power law with an index $\beta = 1/3$ (convention $F_\nu \propto \nu^\beta$). Based on the constraints from the angular diameter of the emitting region, C13 inferred that PTF11agg was initially at least modestly relativistic.

C13 also checked the archival data from three primary high-energy facilities for GRB triggers, i.e. InterPlanetary Network (Hurley et al., 2010), the Gamma-ray Burst Monitor on the *Fermi* spacecraft (Meegan et al., 2009), and Burst Alert Telescope on the *Swift* spacecraft (Barthelmy et al., 2005c). No temporally coincident triggers were reported in the direction of PTF11agg. The X-Ray Telescope (Burrows et al. 2005b) on *Swift* was also later employed to observe the location of PTF11agg on 2011 March 13, but no X-ray source was detected.

Applying DNS Merger Afterglow Model to PTF11agg

In the Blandford-McKee regime, the characteristic synchrotron frequencies and the peak synchrotron flux density $F_{\nu, \max} = 4\pi/3R^3n P_{\nu, \max}$ for a constant circum-medium density could be expressed (see Chapter 4 for detail)

$$\begin{aligned}
\nu_m &= 8.1 \times 10^{11} \text{ Hz } (1+z)^{1/2} \left(\frac{p-2}{p-1} \right)^2 E_{52}^{1/2} \epsilon_{e,-1}^2 \epsilon_{B,-2}^{1/2} t_5^{-3/2}, \\
\nu_c &= 2.9 \times 10^{16} \text{ Hz } (1+z)^{-1/2} E_{52}^{-1/2} n_{0,0}^{-1} \epsilon_{B,-2}^{-3/2} t_5^{-1/2} \\
F_{\nu, \max} &= 1.1 \times 10^4 \text{ } \mu\text{Jy } (1+z) E_{52} n_{0,0}^{1/2} \epsilon_{B,-2}^{1/2} D_{28}^{-2}, \\
\nu_a &= 3.1 \times 10^9 \text{ Hz } (1+z)^{-6/5} \frac{g(p)}{g(3.2)} E_{52}^{1/5} n_{0,0}^{3/5} \epsilon_{e,-1}^{-1} \epsilon_{B,-2}^{1/5},
\end{aligned} \tag{7.1}$$

where $g(p) = \left(\frac{p-1}{p-2}\right) (p+1)^{3/5} \left(\frac{\Gamma(\frac{3p+22}{12})\Gamma(\frac{3p+2}{12})}{\Gamma(\frac{3p+19}{12})\Gamma(\frac{3p-1}{12})}\right)^{3/5}$ is a numerical constant relate to p .

Before applying the above DNS merger afterglow model (see Chapter 6 for detail) to explain the PTF11agg data, we first simply summarize the observational properties of PTF11agg as follows (Cenko et al., 2013):

- Late time radio data suggest that the ejecta should be still relativistic even at a very late epoch;
- The optical light curve starts to decay at the very beginning of observation, i.e., $t_s = 2 \times 10^4$ s, with a simple power law decay slope $\alpha = 1.66 \pm 0.35$. The first optical flux in R band is about $180 \mu\text{Jy}$ (see Figure 63);
- The radio band (8 GHz) light curve reached its peak around 10^7 s, where the peak flux is about $200 \mu\text{Jy}$. The spectral slope for the early radio spectral regime is about $\beta = 1/3$ (until 5.8×10^6 s), implying that the radio peak should correspond to ν_m crossing.

First, to reach a relativistic speed for the ejecta, we need

$$M_{\text{ej}} \leq M_{\text{ej},c} \quad (7.2)$$

where $M_{\text{ej},c} \sim 6 \times 10^{-3} M_{\odot} I_{45} P_{0,-3}^{-2} \xi$ (defined by setting $E_{\text{rot}} \xi = 2(\gamma - 1) M_{\text{ej},c} 2c^2$), above which the blast wave would never reach a relativistic speed (Gao et al., 2013b). Nevertheless, there is no obvious break for late radio light curve, implying that the ejecta is still in the relativistic regime (e.g. $\gamma - 1 \geq 1$) until the end of the observation $t_e = 3 \times 10^7$ s. Since it is in the Blandford-McKee stage, the ejecta evolves as $\gamma \propto t^{-3/8}$, we thus have

$$\max(\gamma_{\text{sd}} - 1, \gamma_{\text{dec}} - 1) \geq \left(\frac{t_e}{t_s}\right)^{3/8}. \quad (7.3)$$

Second, since the R -band light curve starts to decay from the beginning of the observation, we thus have

$$\max(t_{\text{sd}}, t_{\text{dec}}) \leq t_s. \quad (7.4)$$

On the other hand, since the radio light curve (see Figure 63) implies that ν_m crosses the 8 GHz band at about $5.8 \times 10^6 \sim 1.2 \times 10^7$, we thus have

$$8.1 \times 10^{11} (1+z)^{1/2} \left(\frac{p-2}{p-1} \right)^2 E_{52}^{1/2} \epsilon_{e,-1}^2 \tilde{\epsilon}_{B,-2}^{1/2} \left(\frac{t_{\text{cross}}}{10^5} \right)^{-3/2} = 8 \times 10^9, \quad (7.5)$$

where

$$5.8 \times 10^6 < t_{\text{cross}} < 1.2 \times 10^7. \quad (7.6)$$

Moreover, from $\nu_m \propto t^{-3/2}$, one could easily estimate that $\nu_m(t_s) < \nu_{\text{opt}} = 5 \times 10^{14} \text{Hz}$. We thus expect the optical band to fall into the spectrum regime $\nu_m < \nu_{\text{opt}} < \nu_c$. Consequently the observed temporal decay index ($\alpha_{\text{opt}} = 1.66 \pm 0.35$) can be translated directly into the electron spectral index p , i.e., for a constant-density medium as suggested by C13, we find $p = 3.2 \pm 0.47$. At t_s , we have

$$f_\nu(t_s) = F_{\nu, \text{max}} \left(\frac{\nu}{\nu_m} \right)^{-1.1} \approx 180 \mu\text{Jy}. \quad (7.7)$$

Based on the peak flux in the radio band, we get

$$1.1 \times 10^4 (1+z) E_{52} n_{0,0}^{1/2} \tilde{\epsilon}_{B,-2}^{1/2} D_{28}^{-2} \approx 200 \quad (7.8)$$

Moreover, the self-absorption frequency should fall below the radio frequency range,

i.e.,

$$3.1 \times 10^9 (1+z)^{-6/5} E_{52}^{1/5} n_{0,0}^{3/5} \epsilon_{e,-1}^{-1} \tilde{\epsilon}_{B,-2}^{1/5} < 8 \times 10^9. \quad (7.9)$$

Note that the ejecta formed in a DNS merger system would expand into a pulsar wind bubble created by the progenitor pulsars (Gallant & Achterberg, 1999). The radius of the bubble could be about 10^{17} cm (Königl & Granot, 2002). The value of ϵ_B should be relatively large in the bubble (Königl & Granot, 2002). One can easily find that the optical signals of PTF11agg are emitted within this bubble radius (with ϵ_B), while the radio emission is emitted from outside (with $\tilde{\epsilon}_B = \eta \epsilon_B$, and $0 < \eta < 1$, see equations 7.5, 7.8 and 7.9).

From equations 7.2-7.4, we get the following constraints on the ejecta mass and spin down luminosity:

$$\begin{aligned} M_{\text{ej}} &\leq 1.1 \times 10^{-3} \xi M_{\odot} \\ L_{\text{sd},0} &\geq 1.5 \times 10^{48} \xi \text{ erg s}^{-1}. \end{aligned} \quad (7.10)$$

Combining equations 7.5-7.9, we have

$$\begin{aligned} \eta^{1/2} &= 0.006 \xi^{-1} (1+z)^{-1} n^{-1/2} \epsilon_{B,-2}^{-1/2} D_{28}^2 \\ n^{1/2} &= 0.93 \xi^{-1.55} (1+z)^{-1.55} \epsilon_{e,-1}^{-2.2} \epsilon_{B,-2}^{-1.05} D_{28}^2 \\ 1240 (1+z)^{-1.05} \xi^{-1.05} &\leq \epsilon_{e,-1}^{4.2} \epsilon_{B,-2}^{1.05} \leq 3921 (1+z)^{-1.05} \xi^{-1.05}. \end{aligned} \quad (7.11)$$

For a given redshift, we only get three independent constraints on five unknown

z	n (cm $^{-3}$)	ϵ_e	ϵ_B	η	ξ	p
0.5	1.0×10^{-4}	0.4	0.08	0.09	0.3	3.2
1	2.4×10^{-3}	0.4	0.06	0.09	0.3	3.2
3	0.26	0.4	0.03	0.09	0.3	3.2

Table 30 Adopt parameters for fitting the optical and radio data of PTF11agg for different redshift.

parameters, i.e., ξ , n , ϵ_e , ϵ_B and η (note that $p = 3.2$ is fixed). This leaves us some degeneracy in choosing parameters to fit the data.

In the following, we fix $\xi = 1/3$ (i.e. $\sim 10^{52}$ erg spin down energy injected into the ejecta) and $\epsilon_e = 0.4$, and then fit the optical and radio data for different redshifts by adopting appropriate values for ϵ_B , n and η . One fitting result is shown in Figure 63, and the adopted parameters are collected in Table 30. With the chosen parameters, we have derived the corresponding X-ray flux, which is found to be consistent with the non-detection limitation.

In view of the fact that PTF11agg might be the first recognized candidate for DNS merger afterglow, it would be helpful to compare the inferred shock parameter values with those of other relativistic shock related phenomena, such as GRBs. Recently, Santana et al. (2013) performed a careful literature search for ϵ_e and ϵ_B , and found that $\epsilon_e \sim 0.02 - 0.6$ and $\epsilon_B \sim 3.5 \times 10^{-5} - 0.33$ were favored by the observations. With GRB optical afterglow data, Liang et al. (2013) found that the electron spectral index p is distributed in the range from 2 to 3.5¹. Moreover, Shen et al. (2006) performed a general investigation for relativistic sources, such as GRBs (with both prompt and afterglow data), blazars and pulsar wind nebulae, and found a similar broad distribution of p . Our inferred parameters from the DNS merger afterglow model fall well within the ranges of these parameter distributions.

¹Note that medium density profile is relevant for determining the electron index p . For a general circumburst medium density profile $n \propto r^{-k}$ as adopted in Liang et al. (2013), the derived p would be somewhat larger than the value derived by assuming a constant density of the medium

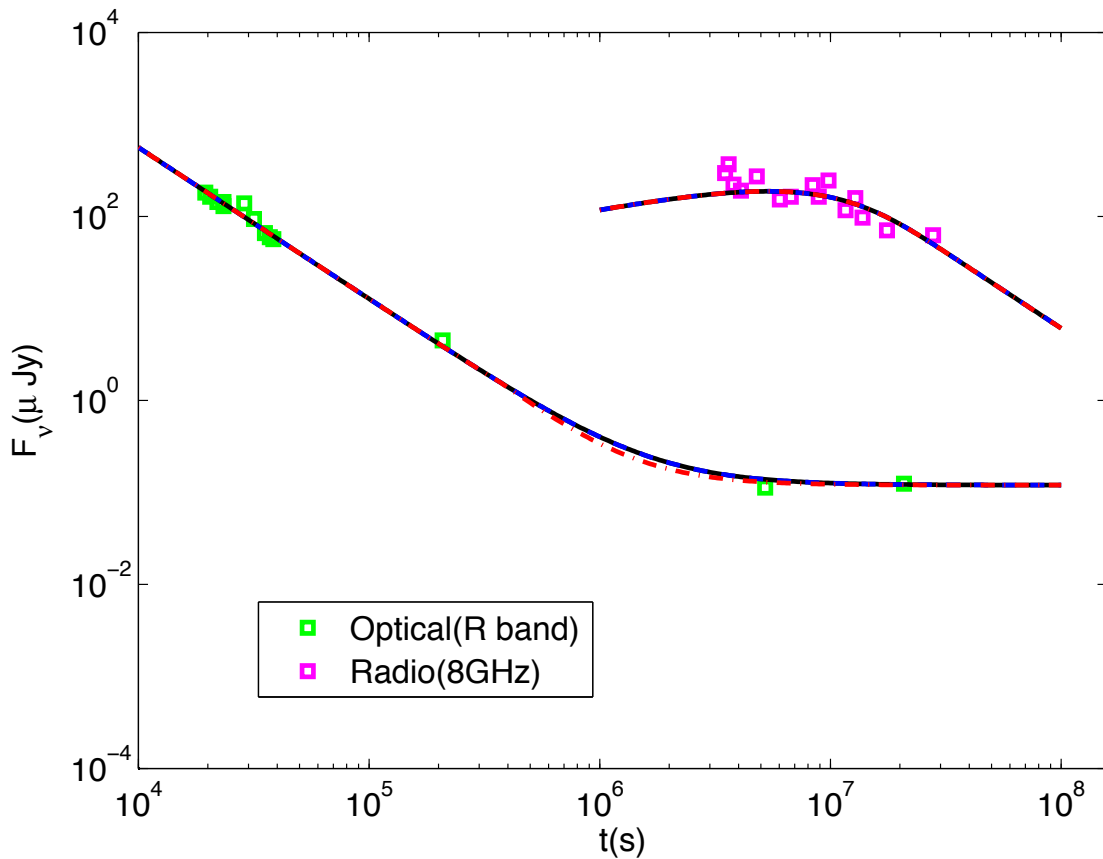


Figure 63 Optical and radio (8 GHz) light curves for PTF11agg, with best fittings by assuming different redshift for the source. The green square denotes the optical observation and the purple squares denote the radio data. The black solid line is for $z = 0.5$, the blue dash line is for $z = 1$ and the red dash-dot line is for $z = 3$.

Discussion

We have proposed a DNS merger origin for the cosmological relativistic fading source PTF11agg. Based on the observational properties of PTF11agg, we analytically constrained the parameter space for the DNS merger afterglow model and then fit the multi-wavelength data by adopting appropriate parameter values. We find that the DNS merger afterglow model could fit both the optical and radio data well regardless of the source redshift. If our interpretation is correct, the following implications can be inferred:

First, the next generation gravitational-wave (GW) detectors are expected to de-

tect GW signals from mergers of two compact objects, with DNS mergers as primary targets. PTF11agg-like transients could be potential electromagnetic counterparts to such GW signals. The study of PTF11agg-like transients would not only shed light on the nature of the DNS merger scenario itself, but also contribute to identifying the astrophysical origin of GW signals.

Second, since DNS mergers are proposed to be the progenitor of short GRBs, the lack of a high energy counterpart for PTF11agg could be due to the fact that our line of sight is not along the direction of the jet axis. If so, there exists the possibility of simultaneously detecting a short GRB afterglow and (off-beam) PTF11agg-like emission, when our line of sight is within the jet opening angle. Since the PTF11agg-like emission component is Doppler de-boosted with respect to the on-beam calculations (Gao et al., 2013b), it is detectable only under favorable condition. Some short GRB afterglow features may be accounted for within this picture (H. Gao et al. 2014, in preparation).

Third, recently the short GRB 130603B has attracted attention by showing an infrared excess in its late emission (Tanvir et al., 2013; Berger, 2013). Even though it was suggested that this emission is consistent with the r -process powered “kilonova” emission with a black hole central engine, some authors have already pointed out that both the mergernova and short GRB afterglow of this burst can be understood within the scenario of a supra-massive magnetar central engine, as long as a large fraction of magnetar spin-energy is lost, possibly by GW radiation (Fan et al., 2013; Metzger & Piro, 2013). If so, the short-lived transient emission from GRB 130603B and PTF11agg may be different manifestations of the same intrinsic phenomenon with different viewing angles and/or magnetar parameters.

Finally, due to the large uncertainty of the DNS merger event rate and the fraction of mergers that produce stable magnetars, it is difficult to predict the detection rate by blind surveys for DNS merger afterglows (e.g. Yu et al., 2013, for a discussion).

C13 suggested the event rate of PTF11agg-like sources is ~ 5 times that of normal GRBs, namely $5 \text{ Gpc}^{-3} \text{ yr}^{-1}$. Assuming a fraction f of DNS mergers may give rise to PTF11agg-like events, one can estimate the DNS merger events rate as $\dot{\mathcal{N}} \sim 5/f \text{ Gpc}^{-3} \text{ yr}^{-1} = 50f_{-1}^{-1} \text{ Gpc}^{-3} \text{ yr}^{-1}$ (Gao et al., 2013c), which is consistent with predictions using other methods (Phinney, 1991; Kalogera et al., 2004; Abadie et al., 2010).

We note that Wang & Dai (2013) also proposed a different model for PTF11agg within the same framework as this Letter. They assumed that the magnetar wind injection is in the form of electron/positron pairs rather than a Poynting flux, and they interpreted the observed emission from the reverse shock region. They obtained different model parameter values and different spectral properties from ours. Future observations with a larger sample of PTF11agg-like transients may be helpful to distinguish between these two models, and consequently lead to a diagnosis of the composition of the magnetar wind.

CHAPTER 8

POSSIBLE HIGH-ENERGY NEUTRINO AND PHOTON SIGNALS FROM GRAVITATIONAL WAVE BURSTS DUE TO DOUBLE NEUTRON STAR MERGERS

This chapter is part of the following published paper :

Gao H., Wu, X.-F., Zhang B., Dai, Z.-G., 2013, Physical Review D 88, 043010

General Picture

As mentioned in Chapter 5, protons are expected to be accelerated in the forward shock powered by a magnetar wind pushing the ejecta launched during the merger process, serving as efficient high-energy cosmic ray accelerators. On the other hand, as propagating to us, photons emitted via magnetic dissipation at a smaller radius from the engine (Zhang, 2013b) would first pass through the external shock front, and have a good chance to interact with the accelerated protons. Strong photo-meson interactions happen at the Δ -resonance, when the proton energy E_p and photon energy E_γ satisfy the threshold condition

$$E_p E_\gamma \geq \frac{m_\Delta^2 - m_p^2}{2} \Gamma^2 = 0.147 \text{ GeV}^2 \Gamma^2, \quad (8.1)$$

where Γ is the bulk Lorentz factor, $m_\Delta = 1.232 \text{ GeV}$ and $m_p = 0.938 \text{ GeV}$ are the rest masses of Δ^+ and proton, respectively. The Δ^+ particle decays into two channels. The charged pion channel gives $\Delta^+ \rightarrow n\pi^+ \rightarrow ne^+\nu_e\bar{\nu}_\mu\nu_\mu$, with a typical neutrino energy $E_\nu \simeq 0.05E_p$. The neutron pion channel gives the $\Delta^+ \rightarrow p\pi^0 \rightarrow p\gamma\gamma$.

Note that the broad-band photons produced in the shocked region could also serve as the seed photons for $p\gamma$ interaction. However, since their peak flux in the X-ray band (Gao et al., 2013b) is much lower than that of the internal dissipation photons (Zhang, 2013b), we do not consider their contribution.

With the multi-messenger era of astronomy ushered in, studying multi-messenger

signals in astrophysical sources is of the great interest (e.g. Bartos et al. (2011)). The high-energy neutrino detectors such as IceCube have reached the sensitivity to detect high energy neutrinos from astrophysical objects for the first time. Gamma-ray bursts (GRBs) have been proposed to be one of the top candidates of PeV neutrinos (Waxman & Bahcall, 1997b). However, a dedicated search of high energy neutrinos coincident with GRBs have so far led to null results (Abbasi et al., 2010, 2011; Ahlers et al., 2011; Abbasi et al., 2012), which already places a meaningful constraint on GRB models (Abbasi et al., 2012; He et al., 2012; Zhang & Kumar, 2013a). Very recently, the IceCube collaboration announced their detections of two neutrino events with an energy approximately 1-2 PeV (Abbasi et al., 2012; Cholis & Hooper, 2013), which could potentially represent the first detections of high-energy neutrinos from astrophysical sources. Among the proposed sources of such cosmic rays, GRBs stand out as particularly capable of generating PeV neutrinos at this level (Cholis & Hooper, 2013; Liu & Wang, 2013). However, the absence of associated GRBs for these two events calls for alternative cosmological PeV neutrino sources. Here we investigate the possible neutrino signals associated with NS-NS mergers with a millisecond magnetar central engine using the photomeson interaction mechanism delineated above.

Initially, the heavy ejecta launched during the merger is not far away from the magnetar, so that in a large solid angle range, the magnetar wind would hit the ejecta before self-dissipation of the magnetar wind happens. In this case, a good fraction (η) of the magnetic energy may be rapidly discharged upon interaction between the wind and the ejecta. The Thomson optical depth for a photon to pass through the ejecta shell is $\tau_{\text{th}} \sim \sigma_{\text{T}} M_{\text{ej}} / (4\pi R^2 m_p)$. By setting the optical depth equals to unity, we define a photosphere radius $R_{\text{ph}} = 2.5 \times 10^{14} M_{\text{ej},-3}^{1/2}$ cm for the ejecta. When $R < R_{\text{ph}}$, the spectrum of the dissipated wind is likely quasi-thermal due to the large optical depth of photon scattering. The typical photon energy can be estimated as $E_{\text{ph,t}} \sim k(L_{\text{sd},0}\eta/4\pi R^2\sigma_{\text{SB}})^{1/4}/\tau_{\text{th}} \sim 27 \text{ eV } L_{\text{sd},0,47}^{1/4}\eta_{-1}^{1/4}M_{\text{ej},-4}^{-1}R_{14}^{3/2}$, where σ_{SB} is the

Stefan-Boltzmann constant. Alternatively, when $R > R_{\text{ph}}$, the typical synchrotron energy could be estimated as $E_{\gamma,t} \simeq 1.8 \times 10^4 \text{ keV } L_{\text{sd},0,47}^{1/2} R_{15}^{-1} \eta_{-1}^{3/2} \sigma_4^2$, where σ is the magnetization parameter of the Poynting flow when the magnetar wind catches the ejecta (Zhang & Yan, 2011a). In order to estimate the value of σ , we assume that the proto-magnetar has $\sigma_0 \sim 10^7$ at the central engine and the magnetized flow is quickly accelerated to $\Gamma \sim \sigma_0^{1/3}$ at $R_0 \sim 10^7 \text{ cm}$, where $\sigma \sim \sigma_0^{2/3}$ (Komissarov et al., 2009). After this phase, the flow may still accelerate as $\Gamma \propto R^{1/3}$, with σ falling as $\propto R^{-1/3}$ (Drenkhahn & Spruit, 2002a). Consequently, we have $E_{\gamma,t} \simeq 1.8 \text{ keV } L_{\text{sd},0,47}^{1/2} \eta_{-1}^{3/2} \sigma_{0,7}^{4/3} R_{0,7}^{2/3} R_{15}^{-5/3}$.

As it is pushed forward by the magnetar wind, at a late time the ejecta is far away enough from the central engine, so that before hitting the ejecta, the magnetar wind already starts to undergo strong self-dissipation, for instance, through internal-collision-induced magnetic reconnection and turbulence (ICMART) process (Zhang & Yan, 2011a). In this case, the typical synchrotron frequency can be still estimated as above, except that the emission radius is set to the self-dissipation radius, which we parameterize as the ICMART radius $R_i = 10^{15} R_{i,15}$, rather than the blastwave radius (Zhang & Yan, 2011a; Zhang, 2013b), i.e. $E_{\gamma,t} \simeq 1.8 \text{ keV } L_{\text{sd},0,47}^{1/2} \eta_{-1}^{3/2} \sigma_{0,7}^{4/3} R_{0,7}^{2/3} R_{i,15}^{-5/3}$. Notice that for a substantial range of M_{ej} , we have $R_{\text{ph}} < R_i$. Overall, the seed photon energy for $p\gamma$ interaction can be summarized as

$$E_{\gamma,t} = \begin{cases} 27 \text{ eV } L_{\text{sd},0,47}^{1/4} \eta_{-1}^{1/4} M_{\text{ej},-4}^{-1} R_{14}^{3/2}, & R < R_{\text{ph}}; \\ 1.8 \text{ keV } L_{\text{sd},0,47}^{1/2} \eta_{-1}^{3/2} \sigma_{0,7}^{4/3} R_{0,7}^{2/3} R_{15}^{-5/3}, & R_{\text{ph}} < R < R_i; \\ 1.8 \text{ keV } L_{\text{sd},0,47}^{1/2} \eta_{-1}^{3/2} \sigma_{0,7}^{4/3} R_{0,7}^{2/3} R_{i,15}^{-5/3}, & R > R_i; \end{cases} \quad (8.2)$$

In the mean time, the magnetar-wind-powered ejecta would interact with the ambient medium, forming a blastwave similar to GRB afterglow. Depending on the unknown parameters such as M_{ej} , B_p (and hence $L_{\text{sd},0}$) (Gao et al., 2013b), the

blastwave could be accelerated to a mildly or even highly relativistic speed, due to the continuous energy injection from the magnetar wind. Protons are accelerated from the forward shock front along with electrons via the first-order Fermi acceleration process. Consequently, when the seed photons due to magnetar wind dissipation (Eq.8.14) pass through the shocked region, significant neutrino production due to $p\gamma$ interaction through Δ -resonance would happen, as long as the condition $\mathfrak{R} \equiv \frac{\Gamma\gamma_M m_p c^2}{E_{p,t}} > 1$ is satisfied. Here, $E_{p,t} = 0.147 \text{ GeV}^2 \Gamma^2 / E_{\gamma,t}$ is the corresponding proton energy for the typical seed photon at Δ -resonance, and γ_M is the maximum proton Lorentz factor. It can be estimated by balancing the acceleration time scale and the dynamical time scale, which gives $\gamma_M \sim \frac{\Gamma t e B'}{\zeta m_p c}$, where ζ is a parameter of order unity that describes the details of acceleration and B' is the comoving magnetic field strength. Once $p\gamma$ interaction happens, significant neutrinos with energy $\epsilon_\nu \sim 0.05 E_{p,t}$ would be released, the neutrino emission fluence may be estimated as

$$f_\nu = \frac{E_{\text{tot}} \times f_{\gamma_{p,t}} \times f_\pi}{4\pi d^2}, \quad (8.3)$$

where $E_{\text{tot}} \sim 4\pi R^3 n \Gamma (\Gamma - 1) m_p c^2 / 3$ is the total energy of all the protons, $f_{\gamma_{p,t}} \equiv \frac{E_{\gamma_{p,t}}}{E_{\text{tot}}}$ is the energy fraction of the relevant protons, and f_π is the fraction of the proton energy that goes to pion production. Assuming a power-law distribution of the shock accelerated protons: $N(E_p) dE_p \propto E_p^{-p} dE_p$ (hereafter assuming $p > 2$), one can obtain $f_{\gamma_{p,t}} = \left(\frac{\gamma_{p,t}}{\gamma_m}\right)^{2-p}$, where $\gamma_m = (\Gamma - 1) \frac{p-2}{p-1} + 1$ is the minimum proton Lorentz factor. The fraction of the proton energy that goes to pion production could be estimated as $f_\pi \equiv \frac{1}{2}(1 - (1 - \langle \chi_{p \rightarrow \pi} \rangle)^{\tau_{p\gamma}})$, where $\tau_{p\gamma}$ is the $p\gamma$ optical depth and $\langle \chi_{p \rightarrow \pi} \rangle \simeq 0.2$ is the average fraction of energy transferred to pion. Notice that f_π is roughly proportional to $\tau_{p\gamma}$ when $\tau_{p\gamma} < 3$ (Zhang & Kumar, 2013a).

Neutrino Energy and Fluence

The dynamics of the blastwave is defined by energy conservation (Gao et al., 2013b)

$$L_0 t = (\gamma - 1)M_{\text{ej}}c^2 + (\gamma^2 - 1)M_{\text{sw}}c^2, \quad (8.4)$$

where $L_0 = \xi L_{\text{sd},0}$ is the magnetar injection luminosity into the blastwave, and $M_{\text{sw}} = (4\pi/3)R^3 n m_p$ is the swept-up mass from the interstellar medium. Initially, one has $(\gamma - 1)M_{\text{ej}}c^2 \gg (\gamma^2 - 1)M_{\text{sw}}c^2$, so that the kinetic energy of the ejecta would increase linearly with time until $R = \min(R_{\text{sd}}, R_{\text{dec}})$, where the deceleration radius R_{dec} is defined by the condition $(\gamma - 1)M_{\text{ej}}c^2 = (\gamma^2 - 1)M_{\text{sw}}c^2$. By setting $R_{\text{dec}} \sim R_{\text{sd}}$, we can derive a critical ejecta mass

$$M_{\text{ej},c,1} \sim 10^{-3} M_{\odot} n^{1/8} I_{45}^{5/4} B_{p,14}^{-3/4} R_6^{-9/4} P_{0,-3}^{-1} \xi^{7/8}, \quad (8.5)$$

which separate regimes with different blastwave dynamics (Gao et al., 2013b):

Case I: $M_{\text{ej}} < M_{\text{ej},c,1}$ or $R_{\text{sd}} > R_{\text{dec}}$. In such case, the ejecta can be accelerated linearly until the deceleration radius $R_{\text{dec}} \sim 3.9 \times 10^{17} M_{\text{ej},-4}^{2/5} L_{\text{sd},0,47}^{-1/10} n_0^{-3/10}$, where bulk Lorentz factor of the blastwave is $\Gamma_{\text{dec}} \sim 12.2 L_{\text{sd},0,47}^{3/10} M_{\text{ej},-4}^{-1/5} n_0^{-1/10}$. After that, the blastwave decelerates, but still with continuous energy injection until $R_{\text{sd}} \sim 1.0 \times 10^{18} \xi^{1/2} L_{\text{sd},0,47}^{-1/4} n_0^{-1/4}$, where $\Gamma_{\text{sd}} \sim 7.5 \xi^{-1/4} L_{\text{sd},0,47}^{3/8} n_0^{-1/8}$. During the acceleration phase, the blastwave passes the non-relativistic to relativistic transition line $\Gamma - 1 = 1$ at radius $R_{\text{N}} \sim 2.2 \times 10^{14} M_{\text{ej},-4} L_{\text{sd},0,47}^{-1}$.

For the different radius range of the typical photon energy shown in Eq. 8.14, we can investigate whether $p\gamma$ interaction at Δ -resonance can occur, and if so, the typical energy and fluence of neutrino emission. We first assume that the blastwave is always non-relativistic when $R \leq R_{\text{ph}}$, since R_{N} is comparable with R_{ph} with a high probability. We first have

$$\mathfrak{R} = \begin{cases} 0.1\eta_{-1}^{1/4} L_{\text{sd},0,47}^{-5/12} M_{\text{ej},-4}^{-1/3} n_0^{1/2} R_{14}^{11/6} < 1, & R \leq R_{\text{ph}}; \\ 26.0\eta_{-1}^{3/2} L_{\text{sd},0,47}^{-1/6} M_{\text{ej},-4}^{2/3} n_0^{1/2} \sigma_{0,7}^{4/3} R_{0,7}^{2/3} R_{15}^{-4/3} > 1, & R_{\text{ph}} < R < R_i; \\ 120.7\eta_{-1}^{3/2} L_{\text{sd},0,47}^{-1/6} M_{\text{ej},-4}^{2/3} n_0^{1/2} \sigma_{0,7}^{4/3} R_{0,7}^{2/3} R_{i,15}^{-5/3} R_{17}^{1/3} > 1, & R_i < R < R_{\text{dec}}; \\ 1.2 \times 10^3 \eta_{-1}^{3/2} n_0 \sigma_{0,7}^{4/3} R_{0,7}^{2/3} R_{i,15}^{-5/3} R_{18}^2 > 1, & R_{\text{dec}} < R < R_{\text{sd}}; \end{cases} \quad (8.6)$$

implying that $p\gamma$ interaction at Δ -resonance could happen only when $R > R_{\text{ph}}$. The typical neutrino energy and fluence for different range could be estimated as

$$\epsilon_\nu = \begin{cases} 1.1 \times 10^{-2} \text{ PeV } \eta_{-1}^{-3/2} L_{\text{sd},0,47}^{1/6} M_{\text{ej},-4}^{-2/3} \sigma_{0,7}^{-4/3} R_{0,7}^{-2/3} R_{15}^{7/3}, & R_{\text{ph}} < R < R_i; \\ 0.21 \text{ PeV } \eta_{-1}^{-3/2} L_{\text{sd},0,47}^{1/6} M_{\text{ej},-4}^{-2/3} \sigma_{0,7}^{-4/3} R_{0,7}^{-2/3} R_{i,15}^{5/3} R_{17}^{2/3}, & R_i < R < R_{\text{dec}}; \\ 0.24 \text{ PeV } \eta_{-1}^{-3/2} n_0^{-1/2} \sigma_{0,7}^{-4/3} R_{0,7}^{-2/3} R_{i,15}^{5/3} R_{18}^{-1}, & R_{\text{dec}} < R < R_{\text{sd}}; \end{cases} \quad (8.7)$$

$$f_\nu = \begin{cases} 1.6 \times 10^{-12} \eta_{-1}^{-0.05} L_{\text{sd},0,47}^{0.65} n_0 \sigma_{0,7}^{-0.93} R_{0,7}^{-0.47} R_{15}^{3.2}, & R_{\text{ph}} < R < R_i; \\ 1.6 \times 10^{-8} \eta_{-1}^{-0.05} L_{\text{sd},0,47}^{0.65} n_0 \sigma_{0,7}^{-0.93} R_{0,7}^{-0.47} R_{i,15}^{1.17} R_{17}^2, & R_i < R < R_{\text{dec}}; \\ 1.6 \times 10^{-6} \eta_{-1}^{-0.05} L_{\text{sd},0,47}^{0.65} n_0 \sigma_{0,7}^{-0.93} R_{0,7}^{-0.47} R_{i,15}^{1.17} R_{18}^2, & R_{\text{dec}} < R < R_{\text{sd}}. \end{cases} \quad (8.8)$$

For better illustration, we take $L_{\text{sd},0} = 10^{47}$ and $M_{\text{ej}} = 10^{-4} M_\odot$ as an example and plot the evolution of ϵ_ν and f_ν for this dynamical case in Figure 64.

Case II: $M_{\text{ej}} \sim M_{\text{ej},c,1}$ or $R_{\text{sd}} \sim R_{\text{dec}}$. In this case, the ejecta would be continuously accelerated until $R_{\text{sd}} = 1.2 \times 10^{18} \xi^3 L_{\text{sd},0,49}^{-1} M_{\text{ej},-4}^{-2}$, where the bulk Lorentz factor reaches $\Gamma_{\text{sd}} = 83.3 \xi M_{\text{ej},-4}^{-1}$. Similar to case I, we have

$$\mathfrak{R} = \begin{cases} 0.01\eta_{-1}^{1/4} L_{\text{sd},0,49}^{-5/12} M_{\text{ej},-4}^{-1/3} n_0^{1/2} R_{14}^{11/6} < 1, & R \leq R_{\text{ph}}; \\ 12.0\eta_{-1}^{3/2} L_{\text{sd},0,49}^{-1/6} M_{\text{ej},-4}^{2/3} n_0^{1/2} \sigma_{0,7}^{4/3} R_{0,7}^{2/3} R_{15}^{-4/3} > 1, & R_{\text{ph}} < R < R_i; \\ 55.9\eta_{-1}^{3/2} L_{\text{sd},0,49}^{-1/6} M_{\text{ej},-4}^{2/3} n_0^{1/2} \sigma_{0,7}^{4/3} R_{0,7}^{2/3} R_{i,15}^{-5/3} R_{17}^{1/3} > 1, & R_i < R < R_{\text{sd}}. \end{cases} \quad (8.9)$$

Again $p\gamma$ interaction at Δ -resonance could happen only when $R > R_{\text{ph}}$. The typical neutrino energy and fluence for different range could be estimated as

$$\epsilon_\nu = \begin{cases} 0.02 \text{ PeV } \eta_{-1}^{-3/2} L_{\text{sd},0,49}^{1/6} M_{\text{ej},-4}^{-2/3} \sigma_{0,7}^{-4/3} R_{0,7}^{-2/3} R_{15}^{7/3}, & R_{\text{ph}} < R < R_i; \\ 0.5 \text{ PeV } \eta_{-1}^{-3/2} L_{\text{sd},0,49}^{1/6} M_{\text{ej},-4}^{-2/3} \sigma_{0,7}^{-4/3} R_{0,7}^{-2/3} R_{i,15}^{5/3} R_{17}^{2/3}, & R_i < R < R_{\text{sd}}; \end{cases} \quad (8.10)$$

$$f_\nu = \begin{cases} 3.2 \times 10^{-11} \eta_{-1}^{-0.05} L_{\text{sd},0,49}^{0.65} n_0 \sigma_{0,7}^{-0.93} R_{0,7}^{-0.47} R_{15}^{3.2}, & R_{\text{ph}} < R < R_i; \\ 3.2 \times 10^{-7} \eta_{-1}^{-0.05} L_{\text{sd},0,49}^{0.65} n_0 \sigma_{0,7}^{-0.93} R_{0,7}^{-0.47} R_{i,15}^{1.17} R_{17}^2, & R_i < R < R_{\text{sd}}. \end{cases} \quad (8.11)$$

In this case, we take $L_{\text{sd},0} = 10^{49}$ and $M_{\text{ej}} = 10^{-4} M_\odot$, and plot the evolution of ϵ_ν and f_ν in Figure 8.

Case III: $M_{\text{ej}} > M_{\text{ej},c,1}$ or $R_{\text{sd}} < R_{\text{dec}}$. Similar to Case II, the ejecta would be accelerated to a relativistic speed of $\Gamma_{\text{sd}} = 16.7\xi M_{\text{ej},-3}^{-1}$ until $R_{\text{sd}} = 5.0 \times 10^{16} \xi^3 L_{\text{sd},0,49}^{-1} M_{\text{ej},-3}^{-2}$. Similarly, one has

$$\mathfrak{R} = \begin{cases} 0.004 \eta_{-1}^{1/4} L_{\text{sd},0,49}^{-5/12} M_{\text{ej},-3}^{-1/3} n_0^{1/2} R_{14}^{11/6} < 1, & R \leq R_{\text{ph}}; \\ 35.1 \eta_{-1}^{3/2} L_{\text{sd},0,49}^{-1/6} M_{\text{ej},-3}^{2/3} n_0^{1/2} \sigma_{0,7}^{4/3} R_{0,7}^{2/3} R_{15}^{-4/3} > 1, & R_{\text{ph}} < R < R_i; \\ 163.1 \eta_{-1}^{3/2} L_{\text{sd},0,49}^{-1/6} M_{\text{ej},-3}^{2/3} n_0^{1/2} \sigma_{0,7}^{4/3} R_{0,7}^{2/3} R_{i,15}^{-5/3} R_{17}^{1/3} > 1, & R_i < R < R_{\text{sd}}. \end{cases} \quad (8.12)$$

No significant neutrino emission at $R < R_{\text{ph}}$, and beyond R_{ph} the typical neutrino energy and fluence for different range could be estimated as

$$\epsilon_\nu = \begin{cases} 8.4 \times 10^{-3} \text{ PeV } \eta_{-1}^{-3/2} L_{\text{sd},0,49}^{1/6} M_{\text{ej},-3}^{-2/3} \sigma_{0,7}^{-4/3} R_{0,7}^{-2/3} R_{15}^{7/3}, & R_{\text{ph}} < R < R_i; \\ 0.2 \text{ PeV } \eta_{-1}^{-3/2} L_{\text{sd},0,49}^{1/6} M_{\text{ej},-3}^{-2/3} \sigma_{0,7}^{-4/3} R_{0,7}^{-2/3} R_{i,15}^{5/3} R_{17}^{2/3}, & R_i < R < R_{\text{sd}}; \end{cases} \quad (8.13)$$

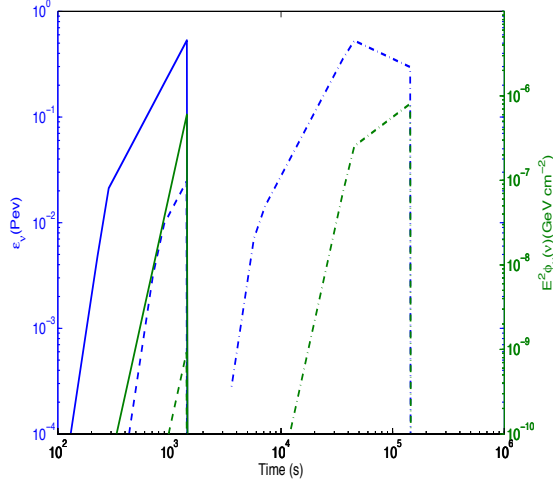


Figure 64 Examples of the evolution of neutrino energy ϵ_ν and fluence f_ν for different dynamics: Case I (dash-dot), Case II (solid) and Case III (dashed). Blue lines represent ϵ_ν and green lines show f_ν . Model parameters: $n_0 = 1, \eta = 0.1, \sigma_0 = 10^7, R_0 = 10^7$, and $D = 300$ Mpc (the advanced LIGO horizon for NS-NS mergers). For the magnetar parameters for each case, see text.

$$f_\nu = \begin{cases} 3.2 \times 10^{-11} \eta_{-1}^{-0.05} L_{sd,0,49}^{0.65} n_0 \sigma_{0,7}^{-0.93} R_{0,7}^{-0.47} R_{15}^{3.2}, & R_{ph} < R < R_i; \\ 3.2 \times 10^{-7} \eta_{-1}^{-0.05} L_{sd,0,49}^{0.65} n_0 \sigma_{0,7}^{-0.93} R_{0,7}^{-0.47} R_{i,15}^{1.17} R_{17}^2, & R_i < R < R_{sd}. \end{cases} \quad (8.14)$$

For this case, we take $L_{sd,0} = 10^{47}$ ergs $^{-1}$ and $M_{ej} = 10^{-3} M_\odot$ and plot the evolution of ϵ_ν and f_ν in Figure 64.

Note that there is another critical ejecta mass $M_{ej,c,2} \sim 6 \times 10^{-3} M_\odot I_{45} P_{0,-3}^{-2} \xi$ (defined by setting $E_{rot} \xi = 2(\gamma - 1) M_{ej,c,2} c^2$), above which the blast wave would never reach a relativistic speed (Gao et al., 2013b). The dynamics is similar to Case III, with the coasting regime in the non-relativistic phase. In this case, we always have $\mathfrak{R} < 1$, therefore no significant neutrino flux is expected.

Detection Prospect

From the above calculation, one can see that when the post-merger product is a millisecond magnetar and the outgoing ejecta could be accelerated to a relativistic speed, \sim PeV neutrinos could indeed be emitted from NS-NS mergers scenario. These neutrinos are well suited for detection with IceCube(Ahrens et al., 2004).

As shown in Figure 64, for different initial conditions, i.e., different combinations of M_{ej} and L_{sd} , the maximum neutrino fluence is always reached at the spin-down time scale. We therefore take the neutrino energy and fluence at this epoch as the typical values for each specific NS-NS merger event. For the events happening at 300 Mpc, the optimistical typical neutrino fluence could be as large as $10^{-6} - 10^{-5} \text{GeV cm}^{-2}$ (corresponding to $\sigma_0 = 10^7, 10^6$ respectively), one or two orders of magnitude lower than the typical fluence of GRBs(He et al., 2012). Given the typical neutrino energy \sim PeV and the IceCube effective area \sim several 10^6 cm^2 (Ahrens et al., 2004; Li, 2013), optimistically only several $10^{-6} - 10^{-5}$ neutrinos are expected to be detected by IceCube for a single event.

In any case, these events would contribute to the \sim PeV neutrino background. The NS-NS merger event rate is rather uncertain, i.e., $(10 - 5 \times 10^4) \text{ Gpc}^{-3} \text{ yr}^{-1}$ (Phinney, 1991; Kalogera et al., 2004; Abadie et al., 2010). Considering that only a fraction of NS-NS merger event would leave behind a massive neutron star rather than a black hole, and that only a sub-fraction of these mergers have the right M_{ej} and $L_{\text{sd},0}$ to make relativistic blastwaves, the event rate of NS-NS mergers that generate PeV neutrinos may be at least one order of magnitude lower, i.e. $\sim (1 - 5 \times 10^3) \text{ Gpc}^{-3} \text{ yr}^{-1}$. Even with the most optimistic estimate, the \sim PeV diffuse background is $\sim 10^{-10} \text{ GeV cm}^{-2} \text{ s}^{-1} \text{ sr}^{-1}$. It takes tens of years to get two events. So these systems are not likely the origin of the two reported PeV events announced by the Icecube collaboration (Aartsen et al., 2013). Nevertheless, compared with the GRB event rate $1 \text{ Gpc}^{-3} \text{ yr}^{-1}$ (Liang et al., 2007a; Wanderman & Piran, 2010), this

scenario may gain the event rate by 1-2 orders of magnitude than GRBs. Noticing that a typical GRB has a fluence 1-2 orders of magnitude higher than a magnetar-wind-powered NS-NS merger remnant, our scenario could contribute to the \sim PeV neutrino diffuse background, which is comparable or slightly lower than that of GRBs.

High Energy Photon Emission

Besides high-energy neutrino emission, the decay of π^0 produced in $p\gamma$ interactions would lead to the production of high energy gamma-ray photons. Assuming that half of the Δ^+ decays go to the π^+ channel (neutrino production), while the other half go to the π^0 channel (γ -ray production), the typical gamma-ray photon energy and fluence values would be comparable to the neutrinos we studied in section *III*. However, such high-energy photons may interact with the synchrotron emission photons in the shock (Gao et al., 2013b) to produce electron/positron pairs, $\gamma\gamma \rightarrow e^\pm$, and initiate an electromagnetic cascade: the pairs would emit photons via synchrotron and inverse Compton, which would be converted back to pairs, and the pairs would emit photons again, etc. Photons can escape only when the $\gamma\gamma$ optical depth becomes lower than unity (Murase & Beacom, 2012a; Murase et al., 2012b). Following the calculation shown in Ref.(Gao et al., 2013b), we find that the $\gamma\gamma$ optical depth exceeds unity for photon energy above $\epsilon_{\gamma\gamma} \sim 100\text{GeV}$. For simplicity, we assume that the total energy of the π^0 -decay photons would finally show up around 100GeV through an EM cascade. These photons are within the energy windows of the Fermi/LAT. In the most optimistic situation, the photon flux for an event at 300 Mpc could be as high as $10^{-11}\text{erg cm}^{-2} \text{s}^{-1}$, which is essentially 10^{-10} photons $\text{cm}^{-2} \text{s}^{-1}$. The effective area of LAT for 100GeV photons is around 9000 cm^2 (Atwood et al., 2009), suggesting that even for $T_{\text{sd}} \sim 10^5$, one single NS-NS merger event could not trigger LAT. Nevertheless, the total diffuse flux from these events could reach \sim several $10^{-7} \text{MeV cm}^{-2} \text{s}^{-1} \text{sr}^{-1}$ optimistically, giving a moderate contribution to the sub-

TeV γ -ray background, i.e., $4 \times 10^{-4} \text{ MeV cm}^{-2} \text{ s}^{-1} \text{ sr}^{-1}$, according to Fermi/LAT observation (Abdo et al., 2010).

REFERENCES

- Aartsen, M. G., Abbasi, R., Abdou, Y., et al. 2013, *Physical Review Letters*, 111, 021103
- Abadie, J., Abbott, B. P., Abbott, R., et al. 2010, *Classical and Quantum Gravity*, 27, 173001
- Abbasi, R., Abdou, Y., Abu-Zayyad, T., et al. 2010, *ApJ*, 710, 346
- Abbasi, R., Abdou, Y., Abu-Zayyad, T., et al. 2011, *Physical Review Letters*, 106, 141101
- Abbasi, R., Abdou, Y., Abu-Zayyad, T., et al. 2012, *Nature*, 484, 351
- Abbott, B. P., Abbott, R., Adhikari, R., et al. 2009, *Reports on Progress in Physics*, 72, 076901
- Abdo, A. A., Ackermann, M., Ajello, M., et al. 2010, *Physical Review Letters*, 104, 101101
- Abramowicz, M. A., Czerny, B., Lasota, J. P., & Szuszkiewicz, E. 1988, *ApJ*, 332, 646
- Acernese, F., Alshourbagy, M., Amico, P., et al. 2008, *Classical and Quantum Gravity*, 25, 114045
- Ahlers, M., Gonzalez-Garcia, M. C., & Halzen, F. 2011, *Astroparticle Physics*, 35, 87
- Ahrens, J., Bahcall, J. N., Bai, X., et al. 2004, *Astroparticle Physics*, 20, 507
- Akerlof, C., Balsano, R., Barthelmy, S., et al. Apr. 1999, *Nature*, 398, 400–402.
- Allen, B., Anderson, W. G., Brady, P. R., Brown, D. A., & Creighton, J. D. E. 2012, *Phys. Rev. D*, 85, 122006
- Aloy, M. A., Janka, H.-T., & Müller, E. 2005, *A&A*, 436, 273
- Atwood, W. B., Abdo, A. A., Ackermann, M., et al. 2009, *ApJ*, 697, 1071
- Barthelmy, S. D., et al. 2005b, *ApJ*, 635, L133
- Barthelmy, S. D., Chincarini, G., Burrows, D. N., et al. 2005a, *Nature*, 438, 994
- Barthelmy, S. D., Barbier, L. M., Cummings, J. R., et al. 2005c, *Space Sci. Rev.*, 120, 143
- Bartos, I., Finley, C., Corsi, A., & Márka, S. 2011, *Physical Review Letters*, 107, 251101
- Begelman, M. C. 1978, *MNRAS*, 184, 53

- Begelman, M. C., Blandford, R. D., & Rees, M. J. 1984, *Reviews of Modern Physics*, 56, 255
- Beloborodov, A. M., Stern, B. E., & Svensson, R. 1998, *ApJ*, 508, L25
- Beloborodov, A. M., Stern, B. E., & Svensson, R. 2000, *ApJ*, 535, 158
- Beloborodov, A. M., Feb. 2002, *ApJ*, 565, 808–828.
- Beloborodov, A. M., Mar. 2003, *ApJ*, 585, L19–L22.
- Berger, E., Kulkarni, S. R., Pooley, G., Frail, et al., Nov. 2003, *Nature*, 426, 154–157.
- Berger, E., Price, P. A., Cenko, S. B., et al. 2005, *Nature*, 438, 988
- Berger, E. 2007, *ApJ*, 670, 1254
- Berger, E. 2011, *Nature*, 55, 1
- Berger, E., Fong, W., Chornock, R. 2013, *ApJ*, 774, L23
- Berger, E. 2013, arXiv:1311.2603
- Bhat, P. N., Fishman, G. J., Meegan, C. A., et al. 1992, *Nature*, 359, 217
- Bhattacharya, D., & van den Heuvel, E. P. J. 1991, *Physics Reports*, 203, 1
- Bhattacharya, D., Jun. 2001, *Bulletin of the Astronomical Society of India*, 29, 107–114.
- Blanchet, L., Damour, T., Iyer, B. R., Will, C. M., & Wiseman, A. G. 1995, *Physical Review Letters*, 74, 3515
- Blanchet, L., Iyer, B. R., Will, C. M., & Wiseman, A. G. 1996, *Classical and Quantum Gravity*, 13, 575
- Blandford, R. D., McKee, C. F., Aug. 1976, *Physics of Fluids*, 19, 1130–1138.
- Blandford, R. D., & Znajek, R. L. 1977, *MNRAS*, 179, 433
- Bloom, J. S., Giannios, D., Metzger, B. D., et al. 2011, *Science*, 333, 203
- Blumenthal, G. R., & Gould, R. J. 1970, *Rev. Mod. Phys.*, 42, 237
- Böttcher, M., Dermer, C. D., Mar. 2000, *ApJ*, 532, 281–285.
- Bower, G. C., Destry, S., Bloom, J. S., et al. 2007, *ApJ*, 666, 346
- Bower, G. C., & Saul, D. 2011, *ApJ*, 728, L14
- Burgay, M., D’Amico, N., Possenti, A., et al. 2003, *Nature*, 426, 531
- Burrows, D. N., Romano, P., Falcone, A., et al. Sep. 2005a, *Science*, 309, 1833–1835.

Burrows, D. N., Hill, J. E., Nousek, J. A., et al. 2005b, *Space Sci. Rev.*, 120, 165

Burrows, D. N., Grupe, D., Capalbi, M., et al. 2006, *ApJ*, 653, 468

Burrows, D. N., Kennea, J. A., Ghisellini, G., et al. 2011, *Nature*, 476, 421

Butler, N. R., Kocevski, D., Jul. 2007, *ApJ*, 663, 407–419.

Cannizzo, J. K., Gehrels, N., Vishniac, E. T., Jan. 2004, *ApJ*, 601, 380–390.

Chandra, P., Frail, D. A., Feb. 2012, *ApJ*, 746, 156.

Champion, D. J., Lorimer, D. R., McLaughlin, M. A., et al. 2004, *MNRAS*, 350, L61

Champion, D. J., Lorimer, D. R., McLaughlin, M. A., et al. 2005, *MNRAS*, 363, 929

Cenko, S. B., Krimm, H. A., Horesh, A., et al. 2012, *ApJ*, 753, 77

Cenko, S. B., Kulkarni, S. R., Horesh, A., et al. 2013, *ApJ*, 769, 130

Chevalier, R. A., Li, Z.-Y., Jul. 1999, *ApJ*, 520, L29–L32.

Chevalier, R. A., Li, Z.-Y., Jun. 2000, *ApJ*, 536, 195–212.

Chiang, J. & Böttcher, M. 2002, *ApJ*, 564, 92

Chincarini, G., Moretti, A., Romano, P., et al. Dec. 2007, *ApJ*, 671, 1903–1920.

Chincarini, G., Mao, J., Margutti, R., et al. Aug. 2010, *MNRAS*, 406, 2113–2148.

Cholis, I., & Hooper, D. 2013, *JCAP*, 6, 30

He, H.-N., Liu, R.-Y., Wang, X.-Y., et al. 2012, *ApJ*, 752, 29

Corongiu, A., Kramer, M., Stappers, B. W., et al. 2007, *A&A*, 462, 703

Corsi, A., & Mészáros, P. 2009, *ApJ*, 702, 1171

Dai, Z. G., Lu, T., May 1998a, *A&A*, 333, L87–L90.

Dai, Z. G., Lu, T., Jul. 1998b, *MNRAS*, 298, 87–92.

Dai, Z. G., Lu, T., Nov. 1998c, *Physical Review Letters*, 81, 4301–4304.

Dai, Z. G., Lu, T., Jul. 1999a, *ApJ*, 519, L155–L158.

Dai, Z. G., Huang, Y. F., Lu, T., Aug. 1999b, *ApJ*, 520, 634–640.

Dai, Z. G., Cheng, K. S., Sep. 2001a, *ApJ*, 558, L109–L112.

Dai, Z. G., Gou, L. J., May 2001b, *ApJ*, 552, 72–80.

Dai, Z. G., Lu, T., Feb. 2002, *ApJ*, 565, L87–L90.

- Dai, Z. G., Wu, X. F., Jul. 2003, *ApJ*, 591, L21–L24.
- Dai, Z. G. 2004, *ApJ*, 606, 1000
- Dai, Z. G., Wang, X. Y., Wu, X. F., & Zhang, B. 2006, *Science*, 311, 1127
- Daigne, F., & Mochkovitch, R. 2003, *MNRAS*, 342, 587
- Derishev, E. V., Kocharovsky, V. V., Kocharovsky, V. V., Jun. 2001, *A&A*, 372, 1071–1077.
- Dermer, C. D., & Mitman, K. E. 1999, *ApJ*, 513, L5
- Dermer, C. D., Böttcher, M., Chiang, J. 2000a, *ApJ*, 537, 255
- Dermer, C. D., Chiang, J., Mitman, K. E., Jul. 2000b, *ApJ*, 537, 785–795.
- Dermer, C. D. 2004, *ApJ*, 614, 284
- Drenkhahn, G., & Spruit, H. C. 2002a, *A&A*, 391, 1141
- Drenkhahn, G. 2002b, *A&A*, 387, 714
- Duncan, R. C., & Thompson, C. 1992, *ApJ*, 392, L9
- Dyks, J., Zhang, B., & Fan, Y. Z. 2005, arXiv:astro-ph/0511699
- Eichler, D., Livio, M., Piran, T., & Schramm, D. N. 1989, *Nature*, 340, 126
- Evans, P. A., Beardmore, A. P., Page, K. L., et al. *MNRAS*, 397, 1177–1201.
- Faber, J. A., & Rasio, F. A. 2012, *Living Reviews in Relativity*, 15, 8
- Fan, Y.-Z., Dai, Z.-G., Huang, Y.-F., Lu, T. Oct. 2002, *ChJAA*, 2, 449–453.
- Fan, Y. Z., Wei, D. M., Wang, C. F., Sep. 2004, *A&A*, 424, 477–484.
- Fan, Y. Z., Wei, D. M., Nov. 2005a, *MNRAS*, 364, L42–L46.
- Fan, Y. Z., Zhang, B., Wei, D. M., Jul. 2005b, *ApJ*, 628, 298–314.
- Fan, Y., Piran, T., Jun. 2006a, *MNRAS*, 369, 197–206.
- Fan, Y.-Z., & Xu, D. 2006b, *MNRAS*, 372, L19
- Fan, Y.-Z., Wu, X.-F., & Wei, D.-M. 2013, arXiv:1302.3328
- Fenimore, E. E., Madras, C. D., & Nayakshin, S. 1996, *ApJ*, 473, 998
- Ferdman, R. D., Stairs, I. H., Kramer, M., et al. 2008, *40 Years of Pulsars: Millisecond Pulsars, Magnetars and More*, 983, 474

- Fishman, G. J., & Meegan, C. A. 1995, *Annual Review of Astronomy and Astrophysics*, 33, 415
- Fox, D. W., Yost, S., Kulkarni, S. R., et al. Mar. 2003, *Nature*, 422, 284–286.
- Freiburghaus, C., Rosswog, S., & Thielemann, F.-K. 1999, *ApJ*, 525, L121
- Gao, W.-H., & Fan, Y.-Z. 2006, *Chin. J. Astron. Astrophys.*, 6, 513
- Gao, H., Lei, W.-H., Wu, X.-F., Zhang, B., Apr. 2013a, *MNRAS*, 435, 2520
- Gao, H., Ding, X., Wu, X.-F., Zhang, B., & Dai, Z.-G. 2013b, *ApJ*, 771, 86
- Gao, H., Lei, W.-H., Zou, Y.-C., Wu, X.-F., Zhang, B., 2013c, *New Astronomy Review*, 57, 141
- Gao, H., Zhang, B., Wu, X.-F., & Dai, Z.-G. 2013c, *Phys. Rev. D*, 88, 043010
- Gallant, Y. A., & Achterberg, A. 1999, *MNRAS*, 305, L6
- Gehrels, N., Chincarini, G., Giommi, P., et al. Aug. 2004, *ApJ*, 611, 1005–1020.
- Gehrels, N., Sarazin, C. L., O’Brien, P. T., et al. 2005, *Nature*, 437, 851
- Gehrels, N., & Razzaque, S. 2013, *Frontiers of Physics*, 2
- Genet, F., Daigne, F., Mochkovitch, R., Oct. 2007, *MNRAS* 381, 732–740.
- Geng, J. J., Wu, X. F., Huang, Y. F., Yu, Y. B. Jul. 2013, *ArXiv e-prints*:1307.4517
- Giacomazzo, B., & Perna, R. 2013, *ApJ*, 771, L26
- Ghisellini, G., Guilbert, P., Svensson, R., 1988, *ApJL*, 334, 5
- Ghisellini, G., Svensson, R., 1991, *MNRAS*, 252, 313
- Ghisellini, G., Padovani, P., Celotti, A., & Maraschi, L. 1993, *ApJ*, 407, 65
- Ghisellini, G., Haardt, F., Svensson, R., 1998a, *MNRAS*, 297, 348
- Ghisellini, G., Celotti, A., Fossati, G., Maraschi, L., Comastri, A. 1998b, *MNRAS*, 301, 451
- Ghisellini, G., Ghirlanda, G., Nava, L., Firmani, C., Apr. 2007, *ApJ*, 658, L75–L78.
- Ghisellini, G., Ghirlanda, G., Nava, L., Celotti, A., Apr. 2010, *MNRAS*, 403, 926–937.
- Golenetskii, S., Aptekar, R., Mazets, E., et al. 2009, *GRB Coordinates Network*, 9647, 1
- Gou, L.-J., Fox, D.B., Mészáros, P. 2007, *ApJ*, 668, 1083
- Granot, J., Piran, T., Sari, R., Mar. 1999, *ApJ*, 513, 679–689.

- Granot, J., Panaitescu, A., Kumar, P., Woosley, S. E., May 2002, *ApJ*, 570, L61–L64.
- Granot, J., Sari, R., 2002, *ApJ* 568, 820–829.
- Granot, J., Kumar, P., Jul. 2003, *ApJ*, 591, 1086–1096.
- Granot, J., Piran, T., Mar. 2012, *MNRAS*, 421, 570–587.
- Harrison, F. A., Bloom, J. S., Frail, D. A., et al. Oct. 1999, *ApJ*, 523, L121–L124.
- Harrison, R., Kobayashi, S., Aug. 2013, *ApJ*, 772, 101.
- He, H.-N., Wu, X.-F., Toma, K., et al. May 2011, *ApJ*, 733, 22.
- Hotokezaka, K., Kiuchi, K., Kyutoku, K., et al. 2013, *Phys. Rev. D*, 87, 024001
- Huang, Y. F., Dai, Z. G., Lu, T., Oct. 1999, *MNRAS*, 309, 513–516.
- Huang, Y. F., Gou, L. J., Dai, Z. G., Lu, T., Nov. 2000, *ApJ*, 543, 90–96.
- Huang, Y. F., Cheng, K. S., May 2003, *MNRAS*, 341, 263–269.
- Huang, Y. F., Wu, X. F., Dai, Z. G., Ma, H. T., Lu, T., Apr. 2004, *ApJ*, 605, 300–306.
- Hulse, R. A., & Taylor, J. H. 1975, *ApJ*, 195, L51
- Hurley, K., Golenetskii, S., Aptekar, R., et al. 2010, in *Deciphering the Ancient Universe with Gamma-Ray Bursts*, Vol. 1279, American Institute of Physics Conference Series, ed. N. Kawai & S. Nagataki, 330
- Ioka, K., Kobayashi, S., Zhang, B., Sep. 2005, *ApJ*, 631, 429–434.
- Ioka, K., Toma, K., Yamazaki, R., Nakamura, T., Oct. 2006, *A&A*, 458, 7–12.
- Jacoby, B. A., Cameron, P. B., Jenet, F. A., et al. 2006, *ApJ*, 644, L113
- Janssen, G. H., Stappers, B. W., Kramer, M., et al. 2008, *A&A*, 490, 753
- Kalogera, V., Kim, C., Lorimer, D. R., et al. 2004, *ApJ*, 601, L179
- Kaneko, Y., Preece, R. D., Briggs, M. S., Paciesas, W. S., Meegan, C. A., & Band, D. L. 2006, *ApJ*, 166, 298
- Kann, D. A., Klose, S., Zhang, B., et al. Sep. 2010, *ApJ*, 720, 1513–1558.
- Kann, D. A., Klose, S., Zhang, B., et al. Jun. 2011, *ApJ*, 734, 96.
- Kasian, L. 2008, *40 Years of Pulsars: Millisecond Pulsars, Magnetars and More*, 983, 485
- Katz, J. I. 1977, *ApJ*, 215, 265
- Klebesadel, R. W., Strong, I. B., & Olson, R. A. 1973, *ApJ*, 182, L85

Kluźniak, W., & Ruderman, M. 1998, ApJ, 505, L113

Kobayashi, S., Piran, T., Sari, R., Nov. 1997, ApJ, 490, 92–+.

Kobayashi, S., Piran, T., Sari, R., Mar. 1999, ApJ, 513, 669–678.

Kobayashi, S., Sari, R., Oct. 2000a, ApJ, 542, 819–828.

Kobayashi, S., Dec. 2000b, ApJ, 545, 807–812.

Kobayashi, S., Zhang, B., Nov. 2003a, ApJ, 597, 455–458.

Kobayashi, S., Zhang, B., Jan. 2003b, ApJ, 582, L75–L78.

Kobayashi, S., Mészáros, P., Zhang, B., Jan. 2004, ApJ, 601, L13–L16.

Kobayashi, S., Zhang, B., Mészáros, P., Burrows, D. 2007, ApJ, 655, 391

Kocevski, D., Ryde, F., & Liang, E. 2003, ApJ, 596, 389

Kocevski, D., Butler, N., Bloom, J. S., Oct. 2007, ApJ, 667, 1024–1032.

Komissarov, S. S., Vlahakis, N., Königl, A., & Barkov, M. V. 2009, MNRAS, 394, 1182

Königl, A., & Granot, J. 2002, ApJ, 574, 134

Kramer, M., Stairs, I. H., Manchester, R. N., et al. 2006, Science, 314, 97

Krawczynski, H., & Treister, E. 2013, Frontiers of Physics, 26

Kulkarni, S. R. et al. Apr. 1999, Nature, 398, 389–394.

Kulkarni, S. R. 2005, ArXiv Astrophysics e-prints (arXiv:astro-ph/0510256)

Kumar, P., Panaitescu, A., Oct. 2000a, ApJ, 541, L1–L54.

Kumar, P., Piran, T., Mar. 2000b, ApJ, 532, 286–293.

Kumar, P., Panaitescu, A., Dec. 2003a, MNRAS, 346, 905–914.

Kumar, P., Granot, J., Jul. 2003b, ApJ, 591, 1075–1085.

Kumar, P., Narayan, R., Johnson, J. L., Jul. 2008a, MNRAS, 750–+.

Kumar, P., Narayan, R., Johnson, J. L., Jul. 2008b, Science 321, 376–.

Kumar, P., & Narayan, R. 2009a, MNRAS, 395, 472

Kumar, P., Barniol Duran, R., Nov. 2009b, MNRAS, 400, L75–L79.

Kumar, P., Barniol Duran, R., Nov. 2010, MNRAS, 409, 226–236.

- Kumar, P., Zhang, B., 2013, *Physics Reports*, to be submitted
- Kuroda, K., & LCGT Collaboration 2010, *Classical and Quantum Gravity*, 27, 084004
- Kyutoku, K., Ioka, K., & Shibata, M. 2012, *ArXiv Astrophysics e-prints* (arXiv:1209.5747)
- Lattimer, J. M., & Schramm, D. N. 1974, *ApJ*, 192, L145
- Lattimer, J. M. 2012, *Annual Review of Nuclear and Particle Science*, 62, 485
- Lazzati, D., Perna, R., Feb. 2007, *MNRAS*, 375, L46–L50.
- Lazzati, D., Morsony, B. J., & Begelman, M. C. 2009, *ApJ*, 700, L47
- Lee, H. K., Wijers, R. A. M. J., & Brown, G. E. 2000, *Physics Reports*, 325, 83
- Lei, W.-H., Wang, D.-X., & Ma, R.-Y. 2005, *ApJ*, 619, 420
- Lei W.H. et al., 2007, *A&A*, 468, 563
- Lei, W.-H., & Zhang, B. 2011, *ApJ*, 740, L27
- Lei, W. H., Zhang, B., Liang, E. W., Mar. 2013, *ApJ*, 765, 125.
- Li, H., & Fenimore, E. E. 1996, *ApJ*, 469, L115
- Li, L.-X., & Paczyński, B. 1998, *ApJ*, 507, L59
- Li, W., Filippenko, A. V., Chornock, R., Jha, S., Mar. 2003, *ApJ*, 586, L9–L12.
- Li, Z. 2013, *ApJ*, 770, L40
- Liang, E., Zhang, B., Virgili, F., & Dai, Z. G. 2007a, *ApJ*, 662, 1111
- Liang, E.-W., Zhang, B.-B., Zhang, B., Nov. 2007b, *ApJ*, 670, 565–583.
- Liang, E.-W., Racusin, J. L., Zhang, B., Zhang, B.-B., Burrows, D. N., Mar. 2008, *ApJ*, 675, 528–552.
- Liang, E.-W., Lü, H.-J., Hou, S.-J., Zhang, B.-B., Zhang, B., Dec. 2009, *ApJ*, 707, 328–342.
- Liang, E., Li, L., Gao, H., et al. 2013, *ApJ*, 774, 13
- Liu, R.-Y., Wang, X.-Y., Mar. 2011, *ApJ*, 730, 1.
- Liu, R.-Y., & Wang, X.-Y. 2013, *ApJ*, 766, 73
- Livio, M., Waxman, E., Jul. 2000, *ApJ*, 538, 187–191.
- Lorimer, D. R. 2008, *Living Reviews in Relativity*, 11, 8

Lu Y., Huang Y.F., and Zhang S.N., 2008, ApJ, 684, 1330

Lynch, R. S., Freire, P. C. C., Ransom, S. M., & Jacoby, B. A. 2012, ApJ, 745, 109

Lyons, N., O'Brien, P. T., Zhang, B., Willingale, R., Troja, E., Starling, R. L. C., Feb. 2010, MNRAS, 402, 705–712.

Lyutikov, M., & Blandford, R. 2003, arXiv:astro-ph/0312347

Madau, P., Thompson, C., May 2000, ApJ, 534, 239–247.

Margutti, R., Guidorzi, C., Chincarini, G., Bernardini, M. G., Genet, F., Mao, J., Pasotti, F., Aug. 2010, MNRAS, 406, 2149–2167.

Maxham, A., Zhang, B., Dec. 2009, ApJ, 707, 1623–1633.

Maxham, A., Zhang, B.-B., Zhang, B., Jul. 2011, MNRAS, 415, 77–82.

McBreen, S., Quilligan, F., McBreen, B., Hanlon, L., & Watson, D. 2001, A&A, 380, L31

McKinney, J. C., & Uzdensky, D. A. 2012, MNRAS, 419, 573

Medvedev, M. V., Loeb, A., Dec. 1999, ApJ, 526, 697–706.

Meegan, C., Lichti, G., Bhat, P. N., et al. 2009, ApJ, 702, 791

Metzger, B. D., Martínez-Pinedo, G., Darbha, S., et al. 2010, MNRAS, 406, 2650

Metzger, B. D., Giannios, D., Thompson, T. A., Bucciantini, N., & Quataert, E. 2011, MNRAS, 413, 2031

Metzger, B. D., & Berger, E. 2012, ApJ, 746, 48

Metzger, B. D., & Piro, A. L. 2013, arXiv:1311.1519

Mészáros, P., Rees, M. J., Mar. 1993, ApJ, 405, 278–284.

Mészáros, P., Rees, M. J., & Papathanassiou, H., 1994, ApJ, 432, 181

Mészáros, P., Rees, M. J., Feb. 1997a, ApJ, 476, 232.

Mészáros, P., Rees, M. J., Jun. 1997b, ApJ, 482, L29.

Mészáros, P., Rees, M. J., Wijers, R. A. M. J., May 1998, ApJ, 499, 301–+.

Mészáros, P., Rees, M. J., Jul. 1999, MNRAS, 306, L39–L43.

Mészáros, P., Ramirez-Ruiz, E., Rees, M. J., Jun. 2001, ApJ, 554, 660–666.

Mészáros, P. 2002, Annual Review of Astronomy and Astrophysics, 40, 137

Mészáros, P., 2006, Reports of Progress in Physics, 69, 2259–2322.

- Meszaros, P., & Rees, M. J. 2014, arXiv:1401.3012
- Mimica, P., Giannios, D., Aloy, M. A., Feb. 2009, A&A, 494, 879–890.
- Moderski R., Sikora M., Lasota J. P. 1997, in Ostrowski M., Sikora M., Madejski, G., Belgelman M., eds, Proc. International Conf., Relativistic Jets in AGNs. Krakow, p. 110
- Morrison, I. A., Baumgarte, T. W., & Shapiro, S. L. 2004, ApJ, 610, 941
- Morsony, B. J., Lazzati, D., & Begelman, M. C. 2010, ApJ, 723, 267
- Murase, K., & Beacom, J. F. 2012a, JCAP, 10, 43
- Murase, K., Beacom, J. F., & Takami, H. 2012b, JCAP, 8, 30
- Nagataki, S. 2009, ApJ, 704, 937
- Nagataki, S. 2011, Publications of the Astronomical Society of Japan, 63, 1243
- Nakar, E., & Piran, T. 2002, MNRAS, 331, 40
- Nakar, E., Granot, J., Oct. 2007, MNRAS, 380, 1744–1760.
- Nakar, E., Ando, S., & Sari, R., 2009, ApJ, 703, 675
- Nakar, E., & Piran, T. 2011, Nature, 478, 82
- Narayan, R., Paczynski, B., & Piran, T. 1992, ApJ, 395, L83
- Narayan, R., & Kumar, P. 2009, MNRAS, 394, L117
- Nava, L., Sironi, L., Ghisellini, G., Celotti, A., Ghirlanda, G., Nov. 2012, ArXiv e-prints:1211.2806
- Nissanke, S., Kasliwal, M., & Georgieva, A. 2013, ApJ, 767, 124
- Norris, J. P., Nemiroff, R. J., Bonnell, J. T., et al. 1996, ApJ, 459, 393
- Norris, J. P., Marani, G. F., & Bonnell, J. T. 2000, ApJ, 534, 248
- Nousek, J. A., Kouveliotou, C., Grupe, D., et al. May 2006, ApJ, 642, 389–400.
- O’Brien, P. T., Willingale, R., Osborne, J., et al. Aug. 2006, ApJ, 647, 1213–1237.
- Oppenheim, A.V., Schafer, R.W., Buck, J.R., 1998, "Discrete-time signal processing" second edit, Vol.2, 52
- Paczynski, B. 1986, ApJ, 308, L43
- Paczynski, B. 1998, ApJ, 494, L45
- Panaitescu, A., Mészáros, P., Rees, M. J., Aug. 1998a, ApJ, 503, 314–+.

Panaitescu, A., Meszaros, P., Jan. 1998b, ApJ, 493, L31.

Panaitescu, A. & Kumar, P. 2000, ApJ, 543, 66

Panaitescu, A., Kumar, P., Oct. 2001, ApJ, 560, L49–L53.

Panaitescu, A., Kumar, P., Jun. 2002, ApJ, 571, 779–789.

Panaitescu, A., Nov. 2005, MNRAS, 363, 1409–1423.

Pe’er, A., Jun. 2012, ApJ, 752, L8.

Peng, F., Königl, A., Granot, J., Jun. 2005, ApJ, 626, 966–977.

Perley, R. A., Chandler, C. J., Butler, B. J., & Wrobel, J. M. 2011, ApJ, 739, L1

Piran, T., Shemi, A., & Narayan, R. 1993, MNRAS, 263, 861

Piran, T. 1999, Physics Reports, 314, 575

Piran, T., Jan. 2005, Reviews of Modern Physics, 76, 1143–1210.

Piran, T., Sari, R., Zou, Y.-C. 2009, MNRAS, 393, 1107

Piran, T., Nakar, E., & Rosswog, S. 2013, MNRAS, 430, 2121

Phinney, E. S. 1991, ApJ, 380, L17

Popham, R., Woosley, S. E., & Fryer, C. 1999, ApJ, 518, 356

Portegies Zwart, S. F., Lee, C.-H., & Lee, H. K. 1999, ApJ, 520, 666

Qin, Y.-P. 2008, ApJ, 683, 900

Racusin, J. L., Karpov, S. V., Sokolowski, M., et al. Sep. 2008, Nature, 455, 183–188.

Ramirez-Ruiz, E., Merloni, A., Rees, M. J. 2001, MNRAS, 324, 1147

Rees, M. J. 1967, MNRAS, 137, 429

Rees, M. J., Mészáros, P., Sep. 1992, MNRAS, 258, 41P–43P.

Rees, M. J., Mészáros, P., Aug. 1994, ApJ, 430, L93–L96.

Rees, M. J., Mészáros, P., Mar. 1998, ApJ, 496, L1+.

Rezzolla, L., Giacomazzo, B., Baiotti, L., et al. 2011, ApJ, 732, L6

Rhoads, J. E. 1997, ApJ, 487, L1

Rhoads, J. E., Nov. 1999, ApJ, 525, 737–749.

Rossi, E., Lazzati, D., Rees, M. J., Jun. 2002, MNRAS, 332, 945–950.

- Rosswog, S., Ramirez-Ruiz, E., & Davies, M. B. 2003, *MNRAS*, 345, 1077
- Rosswog, S., Piran, T., & Nakar, E. 2012, ArXiv e-prints (arXiv:1204.6240)
- Rosswog, S., Piran, T., & Nakar, E. 2013, *MNRAS*, 430, 2585
- Rowlinson, A., O'Brien, P. T., Tanvir, N. R., et al. 2010, *MNRAS*, 409, 531
- Rowlinson, A., & O'Brien, P. 2012, in *Gamma-Ray Bursts 2012 Conference (GRB 2012)*
- Ruderman, M. 1975, *Seventh Texas Symposium on Relativistic Astrophysics*, 262, 164
- Rybicki, G. B., Lightman, A. P., 1979, New York, Wiley-Interscience, 1979. 393 p.
- Santana, R., Barniol Duran, R., & Kumar, P. 2013, arXiv:1309.3277
- Sari, R., Piran, T., Dec. 1995, *ApJ*, 455, L143+.
- Sari, R., Nov. 1997, *ApJ*, 489, L37.
- Sari, R., Piran, T., Narayan, R., Apr. 1998a, *ApJ*, 497, L17+.
- Sari, R., Feb. 1998b, *ApJ*, 494, L49.
- Sari, R., Piran, T., Jun. 1999a, *ApJ*, 517, L109–L112.
- Sari, R., Piran, T., Aug. 1999b, *ApJ*, 520, 641–649.
- Sari, R., Piran, T., Halpern, J. P., Jul. 1999c, *ApJ*, 519, L17–L20.
- Sari, R., Mészáros, P., May 2000, *ApJ*, 535, L33–L37.
- Sari, R., Esin, A. A., Feb. 2001, *ApJ*, 548, 787–799.
- Sari, R., Feb. 2006, *Physics of Fluids*, 18, 027106.
- Shen, R.-F., & Song, L.-M. 2003, *Publications of the Astronomical Society of Japan*, 55, 345
- Shen, R., Kumar, P., & Robinson, E. L. 2006, *MNRAS*, 371, 1441
- Shen, R., Zhang, B., Oct. 2009, *MNRAS*, 398, 1936–1950.
- Soderberg, A. M., Chakraborti, S., Pignata, G., et al. 2010, *Nature*, 463, 513
- Shibata, M., Taniguchi, K., & Uryū, K. 2005, *Phys. Rev. D*, 71, 084021
- Sironi, L., Spitkovsky, A. 2009, *ApJ*, 698, 1523–1549.
- Tagliaferri, G., Goad, M., Chincarini, G., et al. Jul. 2000, *ApJ*, 538, 105–114.

Soderberg, A. M., Berger, E., Kasliwal, M., et al. 2006, *ApJ*, 650, 261

Stairs, I. H., Thorsett, S. E., Taylor, J. H., & Wolszczan, A. 2002, *ApJ*, 581, 501

Tanvir, N. R. et al. 2013, *Nature*, 500, 547

Taylor, J. H., & Weisberg, J. M. 1982, *ApJ*, 253, 908

Taylor, J. H., & Weisberg, J. M. 1989, *ApJ*, 345, 434

Troja, E., Cusumano, G., O'Brien, P. T., et al. Aug. 2007, *ApJ*, 665, 599–607.

Uhm, Z. L., Beloborodov, A. M., Aug. 2007, *ApJ*, 665, L93–L96.

Uhm, Z. L., Jun. 2011, *ApJ*, 733, 86.

Uhm, Z. L., Zhang, B., Hascoet, R., Daigne, F., Mochkovitch, R., Park, I. H., Aug. 2012, *ApJ*, 761, 147

Uhm, Z. L., Zhang, B., Mar. 2013a, ArXiv e-prints:1303.2704

Uhm, Z. L., Zhang, B., Jan. 2013b, ArXiv e-prints:1301.0291

Usov, V. V. Jun. 1992, *Nature*, 357, 472–474.

van Eerten, H. J., Wijers, R. A. M. J., Apr. 2009, *MNRAS*, 394, 2164–2174.

van Eerten, H. J., MacFadyen, A. I., Jun. 2012, *ApJ*, 751, 155.

Vetere, L., Massaro, E., Costa, E., Soffitta, P., & Ventura, G. 2006, *A&A*, 447, 499

Wanderman, D., & Piran, T. 2010, *MNRAS*, 406, 1944

Wang, X. Y., Dai, Z. G., Lu, T., Jan. 2001a, *ApJ*, 546, L33–L37.

Wang, X. Y., Dai, Z. G., Lu, T., Aug. 2001b, *ApJ*, 556, 1010–1016.

Wang, C., Lai, D., & Han, J. L. 2006, *ApJ*, 639, 1007

Wang, L.-J., & Dai, Z.-G. 2013, *ApJ*, 774, L33

Waxman, E., Aug. 1997a, *ApJ*, 485, L5.

Waxman, E., & Bahcall, J. 1997b, *Physical Review Letters*, 78, 2292

Waxman, E., Dec. 1997c, *ApJ*, 491, L19.

Wei, D. M., Lu, T., Sep. 1998, *ApJ*, 505, 252–254.

Weinberg, S. 1973, *American Journal of Physics*, 41, 598

Weisberg, J. M., Nice, D. J., & Taylor, J. H. 2010, *ApJ*, 722, 1030

Wijers, R. A. M. J., Rees, M. J., Mészáros, P., Jul. 1997, MNRAS, 288, L51–L56.
 Wijers, R. A. M. J., Galama, T. J., Sep. 1999, ApJ, 523, 177–186.
 Wong, T.-W., Willems, B., & Kalogera, V. 2010, ApJ, 721, 1689
 Wu, X. F., Dai, Z. G., Huang, Y. F., Lu, T., Jul. 2003, MNRAS, 342, 1131–1138.
 Wu, X. F., Dai, Z. G., Huang, Y. F., & Ma, H. T., 2004, RAA, 4, 455
 Wu, X. F., Dai, Z. G., Huang, Y. F., Lu, T., Jul. 2005, ApJ, 619, 968–982.
 Yi, S.-X., Wu, X.-F., Dai, Z. G., 2013, ApJ, 776, 120,
 Yost, S. A., Harrison, F. A., Sari, R., Frail, D. A., Nov. 2003, ApJ, 597, 459–473.
 Yu, Y.-W., Zhang, B., & Gao, H. 2013, ApJ, 776, L40
 Zhang, B., Mészáros, P., May 2001a, ApJ, 552, L35–L38.
 Zhang, B., Mészáros, P., Sep. 2001b, ApJ, 559, 110–122.
 Zhang, B., Mészáros, P., Jun. 2002a, ApJ, 571, 876–879.
 Zhang, B., Mészáros, P., Feb. 2002b, ApJ, 566, 712–722.
 Zhang, B., Kobayashi, S., Mészáros, P., Oct. 2003, ApJ, 595, 950–954.
 Zhang, B., Mészáros, P., 2004a, International Journal of Modern Physics A, 19, 2385–2472.
 Zhang, B., Dai, X., Lloyd-Ronning, N. M., Mészáros, P., Feb. 2004b, ApJ, 601, L119–L122.
 Zhang, B., Kobayashi, S., Jul. 2005, ApJ, 628, 315–334.
 Zhang, B., Fan, Y. Z., Dyks, J., et al. May 2006, ApJ, 642, 354–370.
 Zhang, B., Feb. 2006b7, Chinese Journal of Astronomy and Astrophysics 7, 1–50.
 Zhang, B., & Yan, H. 2011a, ApJ, 726, 90
 Zhang, B., Apr. 2011b, Comptes Rendus Physique, 12, 206–225.
 Zhang, B., & Kumar, P. 2013a, Physical Review Letters, 110, 121101
 Zhang, B. 2013b, ApJ, 763, L22
 Zhang, B. 2014, International Journal of Modern Physics D, 23, 30002
 Zhang, B.-B., Liang, E.-W., Zhang, B., Sep. 2007a, ApJ, 666, 1002–1011.
 Zhang, B., & Zhang, B. 2014, ApJ, 782, 92

- Zhang, J., Liang, E.-W., Zhang, S.-N., Bai, J.-M. 2012, ApJ, 752,157
- Zhang, W., Woosley, S. E., & MacFadyen, A. I. 2003, ApJ, 586, 356
- Zhang, W., MacFadyen, A., Jun. 2009, ApJ, 698, 1261–1272.
- Zalamea, I., & Beloborodov, A. M. 2011, MNRAS, 410, 2302
- Zou, Y. C., Wu, X. F., Dai, Z. G., Oct. 2005, MNRAS, 363, 93–106.
- Zou, Y.-C, Fan, Y.-Z., & Piran, T. 2009, MNRAS, 396, 1163
- Zou, Y. C., Wang, F. Y., Cheng, K. S., Aug. 2013, MNRAS, DOI:10.1093, ArXiv e-prints: 1307.2650.

VITA

Graduate College
University of Nevada, Las Vegas

He Gao

Degrees:

Bachelor of Science, Astronomy, 2007
Beijing Normal University

Master of Science, Astrophysics, 2010
Beijing Normal University

Publications:

[17] Jiu-Zhou Wang, Ding-Xiong Wang, Wei-Hua Lei, Yuan-Chuan Zou, Bing Zhang, **He Gao** and Chang-Yin Huang, *The quasi-periodic variations in X-ray emission and long-term radio observations: Evidence for two-component jet in Sw J1644+57*, Submitted to Astrophysics Journal.

[16] **He Gao**, Zhuo Li, Bing Zhang, *Fast Radio Burst/Gamma-Ray Burst Cosmography*, Submitted to Astrophysics Journal Letters.

[15] De Pasquale, Massimiliano; Kuin, N. P.; Oates, S.; Schulze, S.; Cano, Z.; Guidorzi, C.; Beardmore, A.; Evans, P. A.; Uhm, Z. L.; Zhang, B.; Page, M.; Kobayashi, S.; Castro-Tirado, A.; Gorosabel, J.; Sakamoto, T.; Fatkhullin, T.; Pandey, S. B.; Im, M.; Chandra, P.; Frail, D.; **Gao, H.**; Kopač, D.; Jeon, Y.; Akerlof, C.; Huang, L.; Pak, S.; Park, W.-K.; Gomboc, A.; Melandri, A.; Zane, S.; Mundell, C. G.; Saxton, C. J.; Holland, S. T.; Virgili, F.; Urata, Y.; Bersier, I. Steele. D.; Tanvir, N.; Sokolov, V. V.; Moskvitin, A. S., *The optical rebrightening of GRB100814A: an interplay of forward and reverse shocks?*, Submitted to Monthly Notices of the Royal Astronomical Society.

[14] Xue-Feng Wu, **He Gao**, Xuan Ding, Bing Zhang, Zi-Gao Dai, Jian-Yan Wei, *A Double Neutron Star Merger Origin for the Cosmological Relativistic Fading Source PTF11agg?*, Astrophysics Journal Letters 781,10, 2014

[13] **He Gao**, Wei-Hua Lei, Yuan-Chuan Zou, Xue-Feng Wu, Bing Zhang, *A Complete Reference of the Analytical Synchrotron External Shock Models of Gamma-Ray Bursts*, New Astronomy Review 57, 141, 2013

[12] Yunwei Yu, Bing Zhang, **He Gao**, *Bright "merger-nova" from the remnant of a neutron star binary merger: A signature of a newly born, massive, millisecond magnetar*, Astrophysics Journal Letters 776,40, 2013

[11] **He Gao**, Bing Zhang, Xue-Feng Wu, Zi-Gao Dai, *Possible high-energy neutrino and photon signals from gravitational wave bursts due to double neutron star mergers*, Physical Review D 88, 043010, 2013

[10] **He Gao**, Xuan Ding, Xue-Feng Wu, Bing Zhang, Zi-Gao Dai, *Bright Broad-band Afterglows of Gravitational Wave Bursts from Mergers of Binary Neutron Stars*, Astrophysics Journal 771,86, 2013

- [9] **He Gao**, Wei-Hua Lei, Xue-Feng Wu, Bing Zhang, *Compton scattering of self-absorbed synchrotron emission*, Monthly Notices of the Royal Astronomical Society, 435,2520, 2013
- [8] Weihua Lei, Bing Zhang, **He Gao**, *Frame Dragging, Disk Warping, Jet Precessing, and Dipped X-Ray Light Curve of Sw J1644+57*, Astrophysics Journal 762,98, 2013
- [7] En-Wei Liang, Liang Li, **He Gao**, Bing Zhang, Yun-Feng Liang, Xue-Feng Wu, Shuang-Xi Yi, Zi-Gao Dai, Qing-Wen Tang, Jie-Min Chen, Hou-Jun L, Jin Zhang, Rui-Jing Lu, Lian-Zhong L, Jian-Yan Wei, *A Comprehensive Study of Gamma-Ray Burst Optical Emission. II. Afterglow Onset and Late Re-brightening Components*, Astrophysics Journal 774,13, 2013
- [6] Liang Li, En-Wei Liang, Qing-Wen Tang, Jie-Min Chen, Shao-Qiang Xi, Hou-Jun L, **He Gao**, Bing Zhang, Jin Zhang, Shuang-Xi Yi, Rui-Jing Lu, Lian-Zhong L, Jian-Yan Wei, *A Comprehensive Study of Gamma-Ray Burst Optical Emission. I. Flares and Early Shallow-decay Component*, Astrophysics Journal 758,27, 2012
- [5] **He Gao**, Bin-Bin Zhang, Bing Zhang, *Stepwise Filter Correlation Method and Evidence of Superposed Variability Components in Gamma-Ray Burst Prompt Emission Light Curves*, Astrophysics Journal 748,134, 2012
- [4] **He Gao**, Nan Liang, Zonghong Zhu, *Calibration of GRB luminosity relations with cosmography*, International Journal of Modern Physics D 21, 1250016 ,2012
- [3] Bin-Bin Zhang, Bing Zhang, En-Wei Liang, Yi-Zhong Fan, Xue-Feng Wu, Asaf Pe'er, Amanda Maxham, **He Gao**, Yun-Ming Dong, *A comprehensive analysis of Fermi Gamma-Ray Burst data. I. spectral components and the possible physical origins of LAT/GBM GRBs*, Astrophysics Journal 730,141, 2011
- [2] Ye Lu, **He Gao**, *A black hole preying on a star for GRB080503: evidence for the second event in this new class*, Science in China Series G 53S, 117L, 2010.
- [1] **He Gao**, Ye Lu, Shuangnan Zhang, *A new class of gamma-ray bursts from stellar disruptions by intermediate mass black holes*, Astrophysics Journal 717,268, 2010

Dissertation Title:

Physics of Gamma-ray Bursts and Multi-messenger Signals from Double Neutron Star Mergers

Dissertation Examination Committee:

Chairperson, Bing Zhang, Ph.D.

Committee Member, Daniel Proga, Ph.D.

Committee Member, Kentaro Nagamine, Ph.D.

Graduate Faculty Representative, Amei Amei, Ph.D.